National Science Foundation under Grant #ATM-9420045, ATM-9118963, and ATM-8919080

OBSERVATIONAL AND NUMERICAL ANALYSIS OF THE GENESIS OF A MESOSCALE CONVECTIVE SYSTEM

by Jason Edward Nachamkin

William R. Cotton, P.I.

Colorado State University

DEPARTMENT OF ATMOSPHERIC SCIENCE

PAPER NO. 643

OBSERVATIONAL AND NUMERICAL ANALYSIS OF THE GENESIS OF A MESOSCALE CONVECTIVE SYSTEM

by

Jason Edward Nachamkin

Department of Atmospheric Science

Colorado State University

Fort Collins, CO 80523

Research Supported by

the National Science Foundation

under Grants ATM–9118963, and ATM–9420045

the CSU CHILL cooperative agreement

under Grant ATM–8919080

February 5, 1998

Atmospheric Science Paper No. 643

ABSTRACT

OBSERVATIONAL AND NUMERICAL ANALYSIS OF THE GENESIS OF A MESOSCALE CONVECTIVE SYSTEM

A high resolution observational and numerical study was conducted on a mesoscale convective system (MCS) that developed in northeastern Colorado on 19 July 1993. Convection was followed from its origins in the Rockies west of Denver as it grew to near mesoscale convective complex (MCC) proportions over the plains. Five–minute surface data was collected from 48 mesonet stations over eastern Colorado, and six–minute dual Doppler data were collected from the CSU–CHILL and Mile High radars. The Regional Atmospheric Modeling System (RAMS) was then used to simulate this case. Initialization with variable topography, soil moisture, and atmospheric conditions facilitated the simulation of the inhomogeneous environment and its interactions with the MCS. Convection was explicitly resolved on the finest of four telescopically nested, moving grids. Storms developed consistently within the model without any artificial triggers such as warm bubbles or cold pools. Comparisons with the observations showed strong agreement down to the scale of the individual Doppler scans.

The results show that convective position was deterministically focused by thermally driven solenoidal circulations and their interaction with a preexisting surface front. Away from the mountains, convection was fed by an intense low level jet less than 200 km across. The jet formed over southeastern Colorado in a region of localized thermal contrasts on either side of the plains inversion.

Interactions between convection and its surrounding environment existed in two modes. When the upward mass flux was of moderate strength, continuity was maintained by linear, low frequency gravity waves. Most of the wave energy propagated rearward from the

convective line, even though strong upper tropospheric shear advected most of the condensate ahead of the line. Almost all of the environmental compensating motions propagated rearward with the waves, inducing upper tropospheric front–to–rear and mid tropospheric rear–to–front perturbations in their wake. Most of the subsidence heating was also restricted to the narrow zone of wave propagation. When the convective mass flux became intense near sunset, condensate, heat and momentum were advected directly into the upper troposphere in a nonlinear outflow. The oval–shaped cold cloud top was defined by the leading edge of the outflow, and unlike the gravity waves, gradients of heat and momentum only slowly dispersed. This suggests that intense MCSs and MCCs with well defined anvils are more likely to produce a balanced disturbance because proportionately less energy is lost to gravity waves.

Jason Edward Nachamkin
Department of Atmospheric Science
Colorado State University
Fort Collins, Colorado 80523
Spring 1998

ACKNOWLEDGEMENTS

I wish to thank Ray McAnelly for his generous advice and guidance. Ray also helped with the field project, provided the software for combining the radar and mesonet data, and provided plots of the satellite data. I also wish to thank Lígia Bernardet, Cathy Finley and Louie Grasso for donating many hard fought hours to improving the model code, and for showing me how to use RAMS.

Many ideas for this research came from getting out in the field and chasing storms. Greg Thompson was instrumental in this arena, not only for his insight, but also for his persuasive abilities. In that light, I wish to thank my advisor Bill Cotton for allowing me the flexibility to investigate the atmosphere in those terms, and for providing me the rare opportunity to round out my education from both a modeling and observational perspective.

Talks with Pat Haertel, Mel Nicholls, and Mike Montgomery provided much insight to the dynamics behind the gravity waves. Jason Knievel, Zach Eitzen, David Mocko, John Knaff, Brian Gaudet, Lígia Bernardet, Jim Edwards, Jim Bresch, Cathy Finley, Louie Grasso, Hongli Jiang and Sue Van Den Heever also provided valuable scientific insight as well as friendship and support. I also wish to thank my Ph. D. committee, Richard Johnson, Roger Pielke, and Chandra for their help with this research.

The data and support for this research were kindly provided by a number of people. Steve Rutledge, Pat Kennedy, Dave Brunkow, and Ken Pattison provided data and field project support from the CSU–CHILL. Bob Rilling (NCAR) provided the Mile High data, and Michele Case (NCAR) was helpful with the radar software. Peter Neilley (NCAR), and Jerome Schmidt (NOAA) provided the MAPS and mesonet data, while the MAPS degribbing software was provided by Greg Thompson (NCAR). Satellite data was obtained from Nan McClurg and CIRA, and Brian Bietler (CSU) provided mesoscale forecasts from the RAMS model during the field project. Computer and software support was provided by Donna Chester, Doug Burks, John Blanco, and Steve Finley. Special thanks goes to the Cotton and Pielke groups, who over the years have worked hard to constantly improve RAMS. Jim Edwards, Bob Walko, and Craig Tremback were in charge of RAMS code implementation and improvement through some or all of this time. Brenda Thompson and Abby Hodges helped with the manuscript preparation. This work was supported by the National Science Foundation, under grants ATM-9118963, ATM-9420045, and through a 20-h minigrant from the CSU-CHILL cooperative agreement ATM-8919080.

Finally, I wish to thank my parents, Bev Ayers-Nachamkin and Jack Nachamkin for their love and support through this journey.

TABLE OF CONTENTS

LIST OF FIGURES

LIST OF TABLES

Chapter 1

INTRODUCTION

Convective instability is released on a continuum of scales in the atmosphere, with individual cumulonimbus clouds being the most basic and common modes of its release (Cotton et al. 1995). However, under the correct conditions, individual convective storms will group into clusters or lines consisting of multiple cells in close proximity. Classified most generically as a mesoscale convective system (MCS), these disturbances appear almost as frequently as the isolated thunderstorms, and are characterized by a broad cloud shield resulting from the merger of the respective thunderstorm anvils. Although MCSs come in many shapes and sizes, they almost always generate heating and momentum perturbations that are larger in scale than the sum of their respective convective cells (Cotton and Anthes, 1989).

The process by which convection affects the atmosphere on the mesoscale is one of the most notable, and as yet unknown features of an MCS. Due to limitations in computer capacity and observational networks cloud–resolving MCS studies are often limited to the contiguous, mature system, and in many cases cover just part of an MCS. Thus, the question of how the MCS affects its environment is often addressed from the rather one–sided MCS–relative point of view. However, this does not mean that the environment is unimportant in consolidating the convection necessary for an MCS. Maddox (1983), Velasco and Fritsch (1987), Tripoli and Cotton (1989a), Trier and Parsons (1993), and Laing (1993a,b) all suggest that the environment plays a crucial role in determining where and when a particularly intense type of MCS known as a mesoscale convective complex (MCC) will develop. However, most of these environmental studies take place on the synoptic scale. Are there unresolved cloud scale environmental features that act to focus intense nocturnal

MCSs? Could this be one reason why many coarse–resolution simulations of these storms involving convective parameterization fail?

Then there is the question of how the individual convective cells affect the surrounding environment. Convective storms start out on very small scales, on the order of a few kilometers, but the resulting MCS circulations are projected onto the mesoscale. Most existing investigations of these circulations have been conducted on mature systems with large stratiform anvils. In these studies, the kinematic storm–relative flows are identified, and the nature of the dynamic forcing is assessed based on the existing structures. While this method is valuable in determining the pertinent forces in mature systems, it does not necessarily explain how the circulations got there. Other factors may have been important when the system was first expanding. For example, some MCSs, especially MCCs, exhibit an explosively growing upper cloud that rapidly becomes quite intense. Is there anything special about the way heat and momentum propagate in an anvil like this as opposed to a weaker system? Deep stratiform anvils have been touted by many as being critical for the development of the consolidated MCS circulations. However, Schmidt and Cotton (1991) and Mapes (1993) suggest that convectively generated gravity waves can also induce these circulations, even in the absence of stratiform precipitation. What are the relative roles of these waves with respect to the stratiform anvil expansion? Once a large stratiform anvil has developed in a mature system, separating the gravity wave effects from the anvil effects is quite difficult. Balanced model simulations such as those used by Olsson and Cotton (1997) would be required to perform such a separation. To mitigate this problem, this study starts with the first convective cells and explicitly investigates the expansion of the circulations into the environment prior to the development of a large stratiform anvil.

This work follows the efforts of Nicholls et al. (1991), Schmidt and Cotton (1991), Mapes (1993), Nachamkin (1994), Klimowski (1994), and McAnelly and Cotton (1997) in studying the fine–scale interactions between convection and its surroundings. This is accomplished through a highly detailed observational and numerical study of a convective system that formed over eastern Colorado during 19–20 July 1993. Extensive dual Doppler and mesonet data were available through most of the early growth stages of the storm as it developed in the mountains and propagated onto the plains. Additionally, the Regional

Atmospheric Modeling System (RAMS) was used to simulate this case. Observed initial conditions were used along with four telescopically nested, interactive grids with spacings of 80, 20, 5, and 1.67 km respectively. Since convection was explicitly resolved on the finest grid, its timing, intensity, position, and structure could be directly compared to the mesonet and dual Doppler volume scans with detail that is rarely available.

Comparisons showed strong agreement between the observed and simulated systems, with many of the same convective scale features appearing in both. The high accuracy of the model was in a large part due to the strong environmental forcing which very deterministically focused the convection. The three–dimensional nature of this forcing is discussed, as well as several fine–scale environmental features that were critical to the rapid intensification of this system. This case was fortuitous in that most of the stratiform anvil advected ahead of the system in the strong upper tropospheric shear. Thus, convectively induced perturbations on the trailing side of the convective line were effectively separated from the diabatic heating within the stratiform anvil.

Chapter 2

BACKGROUND

2.1 Introduction

Convective systems are the result of an intricate interaction between convection and the environmental forcing that generated it. Given conditions generate certain types of convection, which in turn feeds back upon the environment on many scales. Considerable research has been conducted in this area, and in this chapter some of the latest findings are reviewed.

2.2 Response to thermal forcing in an environment at rest

All mesoscale convective systems, regardless of their convective organization, consist of the constructive "upscale" interaction of many individual convective thunderstorm cells. Even more fundamentally, each thunderstorm can be thought of as a column of intense latent heating and cooling that affects the surrounding environment. The term "upscale", and thus MCS, is defined in this work after McAnelly et al. (1997), as a contiguous cloud canopy containing an ensemble of convective storms along with a mesoscale region of stratiform cloud. Such systems take on many shapes with regard to the orientation of the convection and stratiform components (Houze et al. 1990). Central to the definition however, is the existence of widespread mid and upper tropospheric flows that prevail through the entire system. These flows in the form of the front–to–rear flow and rear inflow jet (Smull and Houze, 1987; Houze et al. 1989) are nearly ubiquitous in the quasi-two dimensional squall line system. Other systems with more complex convective organization also exhibit similar features (Stumpf et al. 1991; Fortune el al. 1992; Nachamkin et al. 1994). The underlying theme being that the circulations within the MCS are larger than the individual convective storms that originally brought them forth.

Given that definition, how do these circulations come about? The contiguous precipitation region itself has been implicated in many studies. LeMone (1983) showed that a hydrostatic low forms due to heating from rearward leaning convective towers. Brown (1979), and Smull and Houze (1987) pointed out that the combination of general latent heating within the stratiform anvil and cooling at low levels combine to lower the mid-tropospheric pressure and in turn draw in mid level air. Leary and Houze (1979) and Smull and Houze (1987) also demonstrated that melting and evaporative cooling can aid in the descent of the rear inflow. Lafore and Moncrieff (1989) attributed rear inflow to a horizontal rear–to–front pressure gradient in the mid troposphere beneath the stratiform region. Weisman (1992) hypothesized that horizontal buoyancy gradients along the back edge of an expanding convective system create a circulation that draws in mid tropospheric air from behind the system.

The mechanisms above all imply that mesoscale flows would not develop before the existence of a large stratiform anvil. However, evidence is increasing that such circulations can, in certain conditions, propagate into the clear air surrounding a group of convective cells. Thus, forcing from the convective portion alone can initiate these circulations. This idea seems counter–intuitive when watching a thunderstorm anvil spread across the sky. To the eye, the mass disturbance appears to propagate out at the speed of the visible cloud. However, this is not always the case in a fluid. Instead, compensating motions can propagate outward from the initial disturbance in the form of internal gravity waves that will often outrun the speed of the spreading anvil. Bretherton and Smolarkiewicz (1989), Nicholls et al (1991), Pandya et al., (1993), Mapes (1993), Pandya and Durran (1996), and McAnelly et al. (1997) have described these waves in the linearized, analytic solution, while Bretherton and Smolarkiewicz (1989), Schmidt and Cotton (1990), and Pandya and Durran (1996) have demonstrated their existence in two dimensional, explicit, nonlinear convective models. Mapes (1993) also showed that dye lines in a water tank well outside of a mass disturbance were affected by the passage of internal waves.

The structure of these waves is quite different from the more typical internal sinusoidal disturbances such as mountain waves. The leading edges of these nonsinusoidal waves consist of a pulse of vertical motion that propagates away from the convective heating leaving a

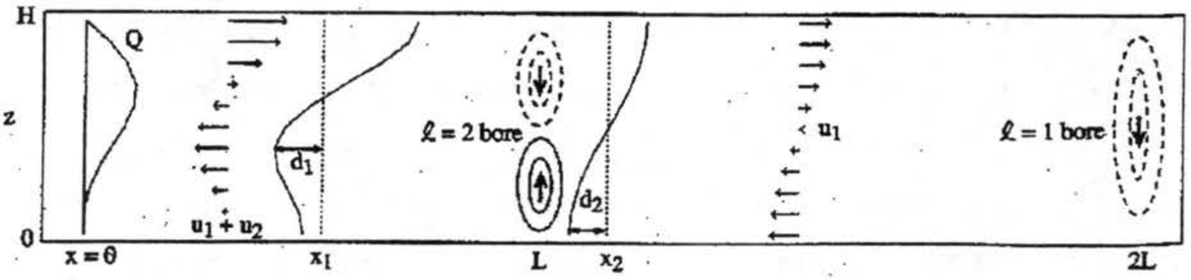

Figure 2.1: Schematic representation of the vertical cross section of the low frequency internal gravity waves, from Mapes (1993). The heat source containing both n1 and n2 forcing defined by Equation 2.4 is shown by the profile Q at x = 0. The vertical motions at the leading edges of the $n1$ and $n2$ modes are denoted by $\ell = 1$ bore and $\ell = 2$ bore respectively. Perturbation horizontal flow induced by the passage of each bore is depicted by the horizontal arrows.

uniform region of horizontal flow in their wake (Fig. 2.1). Thus net parcel displacements are produced with their passage. If the convective heat source is turned off, a second, equal and opposite pulse of vertical motions propagate out, and the entire circulation moves along as a large roll. The phase speed and group velocity equations for nonhydrostatic, Boussinesq, linear, two dimensional flow are shown below,

$$c = u \pm \frac{N^2}{(k^2 + m^2)}, \tag{2.1}$$

$$c_{gx} = u \pm \frac{N m^2}{(k^2 + m^2)^{\frac{3}{2}}}, \tag{2.2}$$

$$c_{gz} = u \mp \frac{N k m}{(k^2 + m^2)^{\frac{3}{2}}}, \tag{2.3}$$

where k is the horizontal wave number, m is the vertical wave number, and N Brunt-Väisällä frequency. Bretherton and Smolarkiewicz (1989) pointed out that these waves (Fig. 2.1) are hydrostatic, and are represented in Equations 2.2–2.3 by modes with low horizontal frequencies and high vertical frequencies ($m >> k$). Both the phase and group (energy) velocity are almost horizontal[1] and equal to $\frac{N}{m}$.

In an atmosphere of constant stability the vertical shape of these waves, or buoyancy bores as referred to by Mapes (1993), is dependent on the strength and vertical wave

[1] Pandya et al. (1993) pointed out that there is vertical energy propagation, and $c_{gz} = \frac{k}{m} c_{gx}$.

number of the heating that created them. The bores are in essence compensating motions that account for the vertical motions forced by the heating. The heating profile Q in Figure 2.1 was defined by Mapes (1993) as

$$Q = Q_0[sin(\frac{\pi z}{H}) - \frac{1}{2}sin(\frac{2\pi z}{H})], \tag{2.4}$$

where Q_0 is the amplitude of the heating and H is the depth of the fluid, which in this case is considered to be the troposphere. The profile in (2.4) represents the combination of convective and stratiform diabatic heating integrated over an entire MCS. The deep heating in the first term on the right hand side of (2.4) forces upward motion through the depth of the troposphere whereas the second term forces upward motion aloft and downward motion below. The resulting bores in Figure 2.1 are simply the manifestation of compensating motions that are required by continuity.

The waves are dispersive with respect to m, so the speed of each bore is dependent upon its vertical structure, with the higher order modes propagating more slowly. The vertical wave number can be represented in terms of the atmospheric depth by $m = \frac{n\pi}{H}$, where n determines how many waves fit into the fluid depth[2]. In an MCS, the bulk of the heating is confined to the troposphere, which in the mid latitudes is about 10 km deep. In this situation, $N \sim 0.01$ and the $n = 1$ ($n1$) mode ($\ell = 1$ in Fig. 2.1) propagates at about 30 m s^{-1}, while the $n = 2$ ($n2$) mode ($\ell = 2$ in Fig. 2.1) propagates at about 15 m s^{-1}. In the tropics, where H is considerably larger, these waves can travel much faster. Although atmospheric convection demonstrates a general propensity to concentrate heating in the $n1$ and $n2$ modes, Mapes (1993) caveats that in the real atmosphere, a continuum of vertical modes are actually forced.

The structure of the horizontal circulations in the wake of the $n2$ mode (Fig 2.1) is quite similar to the front–to–rear and rear–to–front flows. Schmidt and Cotton (1990) and Pandya and Durran (1996) raised the question of whether these circulations can actually develop in the absence of stratiform precipitation. They found that in two dimensions,

---

[2]The general convention followed in this work is to set $n = 1$ for the mode that fits one half of its vertical wavelength within depth H.

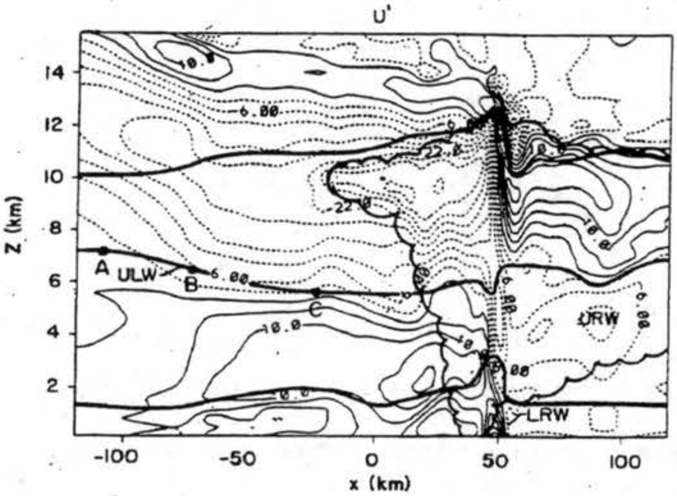

Figure 2.2: Vertical cross section of storm induced perturbation (with respect to the initial conditions) flow in a two dimensional squall line simulation with strong vertical shear, from Schmidt and Cotton (1990). Negative contours are dashed and the contour interval is 4 m s^{-1}. The cloud edge is represented by the dark scalloped line, while the heavy solid lines represent isentropic surfaces.

circulations forced by convective thermal forcing extended into the environment beyond the trailing anvil (Fig. 2.2). Mapes (1993) and Pandya and Durran (1996) showed that as the buoyancy bores spread into the surrounding environment, continuity dictates that horizontal circulations must be *induced* in their wake. As mentioned above, this is somewhat counter-intuitive because it means that the divergent flow at anvil top does not entirely result from parcels spreading directly away from the decelerating updrafts. Instead, the low frequency waves propagate into the environment and induce divergent flow in their wake well outside the visible cloud. Were this not the case, compensating motions could not spread into clear air outside the anvil as Fritsch (1975) suggested.

The fine–scale structure of the buoyancy bores has not been well observed. Most high resolution observational studies of convection employ Doppler radar to investigate mature MCSs where the flow structures are already established (e.g. Rutledge et al. 1988). Unfortunately, radar can only detect flow in places where precipitation sized particles, or at least dense cloudiness already exists. Despite these limitations, some observational evidence for the existence of the buoyancy bores has been documented. Fritsch (1975) composed a conceptual model based on an eclectic collection of aircraft and sounding observations that indicated compensating subsidence should propagate into the environment. He noted however that the structure of the subsidence was unknown at the time. Nachamkin (1994) found that rear inflow in a growing MCS was originally ascending despite the existence of deep stratiform anvil. Descent in the rear inflow later propagated rapidly outward from an intensifying convective cluster, indicative of possible blocking aloft. Using a high resolution sounding network, Johnson et al. (1995) found atmospheric structures resembling the $n2$ mode in the clear air between two adjacent MCSs. Sinking motions dominated the upper troposphere, while weak upward motion persisted below 600 hPa. In the mid troposphere, perturbation winds of up to 12 m s^{-1} flowed towards each MCS, while upper tropospheric perturbation winds flowed away from the MCSs. Johnson et al. (1995) hypothesized that these circulations were responsible for strengthening the capping inversion and thus preventing additional convection from breaking out. Klimowski (1994) observed that rear inflow formed rapidly in-situ behind erect convective cells, and also at the trailing edge of the stratiform precipitation. Klimowski's observations could be used to support the induction of rear inflow by internal waves since rear inflow appeared rapidly after the development of a given cell. However, his observations of rear inflow maxima in the stratiform region also indicate that heating and cooling there as described by Smull and Houze (1987) plays a role. Both mechanisms are likely operating, which is probably why no one has come up with the definitive answer yet!

The theory that a large stratiform cloud shield is necessary to produce mesoscale flows implies that these circulations react to pressure fields forced *locally* by the hydrostatic effects of latent heating and cooling. On the other hand, the internal wave theory implies that the mesoscale flows are induced *nonlocally* by the outward propagation of internal waves away from the original heating and cooling. Both processes are likely occurring and should not be neglected. The stratiform precipitation theory in and of itself, however, does not fully account for the presence of compensating vertical motions outside the contiguous anvil. Continuity dictates that some kind of horizontal circulation must be induced by these motions. As we shall see, the nature and rapidity of the upscale development process is intimately tied to the shape, orientation and strength of the convective latent heating.

2.3 The mesoscale convective complex and its synoptic environment

MCSs are intimately linked to their surroundings. Not only can the effects of convection radiate away to the environment, but the structure of the environmental forcing dictates the nature of any convection to begin with. Since MCSs are driven by deep convection, environmental parameters that favor intense, persistent storms are more likely to favor large, long–lasting MCSs. The exception being environments of high shear, or low bulk Richardson number. These conditions tend to favor more isolated supercells and squall lines (Weisman and Klemp, 1984; Maddox, 1983), however the line between severe storms and MCSs is quite blurry. Supercells and severe storms are observed in MCSs, particularly during the early growth stages (Maddox, 1983; Houze et al. 1990). Although important, shear is only one of many factors that determine the nature of convection.

2.3.1 The mesoscale convective complex

The environmental conditions associated with one particularly intense type of MCS known as a mesoscale convective complex (MCC) have received a lot of attention in recent years. A system is classified as an MCC if the satellite cloud shield meets the criteria defined by Maddox (1983) listed in Table 1. These were meant to differentiate the MCC from smaller, weaker systems, as well as the more linear squall systems. However, the exclusion of the higher eccentricity anvils does not mean that MCCs do not exhibit linear convective organization. Houze et al. (1990) showed that MCCs display all types of convective organization, ranging from leading–line/trailing–stratiform to unclassifiably chaotic. Houze et al. (1990) also found that many intense springtime rainstorms qualitatively resembled MCCs, but did not quite meet the criteria in Table 2.1. The case studied in this dissertation is one such example. An intense, cold oval anvil was maintained for over six hours, but it only marginally met the MCC size criteria.

Cotton et al (1989) applied the Rossby radius of deformation (Frank, 1983), to form the basis of a dynamic definition of an MCC. This quantity is defined by

$$\lambda_R = \frac{NH}{(\zeta + f)^{0.5}(2VR^{-1} + f)^{0.5}} \tag{2.5}$$

Size	**A**. Cloud shield with IR temperature $\leq$ -32 $°C$ must have an area $\geq$ 100,000 km^2 **B**. Cloud shield with IR temperature $\leq$ -52 $°C$ must have an area $\geq$ 50,000 km^2
Initiate	Size definitions **A** and **B** are first satisfied
Duration	Size definitions **A** and **B** must be met for a period $\geq$ 6 hrs
Maximum extent	Contiguous cloud shield (IR temperature $\leq$ -32 $°C$) reaches maximum size
Shape	Eccentricity (minor axis/major axis) $\geq$ 0.7 at time of maximum extent
Terminate	Size definitions A and B no longer satisfied

Table 2.1: Satellite characteristics of an MCC cloud shield after Maddox (1983).

where N is the Brunt-Väisällä frequency, H is the scale height of the circulation, ζ is the vertical component of the relative vorticity, f is the Coriolis parameter, V is the tangential wind around the disturbance, and R is the radius of curvature. Once a system exceeds λ_R, energy from transient disturbances, generally in the form of gravity waves, becomes projected onto the larger scale or balanced circulation. The definition of "balance" varies, depending upon the type of circulations one is looking for. For instance, Cotton et al. (1989) implied that MCCs larger than λ_R were geostrophically balanced. However, Olsson and Cotton (1997) noted that the geostrophic approximation was too restrictive because gradient wind and highly curved flow are not considered to be balanced. In that light, Olsson and Cotton (1997) used the nonlinear balance approximation such that those flows, which are prevalent in MCCs could be included. Regardless of the approximation used, the concept of balance implies that the wind field adjusts to perturbations in the mass field when the scale of the disturbance exceeds λ_R. The divergent flow becomes slaved to the rotational, balanced flow, and the energy being produced within the disturbance is not lost to the far field. In the case of convection, subsidence, and thus heat propagates away as gravity waves in a unbalanced system (Cotton and Anthes, 1989). In a balanced system, however, subsidence is sustained and occurs just outside the region of convection. Balanced systems are generally long–lived, and in cases of weak tropospheric shear, closed vortices on the order of several hundred kilometers across can last for days (Bosart and Sanders, 1981; Bartels and Maddox, 1991; Johnson and Bartels, 1992; Fritsch et al. 1994).

In a composite of MCCs taken over the United States, Cotton et al. (1989) found that the typical value of λ_R for most midlatitude systems was ~ 300 km. This was slightly smaller than the average cloud shield radius of ~ 320 km. In another study, Johnson and Bartels (1992) obtained similar values. With all else being equal, Cotton et al. (1989) noted that the Coriolis parameter tends to dominate Eq. 2.5 in the mid latitudes. Thus, λ_R at higher latitudes will be smaller due to the increase in the background inertial stability. However, these results need to be interpreted with caution since λ_R is difficult to calculate for a given MCC (Cotton and Anthes, 1989; Olsson and Cotton, 1997). Moist processes will affect the value of N, creating locally strong gradients in λ_R. Olsson and Cotton (1997) alson noted that since NH was the speed of the nth pure gravity wave mode, there would be several Rossby radii corresponding to the dominant gravity wave modes. Cotton et al. (1989) chose an average value of $NH = 30$ m s^{-1} based on results from the two dimensional simulations of Tripoli and Cotton (1989). Olsson and Cotton (1997) calculated λ_R separately for the $n1$ and $n2$ modes and obtained 509 and 255 km respectively. The large values resulted from the deep convection, and thus more rapidly propagating modes in that case. If significant relative vorticity develops within a given system, the resulting increase in inertial stability can significantly reduce λ_R (Schubert and Hack, 1982). When Olsson and Cotton (1997) accounted for the storm–relative vorticity at the center of a mesoscale convective vortex that had developed in their MCC simulation, λ_R was reduced to 138 and 69 km for the $n1$ and $n2$ modes respectively.

Some evidence suggests that the convection responsible for MCCs and their qualitatively similar counterparts is fundamentally different from that of weaker MCSs. Maddox (1980), McAnelly et al. (1986), Velasco and Fritsch (1987) all note that most MCC cloud shields grow explosively early in their life cycle, rapidly attaining an oval shape. Maddox (1980), and Velasco and Fritsch (1987) also noted that intense mid latitude systems exhibit very uniform cold cloud shields in which the individual convective cells are difficult to distinguish. However, Velasco and Fritsch (1987) observed that weaker, low latitude systems did not display this structure. Although the cloud shields met the satellite criteria, they contained many irregularities and qualitatively resembled an agglomeration of big thunderstorms. Laing and Fritsch (1997) suggested that the strong early growth may be the distinguishing factor between the intense, symmetric systems and the weaker agglomerations. However, the reasons for this distinction were not readily apparent.

2.3.2 MCC environmental conditions

Some clues to the nature of MCC convection may be found in the environments in which they characteristically develop. These systems are generally found over land (Maddox, 1980; Laing and Fritsch, 1997) in environments of high convective available potential energy (CAPE) (Maddox, 1983; Cotton et al. 1989). Maddox (1983) implied that the deep tropospheric shear was generally weak, however, as mentioned above, recent studies by Houze et al. (1990) and Fortune et al. (1992) have noted several cases that developed in moderate upper tropospheric shear. Maddox (1980), McAnelly and Cotton (1989), Laing and Fritsch (1997) also noted that MCCs closely followed the migration of the polar jet. In accordance with this, the MCC environment has been found to contain varying degrees of baroclinicity. Maddox (1983) noted that MCCs often formed in regions of strong lower tropospheric warm advection, and were often associated with a mid tropospheric short wave trough. Laing (1997) also found that MCC environments tended to exhibit stronger low level baroclinicity than more linear systems. She attributed this to the propensity for many squall lines to propagate along a convectively generated (prefrontal) cold pool, while MCCs were more likely to be anchored to an east–west oriented, nearly stationary surface front. In contrast, Wetzel et al. (1983), Cotton et al. (1989), and McAnelly et al. (1997) found that MCCs could also develop in nearly barotropic environments in the absence of a short wave trough. Most of the systems sampled in those studies occurred late in the convective season, when the polar jet was weak and quite far north. These studies suggest, however, that more than one external, environmental mechanism is at work focusing convection.

With these varied conditions resulting in MCCs, what do most systems have in common? Maddox (1983) and Cotton et al. (1989) found that mesoscale convergence and upward motion often preceded the development of an MCC by as much as 12 hours, regardless of the environmental baroclinicity. This indicates that some aspect of the ambient environment is focusing energy in a specific area. Baroclinic short waves are one possible mechanism for this. Moderate to strong shear associated with the polar westerlies often retards isolated convection in areas not under the influence of a short wave or other convective trigger. However, there are other features common to MCC type convection that are not always associated with baroclinic flow environments.

In most parts of the world MCCs occur in favored zones downwind of mountain ranges (Augustine and Howard, 1991; Velasco and Fritsch, 1987; McAnelly and Cotton, 1989; Laing and Fritsch, 1993a,b, and Laing, 1997). The physiographic barriers play important roles in the development of nocturnal low level jets and capping inversions, which in tandem act to intensify and focus convection (Maddox, 1983; Velasco and Fritsch, 1987; Tripoli and Cotton, 1989a). The low level jet is a focused source of ample lower tropospheric heat and moisture. These jets are often found on the leeward side (with respect to the prevailing deep tropospheric flow) of mountain ranges (McNider and Pielke, 1981), and Velasco and Fritsch (1987), Maddox (1983), and Laing (1997) found evidence of nocturnal low level jets in MCC environments in the Americas and China.

Although the capping inversion has not received much attention in the MCC literature, it plays a large role in creating focused and intense convection. In a comprehensive study of the North American mid tropospheric inversion, Lanicci and Warner (1990a–c) found that air within the capping inversion often originated over the high plateaus of the Mexican and American Rocky Mountains. During the convective season, diurnally heated boundary layer air over the elevated terrain was advected over the plains by the prevailing southwesterly flow. This warm, unstable air, often referred to as an elevated mixed layer (EML), caps the plains boundary layer, and allows for the build–up of very high CAPE. The cap prevents small, unfocused convective systems from developing and releasing the CAPE slowly. Only moderate to strong forcing such as that of a short wave (Maddox, 1983), or lifting of the low level jet above a surface frontal surface (Trier and Parsons, 1993) is enough to break the cap and release the CAPE.

Maddox (1983) and Laing (1997) also note that, the trigger mechanism and its orientation with respect to the forcing is important. MCCs generally occur to the east of the mid tropospheric ridge axis whereas outbreaks of severe weather associated with squall lines and isolated, supercells tend to occur just east of the trough axis, beneath a diffluent upper tropospheric jet core (Miller and McGinley, 1978). The difference here is the trigger for the severe storms is often a front or dryline that sweeps eastward at an angle to the lower tropospheric shear. On the other hand, the MCC trigger is often a stationary east–west front that is nearly perpendicular to the low level jet. In that situation, all of the energy in the low level jet can be concentrated in one confined area.

The unifying theme of the MCC environment thus appears to be that a tremendous amount of energy is released at once over a very consolidated region. This returns to the notion that MCC convection may be different than convection in ordinary MCSs. Perhaps the intensity and longevity of the convective storms within the MCC produces an atmospheric disturbance that is fundamentally different from that of weaker MCSs. At the very least, MCCs are intimately tied to the surrounding environmental forcing, and are not likely to spontaneously develop. Many places such as the Amazon Basin, and most oceanic regions experience widespread convection but relatively few MCCs (Velasco and Fritsch, 1987; Laing, 1997). Although copious amounts of moisture are available, the environment lacks the means with which to focus it into an intense system on the mesoscale.

2.4 Mesoscale topographical influences on convection

It has already been shown that topography can influence the synoptic scale environment, allowing for the development of intense, long–lived convection. However, there are also many smaller, mesoscale–β–scale (20–200 km) and even meso–γ–scale (2–20 km) (Orlanski, 1975) topographical effects that help to initiate and maintain strong convection. The MCS studied herein, developed in eastern Colorado and was strongly influenced by topographically induced flows. Thus we digress a bit here to discuss some of the previous research in–depth.

Wetzel (1973), Maddox (1981), Wetzel et al. (1983), McAnelly and Cotton (1986), Tripoli and Cotton (1989a), and Tremback (1990) have all implicated the Rocky Mountains as being an important birthplace for MCSs from New Mexico to Canada. Mountains are highly efficient at destabilizing the atmosphere in a concentrated region. On the first order, they act as an elevated heat source, producing unstable parcels of air at levels of the atmosphere that are normally cool (Silverman, 1960). More importantly, Braham and Draginis (1960) found that diurnal warming in general forces air to flow up the heated slopes to converge at the top in a convective chimney. This not only provides a region of elevated warm air, but mass and moisture convergence as well. The upslope flow can also advect moisture from lower elevations for further destabilization.

The position and structure of this chimney relative to the top of the peak is dependent upon the ambient flow. Dirks (1969) found that flow over ridge top tended to displace the convergence zone downstream of the mountain top, and vertical motions were sharper, stronger and deeper. The air flowing upslope was also found to have lower potential temperatures (Braham and Draginis, 1960). Holton (1967) indicated that the increased stability can act as a break on the intensity of the upslope flow. Clouds and the increased friction of the complex terrain will also affect the strength of the upslope (Dirks, 1969).

The solenoidal circulation is completed by a return flow of downward motion directly above the upslope. Although Buettner and Thyer (1965) and Fosberg (1967) found this compensating flow to be generally weak and hidden in the ambient winds, its structure plays a vital role in the organization of subsequent convective storms. In an idealized two–dimensional modeling study, Dirks (1969) found that a two–celled circulation resulted from heating along the eastern slopes of the Rocky Mountains and the the adjacent High Plains. Sharp upward motion was found near mountain top with compensating downward motion directly to the lee of the steepest mountain slopes. Another broader area of ascent was found just east of the subsidence in association with the solenoid on the plains. Tripoli and Cotton (1989b) found these circulations to be about 5 km deep in two–dimensional simulations in the absence of convection.

Dirks (1969) hypothesized that these circulations were responsible for the general zone of convective suppression about 100 km downwind of the Front Range. Tripoli and Cotton (1989a,b) further quantified this in a more in–depth numerical simulation in which convection was included. They found that convection is triggered first in the upward branch near mountain top, but then decayed as it encountered the suppression zone. Subsequent redevelopment occurred just east of the suppression zone as the system once again encountered upward vertical motion east of the mountains. The MCS then propagated eastward onto the plains, becoming a well developed system by dark. Perhaps the most important effect of the of the solenoid was the enhancement of the capping inversion over the high plains by the downward branch. As mentioned in the previous section, the inversion prevented convection from erupting ahead of the main system, and allowed CAPE to build up.

Tripoli and Cotton (1989a,b) and Tremback (1990) found that the the mountain–plains solenoid deepened to the tropopause and propagated out onto the plains as it became linked with convection. Both Tripoli and Cotton and Tremback found that propagation of the solenoid did not occur unless convection was simulated. The solenoid may have helped in the organization of the MCS by providing a general region of upward vertical to aid the evaporative outflow in breaking the cap.

The bulk of the above simulations dealt with the two-dimensional aspects of the mountain–plains solenoid. However, significant variations in convective occurrence have been noted across the plains of eastern Colorado as well. Specifically, convection occurs more frequently along the Cheyenne Ridge and the Palmer Divide, two regions of elevated terrain that extend eastward from the northeastern Colorado Front Range (Fig. 3.1). Wetzel (1973), Klitch et al (1985), and López and Holle (1986) have all observed maxima in radar echo frequency, satellite cloud cover, and lightning occurrence respectively over the Palmer Divide. Tripoli (1986) suggested that the subsidence zone to the lee of the Front Range along the Palmer Divide may not be as strong due to the broader slope. In a composite study of Front Range mesonet and National Weather Service station data, Toth and Johnson (1985) found that confluent flow often developed along these ridges in response to diurnal heating. These two effects would tend to enhance convection.

The Denver convergence and vorticity zone (DCVZ) or the Denver cyclone (Szoke et al, 1984) is a special case in which enhanced convergence and cyclonic vorticity occur just north of the Palmer Divide near Denver, Colorado. Szoke et al. (1984) and Szoke and Brady (1989) and many others (including the author on his own personal "field experiments") found this feature to be associated with severe weather in and near Denver. The circulation is almost exclusively found when southerly or southeasterly boundary layer winds blow over the Palmer Divide. Barrier jet formation (Szoke et al. 1984), blocking by the Palmer Divide (Szoke et al. 1984; Smolarkiewicz and Rotunno, 1989; Smith, 1989), formation of an upwind stagnation point on the Palmer Divide (Smith, 1989), tilting and stretching of baroclinically generated vorticity (Smolarkiewicz and Rotunno, 1989), turbulent stress divergence (Dempsey and Rotunno, 1988), and diurnal upslope forcing along the Palmer Divide (Toth and Johnson 1985) have all been put forth as possible causal or contributing mechanisms. In any given case, several of these are likely working in concert. Whatever the cause, this feature can locally enhance or trigger convection in the Denver area.

The superposition of the mountain–plains solenoid and the the Palmer divide effects literally create a cross hair focus that moves eastward with convection. If the plains inversion is strong, convection will be strongly focused as Tripoli and Cotton suggested. A similar effect could occur along an east–west oriented stationary front backed up against the mountains. These mechanisms can result in a concentrated and relatively predictable system even in the absence of synoptic forcing.

2.5 Summary

Much of the work discussed above indicates that MCCs and other intense MCSs are the result of moderate to strong environmental focusing. The forcing occurs on all scales, from the mountain chimney effect only a few kilometers across, to synoptic scale short waves. Not all mechanisms are present all of the time, however, the low level jet is often required for the fluxes of high θ_e air that feed the intense convection. Once convection develops, several feed backs upon the environment result in a large, consolidated system. These range from internal gravity waves to large stratiform anvils. The exact roles that these processes play during the initial growth stages of an MCS is largely unknown. This two–way interaction between convection and its surrounding environment is investigated through the rest of this dissertation.

Chapter 3

DATA AND ANALYSIS METHODS

3.1 The field project

A small field project covering most of northeastern Colorado was conducted during the late July and early August periods of 1992-1994 (McAnelly et al. 1997). The specific goal was to collect comprehensive surface and Doppler radar data from developing MCSs to investigate the genesis process. During the three year period, high quality data were collected for several developing MCSs, including the 19–20 July, 1993 case.

3.1.1 Radar data

Reflectivity and radial velocity data were collected from the CSU–CHILL radar facility (Rutledge et al. 1993) located near Greeley, Colorado (Fig. 3.1), and the NEXRAD prototype Mile High Radar (MHR) (Pratte et al. 1991) located northeast of Denver. Both radars operated in the S-band with approximately 1° beamwidths. Each volume from the CSU–CHILL consisted of 16 constant elevation scans from 0.5° to 26.5° out to a range of 150 km. Volumes from MHR consisted of 11 scans at elevations from 0.5° to 22° out to a range of 150 km. During operations, synchronized volume scans were collected at six-minute intervals, and additional low level surveilance scans out to a range of 252 km were conducted by both radars. For the 19–20 July, 1993 case, full volume scans were collected between 2209 UTC (all times UTC[1]), 19 July and 0000, 20 July, and surveilance scans were collected by the the CSU–CHILL from 2209 to 0100 and MHR from 2209 to 0145.

The radars were separated by a 64 km north-south baseline. The resulting Doppler lobes were constrained rather liberally by the 20° beam crossing angle and the radius of the

[1] To convert to local standard time, subtract seven hours from UTC time.

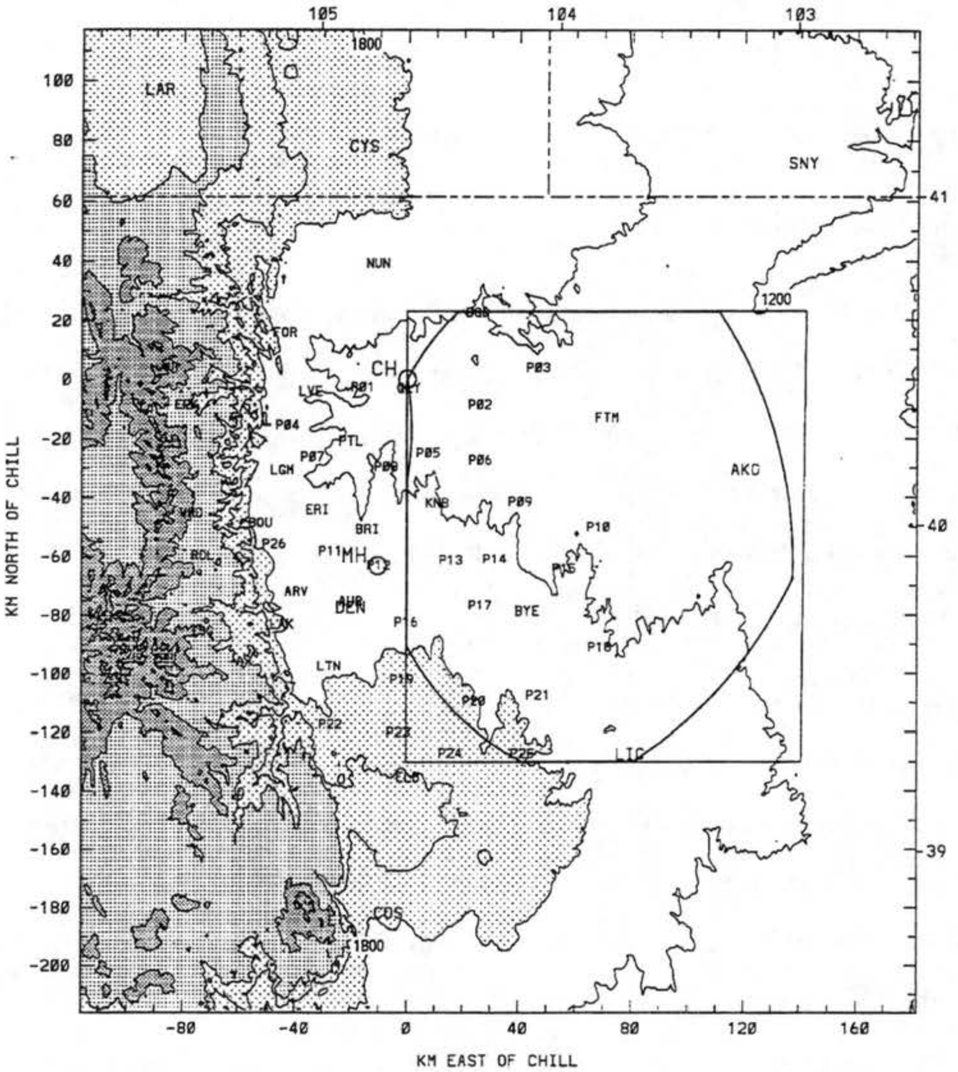

Figure 3.1: The high resolution data collection network used for the northeastern Colorado field project. PROFS mesonet stations and NWS hourly reporting stations are indicated by their three letter identifiers in small and large font respectively. NCAR PAM stations are indicated by by a "P" followed by the station number. The radar analysis grid superimposed on the eastern Doppler lobe is indicated by the rectangle, and the circles labeled CH and MH depict the positions of the the CSU–CHILL and Mile High Radars respectively. Topography is contoured at the 1200 m, 1800 m, 2100 m, 2400 m, 3000 m, and 3600 m MSL levels and shaded at 1800 m, 2400 m, and 3600 m MSL. The left and bottom axes are labeled in km from the CSU–CHILL, while the top and right axes are labeled in longitude and latitude respectively. Dashed lines indicate state boundaries.

2.5 km beamwidth (Fig. 3.1). In this configuration, the lobes, were well placed to observe convection as it moved off the high terrain and onto the plains. Storm-scale features were observed while systems were closer to the radars, allowing for in–depth analyses. At far ranges, however, the center of the lowest beam was 2.5 km above ground level (AGL), and the resolution was quite coarse due to beam broadening. Therefore, much of the analysis will concentrate on the development of broad mid and upper tropospheric mesoscale flow regions. Such features are well sampled despite the coarse resolution (McAnelly et al. 1997).

3.1.2 Other data

Surface mesonet data were collected from stations in two overlapping networks Fig. 3.1. The first, supported by the National Oceanic and Atmospheric Administration (NOAA) Forecast Systems Lab (FSL), was formally known as the Program for Regional Observing and Forecasting Services (PROFS) mesonet. The second consisted of 26 portable automated mesonet (PAM) stations operated by the National Center for Atmospheric Research (NCAR) for the Realtime Analysis and Prediction of Storms (RAPS–93) field project. The average station separation in the combined network was about 20 km. Measurements of pressure, temperature, dewpoint temperature, wind speed, wind direction, maximum wind gust, and rain rate were recorded every five minutes and relayed back to forecasters in real time. The result was a high resolution mesh of surface data through most of the western half of the Doppler analysis region. In epilogue, neither one of these networks is currently in full operation. These data were valuable forecasting and analysis tools and the author laments their loss.

National Weather Service (NWS) surface and upper air sounding data were also collected for analyses on the larger scale. Surface data were available for every hour on the hour, while the sounding data were available every twelve hours at 0000 and 1200. Profiler data were also collected, however, none was available for the 19 July case.

3.2 Analysis methods

3.2.1 Radar data processing

Dual Doppler analysis volumes were created for the following 12 times: 2209, 2227, 2233, 2239, 2245, 2251, 2257, 2309, 2315, 2321, 2333, and 2345. Reflectivity and velocity data from each radar were manually edited and unfolded using the RDSS software package (Oye and Carbone 1981). Data were then interpolated to the Cartesian analysis grid in Figure 3.1 through the use of the SPRINT and CEDRIC software (Miller et al. 1986; Mohr et al. 1986). The grid covered 141 km $\times$ 151 km in the x and y directions with a spacing of 1.5 km. In the vertical, the grid extended from 2.5 km above mean sea level (MSL) ($\sim$ 1 km AGL) to 15 km MSL at intervals of 0.5 km.

Velocity data from each radar were combined by iteratively adjusting the horizontal and vertical wind components through the downward integration of the anelastic continuity equation. Variational techniques were not feasible due to the inadequate sampling of the lower portions of the domain. Prior to the vertical integration, the horizontal wind components were smoothed using a two–step Leise filter (Leise, 1981). Features with wavelengths smaller than $4\Delta x$ (6 km) were strongly damped. Particle fall speed was accounted for by assuming different fall speeds for ice and water above and below the 0°C level respectively. This level was determined from the 1200, 19 July Denver (DEN in Fig. 3.1) sounding to be 4.2 km MSL. Reflectivty data were combined by accepting the maximum value between the Chill and Mile High radars at each grid point. Additional details are as in Nachamkin et al. (1994).

Reflectivity–based estimates of MCS–integrated volumetric precipitation rates were derived from the lowest two scans from the CSU–CHILL volumes. The Marshall–Palmer relation was used to convert reflectivity to rainfall rate as described by McAnelly and Cotton (1992). These were then summed over all observed radar echo associated with the 19 July system to create a time series of MCS–integrated precipitation rate. Separate convective and stratiform precipitation rates were derived by simply assuming all reflectivity above 35 dBZ was convective.

Two Doppler pressure retrievals were conducted at 2233 and 2333 using methods derived by Gal–Chen (1978), and software discussed in Parsons et al. (1987). The environmental mean virtual potential temperature profile was again obtained from the 1200, 19 July

Denver sounding. The local time derivative terms were calculated using two volume scans separated by six minutes at 2230 and twelve minutes at 2327. Error values as described by Gal–Chen and Hane (1981) were less than 0.4 for the data used herein.

The dual Doppler velocities were analyzed both with respect to storm–relative motion and the mean environmental winds. Since the main emphasis was on the mesoscale, "storm" motion was estimated as the average velocity of all discernible reflectivity cells between 2200 and 0000. The rapid expansion of the system made the measurements somewhat arbitrary, however a convective line eventually formed and moved with a fairly consistent velocity of 11.8 m s^{-1} from 246° or $(u, v) = (10.8, 4.8)$ m s^{-1}. The mean environmental winds were calculated as an average between the soundings at 0000, 20 July from Dodge City, KS (DDC) and North Platte, NE (LBF) located in western Kansas and Nebraska. The Denver sounding was excluded due to contamination from the nearby convective complex.

3.2.2 Surface data processing

The raw mesonet pressure data contained systematic biases due to the sloping topography of eastern Colorado. To remove these, the pressures were adjusted to 1500 m MSL using the standard atmospheric lapse rate of 6.5 Kkm^{-1}. Individual station biases were then removed by comparing the mesonet data to adjusted pressure fields from surrounding NWS stations. The comparisons were made during several quiescent periods within one day of each convective system. Most of these corrections were on the order of 1 hPa or less, however the four stations in the western foothills (EPK, WRD, ROL, and, ISG) were excluded from the analyses due to high variabilities in their station pressure biases. Perturbations associated with the diurnal tide did not significantly contribute to the trends over the 2–3 hour mesonet analysis periods, thus they were not removed.

All surface fields were carefully hand analyzed. However, for clarity of presentation, the data have been interpolated to a Cartesian grid using a Barnes objective analysis. The grid covered most of the mesonet, and the horizontal spacing was 3.3 km. Care was taken to make sure the interpolated fields closely resembled the hand analyses.

Chapter 4

ENVIRONMENT AND CASE OVERVIEW

4.1 synoptic overview

The atmosphere over the High Plains on 19 July was primed for MCS activity. At upper levels, an anomalously deep trough for July was located over the western United States. This general pattern remained locked in for most of the summer of 1993, and was responsible for widespread flooding over most of the central plains. The strong flow interacted with very high lower tropospheric moisture to produce repeated MCSs (Bell and Janowiak, 1995). Some of these systems, including the 19–20 July case, originated in the High Plains and grew large as they propagated eastward. McAnelly and Cotton (1986) described this type of evolution in detail for an MCC episode that occurred in 1977.

The contiguous cloud shield produced by the 19–20 July case never took on the well–defined oval characteristics of an MCC (Maddox, 1980). This was mainly due to a partial merger with another MCS cloud shield further north (see Fig. 4.7). However, the cold cloud tops did exceed the MCC time and size criteria. Thus, although the satellite characteristics would classify it as an MCS, the environment in which it developed was more typical of that found for MCCs.

The 19–20 July environment was characterized by fast southwesterly upper tropospheric flow that extended from southern California across most of the northern half of the United States. Most of northeastern Colorado was beneath the right entrance region of a 200 hPa (Fig. 4.1) jet streak, an area often associated with upward motion (Shapiro and Kennedy, 1981). This jet remained quasi–stationary from 18–20 July, and several MCSs propagated along it. The 500 hPa (Fig. 4.2) flow was considerably weaker, although still quite strong for the time of year. Flow over northern Colorado was generally in the 10–15 m s^{-1} range, making for strong upper tropospheric shear between 500 hPa and 200 hPa.

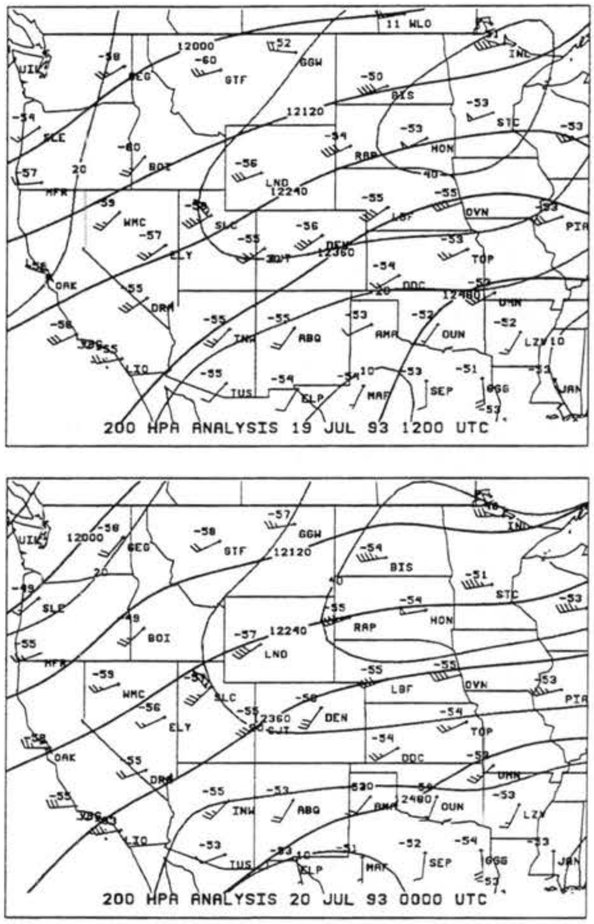

(a)

(b)

Figure 4.1: Constant pressure analysis at 200 hPa for (a) 1200 19 July and (b) 0000 20 July, 1993. Solid contours are height (m MSL) at 120 m intervals, and dotted contours are wind speed (m s^{-1}) at 10 m s^{-1} intervals. Numerical values of temperature (°C) at each station are plotted to the left of each 3–letter station identifier. Wind barbs are in m s^{-1} with one full barb equal to 10 m s^{-1}.

Composites by Maddox (1983) and Laing (1997) found that upper tropospheric jet streaks and significant baroclinicity were common to MCC environments.

The 700 hPa (Fig. 4.3a) ridge axis was located over western South Dakota, Nebraska and Kansas, just east of the MCS genesis region. Confluent height contours and low dew-point depressions over western Kansas and southern Nebraska were indicative of mid tropospheric moisture convergence. Maddox (1983) noted the presence of a similar mid tropospheric ridge in his MCC environmental composites. At 850 hPa (Fig. 4.3b), the low level jet extended from southern Texas into Wyoming. Southeasterly flow funneled moist air into the high plains ahead of low pressure located over southern Idaho. An east–west

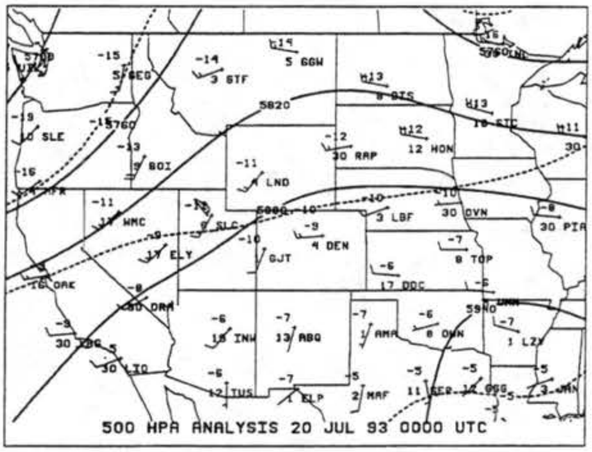

Figure 4.2: Constant pressure analysis at 500 hPa for 0000 20 July. Solid contours are height (m MSL) at 60 m intervals, and dashed contours are temperatures (°C) at 5°C intervals. Numerical values of temperature and dewpoint depression in °C are plotted to the left of the station identifier, with temperatures on top. Wind speeds are in m s^{-1} with one full barb equal to 10 m s^{-1}.

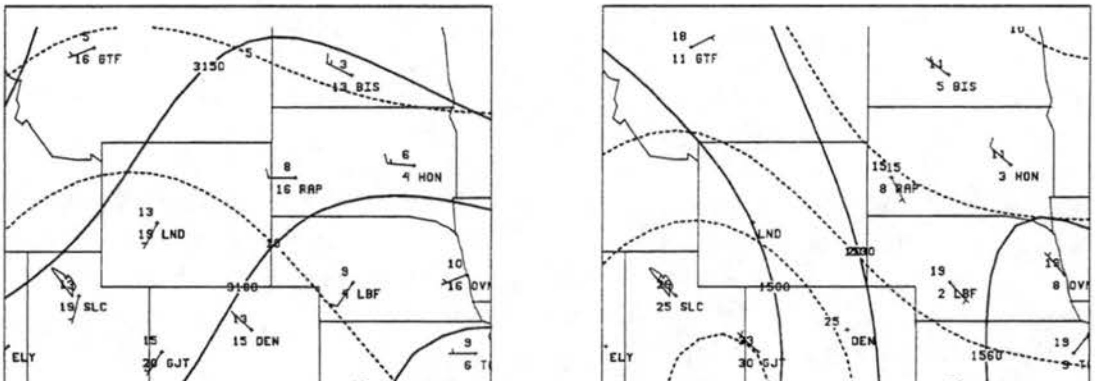

(a) (b)

Figure 4.3: Constant pressure analysis at (a) 700 hPa and (b) 850 hPa for 0000 20 July. In both plots solid contours are height (m MSL) at 30 m intervals, and dashed contours are temperatures (°C) at 5°C intervals. Numerical values of temperature and dewpoint depression in °C are plotted to the left of the station identifier, with temperatures on top. Wind speeds are in m s^{-1} with one full barb equal to 10 m s^{-1}.

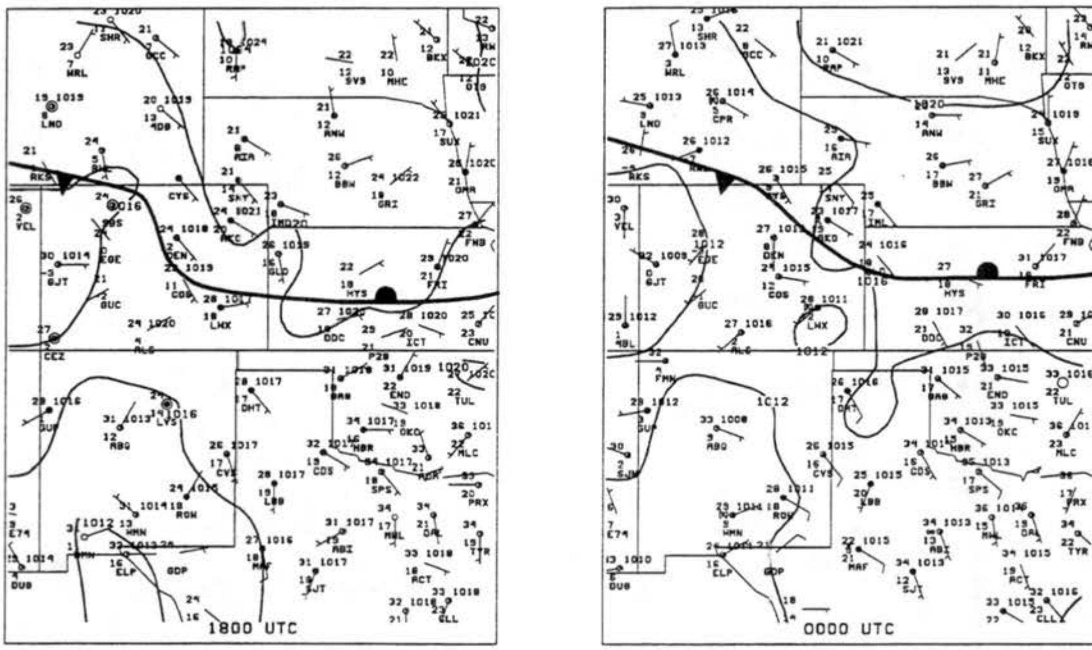

(a) (b)

Figure 4.4: Surface analyses for (a) 1800 19 July and (b) 0000 20 July. Temperatures (°C), weather symbols, and dewpoints (°C) are plotted from top to bottom to the left of the station, while NWS mean sea level pressure (MSLP) is plotted to the upper right. Sky cover in eights is plotted in the circles for those stations reporting it. Wind speeds are in m s^{-1} with one full barb equal to 10 m s^{-1}. MSLP is contoured at 4 hPa intervals, and hand-analyzed fronts have been added.

quasi–stationary front was well defined by the southern edge of the temperature gradient over northern Kansas and Colorado. Strong warm advection was occurring from northeastern Colorado into eastern Wyoming and western Nebraska. The attendant MCS activity which was developing at this time over eastern Colorado and western Nebraska propagated eastward along and north of the front (see Fig. 4.7).

The quasi–stationary front was less defined at the surface. Instead a general north–south temperature gradient existed over most of the plains from Texas to Nebraska. The front slowly meandered northward through eastern Colorado and western Kansas as the day progressed (Fig. 4.4). Southeasterly gradient flow combined with diurnal upslope flow brought deep moisture westward from the rain soaked plains. Dewpoints were very high as a result, with values in many areas at or above 15° C. No obvious convective triggers stood out in the synoptic data, however weak wind confluence was apparent near the surface frontal position in northeastern Colorado at 0000.

4.2 Sounding analysis

The convective potential in northeastern Colorado is best viewed with the 1200, 19 July DEN sounding (Fig. 4.5) because at 0000 DEN was in the wake of the convective system. At 1200 the bulk of the lower tropospheric moisture extended from the surface to about 777 mb (700 m AGL). Modified parcel trajectories based on a dry adiabatic boundary layer lapse rate with a surface temperature of 25°C, and the average water vapor in the lowest 500 m indicated that cloud base would be about 680 hPa. The corresponding convective available potential energy (CAPE) was 1022 $\mathrm{Jkg^{-1}}$. Several eastern Colorado stations observed cloud bases of about 3 km MSL, or about 700 hPa, thus the predicted sounding was a good estimate. Although the CAPE near DEN was rather marginal for the development of strong convection, the 0000, 20 July soundings from LBF and DDC (Fig. 4.6) indicated more energy was available farther east. CAPE in these areas was on the order of 1700 $\mathrm{Jkg^{-1}}$.

The deep dry adiabatic layer that developed over the High Plains favored the development of strong convective outflow. Under these conditions, lower tropospheric gravity wave forcing would be minimal in favor of density current development. The implications of this

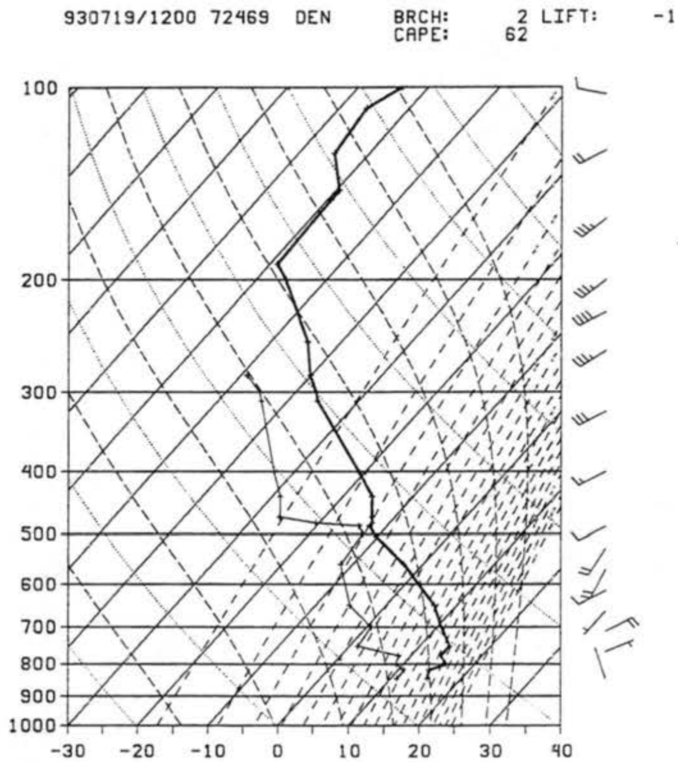

Figure 4.5: Skew-T log-P diagram for Denver (DEN) at 1200 19 July. Temperature (°C) is labeled along the abscissa, while Pressure (hPa) is labeled on the ordinate. Balloon measured Temperatures and dewpoints in °C are plotted as thick and thin solid lines respectively. Winds are in m s^{-1} with a full barbs equal to 10 m s^{-1}. Values of the Bulk Richardson number (BRCH), the lifted index (LIFT), and CAPE are listed at the top of the figure.

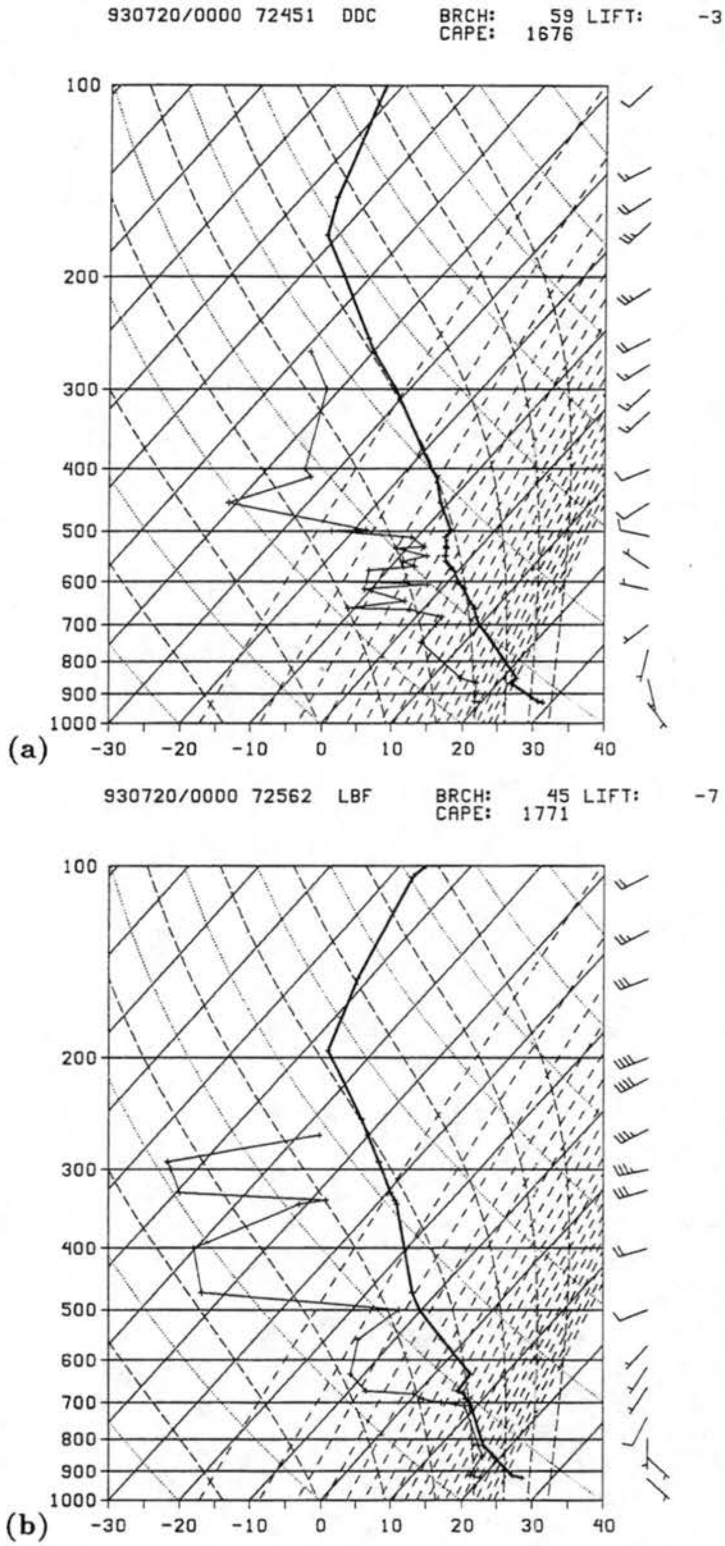

Figure 4.6: Skew-T log-P diagrams at (a) Dodge City, Kansas (DDC) and (b) North Platte, Nebraska (LBF) for 0000 20 July. Details are as in Figure 4.5.

will become more apparent in later chapters when the gravity wave response is investigated. Farther east the boundary layer was much shallower however, as evidenced by the DDC and LBF soundings. Model results, discussed later, indicate that wet soil in these areas was responsible for the lack of deep heating. Lower tropospheric gravity waves are far more likely to occur in these more stable environments.

All of the profiles exhibit strong westerly flow above 500 hPa. Given that storm motion was about 12 m s^{-1}, most of the upper tropospheric anvil would be advected downstream unless the upstream flow was blocked by convective divergence.

4.3 Satellite overview

Prior to the development of the first convective cells at 2000, skies over the region were generally partly cloudy. The strong daytime heating allowed convection to develop and grow in several places along and just east of the Rocky Mountains. Convection first formed in the high mountains along the Colorado Front Range, and subsequently moved eastward along the Cheyenne Ridge, Palmer Divide, and Raton Mesa.

The MCS investigated in this work formed in north central Colorado, just north of the Palmer Divide at about 2000. By 2100 the cloud tops reached the -60°C level as indicated by the dark grey shading in Figure 4.7a. A second region of convection was apparent just north of the Colorado/New Mexico border near the Raton Mesa.

Between 2100 and 2330 (Fig. 4.7b) the northeastern Colorado MCS steadily grew, becoming mainly linear in shape with a northeast–southwest orientation. The coldest cloud tops were located in the southern and central portions of the anvil, while considerable cloud material advected downstream. Convection in southern Colorado weakened considerably as it advected eastward, and subsequent storms consistently redeveloped on the western and southern flanks of the original convection. As a result, this system propagated almost due south into New Mexico. Additional convection was also developing in the Nebraska panhandle along the eastern portions of the Cheyenne Ridge. This convection eventually developed into a long–lived MCS that moved through Nebraska, just to the north of the system studied here.

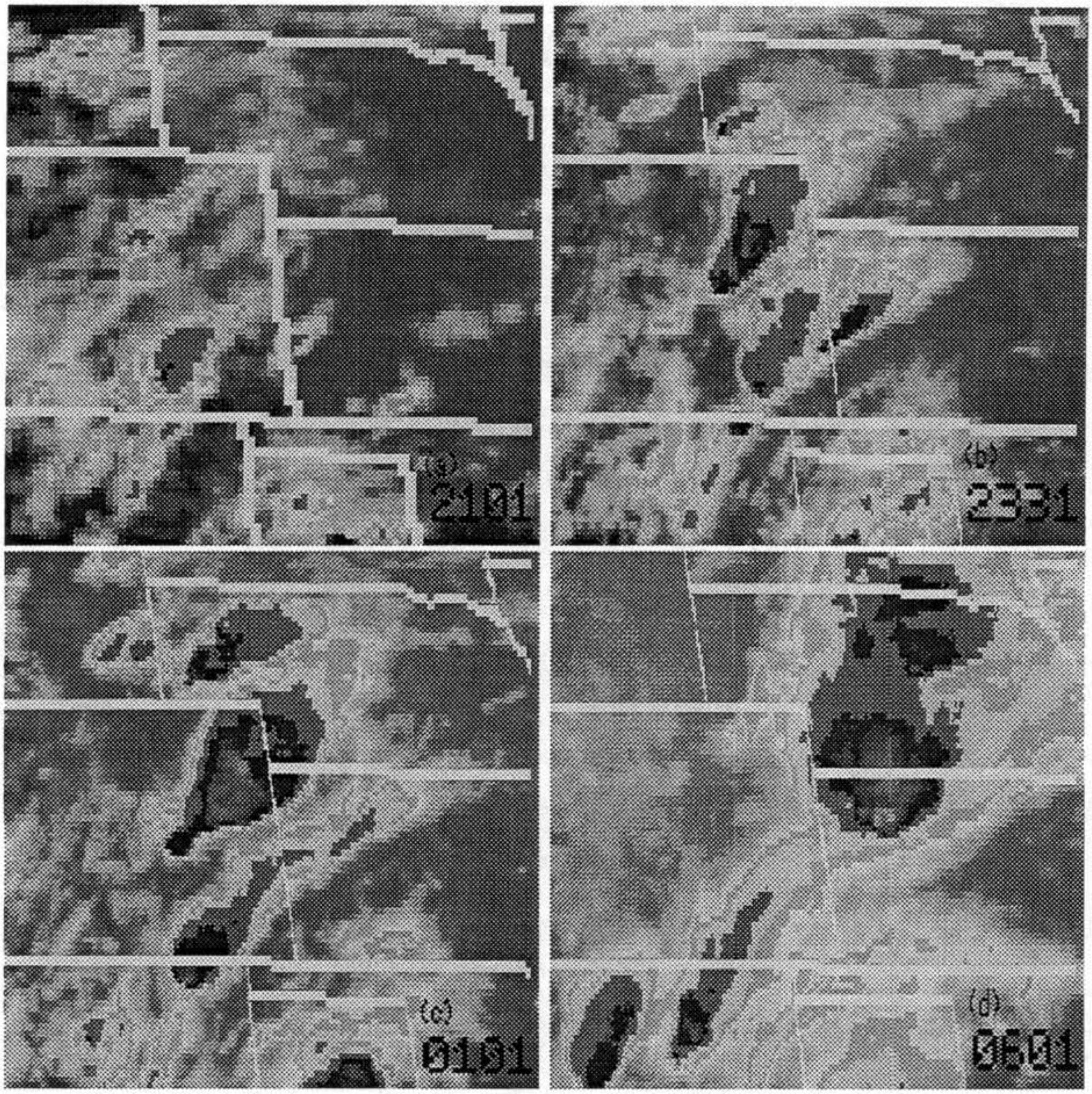

Figure 4.7: Infrared enhanced satellite images for (a) 2101 19 July, (b) 2331, (c) 0101 20 July, and (d) 0601. IR cloud top temperatures are shaded using the MB enhancement at the following increments: -33°C (medium gray), -43°C (light gray), -54°C (dark gray), and -60°C (black). Temperatures colder than -60°C are gray shaded back to white at -75°C.

Between 0000 and 0100, 20 July (Fig. 4.7c), the northeastern Colorado MCS underwent sudden, rapid growth. The cloud shield blossomed into a typical oval shape with very cold cloud tops in the southwestern quadrant. The western and southern edges of the cloud shield were quite well defined with a very sharp demarcation between cold cloud tops and clear air. However, the eastern and northern cloud edges were much more diffuse, with a broad gradient in the cloud top temperatures. The convection appeared to pulse somewhat between 0200 and 0300 with new cold clouds developing on the southwestern edge of the system. From then on, however, the cloud shield steadily grew as the system slowly moved east. Up to 12.7 cm of rain fell on parts of western Kansas as the system moved through. By 0600 (Fig. 4.7d), the cloud shield had partially merged with the system further north. The western edge of the cold cloud area was not as sharply defined as it was earlier, despite the persistence of strong convection and environmental flow.

4.4 Reflectivity overview

The first convective cells appeared on radar, just after local noon or 1800 UTC, which is typical of Colorado convection (Wetzel, 1973). By 1858 (Fig. 4.8a), three cells were moving off the highest terrain into the foothills. The southeasternmost cell, located about 100 km from CSU–CHILL, was the strongest, with core reflectivities just over 45 dBZ. Radial velocities (not shown) indicated this storm possessed significant rotation.

Over the next two hours, the southern cell continued to traverse the foothills, while the storms further north rapidly dissipated. Several new convective storms formed in the vicinity of the original southern cell, and after a couple of mergers two dominant multicell storms emerged (Fig. 4.8b). Mesonet winds and strong reflectivity gradients on the southern edges of the storms indicated that convection was feeding on strong inflow from the south.

At the same time, new convection was rapidly developing along a line extending northeastward from the easternmost cell in Figure 4.8b. A strong convergence zone at the surface is clearly visible in the mesonet winds along this appendage. By 2200 (Fig. 4.8c) this new development had grown explosively, giving the system a more north–south orientation. The westernmost multicell storm dissipated during this time, and its remnants are a weak stratiform appendage at $x = 0, y = -100$ km in Figure 4.8c. Convection continued to exhibit

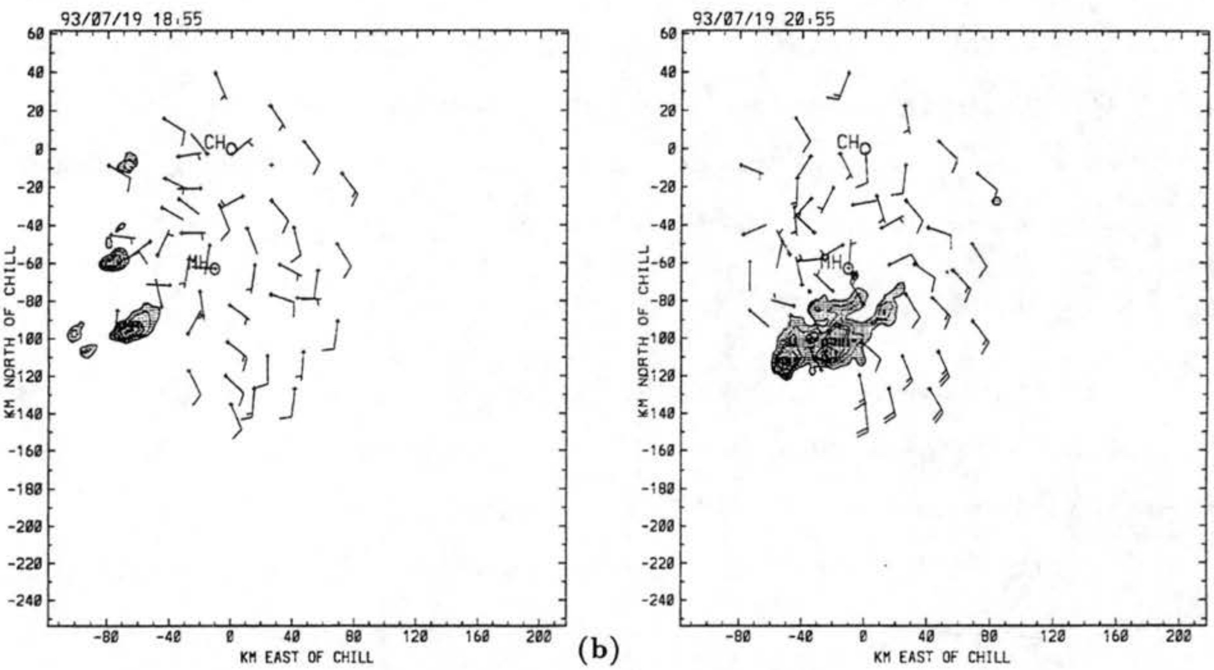

(a) (b)

Figure 4.8: Surface mesonet and low level reflectivity analysis for (a) 1855, (b) 2055, (c) 2155, (d) 2230, (e) 2330, and (f) 0055. Mesonet winds are in m s^{-1} with one full barb equal to 5 m s^{-1}. Reflectivity from the CSU–CHILL at 2 km AGL is contoured at 7.5 dBZ intervals starting at 15 dBZ, while the 15, 30, and 45 dBZ levels are shaded. The eastern Doppler lobe and analysis grid are plotted in (d).

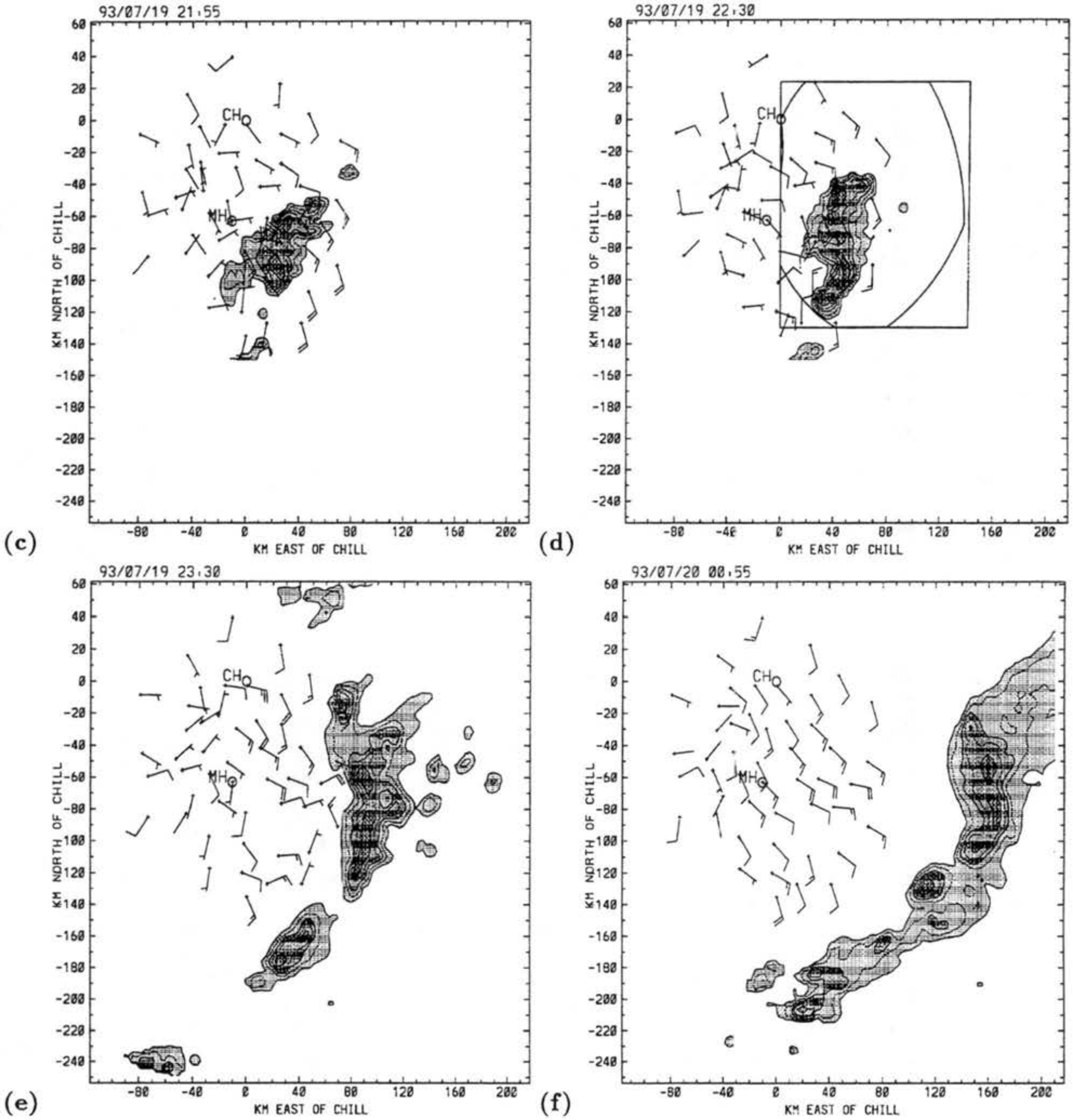

Figure 4.8: continued

rotation on radar, prompting the Denver NWS to issue a tornado warning at 2137. No tornadoes were reported, however wind gusts to 27 m s^{-1} occurred near Strasburg, CO ($x = 41, y = -79$ km).

As the north-south line moved east, a meso-β-scale bow echo developed (Fig. 4.8d), and persisted from 2209 to 2309. Strong winds, heavy rain and hail continued to accompany the line. By 2332 (Fig. 4.8e) however, the system lost most of its bow echo organization, and several new convective cells, developed ahead of the main squall. These smaller cells moved erratically compared to the line, as most of them slowly drifted to the northeast, or even to the northwest. None of these storms became very strong before the line caught up and merged with them.

Additional convection also developed to the southwest of the main squall, most likely on the southern edge of the surface outflow. These southwestern storms remained weak until after 0000, 20 July. At which point, the convective line began backbuilding southwestward. One of these backbuilding cells can be seen in Figure 4.8f as the northernmost storm near $x = 120, y = -130$ km.

By 0055 (Fig. 4.8f) all of the isolated cells ahead of the convective line had either dissipated or merged with the main system. Reports of wind gusts to 27 m s^{-1} (Storm Data, 1993) and radar indicated rotation accompanied the reintensification of the convective line into a bow echo. A considerable stratiform anvil that had been advecting to the northeast for much of the afternoon was now sampled by the lowest scan. However, since the beam at this range was over 2.5 km AGL, much of the precipitation may not have reached the ground. Shortly after 0055, data collection was ceased as the system moved out of range. As the MCS continued to propagate into Kansas, manually digitized radar plots indicate that the strongest convection was concentrated in the southwestern quadrant of the system by 0600.

4.5 Summary

Synoptic conditions over the High Plains were quite favorable for MCS development. Lower tropospheric warm advection, mid tropospheric confluent flow, and high soil moisture contents provided an ample and constant moisture supply. At upper levels, the right entrance region of the quasi–stationary upper tropospheric jet streak provided general synoptic lift over the entire area. Although a weak synoptic front was apparent near the surface, the initial triggering and focusing of convection was closely linked to topographical features. Storms first developed in the mountainous terrain and moved onto the plains along and north of the Cheyenne Ridge, the Palmer Divide, and the Raton Mesa. In the next chapter the development, propagation and organization of the northeastern Colorado MCS are more specifically investigated.

Chapter 5

RADAR AND MESONET ANALYSIS

5.1 Introduction

The organization of the 19–20 July northeastern Colorado MCS as interpreted by mesonet and the Doppler radar analyses are discussed in this chapter. Since the Doppler data were limited to the volume covered by adequate condensate, the focus will be on the system itself as opposed to the surrounding environment. Initial triggering mechanisms and the evolution of the in–cloud flow structure will be analyzed to determine how, when, or if this system became organized on the mesoscale.

5.2 Preconvective environment and early MCS growth

The role of topography in triggering and focusing convection in northeastern Colorado is well depicted by the mesonet data. At 1700 UTC, (Figs. 5.1, 5.2), or about an hour before the first mountain storms developed, a weak cyclonic gyre covered most of the mesonet east of the foothills. Although the cyclonic flow was rather ill–defined, it could be classified as a weak Denver cyclone. Southeasterly flow curved around the northeastern portions of the network, eventually becoming easterly closer to the foothills. The easterlies gave way to weak northerlies in the western Denver metropolitan area (e.g. stations ERI, AUR, and LTN), and the northerlies eventually converged with weak east–southeasterly flow coming over the Palmer Divide. Szoke et al. (1984) observed a similar pattern in their diagnosis of the Denver cyclone or Denver convergence and vorticity zone (DCVZ). As discussed in Chapter 2, The DCVZ frequently forms to the lee of the Palmer Divide when synoptic flow is southeasterly as it was on 19 July. Mass convergence along the southern and eastern edges of the DCVZ will often trigger or enhance convection. The pattern of general divergence in

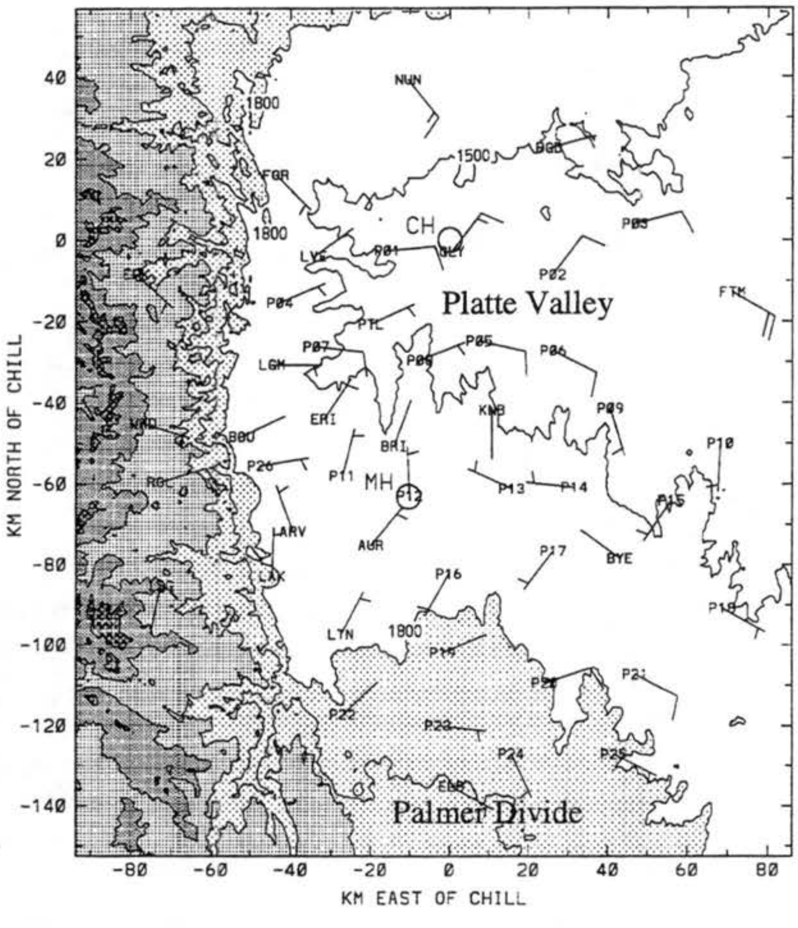

Figure 5.1: Surface mesonet analysis for 1700. Mesonet winds are in m s^{-1} with a full barb equal to 10 m s^{-1}. Topography is contoured at the 1200 m, 1800 m, 2100 m, 2400 m, 3000 m, and 3600 m MSL levels and shaded at 1800 m, 2400 m, and 3600 m MSL. The locations of the Palmer Divide and the Platte Valley are labeled.

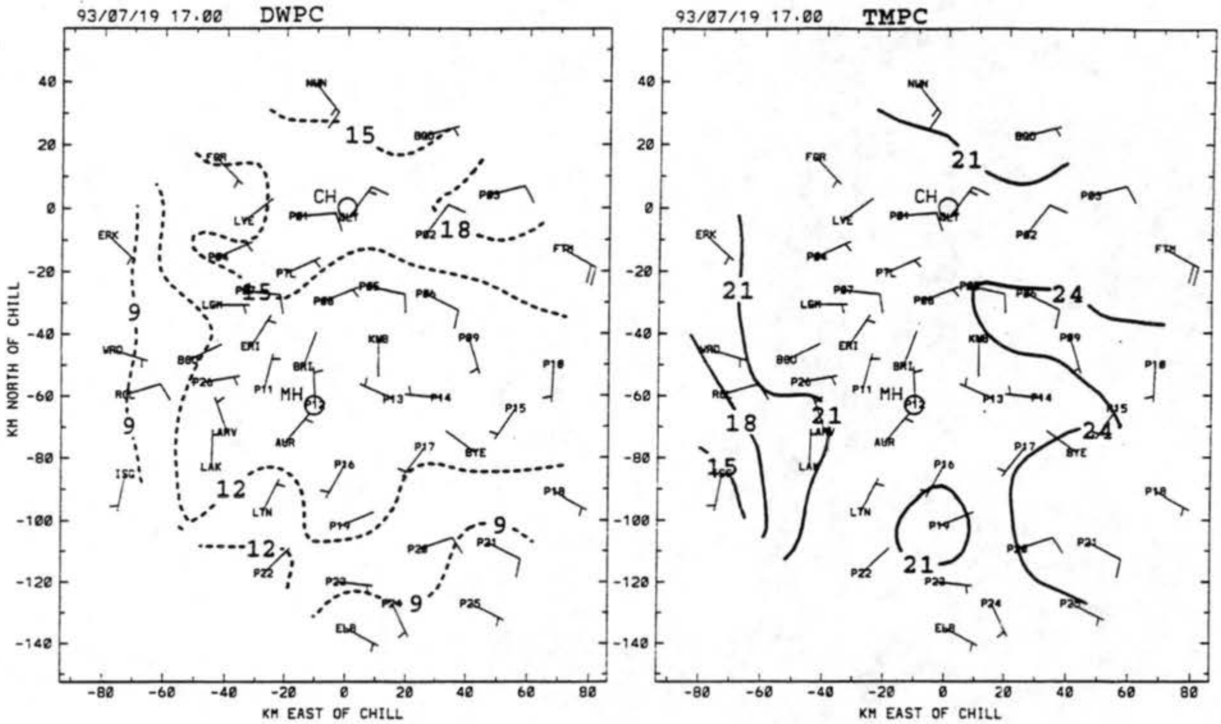

(a) (b)

Figure 5.2: Surface mesonet analysis for 1700. Winds are in m s^{-1} with one full barb equal to 5 m s^{-1}. In (a) dewpoint temperatures in °C are contoured at intervals of 3°C, while in (b) temperatures in °C are contoured at intervals of 3°C. The x and y axes are km east and north of CHILL respectively.

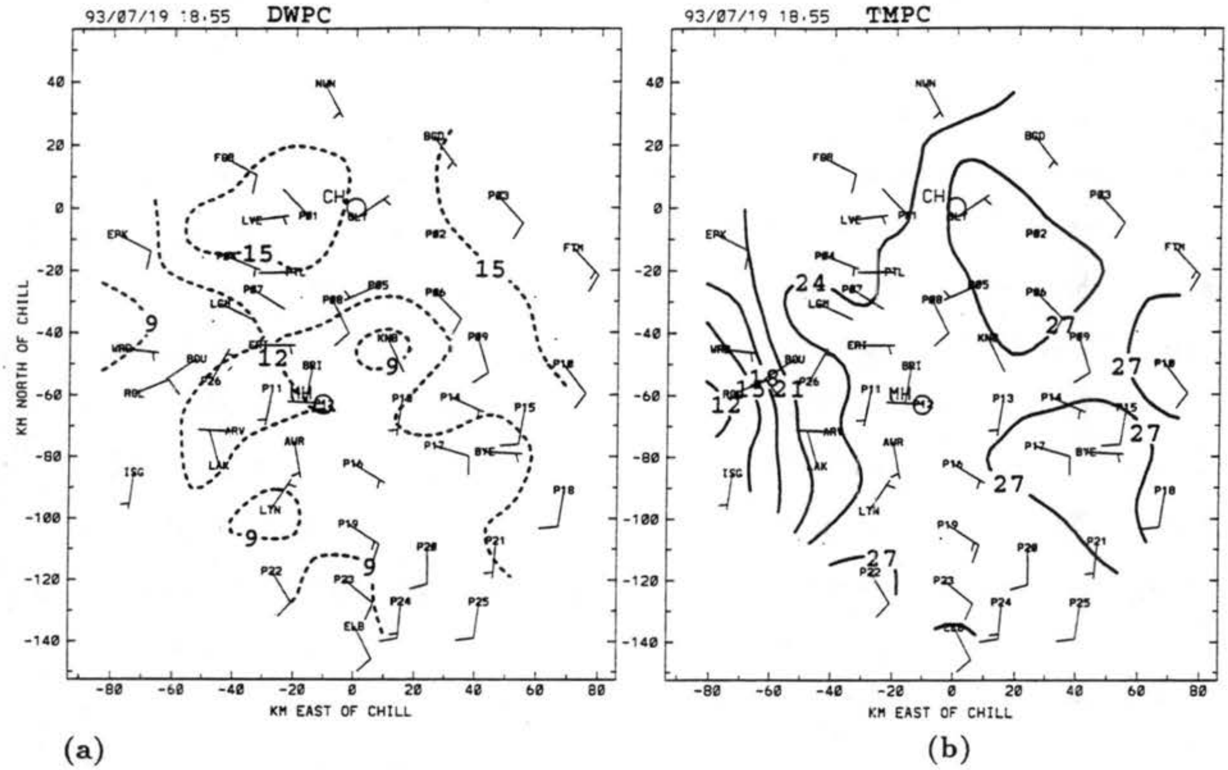

Figure 5.3: Mesonet analysis for 1855. Plot details are the same as Figure 5.2.

the Platte Valley and convergence along the Palmer Divide was also similar to that observed by Toth and Johnson (1985).

The bulk of the lower tropospheric moisture in the late morning of 19 July was pooled in the Platte Valley (Fig. 5.2). Dewpoints there had been 3–6°C higher than those on the divide since before 1200 (not shown). Temperatures across the plains at 1700 were more uniform, however, with a slight warming in the eastern portions of the network. Meanwhile, temperatures at the foothills stations of EPK, WRD, ROL, and ISG on the western edge of the network were lower, mainly due to the increased elevation. Dewpoints at these stations rose several degrees Celsius through the late morning as moisture laden air advected upslope. By 1800, the atmosphere was sufficiently destabilized to support the first convective storms over the highest terrain.

At 1855 (Fig. 5.3) warm, dry air was advecting northward off the Palmer Divide and into the Platte Valley east of the Mile High radar, where dewpoints had fallen by 3°C. The highest potential temperatures (not shown) east of the mountains were in the driest regions whereas a narrow band of lower potential temperatures stretched along the lobe of 12°C dewpoints west of Mile High. Wilczak and Christian (1990) noted a similar potential temperature pattern in their analysis of a much stronger Denver cyclone.

Dewpoints on the Palmer Divide (south of $y = -120$ km in Fig. 5.3) remained nearly unchanged from their values at 1700 despite the advection of moist air from the south. The lower tropospheric moist layer evident in the 1200 Denver sounding (Fig. 4.5) was likely quite shallow over the Palmer Divide due to the elevated terrain. Thus, dry air from aloft could quickly mix down with the growth of the heating-induced adiabatic boundary layer. At the same time, however, mass convergence in the same region was steadily increasing in strength (Fig. 5.4a,b). This was mainly due to strengthening southeasterly flow that was coming up and over the Palmer Divide and meeting with the light and variable flow in the DCVZ. Any upward motions associated with the increased convergence would destabilize the boundary layer, and contribute to the mix-out process.

Temperatures at the foothills stations of ISG and ROL decreased between 1700 and 1855 (Fig. 5.3) in response to the convective cells moving eastward from the higher terrain. Radar echos are visible near both of these stations in Figure 5.4b. As mentioned in the last chapter, the storms south of ISG steadily grew between 1855 (Fig. 5.4b) and 2100 (Fig. 5.4c) as they moved east. New storms developed south and east of the original cell and propagated directly into the regions of highest mass convergence by 2100. Meanwhile, all of the cells along the northern Front Range, which were moving into a region of slightly divergent low level flow, completely dissipated by 2100. Results from the modeling study, discussed in Chapter 7, indicate the east–west convergence zone along the Palmer Divide actually extended westward through the foothills, almost to mountain top. Such a feature would allow the storms to survive the trip through the mountain–plains solenoid suppression zone (Dirks, 1969; Tripoli and Cotton, 1989a) discussed in Chapter 2.

On the Palmer Divide, southeasterly flow steadily increased between 1855 and 2100 and was now sustained at about 10 m s^{-1} (Fig. 5.5). Dewpoints in this region had risen 1–3 °C above their late morning lows despite the increasing temperatures, indicating strong moisture advection was taking place. The driest air was now in the Platte Valley to the northeast of the developing convection. Very strong convergence existed all along the leading

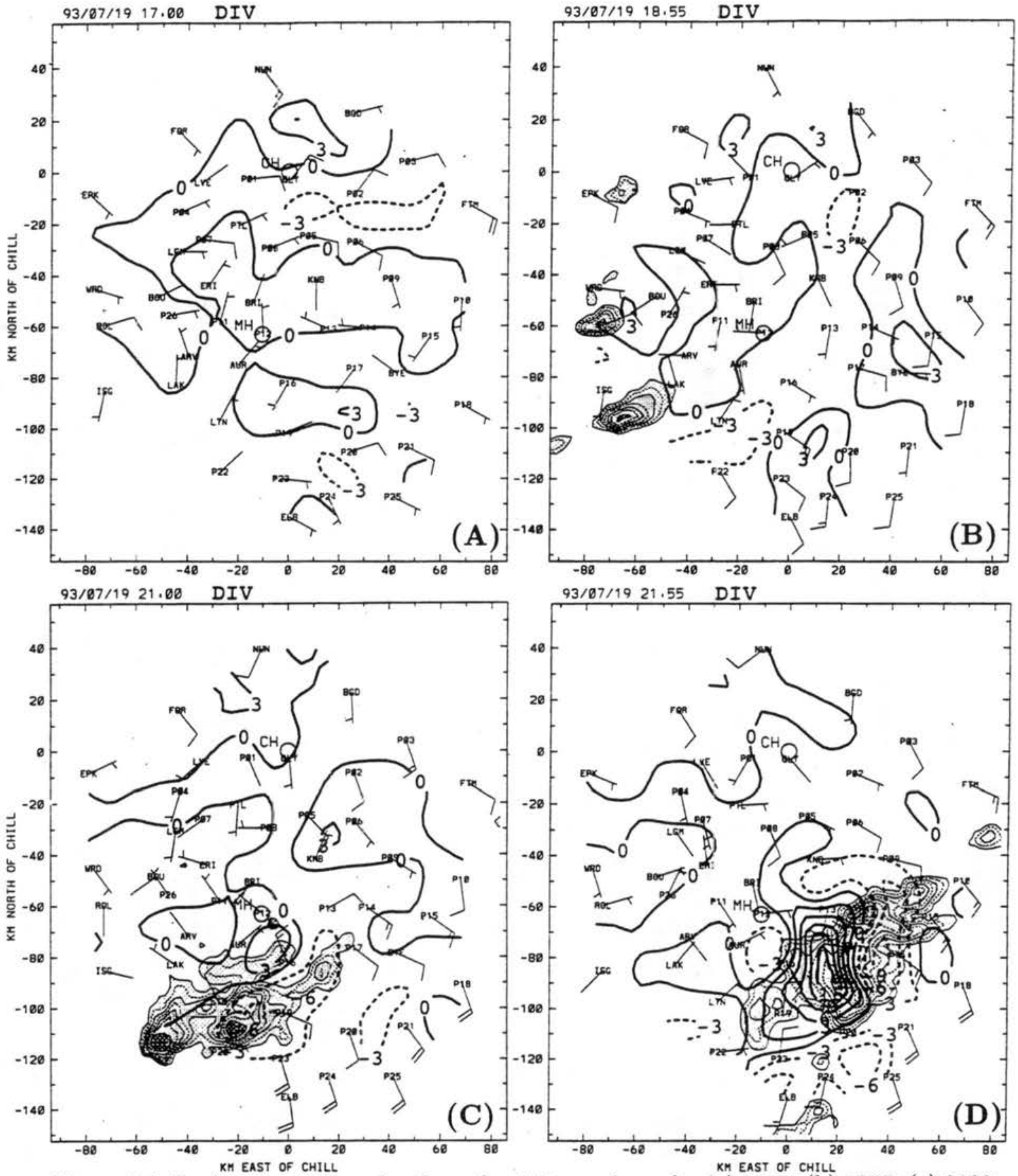

Figure 5.4: Surface mesonet and radar reflectivity analyses for (a) 1700, (b) 1855, (c) 2100, and (d) 2155. Winds are in m s^{-1} with one full barb equal to 5 m s^{-1}. Divergence (s^{-1}) multiplied by 10^4 is contoured in all plots at intervals of 3×10^{-4} s^{-1}. Negative contours are dashed. Reflectivity from the CSU–CHILL at 2 km AGL is contoured at 7.5 dBZ intervals starting at 15 dBZ while the 15, 30 and 45 dBZ levels are shaded.

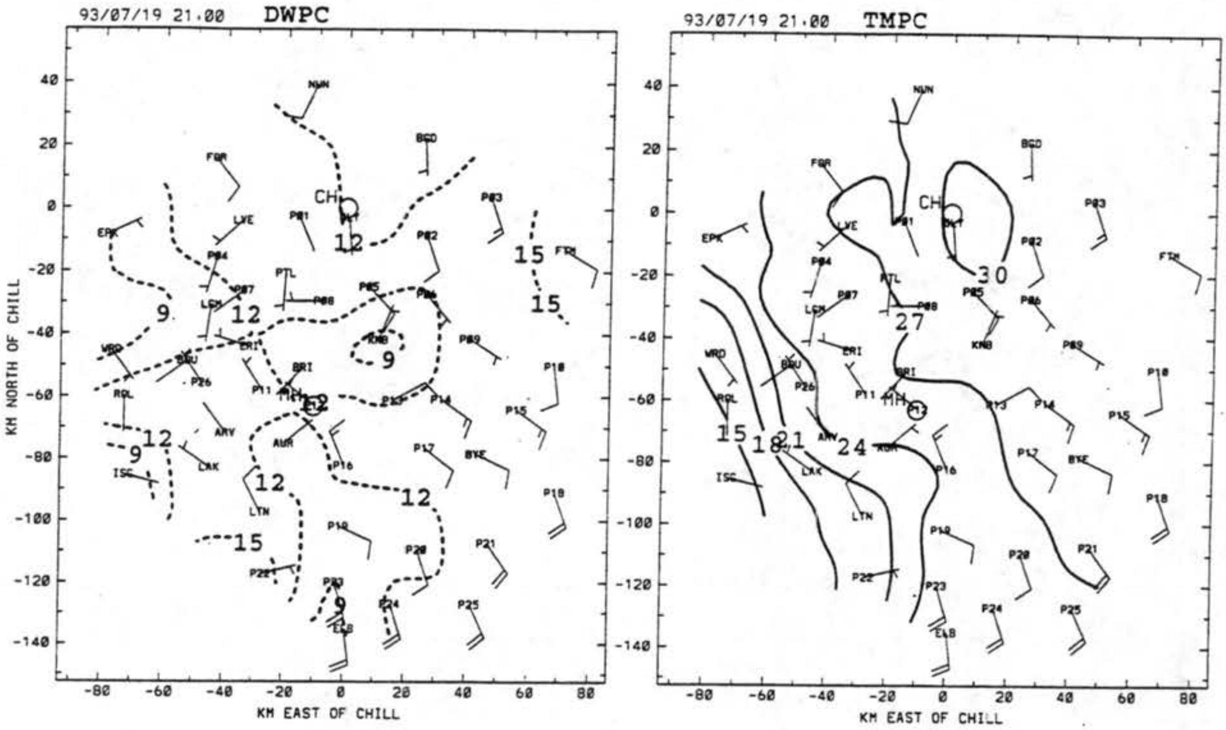

(a) (b)

Figure 5.5: Mesonet analysis for 2100. Plot details are the same as Figure 5.2.

edge of the southeasterlies, with the strongest convergence closest to the convective storms (Fig. 5.4c). The convergence pattern is similar to that seen by Toth and Johnson (1985) at 1100 MST or 1800 UTC, although a mean southeasterly flow is superimposed on the upslope pattern. The subsequent northeastward extension of the convective cluster was well anticipated by the mesonet convergence fields. By 2155 (Fig. 5.4d), convection and its resultant strong divergent outflow was rapidly expanding into the mesonet. The strong convergence south and east of the system was the result of both increased convective outflow, and increased environmental inflow.

In the context of MCS organization the initial convective structure was dictated by the strong convergence in the mountains and to the lee of the Palmer Divide. Thus, in this sense, the convective system was well organized from the start. Only those storms located in the regions of organized convergence survived the traverse from the foothills to the plains. Tripoli and Cotton (1989a) and Wilczak and Christian (1990) point out that forced vertical motions generated by topographically–induced convergence zones can result in the preferential development of convection before the convective temperature (TC) is reached in any part of the region.

The increased potential temperatures in the higher terrain due to heating at lower pressure were another important factor. TC in the 1200 Denver sounding was 35°C with an associated potential temperature of 318 K. Potential temperatures at stations WRD, ROL, and ISG had reached or exceeded this value by 1700. Potential temperatures along the Palmer Divide were also 3–5°C higher than those in the Platte Valley. By 1855, potential temperatures at stations P22, P23 and P24 had reached 318 K. This warmer air combined with the convergence strongly favored convective development along the Palmer Divide.

Whether they be topographic or frontal in nature, most extratropical MCSs form in regions of enhanced convergence. The initial organizing influence of this convergence is quite important because these systems often form at night and/or in environments with high mid tropospheric temperatures, both of which act to inhibit convection by making TC in many regions very difficult to attain. In this situation, much of the environmental CAPE is released in a focused and intense system as opposed to many smaller, less intense cells.

5.3 MCS expansion as viewed by the mesonet

A small but intense mesohigh and its associated density current were observed almost as soon as the 19 July MCS entered the southern portion of the mesonet around 2130 UTC (Fig. 5.6a). As the center of a convective cell passed directly over station P19 between 2125 and 2130, the pressure increased by almost 5 hPa and the five–minute rain–rate exceeded 13 mm hr^{-1}. Several reports of flash flooding with total rainfall amounts of 50 mm around the area corroborate this measurement. Despite the dense network, P19 was the only station to record a direct hit from such an intense core. In general, measured perturbation pressures within the mesohigh were about 1 hPa below those measured at P19, however, convective cores between stations may have continued to produce higher pressures.

Over the next hour, the mesohigh expanded along with the radar echo, and the first signs of a discernable wake low (Fujita, 1963; Johnson and Hamilton, 1988) appeared by 2230 (Fig. 5.6b). This "wake low" was more generally characterized by a tightening of the

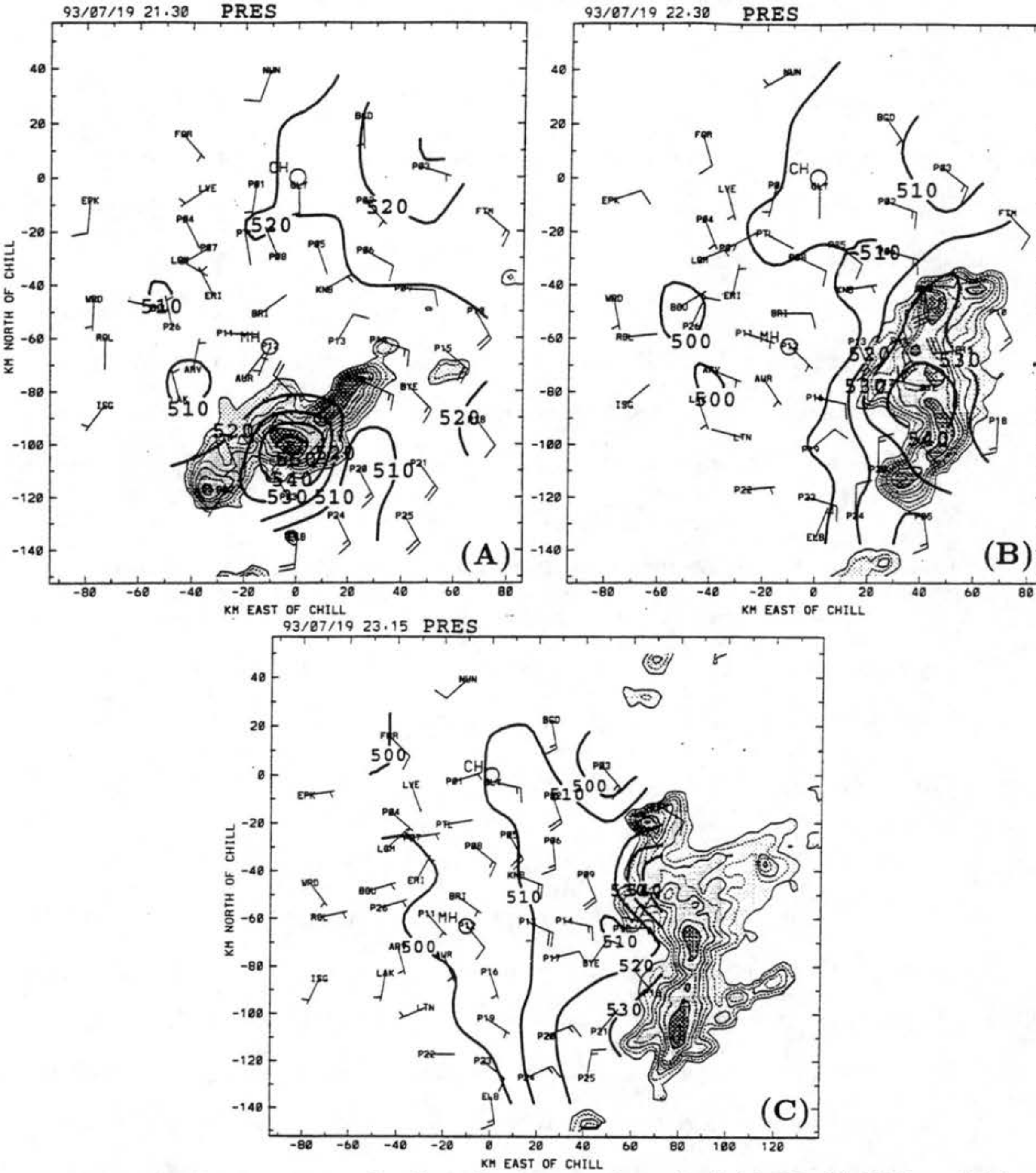

Figure 5.6: Surface mesonet and radar reflectivity analyses for (a) 2130, (b) 2230, and (c) 2315. Winds are in m s^{-1} with one full barb equal to 5 m s^{-1}. Pressure (hPa) adjusted to 1500m is contoured at 1 hPa intervals. All values are plotted with the leading 8 missing, thus 540 = 854.0 hPa. Radar reflectivity from the CSU–CHILL at 2 km AGL is contoured at 7.5 dBZ intervals starting at 15 dBZ while the 15, 30 and 45 dBZ levels are shaded.

gradient at the western edge of the mesohigh rather than a well–defined meso low; however a small closed low did develop as the system exited the network (Fig. 5.6c).

Nachamkin et al. (1994) found that both the mesohigh and the wake low in a growing MCS simultaneously strengthed quite rapidly to form a strong gradient between them. To investigate if this was happening in this case, an attempt was made to quantify the strength of the surface pressure features. As Fujita (1963) points out, the mesohigh and the wake low can be partially hidden due to fluctuations in the environmental pressure field. At least two trends were apparent in the 19 July data. First, surface pressure was increasing towards the east in association with the southeasterly synoptic pressure gradient, and second, pressures across the network were slowly falling. The strength of the MCS pressure dipole was thus quantified at individual stations based simply on the mesohigh–wake low gradient strength. Stumpf et al. (1991) and Nachamkin et al. (1994) showed that strong mesohigh–wake low gradients indicate the presence of sharp and rapid descent in a rear inflow jet, which is often present in a mature system (Smull and Houze, 1985).

Two measurements of the gradient strength were derived from the 5 minute time series from each mesonet station. First, the absolute difference between the pressure maxima/minima was calculated as the highest mesohigh pressure minus the lowest wake low pressure at each station (Fig. 5.7). Second, the maximum rate of pressure drop within the gradient at each station was measured (Fig. 5.8). For the rate calculation, pressure falls at a given station had to last for at least ten minutes and account for at least eighty percent of the mesohigh–wake low difference.

The results are quite interesting. The biggest absolute difference between the mesohigh and the wake low was at station P19 (Fig. 5.7), and was largely due to the passage of a strong cell and its small mesohigh (Fig. 5.6a). However, the mesohigh–wake low gradient there (Fig. 5.8) was diffuse. Strong gradients did not consistently appear until about 2230, when the back edge of the storm passed over station P17. After that, several stations recorded rapid drops in pressure including 2.7 hPa in 10 minutes at P15 and 3.1 hPa in 10 minutes at P10. The absolute pressure differences also increased after 2230, with values approaching those recorded at P19.

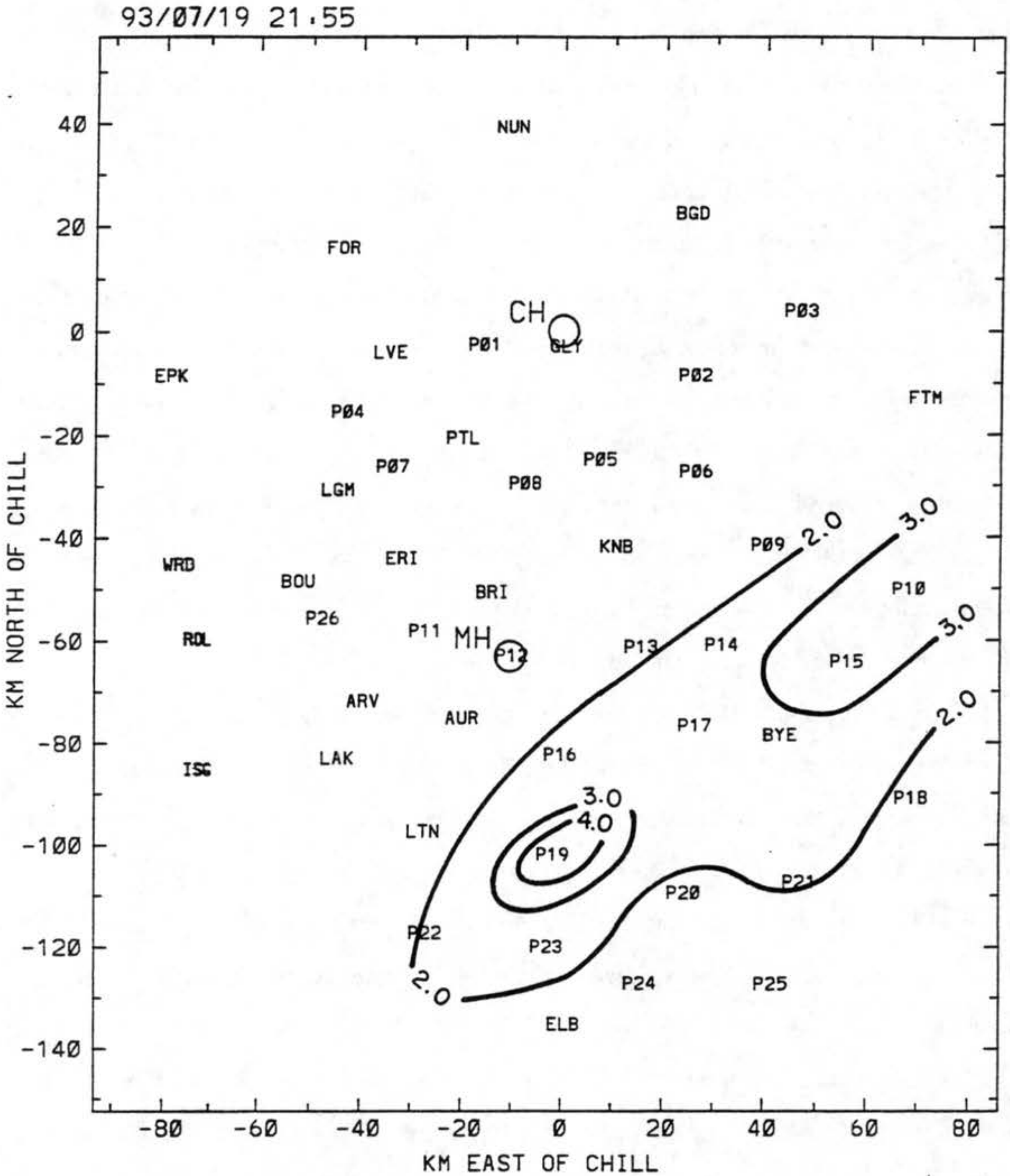

Figure 5.7: Mesohigh minus wake low pressure differences. Contours are in hPa at 1 hPa increments.

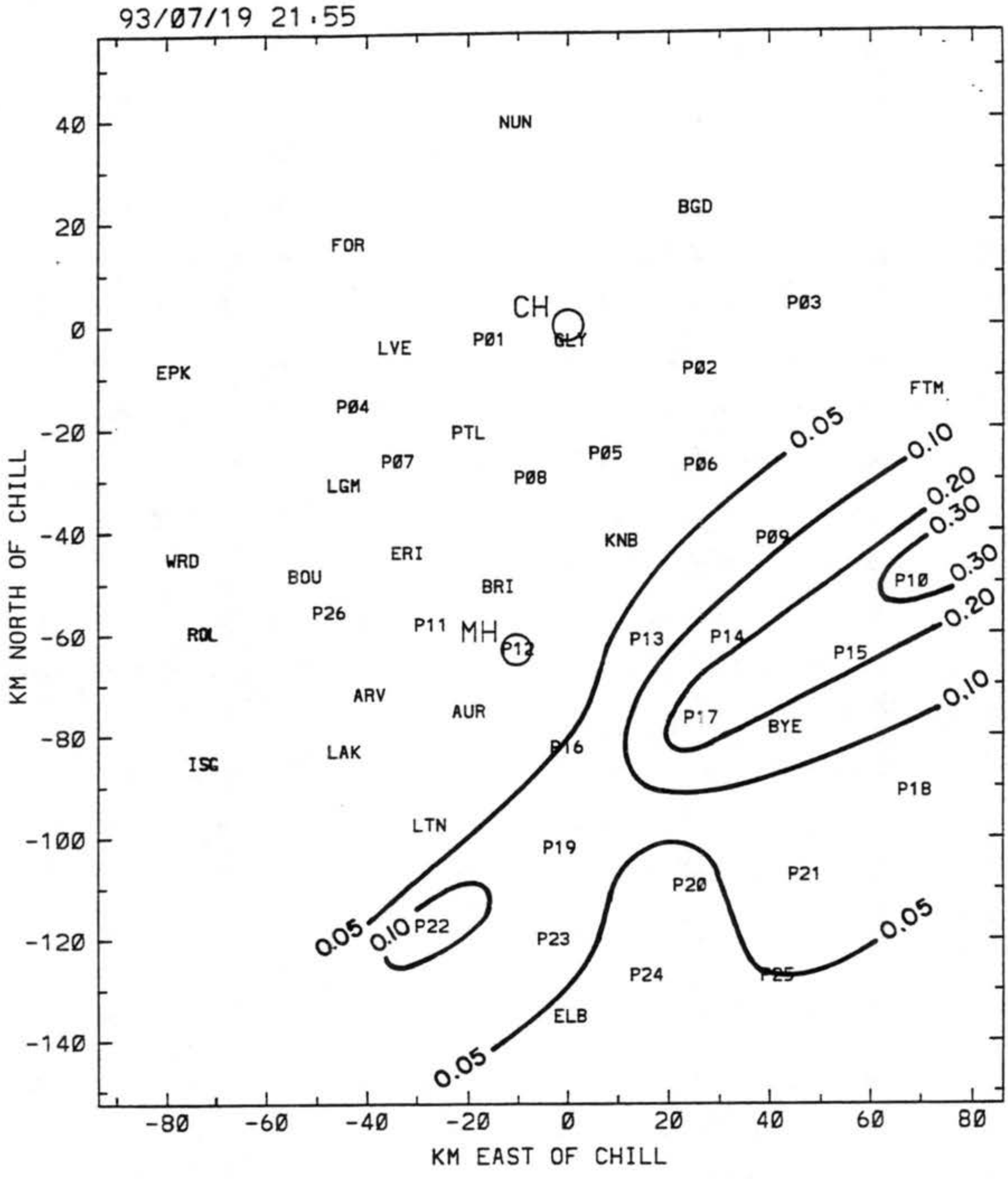

Figure 5.8: Mesohigh/wake low gradient strength as measured by maximum pressure fall rates in hPa min^{-1} at each station. Contour intervals are 0.1 hPa min^{-1}, and the 0.05 hPa min^{-1} contour is also plotted.

The development and track of the strongest pressure gradient was well correlated with that of a radar echo notch located near $x = 30$, $y = -100$ km in Fig. 5.6b, and $x = 60$, $y = -70$ km in Fig. 5.6c. The most rapid pressure falls were located just north of the rear echo notch. The notch, which developed shortly before the strong pressure gradients were observed, was initially located behind the bow echo in the leading line. As time went on, however, the bowed appearance in the convective line became less obvious (Fig. 5.6c). A narrow region of stratiform precipitation that had been trailing the MCS before the echo notch developed (Fig. 5.4d) rapidly dissipated as the notch developed. This combined with the increased wake low gradient indicates the development of strong descent near and north of the notch. Notably, once the echo notch became established, there was almost no trailing stratiform anvil. However, the Doppler results in the next section and model results in Chapter 7 indicate the presence of a rear inflow jet in the clear air.

Since the trailing edge of the line was between mesonet stations when the surface gradient developed, it is hard to determine if the gradient intensified as rapidly as in Nachamkin et al. (1994). Based on the track in Figure 5.8, the gradient tightened somewhere between stations P19 and P17, or between the times of 2200 and 2240. The correlation between the gradient and the rear echo notch indicates the two may have developed together. Again, the Doppler results will shed more light on this issue.

5.4 Doppler radar results

5.4.1 The philosophy of the relative wind

The dual Doppler winds are investigated in both the storm–relative and environment–relative frameworks in this section. Both of these approaches can facilitate very different views on the complicated question of system organization. The storm–relative frame, which is often used in MCS dual Doppler studies, defines the wind field with respect to the propagating convective system, and a constant storm motion is subtracted from all levels. When storm–relative features such as the rear inflow jet, or front–to–rear flow become dominant on the mesoscale, it is generally accepted that the system has attained a degree of organization that is larger than the individual convective cells of which it was composed. However, these storm–induced winds can also be thought of as a perturbation u' upon the ambient environmental wind $\overline{u}$ such that $u' = u - \overline{u}$, where u is the total wind field. This view is different from the storm–relative framework in that the constant subtracted from each level can vary with height. This method defines the degree of mesoscale organization with respect to the environment as opposed to that with respect to the storm. In a highly sheared environment, significant and coherent mesoscale accelerations can be hidden in the storm–relative framework. For instance, a growing convective line will produce accelerations away from the line aloft and towards the line at mid levels. At the same time, wind speeds generally increase with height. Thus the storm–induced accelerations will reduce or eliminate the shear on the upstream side of the line. Subtracting a constant storm motion from all levels would not depict these accelerations well at all.

Both frameworks have significant drawbacks. Storm relative flow can be difficult to define, especially if the convective system is expanding and individual cells are moving in different directions. Errors in storm motion can lead to misinterpretations in the strength and direction of the storm relative wind field. There are also several ways to define system motion. Does one track the motion of the overall average MCS cluster or just average the motions of all the individual convective elements, a question the author has often agonized over. In the case studied here, a well defined, although constantly expanding, convective line developed. As mentioned in Chapter 3, storm motion was determined from the average of all discernable convective elements.

By the same token, errors in the environmental wind field can lead to a misdiagnosis in the storm–induced accelerations. In this case, the North Platte, NE and Dodge City, KS 0000 UTC soundings were averaged to obtain a horizontally homogeneous basic state (Fig. 5.9) to which the Doppler winds were then compared. The Denver sounding was not used because the winds were influenced by convection. This illustrates one of the drawbacks of subtracting out an environmental mean sounding in that one must be careful not to let the convective perturbations contaminate the mean. It is also important to realize that the environment on this day was obviously not horizontally homogeneous. The mid and upper tropospheric winds, although rather uniform in direction, generally increased in speed from south to north across the region. Thus the effects on the environment may be underestimated the further south one looks. The time evolution of the synoptic environment

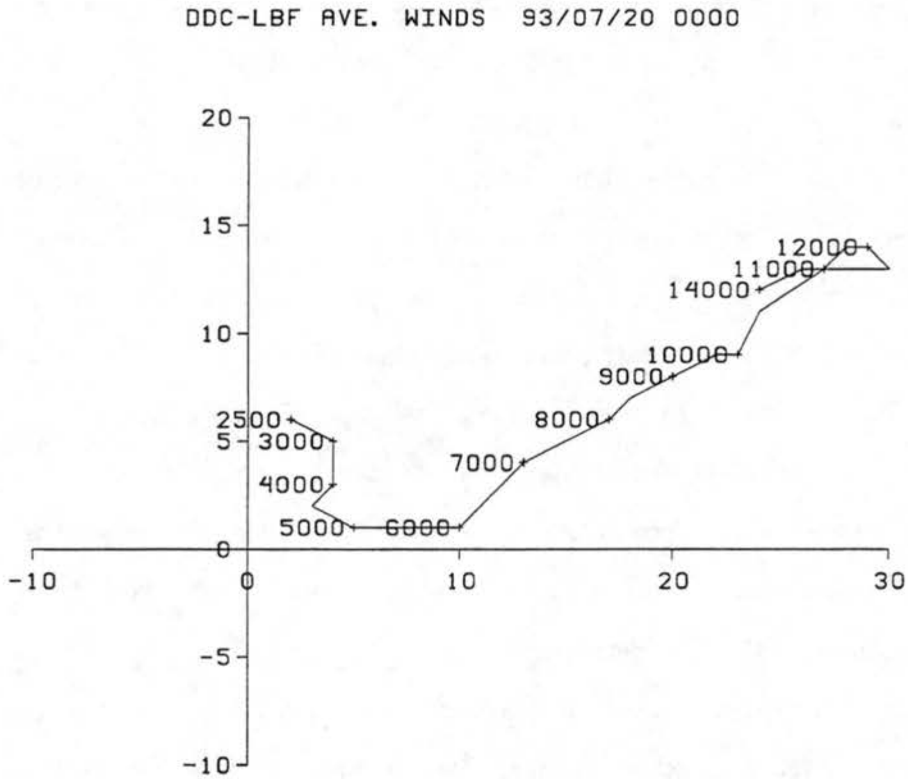

Figure 5.9: Hodograph plot of the environmental average wind profile ($\overline{u}$). The x and y axes represent the u and v wind components in m s^{-1}, and the wind profile is labeled in meters MSL.

can also be a factor. However as noted in Chapter 4, the general pattern was not very progressive and lacked any well defined short waves, thus the effect was deemed to be minor. Despite these drawbacks, both methods can yield important, complementary clues to the storm structure and its gross effects on the environment, and thus they are both used.

5.4.2 Early MCS structure: The 2209 Doppler analysis

This system was well organized almost as soon as it developed. By 2209, or about half an hour after the line initially expanded in the DCVZ, the basic mid tropospheric features that were present through the entire analysis had already developed. Storm-relative (V_{storm} was 11.8 m s^{-1} from 246°) rear inflow (Fig. 5.10) was already penetrating the MCS along the entire western side at $z = 5$ km MSL (all heights MSL), which is quite early for such a well defined feature. The strongest rear inflow was generally north of $y = -82$ km, where storm-relative flow at this level was more northwesterly or even northerly. Although the rear inflow was in a region of trailing stratiform precipitation, reflectivities were generally less than 30 dBZ. Cross sections (Figs. 5.14, 5.15, 5.16) indicate the trailing stratiform echo extended up to 30 km behind the leading line, and echo tops were generally below $z = 10$ km. Much of this trailing echo eroded with time as the wake low developed, yet cross sections continued to indicate the presence of rear inflow. On the eastern flank at $z = 5$ km, strong storm-relative easterlies were present, although most of the high θ_e air feeding the convection was below this level. Northerly flow fed into the northern flank of the system, giving a combined effect of strong mid tropospheric convergence from all sides.

The perturbation flow at $z = 5$ km (Fig. 5.11) is similar to the storm-relative flow (Fig. 5.10) in that both indicated coherent accelerations towards the system from all directions. The biggest difference between the two reference frames was in the southwestern portion of the MCS. Although storm-relative rear inflow appeared to be weak there, the environmental perturbations were more uniform along the entire western flank.

A close examination of Figure 5.10 reveals the early developmental stages of the bow echo in the portion of the line south of $y = -82$ km. Here the highest reflectivities on the western side of the line showed a tendency to bow outwards, between $y = -94$ and -106 km.

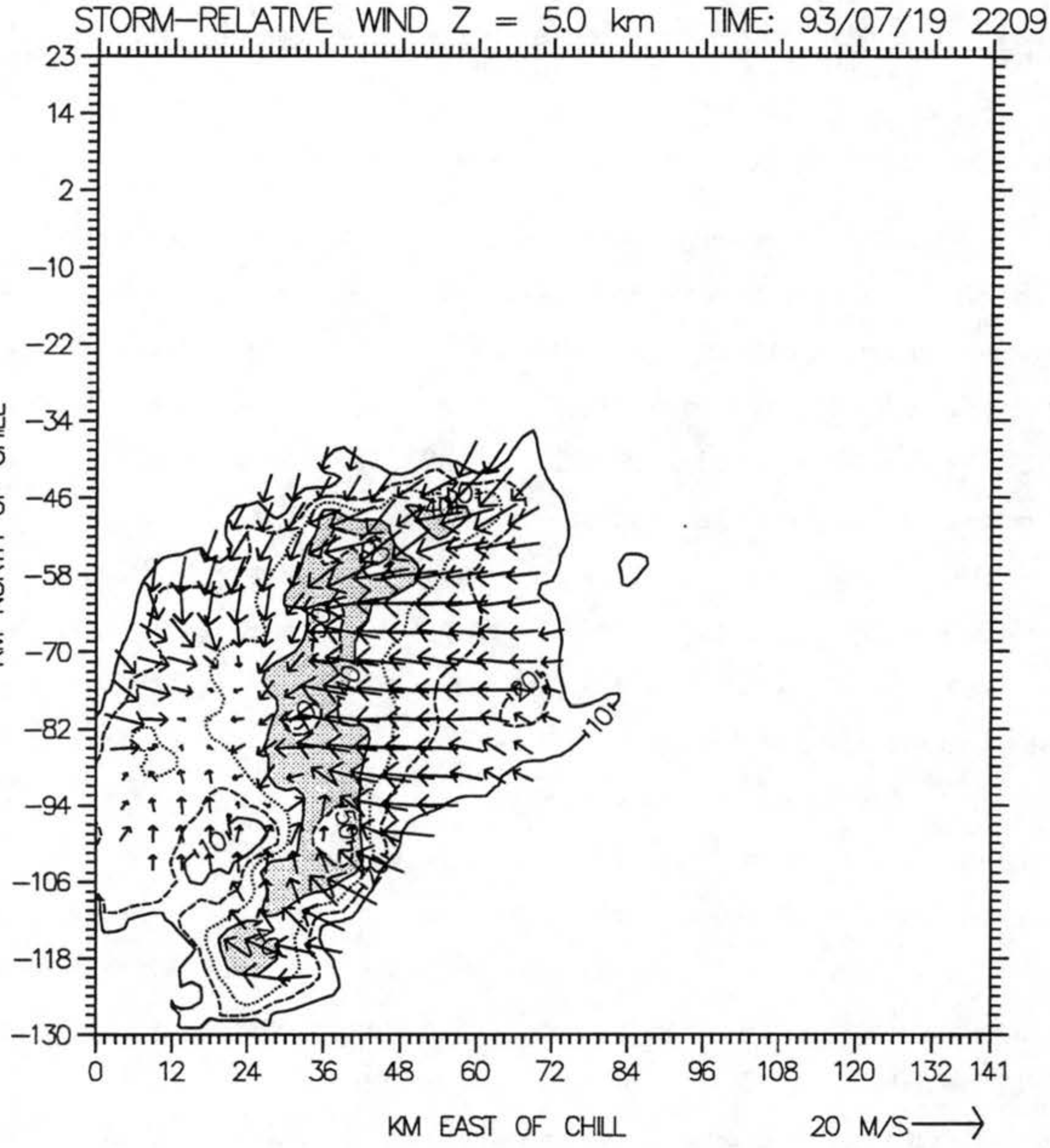

Figure 5.10: Dual Doppler winds and radar reflectivity at $z = 5$ km MSL for the 2209 UTC 19 July volume. Wind vectors are storm–relative, and are scaled by the 20 m s^{-1} vector at the lower right. Reflectivity is contoured at 10 dBZ intervals starting at 10 dBZ, while values between 40 and 50 dBZ are shaded.

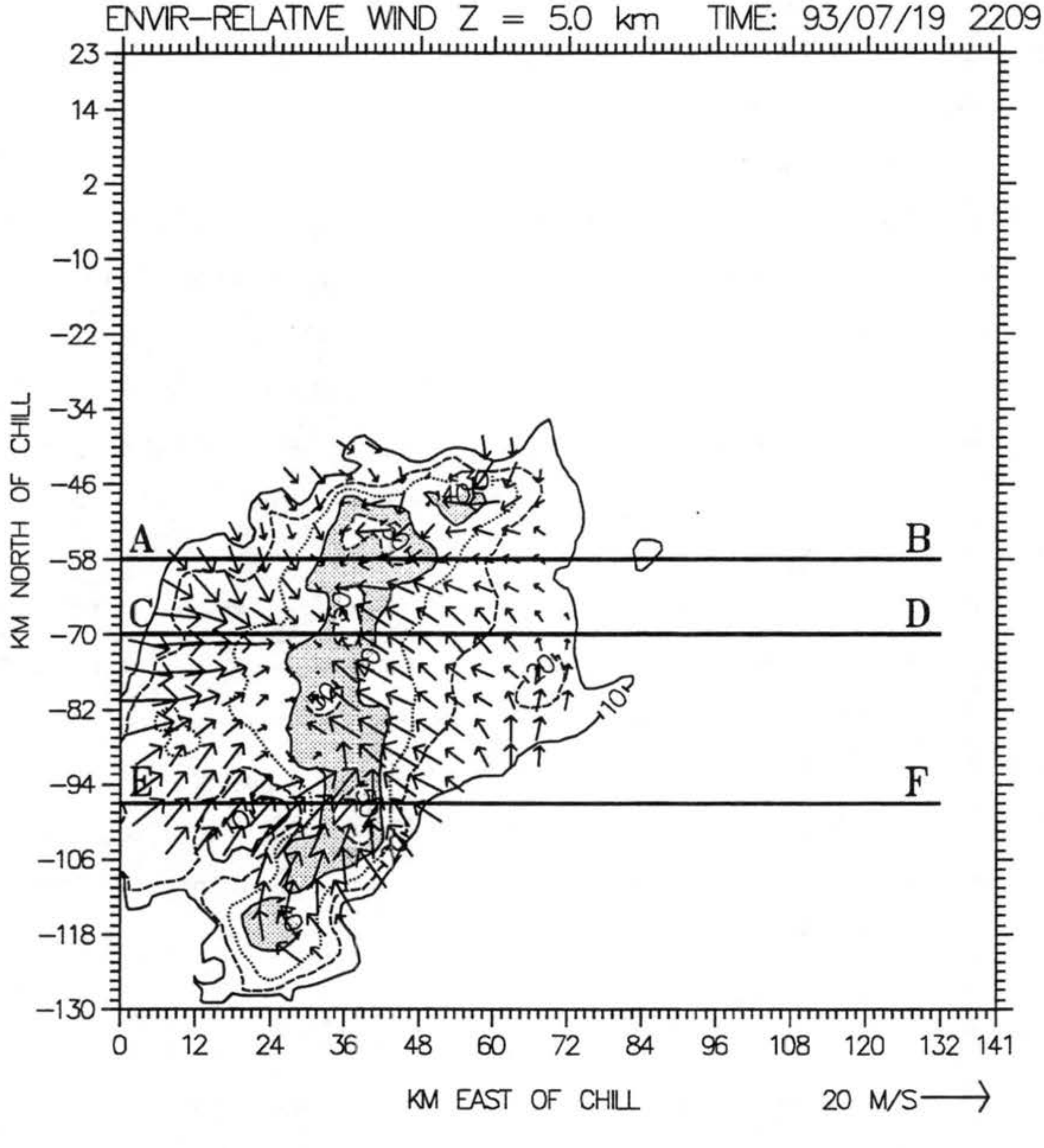

Figure 5.11: Dual Doppler winds and radar reflectivity at z = 5 km MSL for the 2209 UTC 19 July volume. The environmental winds are subtracted from the vectors. Bold lines denote the positions of vertical cross sections. Other details are as in Figure 5.10.

The reflectivity notch is also visible as a hole in the shallow trailing stratiform cloud just west of the bow center. A small closed cyclonic vortex is even apparent on the northwestern portion of the bow, centered at $x = 33, y = -91$ km, while anticyclonic shear is visible on the south side of the bow. Interestingly, this was the region where the storm relative rear inflow was the weakest. This was also the cell that produced the 27 m s^{-1} wind gusts at Strasburg at about this time.

At $z = 11$ km (Figs. 5.12, 5.13) the system was dominated by storm–relative outflow downstream and environment–relative blocking upstream. Ambient winds decelerated and turned mainly to the north as they approached the system. The perturbation winds (Fig. 5.13) indicate that the storm was having the greatest effect on the flow upstream of the convective line. The westward pointing vectors there are indicative of strong deceleration and blocking of the ambient flow by the entire convective line. Downstream, the two counter–rotating vortical perturbations look very much very much like wake created by an isolated obstacle in flow with a low Froude number (Smolarkiewicz and Rotunno, 1989; Smith, 1989). Fujita (1982) also documented similar vortical perturbations in the downstream anvil of a severe thunderstorm complex. Note that the anvil in Fig. 5.13 is advected farthest east on the northern and southern edges of the system, where air was flowing around the obstacle. The dual perturbations in the vorticity existed between $z = 8$ and $z = 12$ km, although the closed vortices were not apparent below $z = 10$ km. The coherent nature of these upper tropospheric perturbations is further evidence that the convective cells were perturbing the atmosphere together as a whole.

The vertical storm circulations derived from the storm–relative and environment–relative winds are considerably different from one another. The storm–relative winds (Figs. 5.14a, 5.15a, 5.16a) suggest that convection was dominated by an overturning circulation with air accelerating in from the east at low to mid levels, rising almost vertically in the main updrafts[1] (Figs. 5.14c, 5.15c, 5.16c) and ejecting eastward in strong outflow. Rear inflow was present, especially in the northern cross sections, but relatively weak. The strongest

[1]The magnitudes of the vertical velocities were likely underestimated due to smoothing of the horizontal wind components during the analysis.

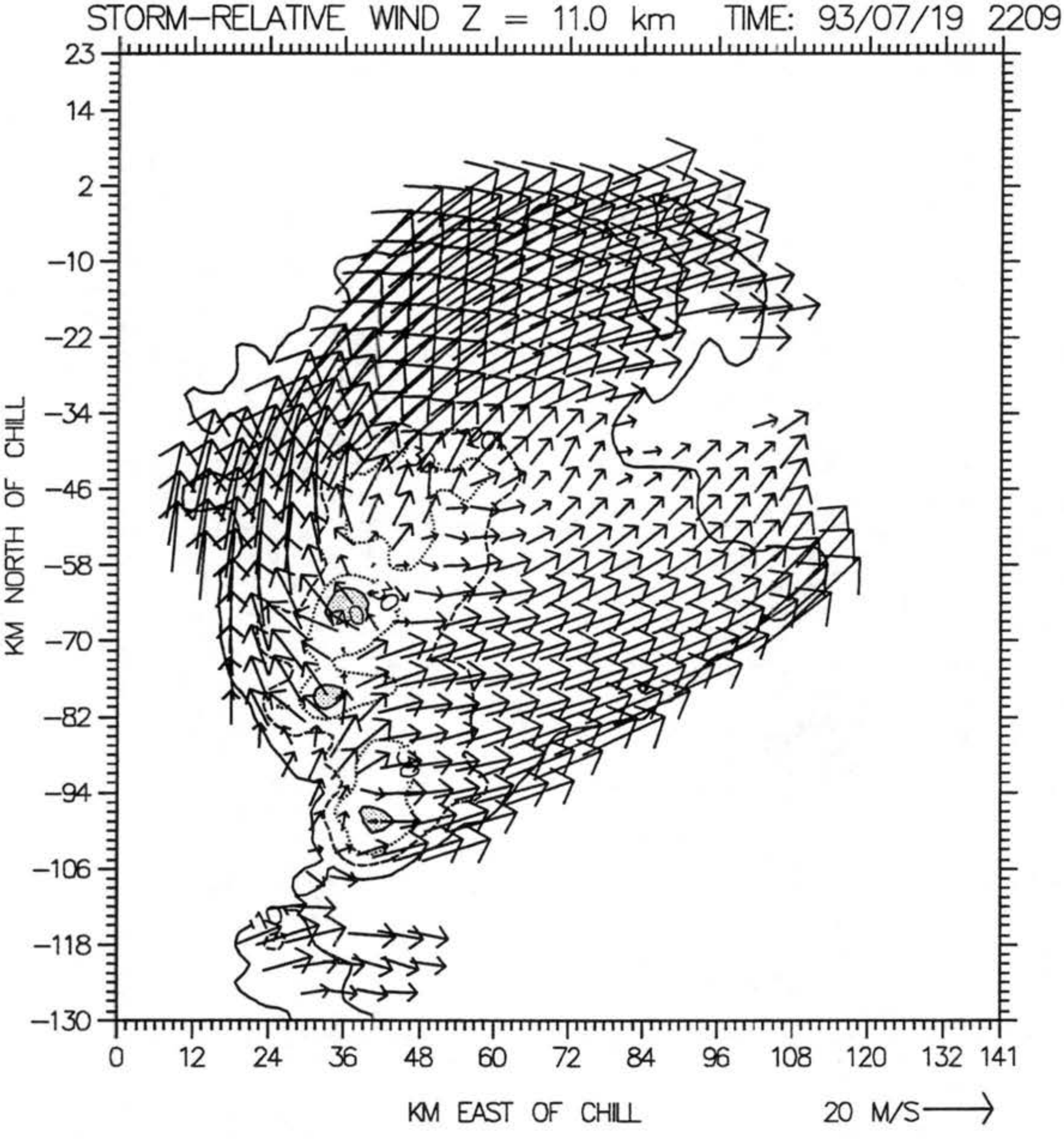

Figure 5.12: Dual Doppler winds and radar reflectivity at z = 11 km MSL for the 2209 UTC 19 July volume. Vectors are storm–relative. Other details are as in Figure 5.10.

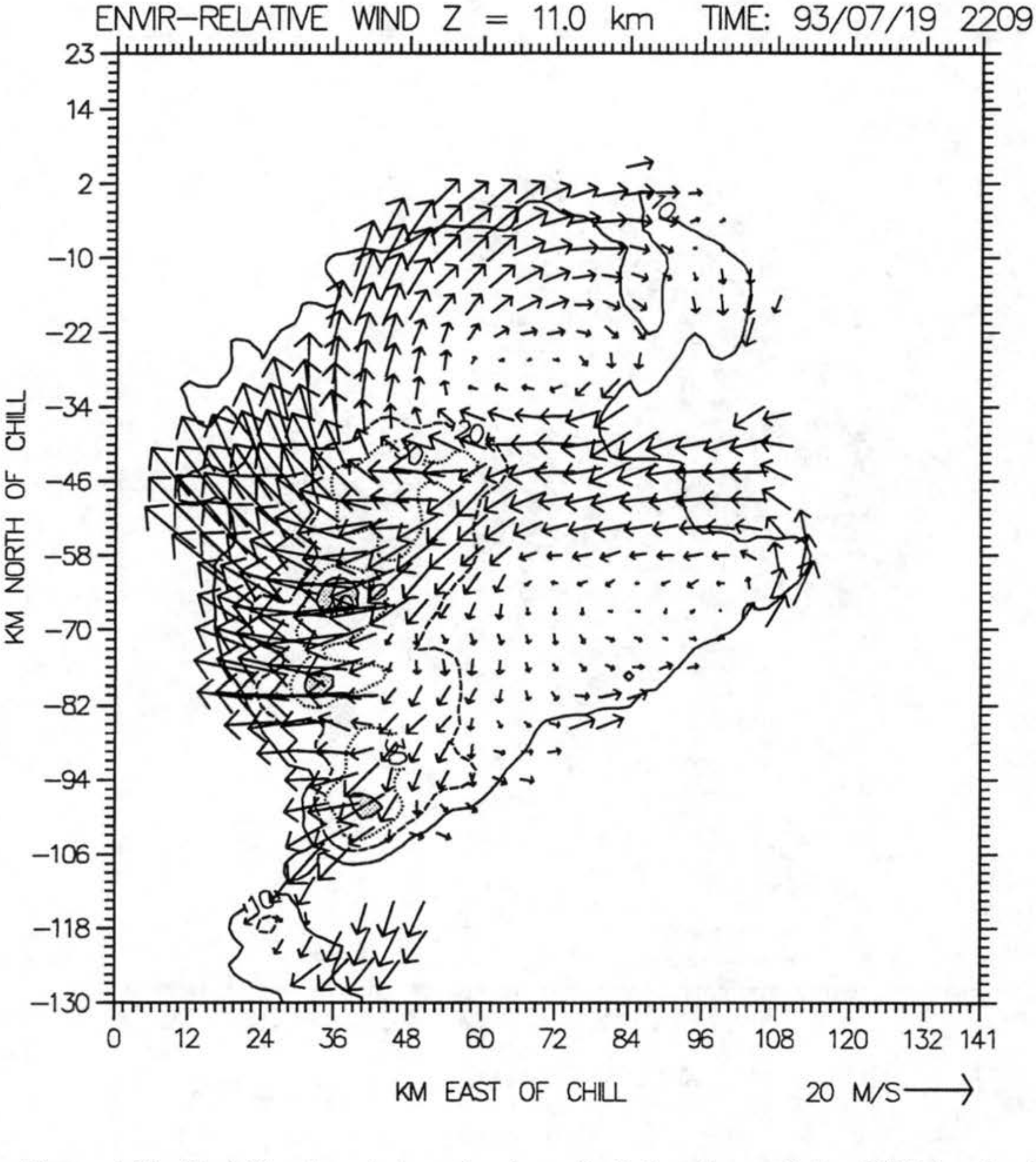

Figure 5.13: Dual Doppler winds and radar reflectivity at z = 11 km MSL for the 2209 UTC 19 July volume. Vectors are relative to the environmental winds. Other details are as in Figure 5.10.

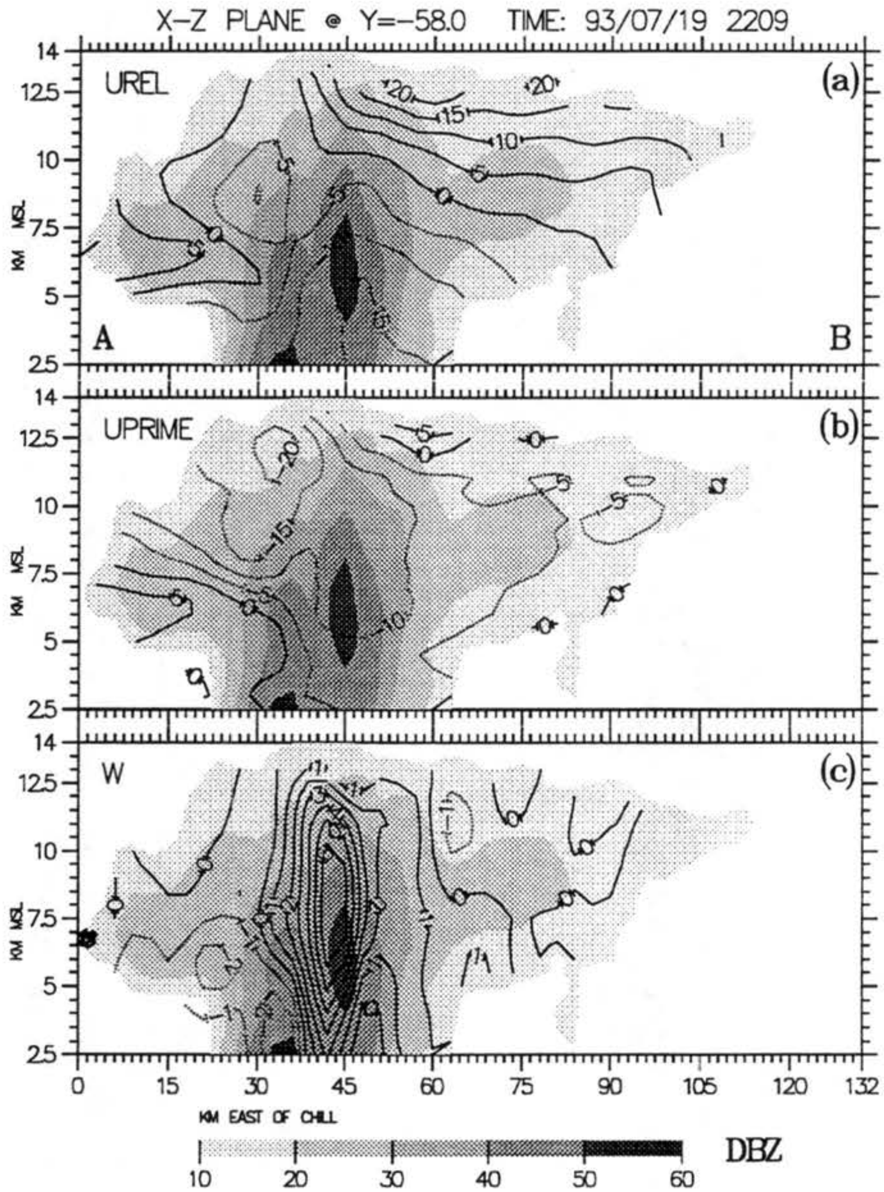

Figure 5.14: Vertical cross sections taken at $y = -58$ km for the 2209 Doppler volume. Radar reflectivity is shaded in all plots as defined by the color bar at the bottom of the figure. The bold letters at the bottom of (a) correspond to those in Fig. 5.3. Storm–relative and environment–relative u component winds are contoured at 5 m s^{-1} increments in (a) and (b) respectively. Vertical velocity is contoured at 1 m s^{-1} increments in (c).

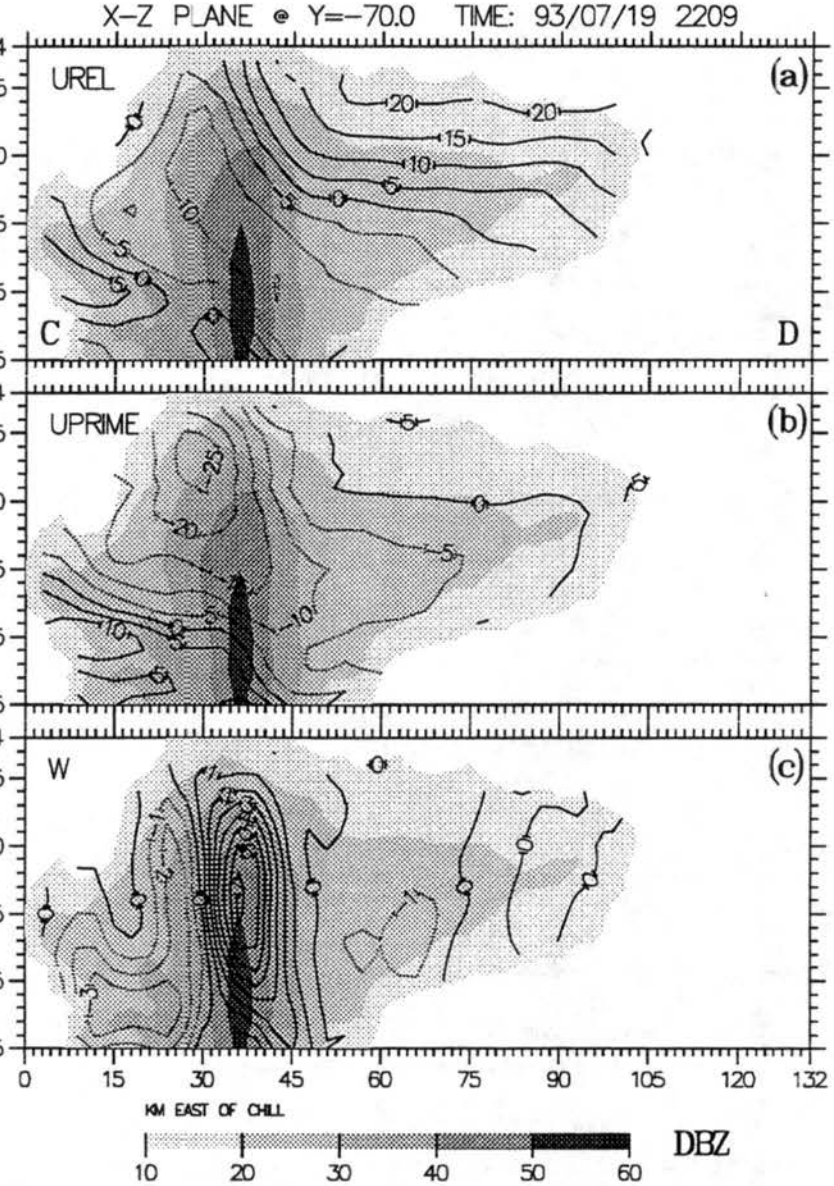

Figure 5.15: Vertical cross sections taken at $y = -70$ km for the 2209 Doppler volume. Other details are as in Figure 5.14.

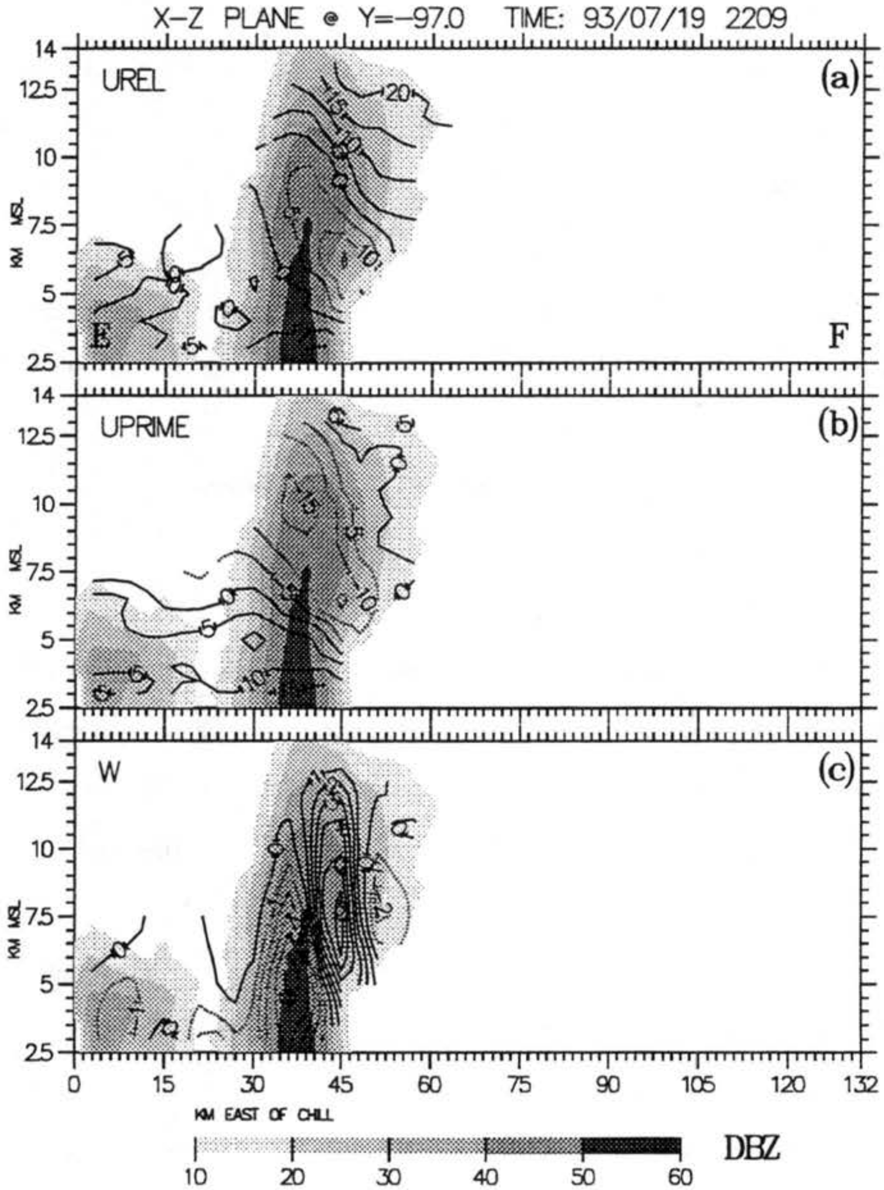

Figure 5.16: Vertical cross sections taken at $y = -97$ km for the 2209 Doppler volume. Other details are as in Figure 5.14.

storm–relative westerlies in the rear inflow were at the back of the anvil, suggesting, as in Klimowski, (1994), that rear inflow continued out into the echo–free air. The upper tropospheric winds on the western side of the convective line were stagnant with respect to the storm. The line of zero flow was on the westernmost edge of the reflectivity, suggesting that the blocking aloft also extended into the post–MCS environment. The strongest perturbations in the environment–relative cross sections (Figs. 5.14b, 5.15b, 5.16b) are on the western side of the convective line. There, the nearly stagnant storm–relative flow aloft represented considerable front–to–rear perturbations with respect to the environmental winds. Meanwhile, the downstream upper tropospheric anvil outflow was only a few meters per second above the original environmental flow. In fact, most of the perturbations east of the line were dominated by deep environment–relative easterlies. In contrast, perturbation winds on the western side of the convective line displayed a strong vertical gradient between front–to–rear and rear–to–front accelerations. These gradients were not as apparent in the storm–relative winds, as rear inflow environment–relative perturbations were about 5 m s^{-1} stronger than the storm–relative rear inflow.

Although both relative frameworks provided useful information, the data must be interpreted carefully. Storm–relative winds suggest that the downstream stratiform anvil resulted from the *active* downwind injection of condensate from the strong updrafts. However, environment–relative winds indicate that condensate was instead *passively* advecting downstream in the mean environmental flow. This is very interesting because the storm–induced environment–relative flow was not at all correlated with the position of the anvil. Instead, environmental perturbations resembled a leading–line/*trailing*–stratiform structure even though the bulk of the stratiform anvil was advecting ahead of the line. The lack of strong velocity gradients at the western edge of the observable echo suggest that the perturbations extended into the clear air. These results are consistent with the results of Schmidt and Cotton (1990), and Pandya and Durran (1996), who suggested that gravity wave–induced accelerations have significant upstream affects on environments with strong shear. This topic will be revisited in great detail in Chapter 7.

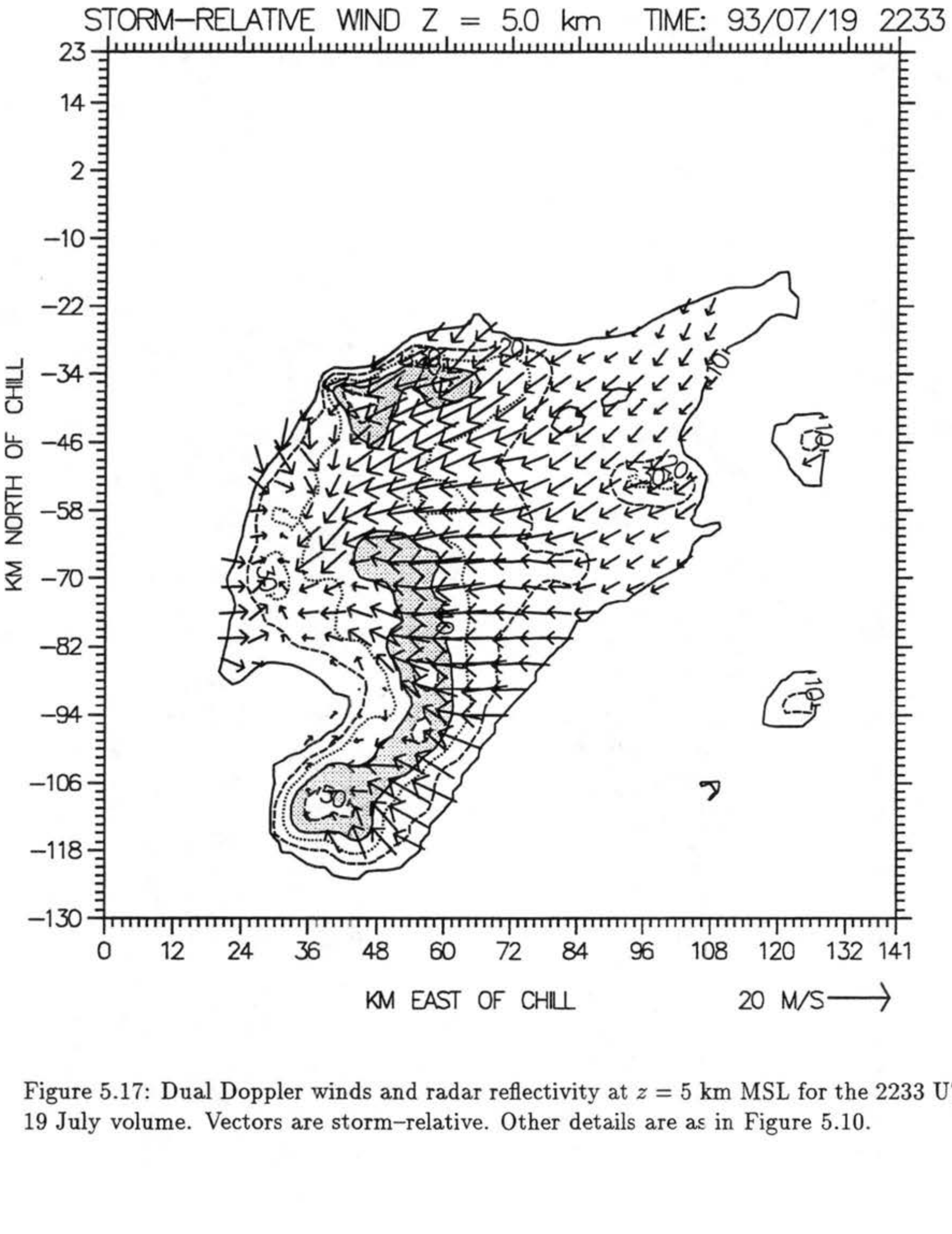

Figure 5.17: Dual Doppler winds and radar reflectivity at $z = 5$ km MSL for the 2233 UTC 19 July volume. Vectors are storm-relative. Other details are as in Figure 5.10.

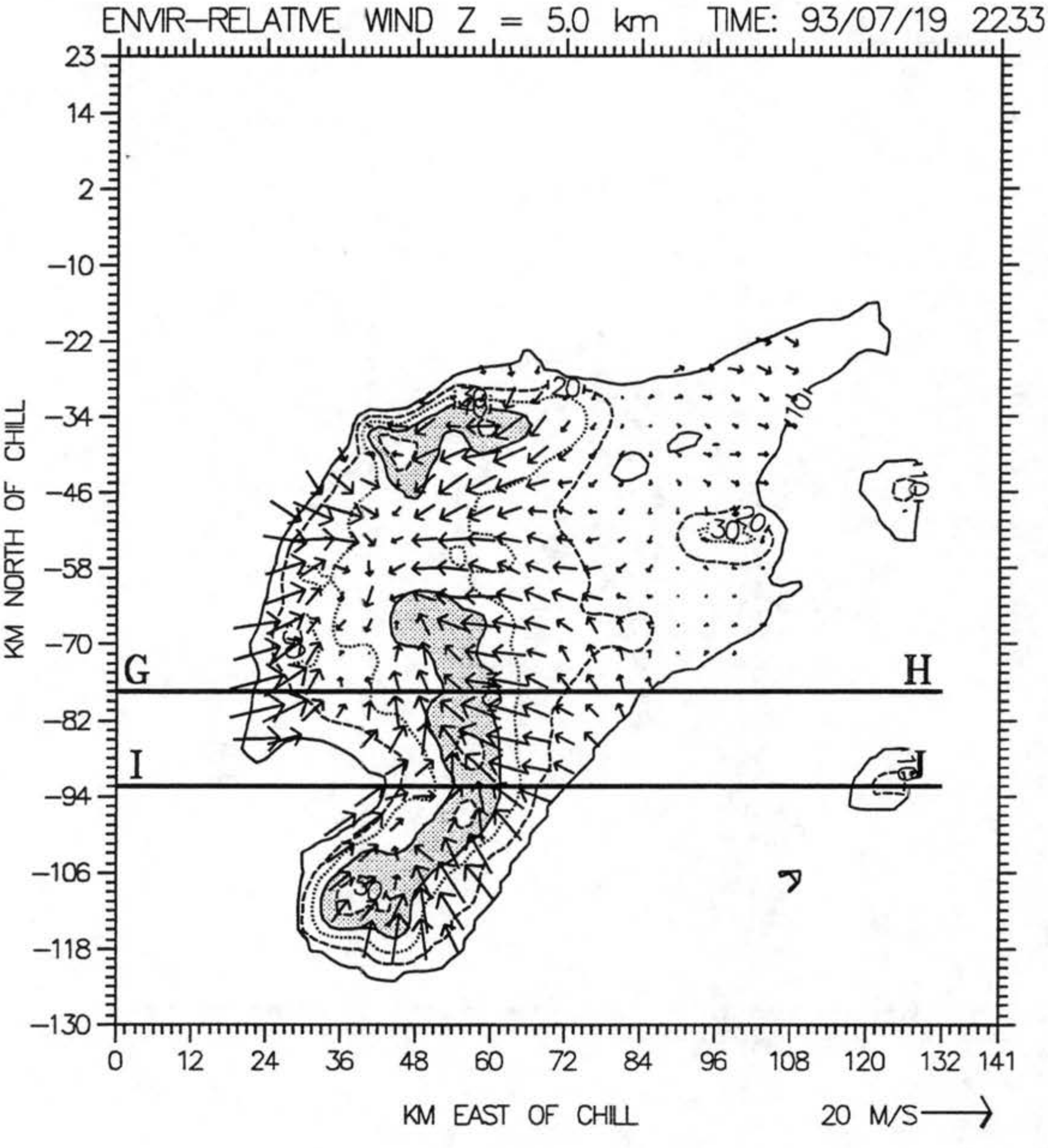

Figure 5.18: Dual Doppler winds and radar reflectivity at z = 5 km MSL for the 2233 UTC 19 July volume. The environmental winds are subtracted from the vectors. Bold lines denote the positions of vertical cross sections. Other details are as in Figure 5.10.

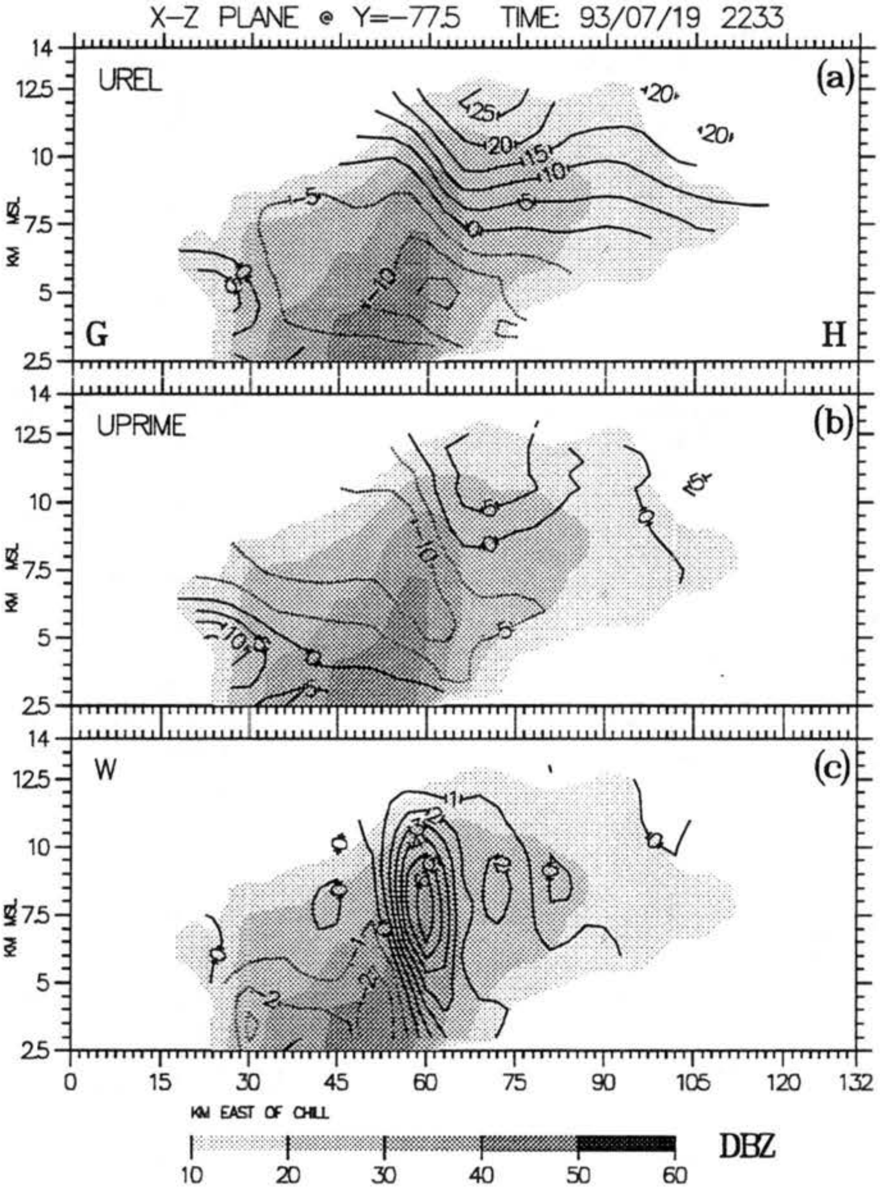

Figure 5.19: Vertical cross sections taken at $y = -77.5$ km for the 2233 Doppler volume. Other details are as in Figure 5.14.

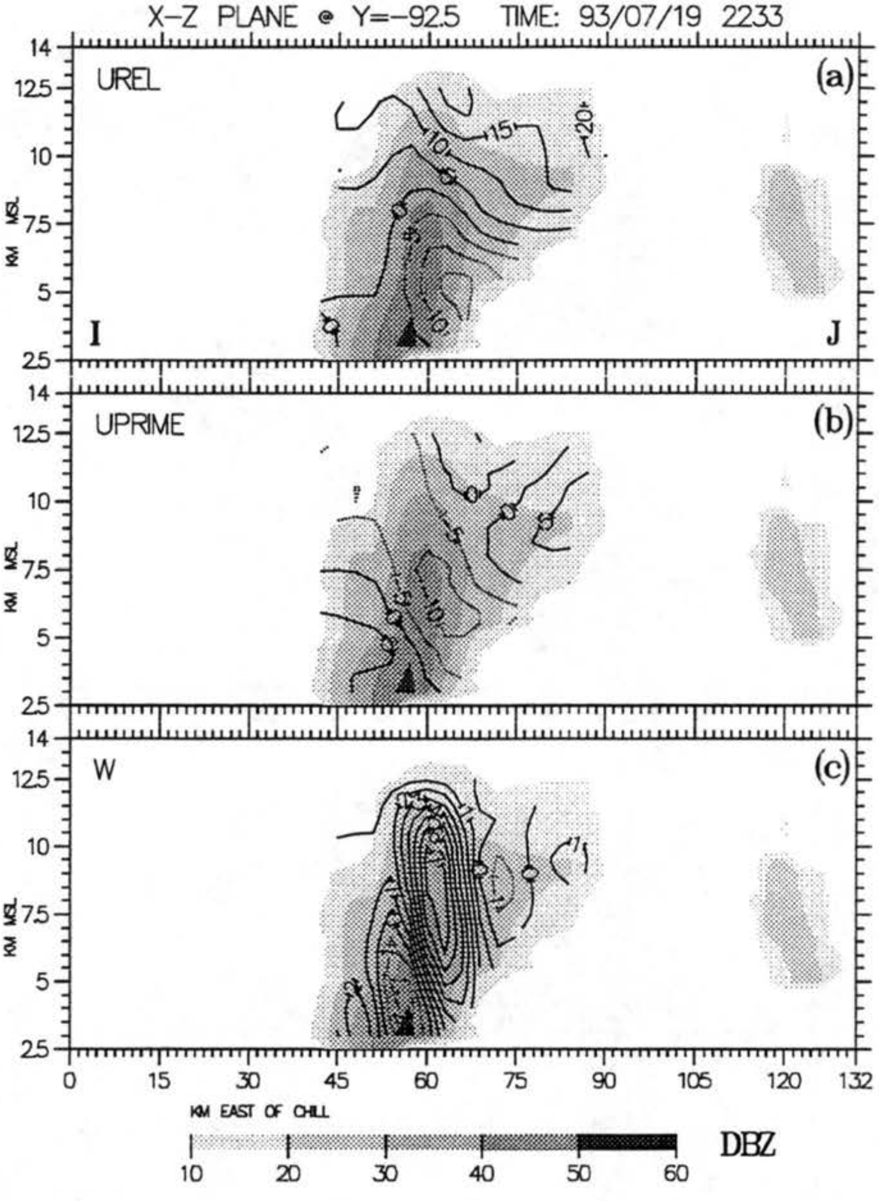

Figure 5.20: Vertical cross sections taken at $y = -92.5$ km for the 2233 Doppler volume. Other details are as in Figure 5.14.

5.4.3 MCS Growth and evolution: the 2233 and 2321 analyses

As the MCS expanded over the next 1.5 hours, the same basic flow structure found at 2209 continued to prevail. At 2233 (Figs. 5.17, 5.18), the mid tropospheric flow was still dominated by front–to–rear inflow on the eastern side of the line and rear inflow on the western side. The bow echo had grown in size, but the tight cyclonic vortex in the storm–relative winds was no longer discernable. Instead a growing region of cyclonic vorticity dominated the northwestern portions of the bow echo, with continued anticyclonic vorticity further south. The reflectivity notch had also grown, and most of the stratiform echo southwest of the line had dissipated.

In contrast to 2209, storm–relative easterlies were present 10 to 15 km west the northern portions of the bow echo. The mesohigh/wake low pressure gradient was strengthening at this time, with the strongest gradient at the western edge of the system just north of the echo notch. Significant convergence between rear inflow westerlies and the front–to–rear easterlies was observed in that region (Figs. 5.17, 5.19). The resulting downward motion was likely enhancing the effects of the evaporative processes (Johnson and Hamilton, 1988) in the development of the wake low. Note that the strongest lower tropospheric downward motion was in the convergence zone near the back edge of the shallow trailing stratiform region (Fig. 5.19). Stumpf et al. (1991) observed a similar configuration in a much larger system during the PRE–STORM experiment. In that MCS, the strongest mesohigh–wake low gradient was in a region of strong convergence between rear inflow westerlies and deep front–to–rear easterlies. The 19 July case differed from theirs, however, in that no deep trailing stratiform anvil was present. In the northern portions of the system, rear inflow was only visible on radar at the extreme western edge of the existing stratiform echo (Figs. 5.17, 5.18, 5.19). Further south, the extent of the rear inflow in the echo notch region (Fig. 5.20) was unknown due to the lack of radar returns. Although no storm–relative rear inflow was present at the western edge of the reflectivity in this region, 5 m s^{-1} westerly perturbation flow did exist at mid levels (Fig. 5.20b).

The upper tropospheric anvil at 2233 was still dominated by a blocking pattern, with continued northward deflection of the storm–relative flow (Fig. 5.21). The decelerations on

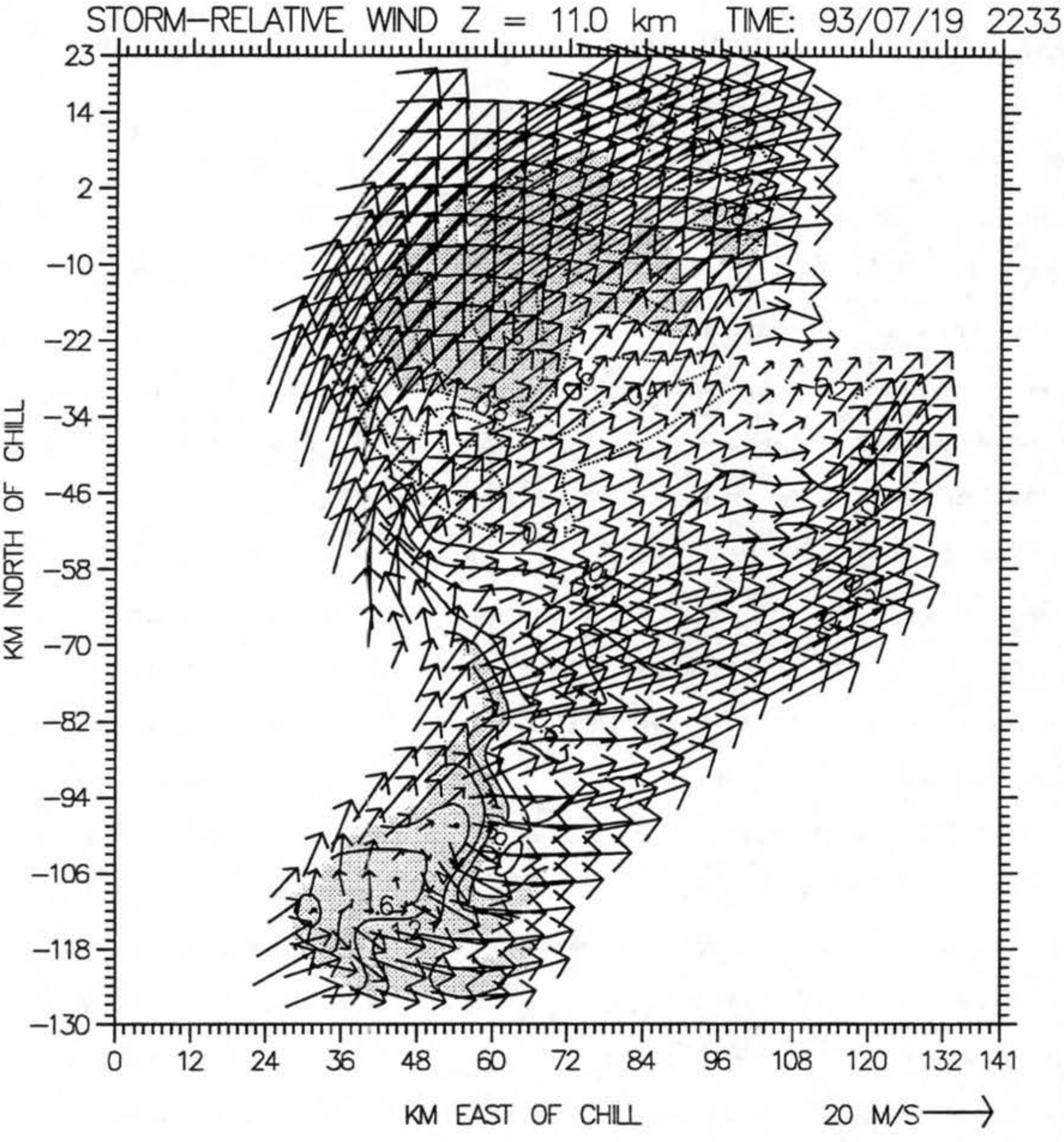

Figure 5.21: Dual Doppler winds and perturbation pressures at z = 11 km MSL for the 2233 UTC 19 July volume. Vectors are storm–relative and are scaled by the 20 ms^{-1} vector at the lower right. Perturbation pressure is contoured at 0.2 mb intervals, and values with absolute magnitudes greater than 0.8 are shaded.

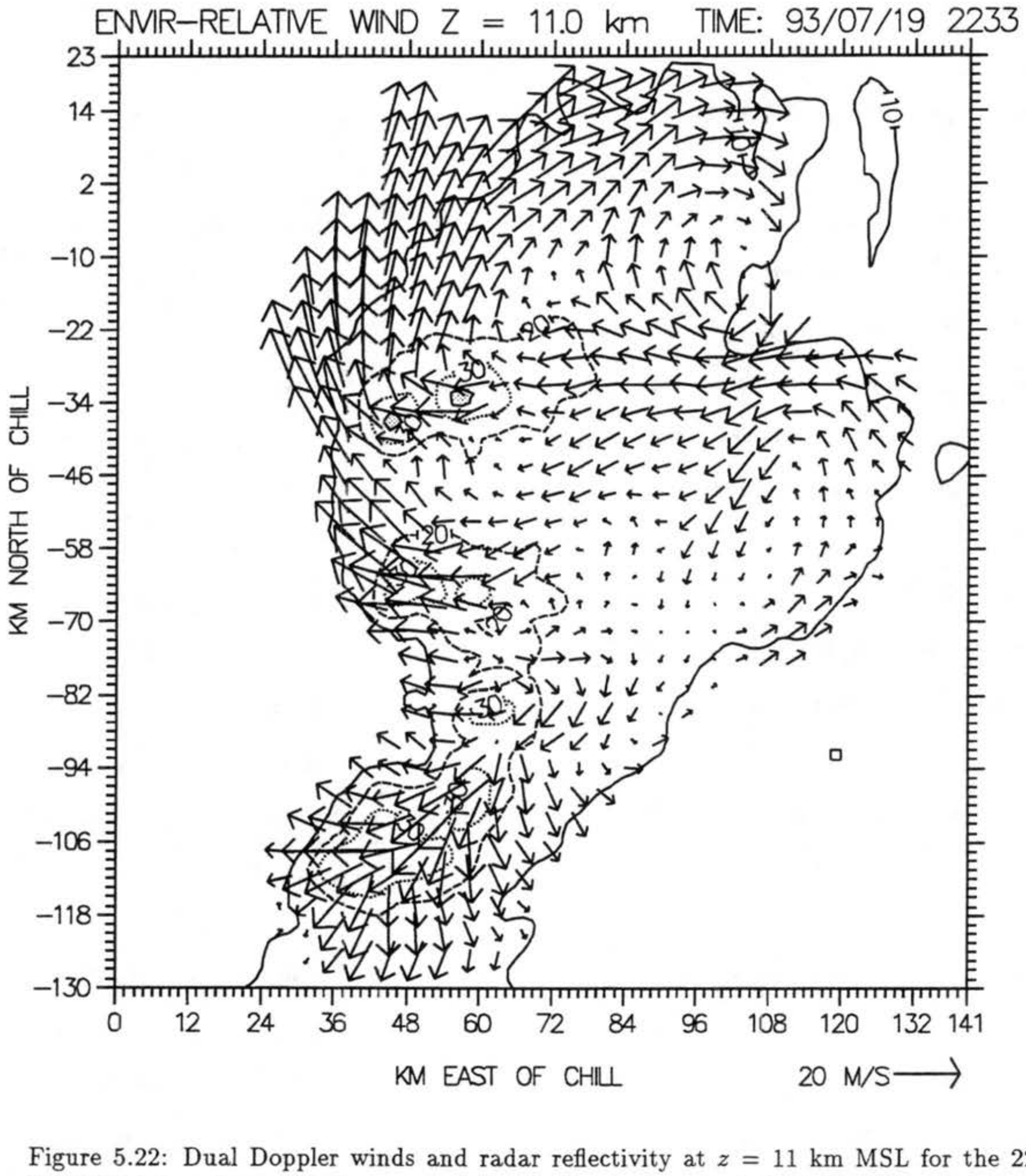

Figure 5.22: Dual Doppler winds and radar reflectivity at z = 11 km MSL for the 2233 UTC 19 July volume. Vectors are relative to the environmental winds. Other details are as in Figure 5.10.

the upwind side (Fig. 5.22) were slightly weaker than those at 2209 (Fig. 5.13), however the system continued to perturb the environmental flow in a unified manner. The wake vortices in the perturbation flow were smaller and further away from the convective line than at 2209, suggesting that some of the vorticity was shedding eastward. The perturbation pressure retrieval analysis at 2233 (Fig. 5.21) typified the structure seen at other times, with the highest pressures appearing on the upwind side of the system. A significant component of the pressure gradient was oriented in an east–west direction. The southwesterly storm–relative flow on the western side of the line was generally perpendicular to this gradient. The strongest mesohigh aloft was well correlated with the most intense convective cells, and the shape of the pattern suggests that high pressure extended well west of the detectable echo. On the eastern side of the system, there was even a hint of lowered pressure near the center of the northern perturbation vortex (near $x = 103.5$, $y = -10$ km).

At 2321, the expansion trend continued, and Figures 5.23 5.24, 5.25, and 5.26 indicate the same basic MCS flow structure. Although the convective line remained strong and a rear echo notch persisted in the trailing stratiform region, the convective bow echo structure had almost completely disappeared. Three new convective cells centered near (x, y) coordinates $(115.5, 34)$, (105, -112), and (117, y=-82) in Figure 5.23 were among the storms developing ahead of the convective line at this time. A meridional $(y - z)$ cross section at $x = 108$ km (Fig. 5.27) shows numerous cellular inhomogeneities in the leading stratiform reflectivity. These were mostly absent from the leading anvil before 2245. With the growth of the leading anvil, flow began converging into it on the northern and southern edges (Figs. 5.23, 5.24). This trend shows up best in the environment–relative winds at $z = 5$ km, however, both frameworks in Figure 5.27 indicate the flow on the northern flank of the anvil was similar to an elevated rear inflow jet. Embedded convective cells combined with the long distance from the radars precluded any further analysis of this feature.

5.4.4 Time series of MCS–total averaged variables

The time evolution of the system as a whole is depicted in the time series of several radar derived variables. The MCS–integrated volumetric precipitation rate shown in Figure 5.28 was derived from the lowest two elevation scans as described in Chapter 3. This is basically

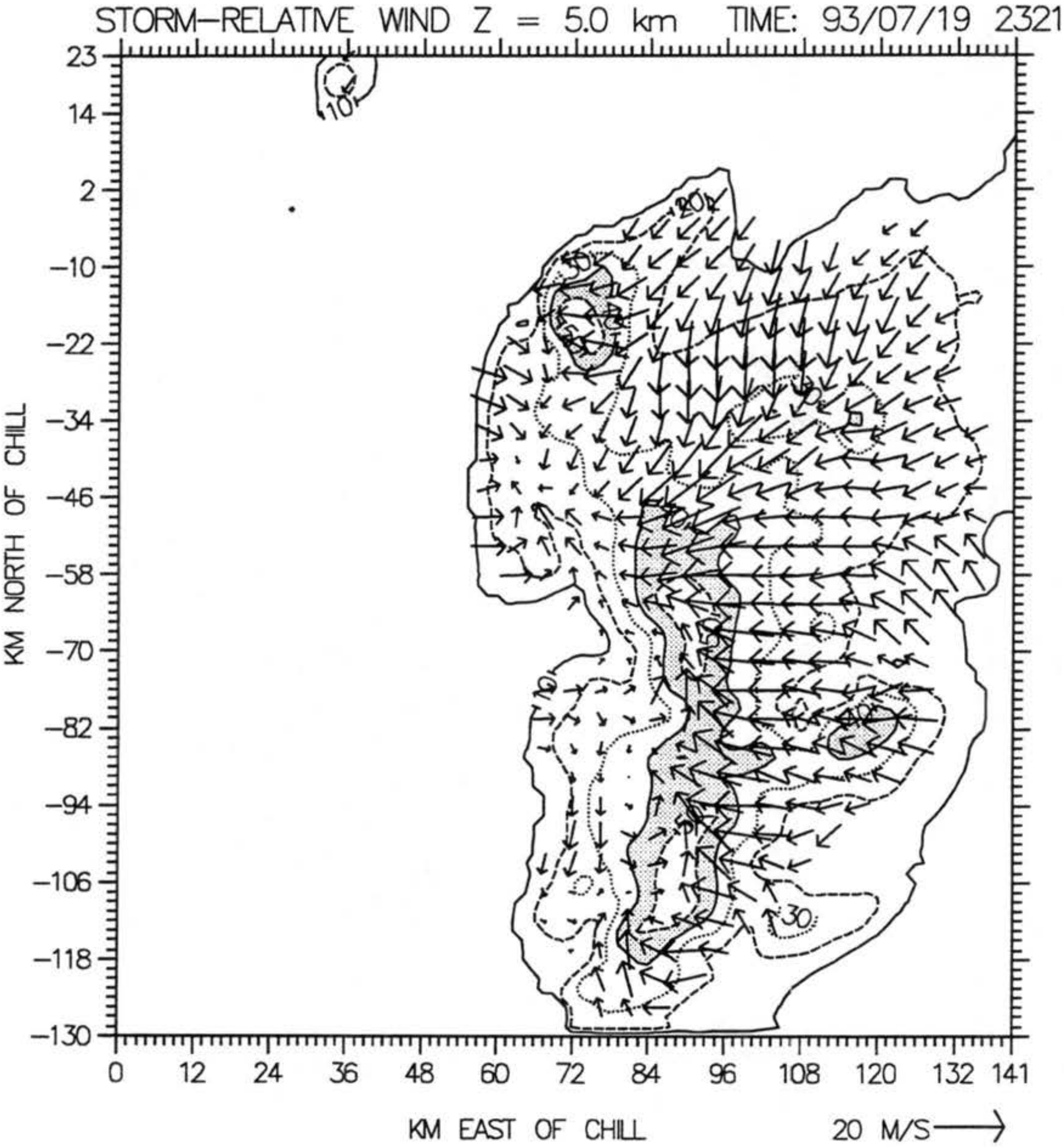

Figure 5.23: Dual Doppler winds and radar reflectivity at $z = 5$ km MSL for the 2321 UTC 19 July volume. Vectors are storm–relative. Other details are as in Figure 5.10.

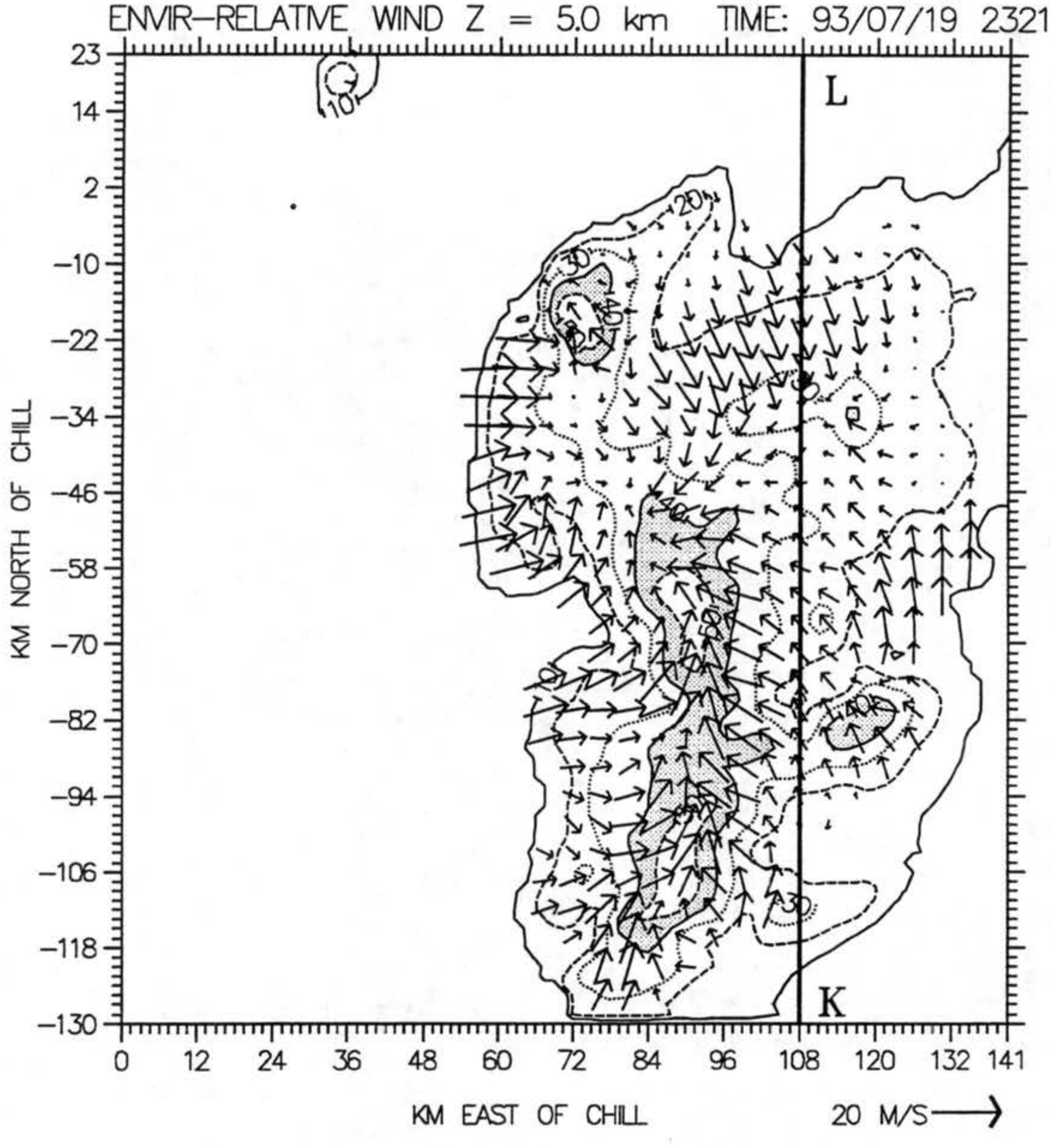

Figure 5.24: Dual Doppler winds and radar reflectivity at $z = 5$ km MSL for the 2321 UTC 19 July volume. Vectors are relative to the environmental winds. The bold line denotes the position of a vertical cross section. Other details are as in Figure 5.10.

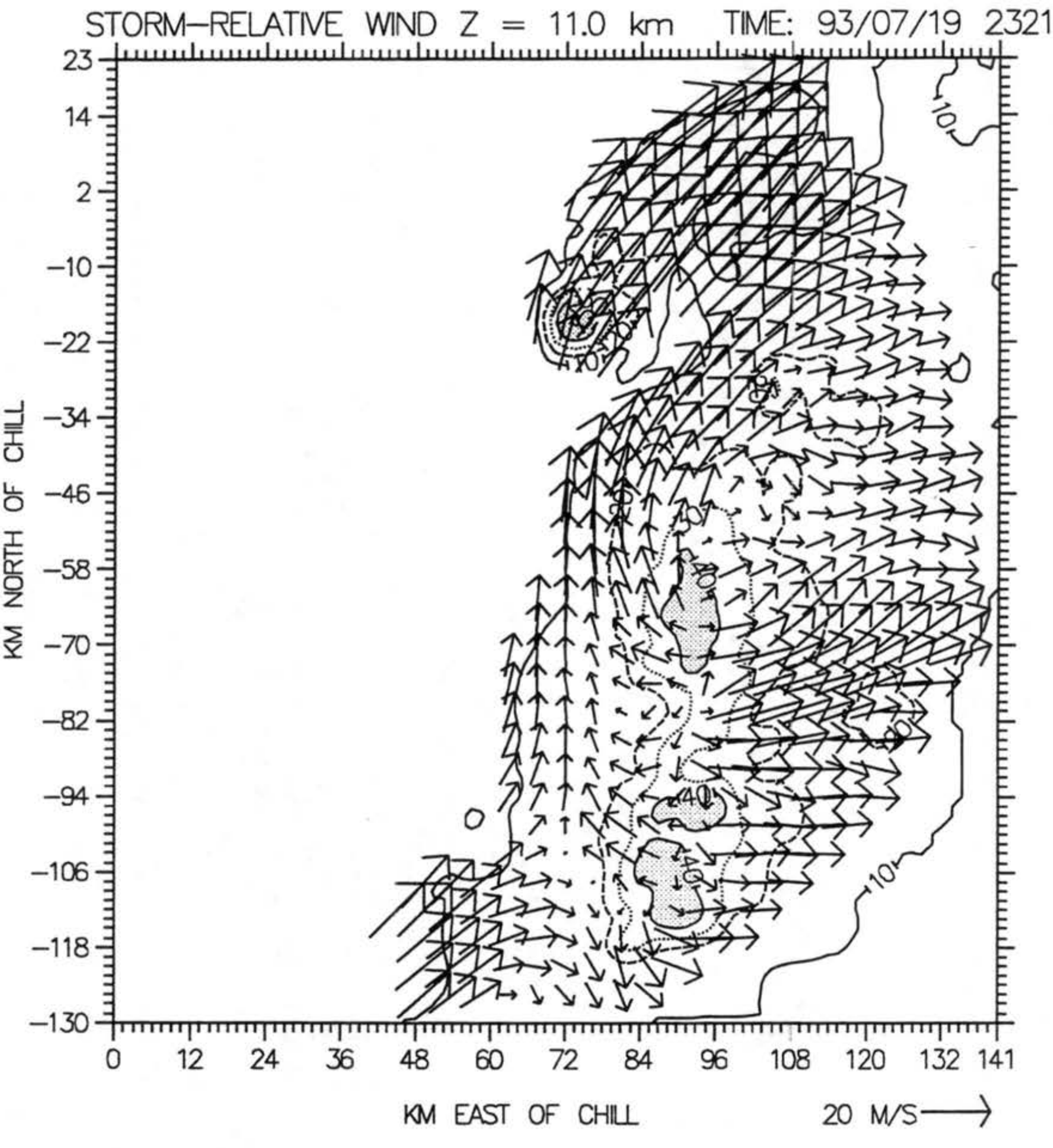

Figure 5.25: Dual Doppler winds and radar reflectivity at z = 11 km MSL for the 2321 UTC 19 July volume. Vectors are storm–relative. Other details are as in Figure 5.10.

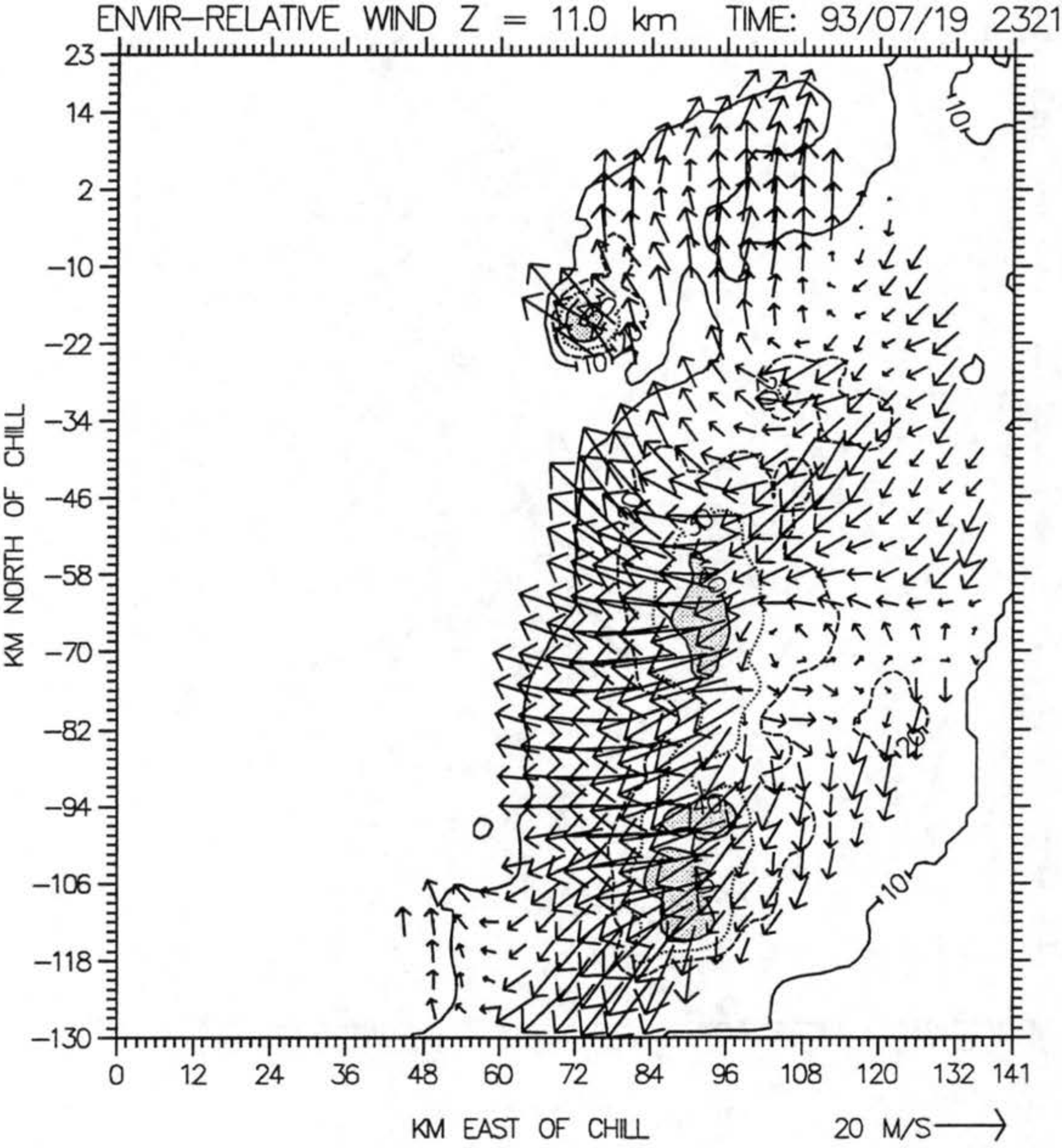

Figure 5.26: Dual Doppler winds and radar reflectivity at z = 11 km MSL for the 2321 UTC 19 July volume. Vectors are relative to the environmental winds. Other details are as in Figure 5.10.

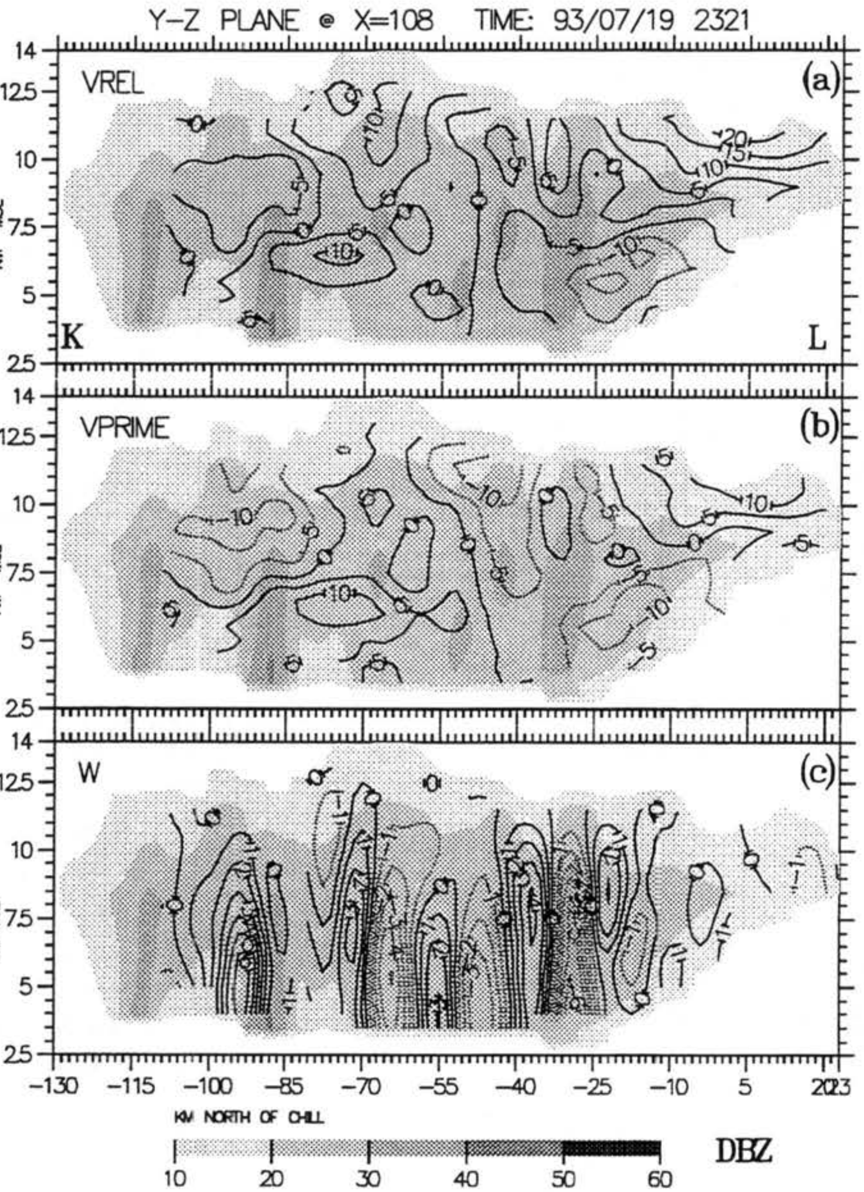

Figure 5.27: Vertical cross sections taken at x = 108 km for the 2321 Doppler volume. Storm–relative and environment–relative v component winds are contoured at 5 m s^{-1} increments in (a) and (b) respectively. Vertical velocity is contoured at 1 m s^{-1} increments in (c). Other details are as in Figure 5.14.

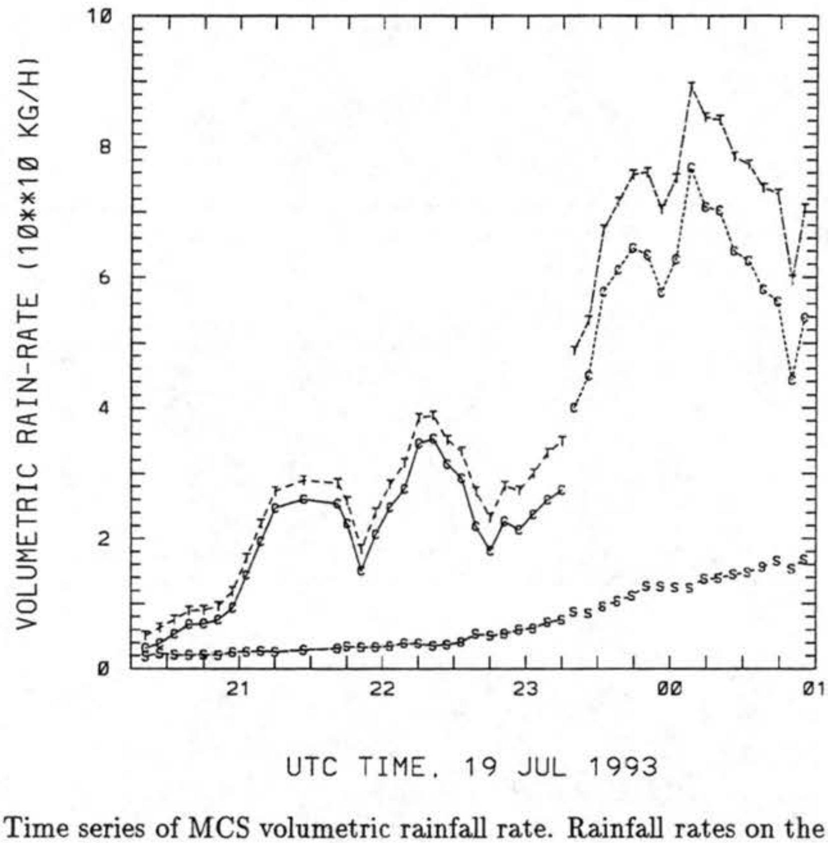

Figure 5.28: Time series of MCS volumetric rainfall rate. Rainfall rates on the ordinate are in increments of 10^{10} kg h^{-1}, while time in hours UTC is on the abscissa. Rainfall rates for the total MCS, as well as the convective and stratiform components are labeled by 'T', 'C', and 'S' respectively.

an estimate of the rain rate produced by the entire system at each volume scan, with the time series providing a reliable indication of the bulk rainfall production tendencies in this system (McAnelly and Cotton, 1992). Dual Doppler and hence short range reflectivity data were available between 2209 and 2345. However, as the system propagated out of the network, reflectivities from the long range scans were used (hence the gap at 2315 in Fig. 5.28). Vertical profiles of MCS–averaged divergence and vorticity, and MCS–integrated vertical mass flux were also derived for all of the Doppler volumes. These profiles were created by horizontally averaging or integrating all available grid point data at each level. The values are all reasonable except near storm top (above z = 12 km) and near the surface, where the lack of grid points with observable echo may lead to unrepresentative averages. The integrated mass flux was calculated by summing over all vertical motions at each level, with the assumption that mass varied with height as $\rho = 1.2e^{-0.1z}$, where z is height in km.

The volumetric rainfall rates (Fig. 5.28) depict three general periods of intense growth. The first one occurred between 2100 and 2130 as the system moved out of the mountains and into the DCVZ; the second occurred between 2200 and 2230 as the bow echo intensified; and the third occurred as the system left the network and came under the influence of the low level jet (more on that in the modeling chapters). The divergence and vertical mass flux fields (Figs. 5.29, 5.30) showed good qualitative agreement with the rainfall rate curve. The higher rainfall rates occurred during times of heightened positive mass flux and strong mid tropospheric convergence. The decrease in the strength of the upward mass flux towards the end of the period was due to convection moving out of the network.

Although the MCS was in its early stages, the convergence profiles were more like those in more mature systems. Convergence was maximized in the mid troposphere while divergence was maximized in the upper and lower troposphere. In turn, the vertical mass flux was maximized at 8 km with significant downward motion below z = 4.5 km. As mentioned in McAnelly et al. (1997), lower tropospheric divergence and integrated mass flux were undersampled due to the lack of sufficient scatterers in portions of the updraft clouds that were rain–free. Radar beam geometry also lead to a general undersampling of the lower troposphere. Thus, although these data still indicate that a significant portion of the MCS was generating a signature indicative of mature convective systems, the profile

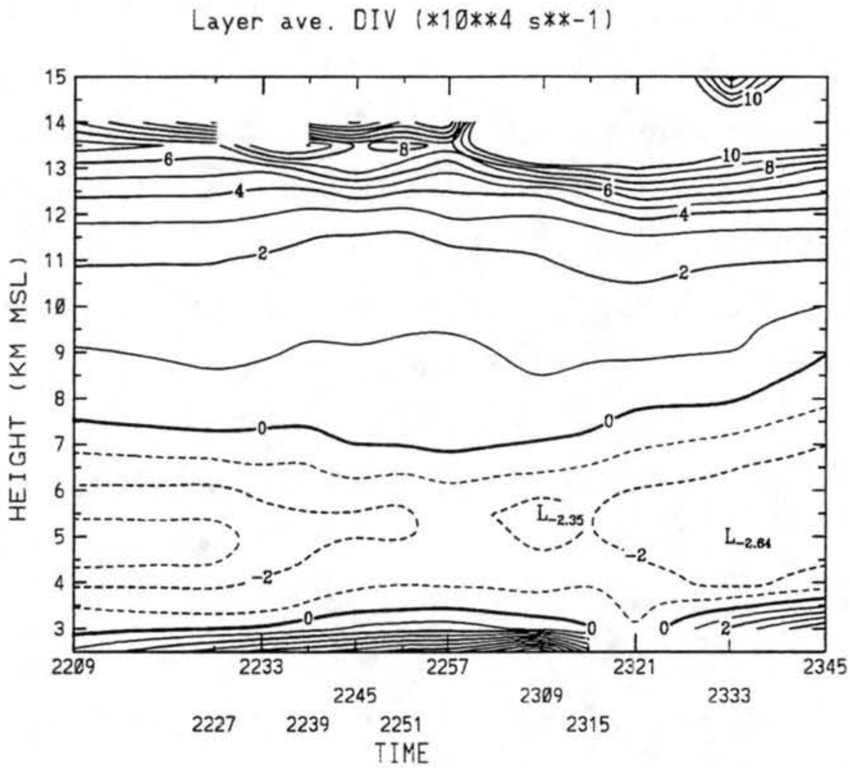

Figure 5.29: Time series of vertical profiles of MCS–averaged divergence (s^{-1}). All values have been multiplied by a factor of 10^4, thus the contour interval is $1 \times 10^{-4}s^{-1}$. Contours of negative divergence are dashed. All of the dual Doppler volume times in UTC are listed along the abscissa.

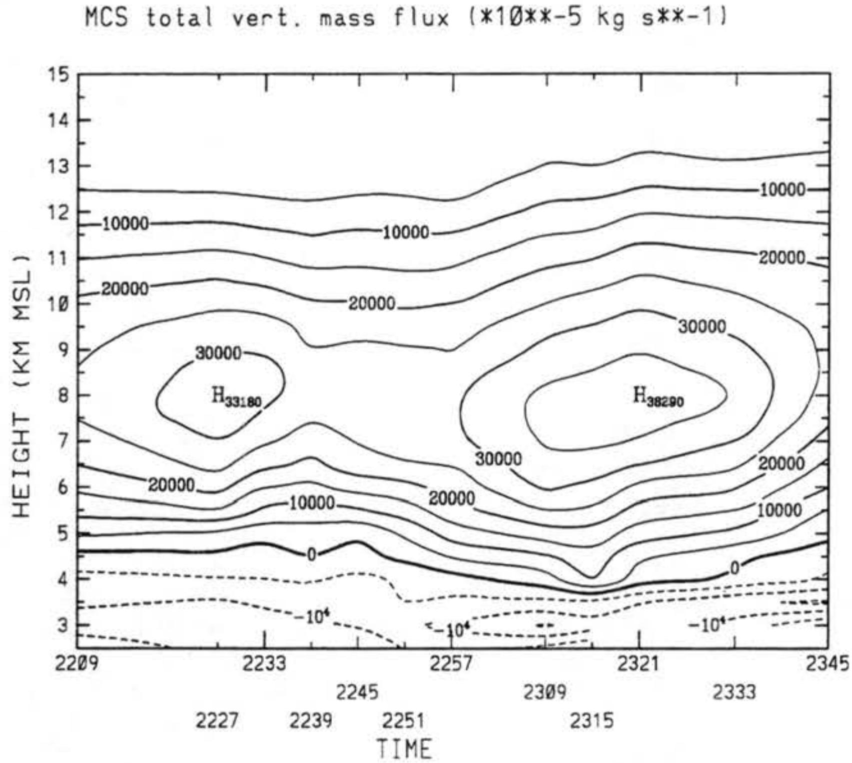

Figure 5.30: Time series of vertical profiles of MCS–integrated total vertical mass flux. All values have been multiplied by a factor of 10^{-5}, thus the contour interval is 5000×10^5 kg s^{-1}. Contours of downward mass flux are dashed. All of the dual Doppler volume times in UTC are listed along the abscissa.

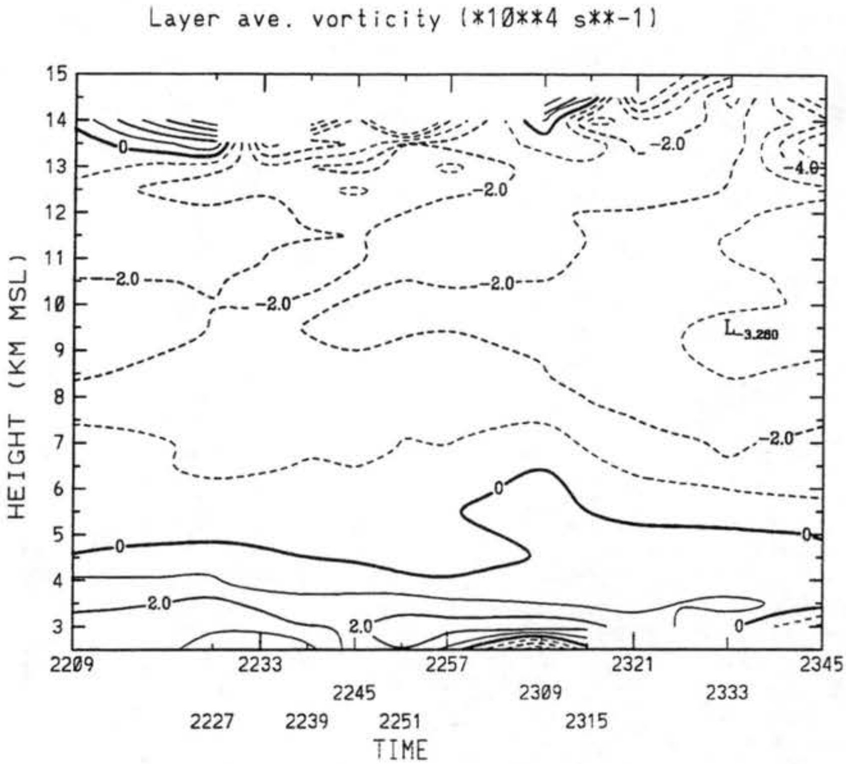

Figure 5.31: Time series of vertical profiles of MCS–averaged vorticity (s^{-1}). All values have been multiplied by a factor of 10^4, thus the contour interval is $1 \times 10^{-4} s^{-1}$. Contours of anticyclonic vorticity are dashed. All of the dual Doppler volume times in UTC are listed along the abscissa.

may have been partially offset by undersampled updrafts. This issue will be revisited in greater detail with the modeling work.

The predominance of strong anticyclonic relative vorticity (Fig. 5.31) above $z = 5$ km system is intriguing. Cotton et al. (1989) observed that MCCs develop in environments characterized by deep anticyclonic synoptic vorticity, while Blanchard et al. (1997) have even observed local regions of negative absolute vorticity. However, the radar measured relative vorticity above $z = 7$ km was about three times greater than the Coriolis parameter f at 40° latitude. Fritsch and Maddox (1980a,b) have documented upper tropospheric anticyclones above large, mature MCCs, and the results in Figure 5.31 indicate this process begins almost as soon as convection perturbs the flow aloft.

Since anticyclonic flow developed so soon after the appearance of strong convection the perturbations were not likely the result of Coriolis accelerations on divergent outflow aloft as discussed by Skamarock et al. (1994). The bulk of the anticyclonic vorticity was in the western and northern portions of the system where air was diverting around it. Such a pattern will develop if an obstacle is placed in an otherwise geostrophically balanced flow characterized by a low Froude number. Here the Froude number is defined as $F = \frac{u}{Nh}$ where u is the velocity perpendicular to the barrier while N is the Brunt Väisällä frequecncy and h is the height of the barrier. The Froude number of the flow approaching the system at $z = 11$ km was estimated from the 0000, 20 July Denver sounding and the height of the radar returns ($u = 30$ m s^{-1}, $N = 0.01$ s^{-1}, $h \approx 3000$ m[2]) to be about 0.75. This estimate may be a little high since values of N went up sharply at the tropopause (12 km). However, it was still less than one, indicating that air should go around as opposed to over the obstacle. The downstream vortices in the perturbation flow are another indication that the Froude number was less than one. This situation is similar to the development of barrier jets on the upwind side of mountain ranges such as that observed by Bell and Bosart (1988). In both cases, the ambient flow slows down as it approaches the obstacle and flows toward lower pressure, which in the case of most mid latitude northern hemispheric convective systems is towards the north.

5.5 Discussion

The vertically erect updrafts and radar reflectivity cores in this system indicate that the convective heating profile was also erect. At the same time, the low reflectivities in the stratiform anvil indicate that it was not significantly contributing to the MCS heating. Klimowski (1994) noted a similar structure in newly growing convection on the southern side of an established squall line. In that case, elevated storm–relative rear inflow rapidly developed from erect convective towers with relatively little stratiform precipitation. Klimowski also noted that the highest rear inflow velocities were generally located behind the strongest convective cells. Grady and Verlinde (1997) also observed elevated rear inflow in the early stages of another Colorado High Plains squall line. They pointed out that convective updrafts were erect even when the theory of Rotunno et al. (1988) predicted a rearward tilt.

---

[2] This value was used because observable radar echos extended to 15 km, or 3000 m above the 11 km level.

Weisman (1992) found that elevated rear inflow was generally associated with strong, erect convective cells. He contended that a vorticity balance between front–to–rear and rear–to–front flow helped to keep the rear inflow elevated. Elevated rear inflow in turn helped to keep the convection erect.

Experiments by Nicholls et al. (1991) and Mapes (1993), discussed in Chapter 2, help put these observations in context. Their results indicate that a heat source will affect its surrounding environment through the outward propagation of low frequency gravity wave energy. The heat sources used in their experiments were vertically erect, and consisted of a linear combination of the n1 and n2 forcing modes. The resultant asymmetric heating profile was characterized by an elevated heating maximum in the upper troposphere with either no heating (Mapes, 1993) (Fig. 2.1) or slight cooling (Nicholls et al., 1991) in the lower troposphere. Gravity wave energy propagating away from this heat source typically induces divergent accelerations in the upper and lower troposphere and convergent accelerations in the mid troposphere at considerable distances from the source (Fig. 2.1). Such flow is characteristic of a mature MCS, and although the heating profiles in these experiments were meant to represent such a system, any disturbance with this signature will produce the same kind of perturbation.

Despite radar limitations, MCS–average convergence and vertical mass flux profiles for the 19 July case (Figs. 5.29, 5.30) indicate the propensity for an elevated convergence maximum. Rear inflow accelerations also developed despite the erect updrafts and lack of trailing stratiform anvil. In this situation, mechanisms for mid tropospheric mesolow development discussed by Brown (1979) and LeMone (1983) were relatively inactive, and the mid tropospheric environment–relative accelerations were likely the result of gravity wave propagation. When the environmental shear is deep and strong, as it was in this case, Schmidt and Cotton (1990), Weisman (1992) and Grady and Verlinde (1997) have shown that convection tends to remain erect. However, gravity wave–induced accelerations can provide a more favorable environment rearward tilt by reducing the upper tropospheric shear. In cases when shear is weak, the linear perturbations may alone be strong enough to actually reverse the storm–relative flow. Once this happens, deep trailing stratiform anvils can develop as condensate advects rearward of the convective line. When shear is strong, other processes such as the nonlinear advection of momentum and condensate by convection may be required. In any case, MCS genesis is defined here as *the point at which the deep tropospheric storm-relative flow reverses, allowing for the development of a deep trailing stratiform anvil.* In this case, this transition likely occurred when the characteristicly large oval anvil developed, or shortly after the MCS left the observational network. Fortunately, the simulated MCS also produced a trailing anvil, and the process of wind reversal is investigated in Chapter 7.

The development of stronger environment-relative accelerations on the upstream side of the convective line is a more complicated issue involving the shape of the heat source and its interactions with strong upper tropospheric flow and shear. Schmidt and Cotton (1990) noticed the preferential amplification of gravity wave energy on the upstream side of convection, which would help explain the observed tendencies. Due to the lack of observations in clear air, this topic cannot be fully addressed with the observational data, but it will be revisited in Chapters 7 and 8.

5.6 Summary

Topography played a major role in the initial organization of this MCS. Convection initially developed in the highest mountains as moist upslope flow became unstable. However, only those storms along the Palmer Divide traversed the mountain–plains solenoid suppression zone without dissipating. As discussed in Chapter two, the Palmer Divide has long been known as a focal point for storm development. The elevated terrain in conjunction with the nearby Rockies block and divert the boundary layer southeasterly winds, leading to the formation of the DCVZ. This strong region of convergence and cyclonic vorticity is often found just downwind and parallel to the highest elevations of the Palmer Divide. The enhanced moisture convergence counteracts the detrimental effects of boundary layer drying due to mix–out, and creates a favorable environment for convection.

The Palmer Divide also allowed localized convection to break out before most of the region had reached convective temperature. Much of the environmental instability was thus focused in one intense cluster of storms. Had the entire region been allowed to reach convective temperature, storms would have developed everywhere and rapidly used up the environmental instability. Such an evolution would have resulted in many short–lived, less intense cells with relatively little mesoscale organization. Instead, the cap held, and as convection intensified a density current developed and began propagating out onto the plains. The density current played the same role as the topographic convergence, preferentially breaching the mid tropospheric inversion in one localized region.

Although it consisted mainly of erect convective cells, the 19 July MCS was able to generate environmental perturbations that were similar to systems with mature upshear–tilted convection and much larger stratiform anvils. The atmospheric response was characteristic of the propagation of low frequency gravity wave energy from heat sources with elevated heating maxima. By simple geometry, such disturbances from several cells in close proximity will produce a stronger, more concentrated environmental perturbation than if the cells were far apart. Thus another advantage to a local concentration of convection becomes apparent. The increased strength of the combined gravity waves is more effective at perturbing the environment and decreasing the ambient shear. The reduction and eventual storm–relative reversal of the upper tropospheric flow in turn sets up the framework for stratiform anvil development.

Although these observations provided much insight, many aspects of this system and especially its surrounding environment remain unknown due to limitations of the network. Other than soundings and the mesonet, no data were available outside the contiguous MCS anvil. The vertical structure of the topopgraphically forced circulations and their interactions with the preexisting frontal boundary were unsampled. Interactions between the MCS and its surrounding environment could only be inferred from observations from within the system. The coarse resolution mandated by the long baseline made radar detection of the subtle vertical motions at the gravity wave fronts (often less than 1 m s−1) nearly impossible. The model results offer an opportunity to view the MCS evolution from the perspective of its interactions with the surrounding environment. Although the model contains many simplifications of the atmosphere, comparison with the high resolution observational data set offers a high standard of ground truth that is rarely available.

Chapter 6

MODEL OVERVIEW

6.1 Model set–up

The Regional Atmospheric Modeling System (RAMS), version 3b (Pielke et al., 1992) was used to simulate the 19 July 1993 case. The main advantage of the model is the widespread data set provided both inside and outside the convective system. The Doppler radar, for example, was unable to detect the extent to which the storm–induced circulations extended into the echo–free environment. In this respect, the model should be thought of as a tool to help interpret the observations. To the extent that the model can reproduce the 19 July MCS, additional inferences can be made as to how this system interacted with its environment.

To reproduce this case at a scale comparable to the Doppler radar observations, an ambitious effort was made to simulate it in a heterogeneous, time–varying environment initialized with the observed data. Convection was explicitly resolved with the nonhydrostatic, compressible set of equations. The term "explicit" is of course relative in that ultimately the grid discretization will require the use of parameterization to account for subgrid scale turbulent motions. "Explicit" in this case means that the dominant motions within each individual thunderstorm were resolved by the model without the use of convective parameterization. Weisman et al. (1997) showed that this could be accomplished with grid spacings of 4 km or less. The lack of a dependency on convective parameterization is desirable because the environmental response is quite sensitive to the vertical structure of the convective heating (Nicholls et al., 1991; Pandya and Durran, 1996), as well as to other assumptions built into the parameterization such as the adjustment time scale and trigger mechanisms. The MCS genesis process itself involves the combined effects of many convective cells and their attendant circulations. Any attempt to simulate it should include enough resolution to capture feedbacks between each cell and its environment as realistically as possible.

The simulation was quite demanding in several ways. Not only did the convection have to be explicitly resolved, but the evolution of the surrounding synoptic weather pattern also had to be simulated over a large area. To facilitate this with minimal computer usage, a series of telescopically nested grids was specified as shown in Figure 6.1. Grid #1, the coarsest and largest grid, was specified with a horizontal ($\Delta x = \Delta y$) spacing of 80 km, and covered most of the western and central United States (Fig. 6.1a). Grid #s 2, 3, and 4 were successively nested within their larger host grid (Fig. 6.1), with horizontal spacings of 20, 5, and 1.67 km respectively. The σ_z terrain–following vertical coordinate system was used, and all grids shared the same vertical spacing. This spacing was stretched with a stretch ratio of 1.12 from a Δz of 100 m near the ground to a maximum of 800 m near 7.5 km. Between 7.5 km and model top (19.5 km), the grid spacing was kept constant at 800 m. The timestep was set to 90, 45, 15, 5 seconds on grid #s 1–4 respectively. When fully activated, this simulation occupied 144 megabytes of internal computer memory. One hour of simulation took more than 24 hours of wall clock time to run on an IBM RISC 6000 370 workstation.

Two–way interactive nesting (Clark and Farley, 1984; Clark and Hall, 1991) was used for the nested grids. Boundary values for each of the finer grids were interpolated from its parent coarse grid. The fine grid solutions were in turn communicated to the coarse grid by averaging the fine grid values. Klemp and Wilhelmson (1978a,b) radiative conditions were applied to all of the lateral grid boundaries. Since this was a simulation of an inhomogeneous time varying system, the lateral boundary conditions for grid # 1 and the top boundary conditions for all grids also had to be specified in a time–dependent way. To do this, values at these boundaries were adjusted to the observations using Davies (1983) nudging. The relaxation was conducted on the five outermost grid points in the x and y directions and the six uppermost grid points in the z direction.

Grid #s 1 and 2 were stationary, while grid #s 3 and 4 could move to follow the MCS. Grid motion was accomplished by the successive time–dependent addition of a column

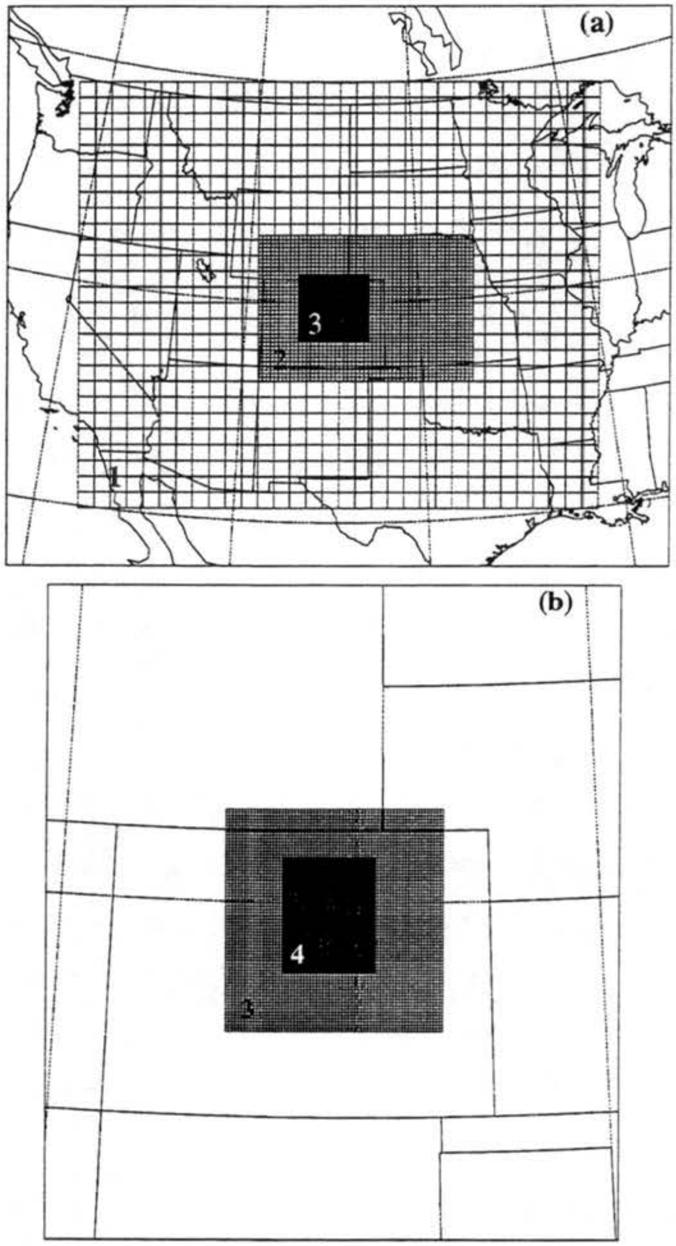

Figure 6.1: Grid configuration for the variably initialized primitive equation simulation. Grid nos. 1, 2, and 3 are shown in (a) and grid nos. 3 and 4 are shown in (b).

and/or row of grid points along the leading edges of the grid, concurrent with the removal of old grid points from the trailing edges of the grid.

6.2 Model numerics and parameterizations

This simulation required the use of several parameterizations, the most important of which are discussed in this section. Some of these were literally separate numerical models unto themselves. The numerical algorithms used by the model are also briefly discussed.

The microphysics was parameterized with the bulk one–moment scheme of Walko et al. (1995). The mixing ratios of vapor, cloud water, rain, snow, pristine ice, aggregates, graupel and hail were all predicted based on a gamma size distribution.

Long and shortwave radiative processes were parameterized using the Mahrer and Pielke (1977) scheme. Atmospheric scattering of shortwave radiation by oxygen, carbon dioxide and water vapor was parameterized, as were the longwave absorption and emission by these gasses. However, the effects of condensed liquid and ice were neglected for all wavelengths. The radiation calculations were updated every 15 minutes, and the longitudinal variation of shortwave radiation was also included.

The soil and vegetative cover were parameterized using the techniques described in Tremback and Kessler (1985) and Avissar and Mahrer (1988). The ensuing surface fluxes were calculated using the scheme of Louis et al. (1981). Diffusion was based on the Smagorinsky (1963) deformation K scheme with dependencies on the Brunt–Väisällä Frequency (Hill, 1974) and the Richardson number (Lilly, 1962). The scheme was anisotropic to account for horizontal grid spacings that were large compared to the vertical spacings.

On all grids, the physical equations were all discretized on the Arakawa–C (Messinger and Arakawa, 1976) setup. Advection was calculated using a hybrid scheme such that the velocity components and pressure were updated using leapfrog time differencing and all other variables were updated using forward differencing. The acoustic terms were calculated with Klemp and Wilhelmson (1978a) time split scheme.

6.3 Model initialization and integration

The model was integrated for 15 hours starting at 1200 UTC 19 July 1993. The initial fields consisted of data from the FSL Mesoscale Analysis and Prediction System (MAPS)

(Benjamin et al., 1991), a precursor to the current Rapid Update Cycle (RUC) model. These data included aircraft reports as well as mesonet and profiler data that were not ordinarily available. In addition to the MAPS data, the National Weather Service standard surface and upper air observations were used to augment the resolution of the MAPS grid near the surface and above the highest MAPS grid level. All data were combined and interpolated to the model σ_z surfaces with the RAMS isentropic analysis package (Tremback, 1990). The resultant fields were in hydrostatic balance to prevent the generation of spurious gravity waves. Additional analysis files were created from the 0000 and 1200 20 July data to facilitate the Davies nudging. The boundary forcing through the simulation thus consisted of a linear interpolation of data between the closest two times.

Grids #s 1–3 were started at the time of model initiation, while grid #4 was spawned six hours into the run at 1800. All grids remained fixed at their initial positions in Figure 6.1 until 2030, when convection began propagating off the mountains. To conserve computer time and disk space, the microphysical parameterization was not activated until 1800. Without the microphysics, clouds were still permitted to form, however precipitation processes could not occur. The first convective storms did not develop on grid #4 until 1900, thus the lack of microphysics was not a problem.

Topography (Fig. 6.2) was interpolated onto grid #s 1 and 2 from the United States Geological Survey (USGS) topographical data set, which was accurate to 30 seconds ($\sim$ 900 m). To help preserve the elevations of the tallest mountain peaks, the average topography height was calculated from a combination of silhouette and conventional averaging with weightings of 0.75 and 0.25 respectively. Since grid #s 3 and 4 were allowed to move, the topography was interpolated onto these grids from grid #2. Although this effectively limited the topographical grid spacing to 20 km on these grids, the basic features of the Rocky Mountains, the Palmer Divide and the Cheyenne Ridge were still well resolved.

Soil moisture was initialized from rainfall observations over the previous three months using the antecedent precipitation index (API) method of Wetzel and Chang (1988). Due to the lack of reliable precipitation data in the mountains, soil moisture values above 2400 m were increased from the default of 0.06 m^3 m^{-3} to 0.18 m^3 m^{-3}. Without this assumption, the low soil moisture resulted in uncharacteristically strong upslope flow. All soil moisture

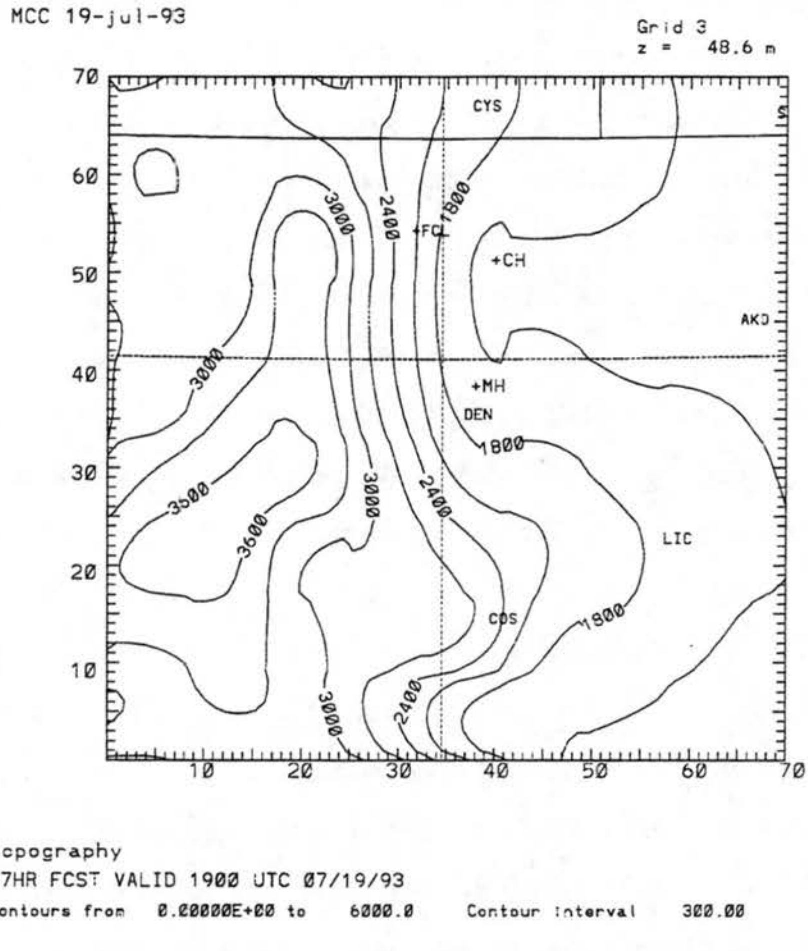

Figure 6.2: Model topography on grid # 3. Contours are in m at every 300 m. The i and j indices of the grid points are labeled along the x and y axes respectively.

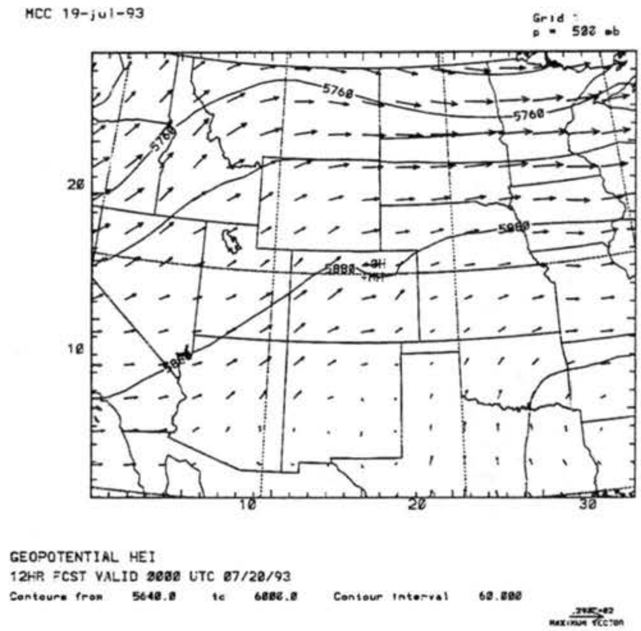

Figure 6.3: Constant pressure analysis of the 12 hour forecast on grid #1 valid at 0000 20 July. Geopotential height in meters is contoured at 60 m intervals, and vector winds in meters per second are plotted at every other grid point. The 29 m s^{-1} vector is scaled at the lower right portion of the figure.

values were subsequently smoothed using a 9–point linear filter. The variable vegetation data was initialized from a 1° (111 km) data set based on Loveland et al. (1991).

The big advantage of the high resolution and heterogeneous initialization was that no warm bubbles or cumulus parameterization were required to initiate or represent convection. Storms formed on simulated convergence zones and hot spots that were consistent with the observations. As discussed above, the explicit convection allowed the MCS genesis process to be more fully resolved because the heat and momentum transports were not relegated to an artificial parameterization. A disadvantage of this set up, however, was that convection outside of grid #4 was not well resolved. Any interactions between the 19 July MCS and other surrounding systems such as those in Wyoming and southern Colorado were not simulated.

6.4 Comparison with observations

6.4.1 Synoptic overview

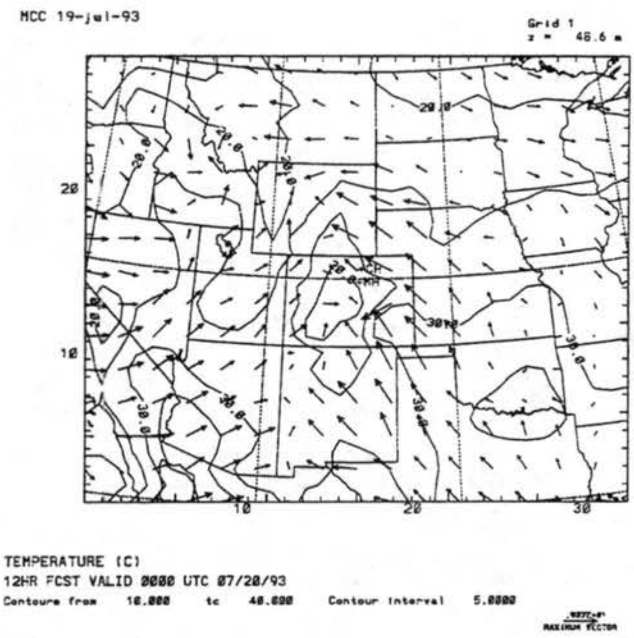

Figure 6.4: Simulated temperature and vector winds on grid #1 at the lowest σ_z level (49 m AGL) at 0000 20 July. Temperatures are in Celsius and are contoured at 5° intervals. Winds are in meters per second and a 9 m s^{-1} vector is scaled at the lower right.

Comparison with the observations will be an ongoing process through the next two chapters, however the overview here provides a general evaluation of the model performance. The 12 hour forecast valid at 0000 20 July on grid #1 at 500 hPa is shown in Figure 6.3, and can be compared to the observations in Figure 4.2. The mid to upper tropospheric evolution between 1200 and 0000 was well simulated by the model. Most heights and wind speeds were within 2 dam and 5 m s^{-1} of the observations, respectively. The biggest differences occurred near the US–Canadian border, where model heights were up to 6 dam lower than the NWS observations. This is a little surprising given the Davies nudging, however the MAPS heights (not shown) were lower in this region than those derived from the NWS soundings (Fig. 4.2). Since sounding data in Canada were relatively sparse, both the observed and modeled data may have contained errors. Fortunately, this region was about 1000 km from the MCS, and any detrimental effects were assumed to be minimal. The ripple in the 5880 m contour in the model data over Colorado was in response to the growing convection at that time. A similar feature was not apparent in the sounding data; however, the MCS was between sounding stations, and thus it was not well resolved. Although the fields are not shown, similar agreement between the model and the observations was found at the 850, 700 and 200 hPa levels.

The surface evolution (Figs. 6.4, 4.4b), was generally well simulated, although the strength of the upslope flow in eastern Colorado at 0000 was slightly overpredicted despite the increased moisture in the mountains. Simulated wind speeds there were 6 to 10 m s^{-1} whereas most observations were closer to 5 m s^{-1}. Wind direction, however was well simulated. Model temperatures at this scale were within 5°C of the observations in most areas. The exceptions were in the mountainous terrain in north central Colorado, where the simulated temperatures were consistently too low. Most of the reporting stations were located in valleys, which in the smoothed model topography were up to 300 m above their true elevation. This bias accounted for the majority of errors in these regions.

An important feature that the model managed to capture was the weak north–south temperature gradient from the plains of eastern Colorado into Kansas and Nebraska. The strongest warm advection at the surface was located along the southern portions of this gradient, which corresponded to the track of the MCS. Maddox (1983) showed that large nocturnal convective systems often require warm advection for sustenance. Although convection was ongoing in the model at 0000, the cold pool and outflow were poorly resolved on the 80 km grid. Temperatures showed no trace of it, and the winds were only slightly divergent near MH in Figure 6.4. However, this was not the case on the finer grids.

6.4.2 Anvil condensate overview

The ability of the model to reproduce the 19 July system becomes apparent in the condensate fields at 10744 m (Fig. 6.5) which can be compared to the satellite observations (Fig. 4.7). Deep convection started developing in the model at 1900, which was about an hour later than it was first observed on radar. However, the modeled upper tropospheric cloud shield rapidly grew to the size and shape of the satellite cloud shield by 2100 (Figs. 6.5a, 4.7a). The position of the modeled storm over north central Colorado was also quite accurate. Notice, however that the convection over the Raton Mesa was not captured at all by the model at this time due to the limited size of the cloud resolving grid #4.

By 2330, (Fig. 6.5b) the main system had moved into northeastern Colorado and was centered near 40 N, 103.5 W. Two other weak cells located near 39.25 N, 104.5 W and 38.25 N, 104.5 W had also developed to the southwest of the main system. The strongest convection in the main MCS, as indicated by the higher water contents, was elongated in the north–south direction. The coldest satellite cloud tops in Figure 4.7b exhibited a similar orientation. Most of the anvil was advecting rapidly downwind, while the deep convection remained close to the western edge of the cloud shield. Doppler radar observations in Chapter 5 portrayed a similar leading anvil structure.

The northernmost of the two simulated trailing cells was initiated as the ambient southeasterlies interacted with the trailing outflow boundary from the main system. Weak convection was observed on radar at this time in a similar position to the southwest of the main convective line (Fig. 4.8e). The corresponding cloud tops were quite low and warm, and are barely visible on satellite in Figure 4.7b.

The southernmost trailing cell was well south of the outflow boundary, and entirely contained on grid #3. Surface forcing along the elevated terrain in that region was strong enough to initiate convection despite the coarse 5 km grid spacing. Similar experiments with this model have shown that convection is surprisingly well predicted at this resolution if the forcing is strong enough (Grasso, personal communication). In this case, the model may have been responding to the same forcing that initiated the convective storms that were observed in southern Colorado. The simulated storms developed two hours later than those anvils first appeared on satellite, but the coarse resolution likely delayed their initiation.

By 0100 (Fig. 6.5c), the convection on grid #3 had dissipated, but the remnant anvil was still apparent as an appendage extending southwestward from the main convection. The predicted eastward progression of the main system was still reasonable with respect to the satellite (Fig. 4.7c), however the modeled system was beginning to deviate south of the observed track. The simulated cloud shield was also not quite as broad in the east–west sense as the satellite, although the different map projections make the distinction difficult. At this time, convection was growing rapidly, and the anvil was undergoing a transition towards a more consolidated entity.

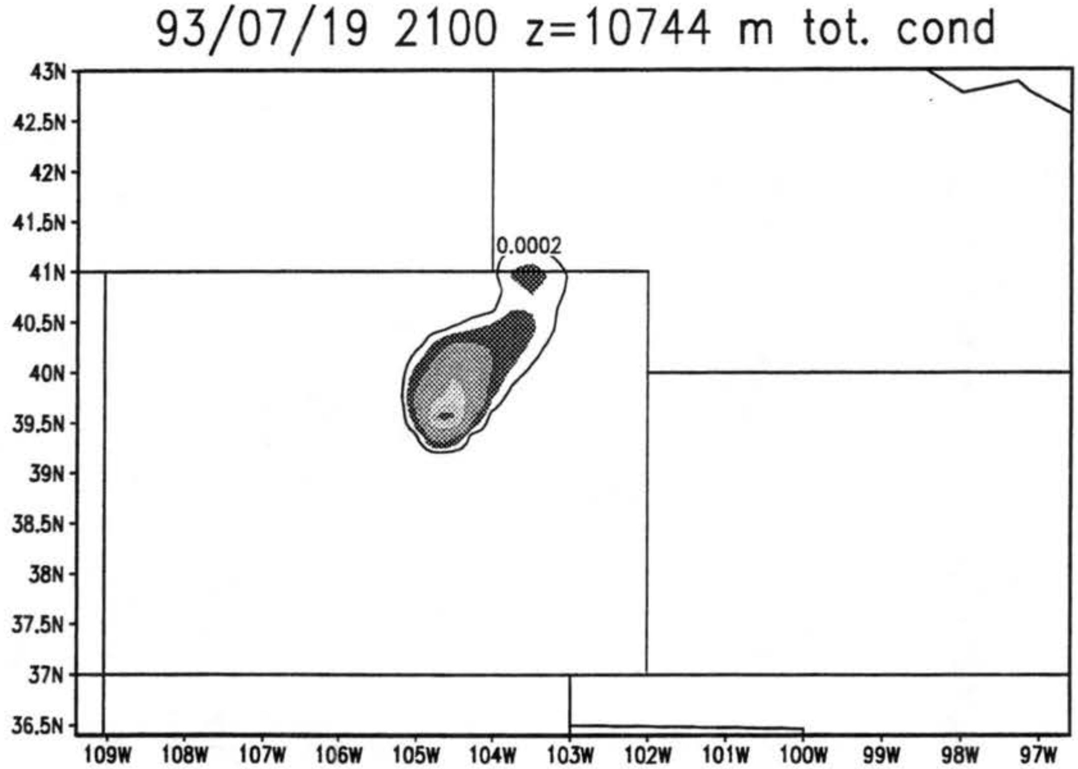

(a)

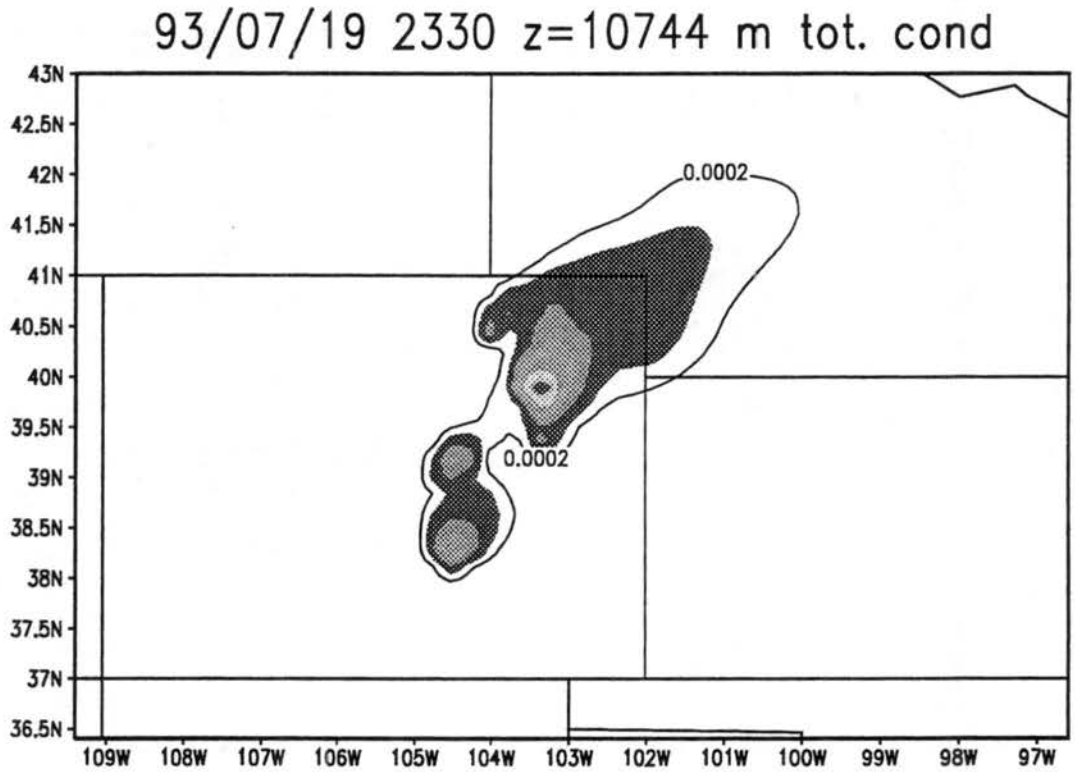

(b)

Figure 6.5: Total model condensate (all ice and water constituents combined) on grid #2 at σ_z = 10744 m, which at this level is approximately a flat surface. The times plotted are (a) 2100, (b) 2330, (c) 0100, and (d) 0300. Condensate greater than 0.0002 kg kg^{-1} contoured, and all condensate above 0.0005 kg kg^{-1} is shaded with an interval of 0.0005 kg kg^{-1} according to the scale in (d).

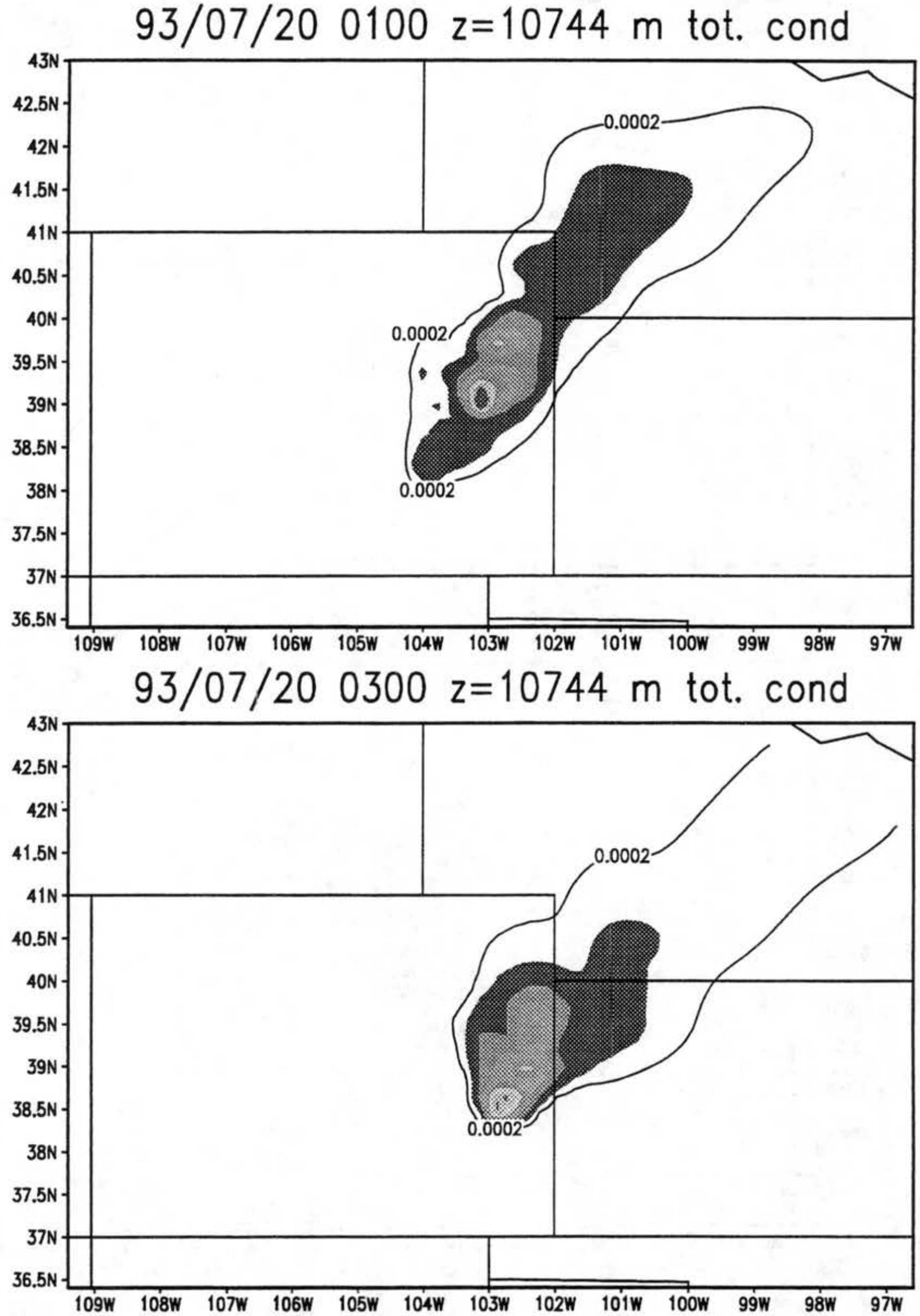

(c)

(d)

Figure 6.5: Continued

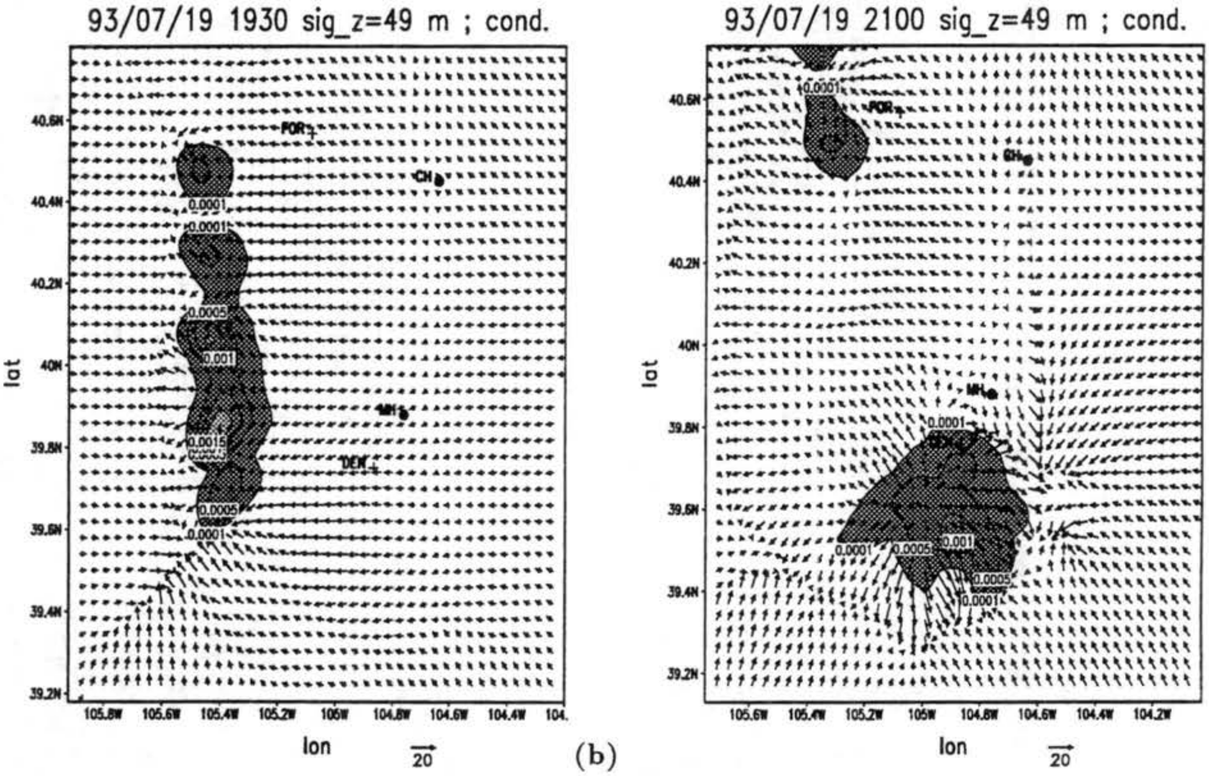

(a) (b)

Figure 6.6: Total model condensate (all ice and water constituents combined) and ground relative vector winds at $\sigma_z = 49$ m on grid #4. The times plotted are (a) 1930, (b) 2100, (c) 2200, (d) 2330, (e) 0030, and (f) 0030. The positions of the Chill (CH) and Mile High (MH) radars are plotted as well a few NWS reporting stations. Note that the grid moves with time. Areas of condensate greater than 0.0001 kg kg^{-1} are shaded and contoured, and all condensate above 0.0005 kg kg^{-1} is shaded and contoured with an interval of 0.0005 kg kg^{-1}. The wind vectors are plotted in meters per second (scaled at the bottom of each plot) at every 0.04° lat. and lon., which is approximately $2\Delta x$. The dashed lines in (c) represent mass convergence zones.

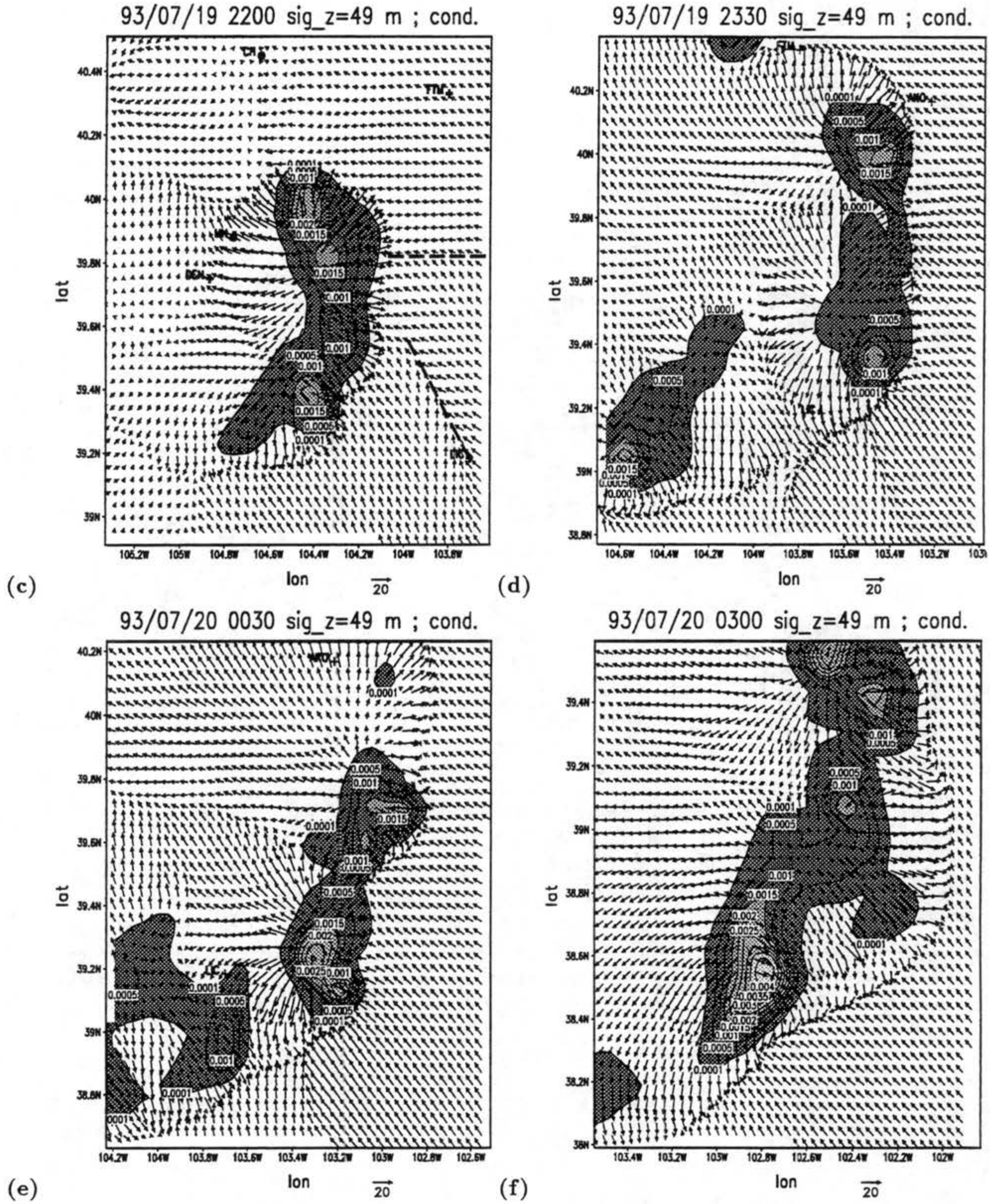

Figure 6.6: Continued

After 0200 the simulated contiguous anvil displayed many of the characteristics of a consolidated MCS (Fig. 6.5d). Although several storms were active at the time, the individual cells could no longer be discerned as distinct protuberances in the outer cloud perimeter. The anvil was more rounded and symmetric in shape as opposed to its elongated appearance at earlier times. Most importantly, deep convection was centrally located within the cloud shield, and a significant portion of the northern convective line now exhibited trailing stratiform anvil. The strongest storms were occurring in the southwest quadrant of the MCS, a trait often observed in convective systems (Houze et al., 1990). At this point, the modeled system had achieved genesis according to the proposed definition in Chapter 5, and the model integration was terminated.

6.4.3 Near–surface condensate overview

A comparison between low level radar reflectivity (Fig. 4.8) and the model condensate[1] fields on grid #4 at the lowest model sigma level (Fig. 6.6) indicates that several aspects of the storm–scale evolution were well simulated. At about 1900, convection had developed in the simulation along a north–south line parallel to the highest terrain (Figs. 6.6a, 4.8a). Although the areal coverage of precipitation was greater in the model, the position and orientation were correct. Like the radar, the strongest cells were at the southern end of the line.

By 2100 (Figs. 6.6b, 4.8b) the simulated southern convective cells had consolidated into a single cluster which corresponded well to the two main cells on radar. Simulated updrafts at mid levels actually displayed two consolidated cores located just north of the two condensate lobes at the extreme southern edge of the precipitation at 105 w and 104.8 w. Most of the convection to the north of the main cluster had dissipated in the model, and the remaining cells were rapidly weakening. One cell moved across the northern boundary of grid #4 before dissipating, however it did not last long on grid #3.

As convection moved off the mountains, the DCVZ was developing in the model. The eastern edge of the DCVZ is apparent in Figure 6.6b as a line of highly convergent flow

---

[1] Condensate at this level was mostly rain, however some hail was also mixed in.

extending south from CH toward the eastern edge of the existing convection. The strongest convergence was south of MH, where towering cumulus were already developing in the model. A similar pattern is revealed in the mesonet winds (Fig. 5.4c), as winds converged from all directions on the east side of the DCVZ. Due to the relatively coarse spacing of the mesonet stations, the fine–scale details of the observed convergence zone are unknown. The model depicts a very sharp boundary on the order of a few kilometers across.

Between 2100 and 2200 (Fig. 6.6c), convection rapidly developed along the convergence zone. Low level outflow increased in coverage and the system developed the familiar north–south linear orientation. The modeled convective line even took on the bowed appearance observed on radar (Fig.4.8d), although it did so about half an hour faster than was observed. Simulated outflow wind speeds reached 34 m s^{-1}, which was close to the 27 m s^{-1} measured wind gusts.

Two convergence zones indicated by the dashed lines in Figure 6.6c were apparent ahead of the convective line by 2200. Observations were limited since this area was east of the mesonet. However, the scattered weak convection on radar ahead of the line at 2330 (Fig. 4.8e) suggests the existence of similar convergence features. Just before 2300, convection developed in the model north of Limon (LIC) along the southernmost convergence zone. This simulated cell grew considerably stronger than its observed counterparts, and soon intercepted much of the southeasterly inflow from the southern half of the convective line. As a result, that portion of the original line partially dissipated in favor of the new cell. The line and the cell merged by 2330 (Fig. 6.6d), but from that point on the agreement between the model and the observations was not as good. The MCS continued to propagate as a line, but the discrete propagation temporarily weakened the outflow boundary, and a second bow echo did not evolve at 0100 as it did on radar. Instead, the northern and southern convective components retained their identity to some degree.

As mentioned in the previous section, additional storms developed along the trailing outflow boundary to the southwest of the main convective line. These cells, evident in Figure 6.6d, e, were generally weak as the boundary layer near these storms had become somewhat drier through the day and CAPE was correspondingly reduced. The main convective line, however, was propagating eastward into increasingly moist air. By 2330, the low level jet

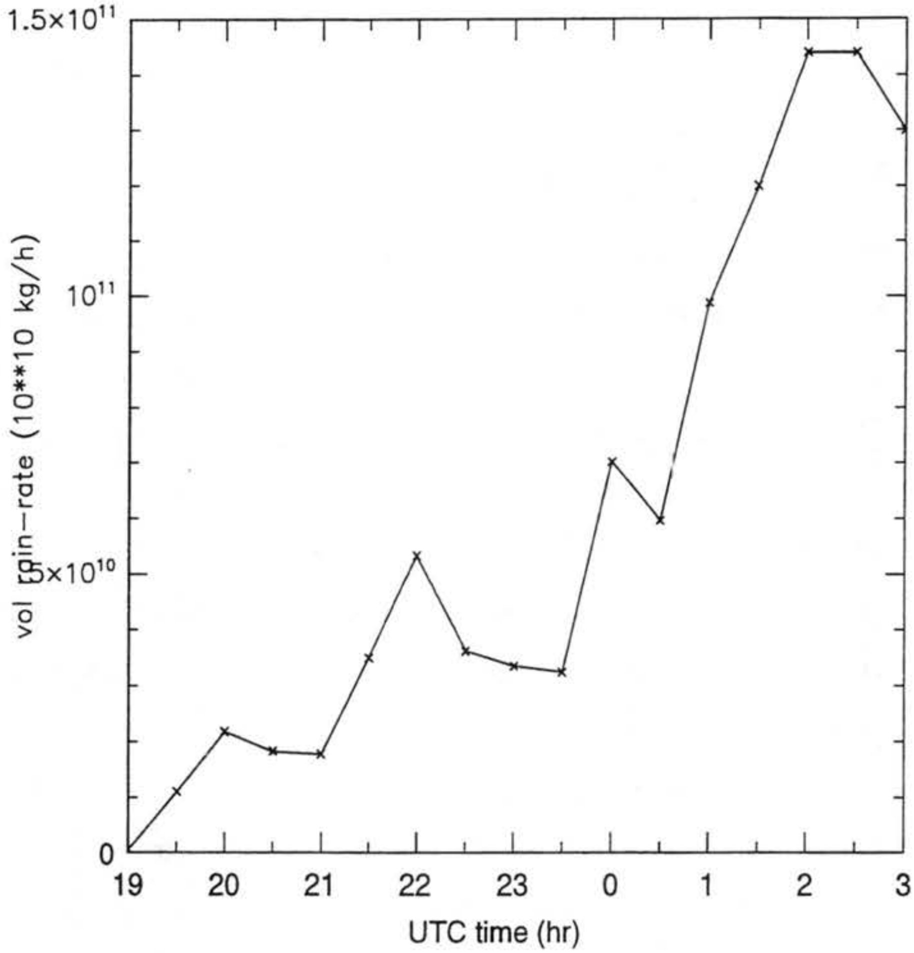

Figure 6.7: Time series of the simulated total (convective and stratiform) MCS volumetric rain rate. Rain rates on the y axis are in increments of 10^{10} kg h^{-1}, while time in hours UTC is on the x axis.

was also increasing in strength and convection began intensifying rapidly. Maximum total water mixing ratios increased from 2.5 g kg^{-1} at 2330 to over 4.0 g kg^{-1} by 0300 (Fig. 6.6f), for a corresponding increase in rainfall rate from 61 mm hr^{-1} to 104 mm hr^{-1}. The convective line also increased in length and was beginning to exceed the limits of grid #4. Several active cells were present along the line, with the strongest ones in the south. The outflow boundary was large and consolidated by 0300 (Fig. 6.6f) as it surged ahead of the central portions of the convective line. Although no high resolution radar data were available beyond 0145, manually digitized radar (MDR) plots at 0300 (not shown) indicated that the strongest convection shifted to the southwestern portions of the line. The exact chain of events was hard to diagnose due to the coarse resolution.

The evolution of the simulated convection is summarized in a more quantitative way in the MCS–total volumetric rainfall rate time series (Fig. 6.7). Like the radar results, the MCS–total volumetric rain rates were calculated from the lowest σ level total condensate fields on grid #4. Precipitation from all portions of the MCS except the isolated cells along the trailing outflow boundary was included. Although the small scale details and timing of the maxima and minima in each time series are different, both the modeled (Fig. 6.7) and the observed (Fig. 5.28) time series displayed a similar overall pattern. The peak in the simulated rain rate at 2200 occurred as the convection attained the bow echo structure. A similar peak occurred in the observed rain rates at 2230 as the bow echo formed on radar. The rain rates in both time series then decreased after the bow echo stage, however the observed rates recovered more quickly from the decline. The simulated rain rates between 2230 and 2330 slowly decreased as the simulated storm developed out of place ahead of the line, weakening it. However, by 2330 both time series showed rapid increases in intensity. The observed rain rates began declining again after 0030, and while the model depicted a similar decline between 0000 and 0030 it was followed by renewed growth after 0030. After 0000, the results from the precipitation analysis were degraded by the extreme distance of the storm from the radars. However, MDR, satellite, and surface rainfall reports all suggest continued growth in the observed volumetric precipitation rate as the MCS moved into Kansas, implying that the simulated growth through 0200 likely occurred. Finally, the model–derived values were consistently about 30% higher than those derived from radar. These differences may have resulted from a combination of errors from both the reflectivity–derived rain rates, and the physical assumptions from the model. The good qualitative agreement between both solutions indicates that despite any such systematic errors, the development of simulated rainfall matched the observed growth very well.

6.5 Summary

Given all of the assumptions that went into the model, the degree of agreement with the observations is remarkable. The shape, position, and intensity of the convective system were well reproduced. Mesonet observations discussed in Chapter 5, and additional model results in the next chapter show that strong topographic forcing shaped the storm through much of its early development. As the system propagated onto the plains, the topography played less of a role compared to the outflow forcing. At that point, small differences in storm placement and strength, such as the incorrectly simulated cell ahead of the line, caused more significant differences from the observations.

When comparing the model results to the observations, it is good to keep in mind that these are essentially two different systems under very similar conditions. Although the position and timing of each individual convective cell was not identical between the model and observations, the general interactions between the storms and their environment were quite similar. Both cases exhibited cells oriented in a meridional line in strong upper tropospheric flow, and portrayed a strong resemblance in the solutions at anvil level. The proposed MCS genesis process is generic enough such that the key players, namely the low frequency gravity waves, played very similar roles in both cases.

Chapter 7

MODEL RESULTS

7.1 Introduction

In this chapter, as in Chapter 5, the problem of MCS genesis is addressed from two angles. First, the mesoscale environmental circulations that favored convective growth in such a specific place are explored. The mountain–plains and Palmer Divide–Platte Valley solenoids as well as the DCVZ have already been found to be important. However, the three–dimensional structure of these circulations and their interactions with the preexisting synoptic front could not be studied with the limited observations. Furthermore, the low level jet and its eventual interaction with convection over eastern Colorado was completely unsampled. To the extent that the model correctly simulated this event, it offers a very powerful tool with which to investigate the complex environmental circulations that governed the position and intensity of the convection.

The focus is then reversed in the second half of the chapter as the effects of the developing MCS upon its environment are investigated. Again the observations of the storm, although of high quality, were limited mainly because the Doppler radar could not detect motions outside the contiguous echo. The model was able to simulate features such as the subtle vertical motions along the leading edges of the gravity waves that the Doppler radar missed. The high resolution in the simulation combined with the explicitly resolved convection permit a thorough investigation of the momentum and thermodynamic fields both inside and outside the MCS. Most importantly, the fine–scale results offered the unprecedented opportunity to directly compare the model generated circulations within the MCS with the dual Doppler derived winds. The model did a good job simulating these circulations, in part because the MCS was so strongly forced. Such favorable agreement with the observations offers additional confidence that the environmental interactions outside the system were correctly simulated.

7.2 Mesoscale influences on convective focusing

7.2.1 Evolution of the preconvective mesoscale environment

The preexisting quasi–stationary surface front over eastern Colorado was a significant deviation from a horizontally homogeneous environment, and interactions between this front and the diurnal solenoidal circulations eventually dictated the structure and evolution of the MCS. The exact frontal position was difficult to determine from the initial fields on grid #2 at 1200, which were basically the observations interpolated to the model grid. The potential temperature (θ) gradient (Fig. 7.1b) was generally north of the Colorado/Nebraska border. However, the windshift line was located near the Palmer Divide, well south of the main θ gradient. East–northeasterlies covered most of northeastern Colorado while light and variable winds existed further south. The equivalent potential temperature (θ_e) and dewpoint fields (Fig. 7.1c, d) were more consistent with the wind field, in that a strong zonal gradient extended across northeastern Colorado into southern Nebraska. Overnight convection across eastern Colorado and western Kansas may have contributed to this disjointed structure, however thermal fields are also often difficult to track across variable topography (Fig. 7.1a) due to innate vertical gradients in potential temperature.

After six hours of simulation on grid #s 1–3, the front was still best defined by the convergent windshift boundary and the equivalent potential temperature gradient (Fig. 7.2b). The boundary remained quasi–stationary across eastern Colorado while θ_e on both sides increased with the diurnal temperatures. In the high foothills west of Denver (DEN), upslope flow was advecting moist air to higher elevations. Equivalent potential temperatures there were as high as those out on the plains, indicating the build–up of significant instability.

The potential temperature contours at 1800 were generally oriented from northwest to southeast over most of High Plains on grid # 2 (Fig. 7.2a). However, a deviation was apparent along the northern Palmer Divide between DEN and Limon (LIC), where the contours were more zonally oriented. It will be shown below that the Palmer Divide–Platte Valley diurnal solenoid was acting to locally tighten the gradient here. Elsewhere, potential

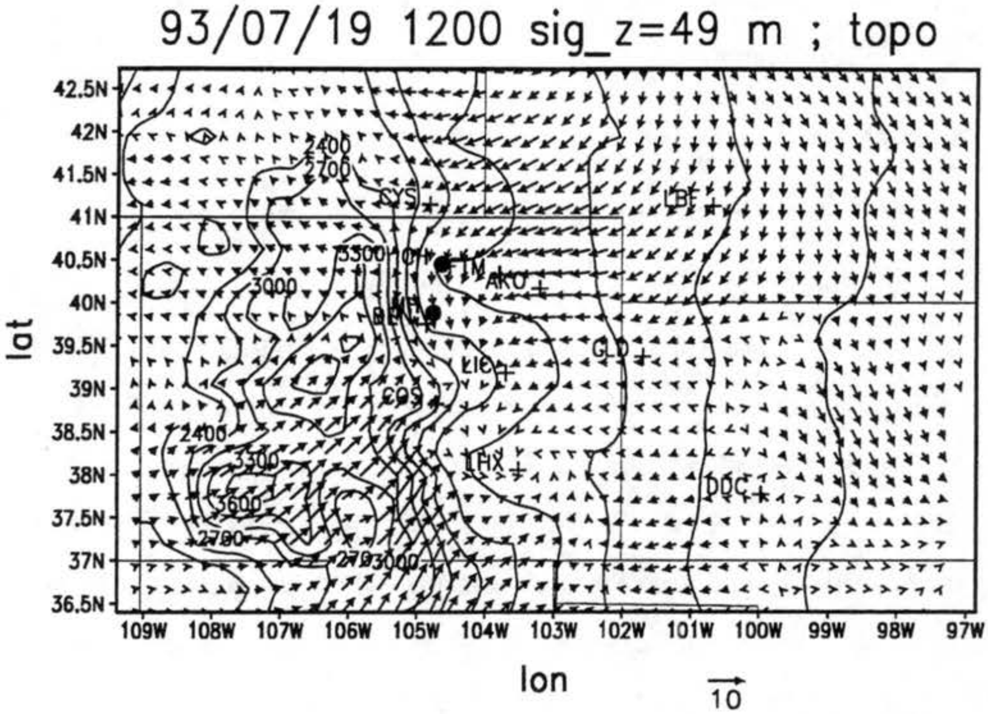

(a)

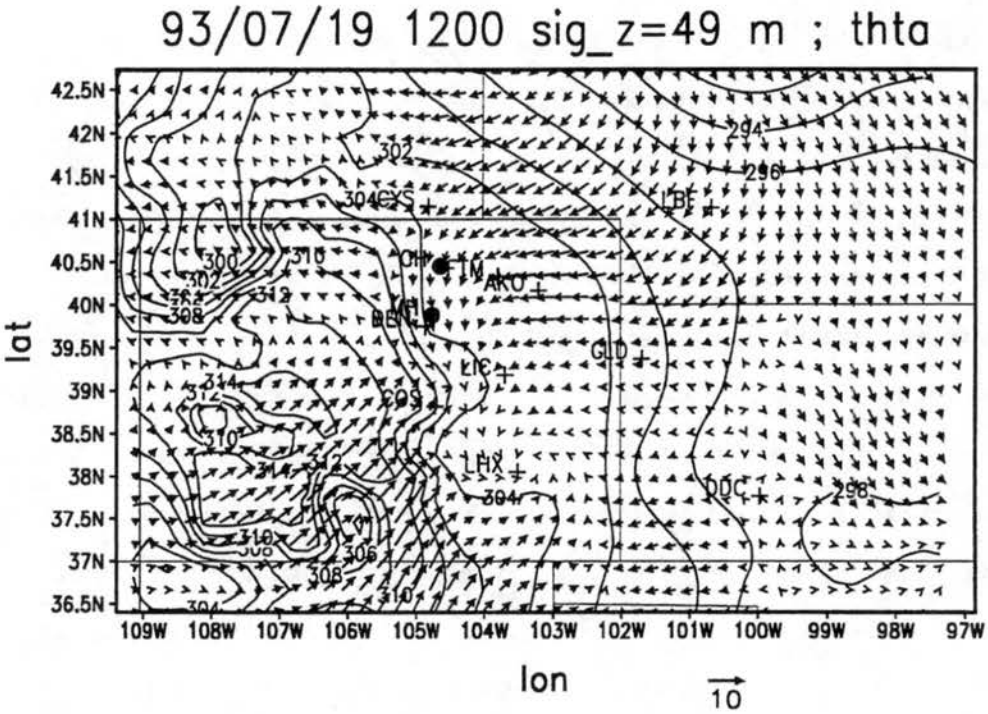

(b)

Figure 7.1: Initial (1200 19 July) fields on grid #2 at the lowest model σ level (49m AGL). Topography is contoured at 300 m intervals in (a); potential temperature is contoured at 2 K intervals in (b); equivalent potential temperature is contoured at 4 K intervals in (c); and dewpoint temperature is contoured at 4°C intervals in (d). Wind vectors are plotted and are scaled in m s^{-1} at the lower right of each panel.

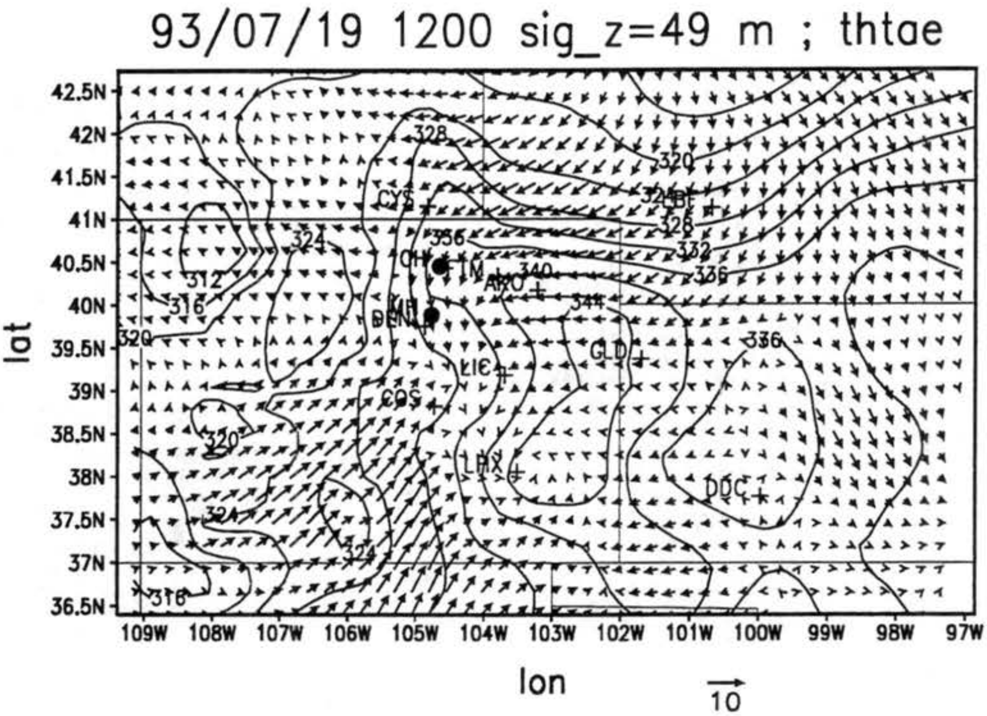

(c)

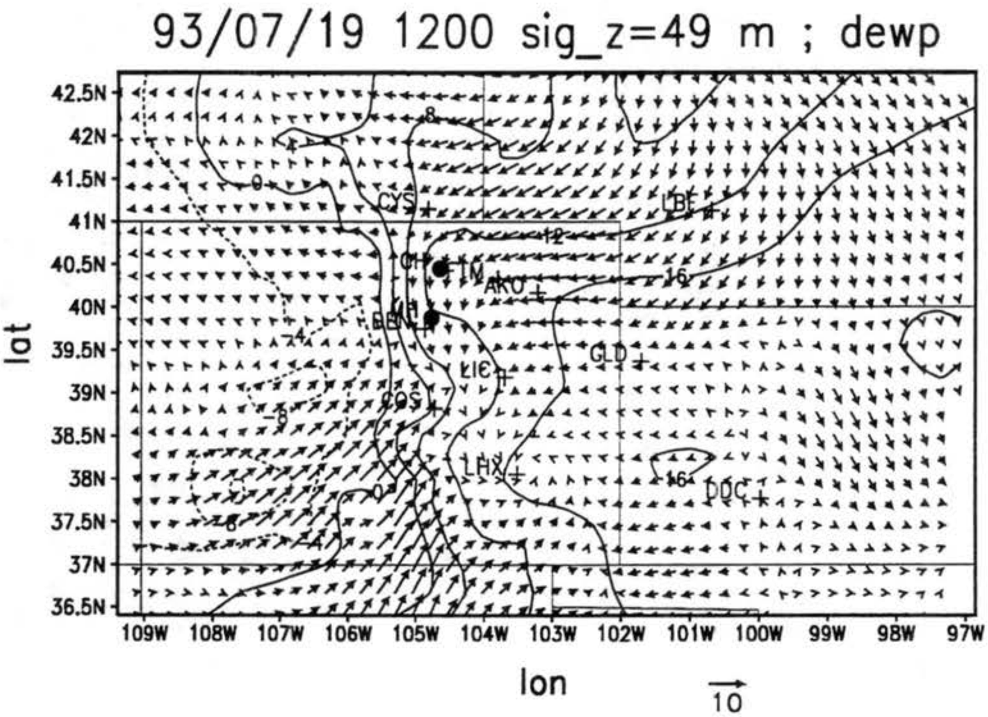

(d)

Figure 7.1: Continued

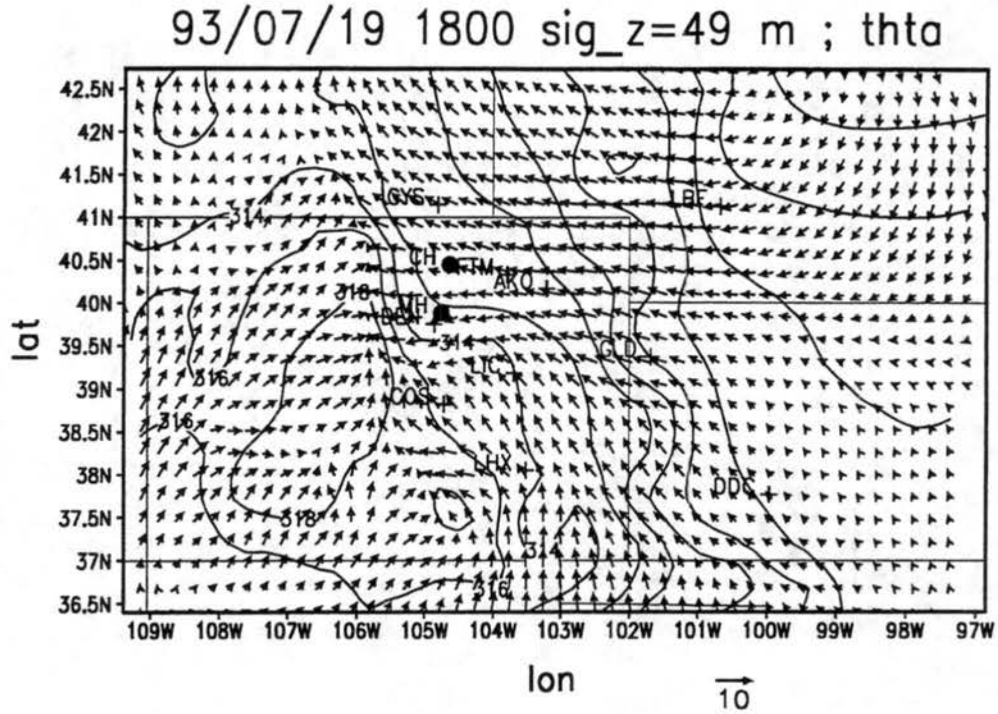

(a)

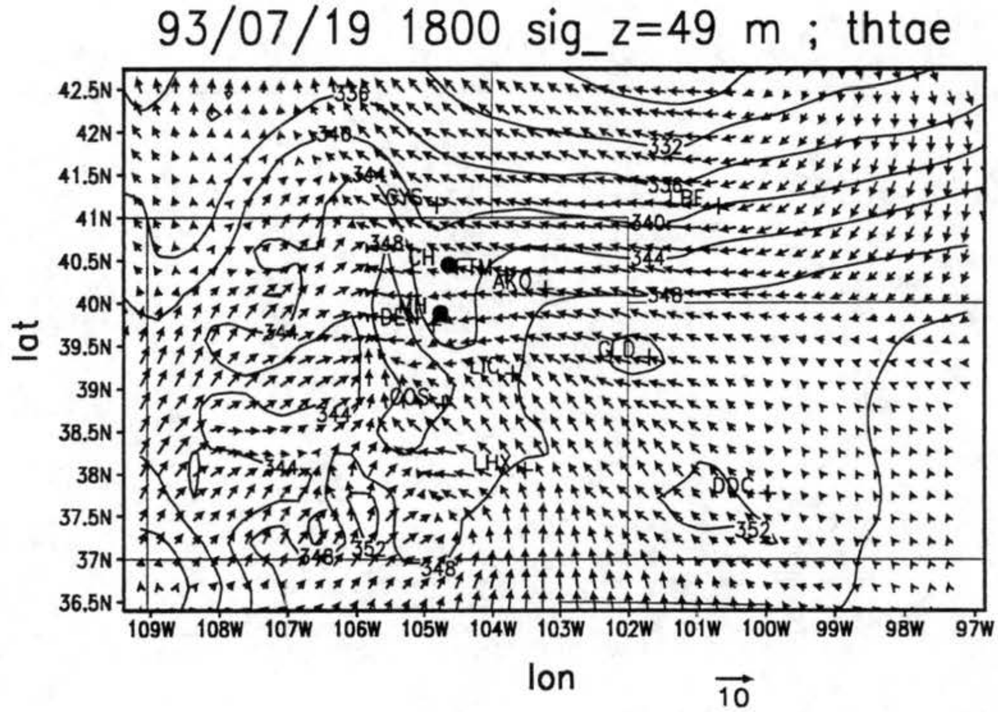

(b)

Figure 7.2: Model output on grid #2 at the lowest model σ level at 1800. Potential temperature is contoured at 2 K intervals in (a) and equivalent potential temperature is contoured at 4 K intervals in (b). Wind vectors are plotted as in Fig. 7.1

temperatures over the region north of the front were slightly cooler due to the cold air advection in the easterly flow. South of the front, southeasterly winds were more parallel to the θ gradient and advection was less efficient. Thus, although the raw potential temperatures did not indicate a strong boundary, the meridional wind differences across the front were enough to superimpose a subtle north–south gradient upon the general topographically induced pattern. This changed the strength of the capping inversion across the region, allowing areas south of the front to be more susceptible to mix–out. The subsequent variations in boundary layer depth came to be quite important to the evolution of the convective system and the low level jet.

7.2.2 Simulated flow on grid #3 and comparison to observations

Despite the variations in the large scale environment, the characteristic Front Range diurnal upslope pattern observed by Toth and Johnson (1985) was still apparent in the wind field on grid #3 at 1800[1] (Fig. 7.3a). Divergent winds covered most of the Platte Valley, while convergent flow existed along the downwind side of the Palmer Divide. Simulated upslope extended well into the foothills ending in a strong convergence zone just downwind from mountain top. This contrasts somewhat with Toth and Johnson (1985), who found that upslope did not extend to such high elevations. However, observed easterlies at the foothills mesonet stations (Fig. 5.2) indicate that upslope flow extended well into the foothills. Superimposed upon this general pattern, was a zone of much weaker flow along the Front Range between the locations of CHILL and Mile High. Winds here were almost calm while surrounding velocities were generally 5–10 m s^{-1}. This area was actually the surface reflection of the secondary plains up–branch of the two–celled mountain–plains circulation discussed by Dirks (1969) and Tripoli and Cotton (1989a). This branch appears in the vertical cross sections as a region of weak upward motion just east of the mountain–plains interface (near $x = 50$ in Fig. 7.4d).

As mentioned previously, the convergent circulation along the Palmer Divide was enhancing the preexisting environmental baroclinicity (Fig. 7.3b). Northeasterlies advected in

---

[1] Grid #4 was spawned just after 1800, thus the analyses on grid #3 at this time contain no effects from that grid.

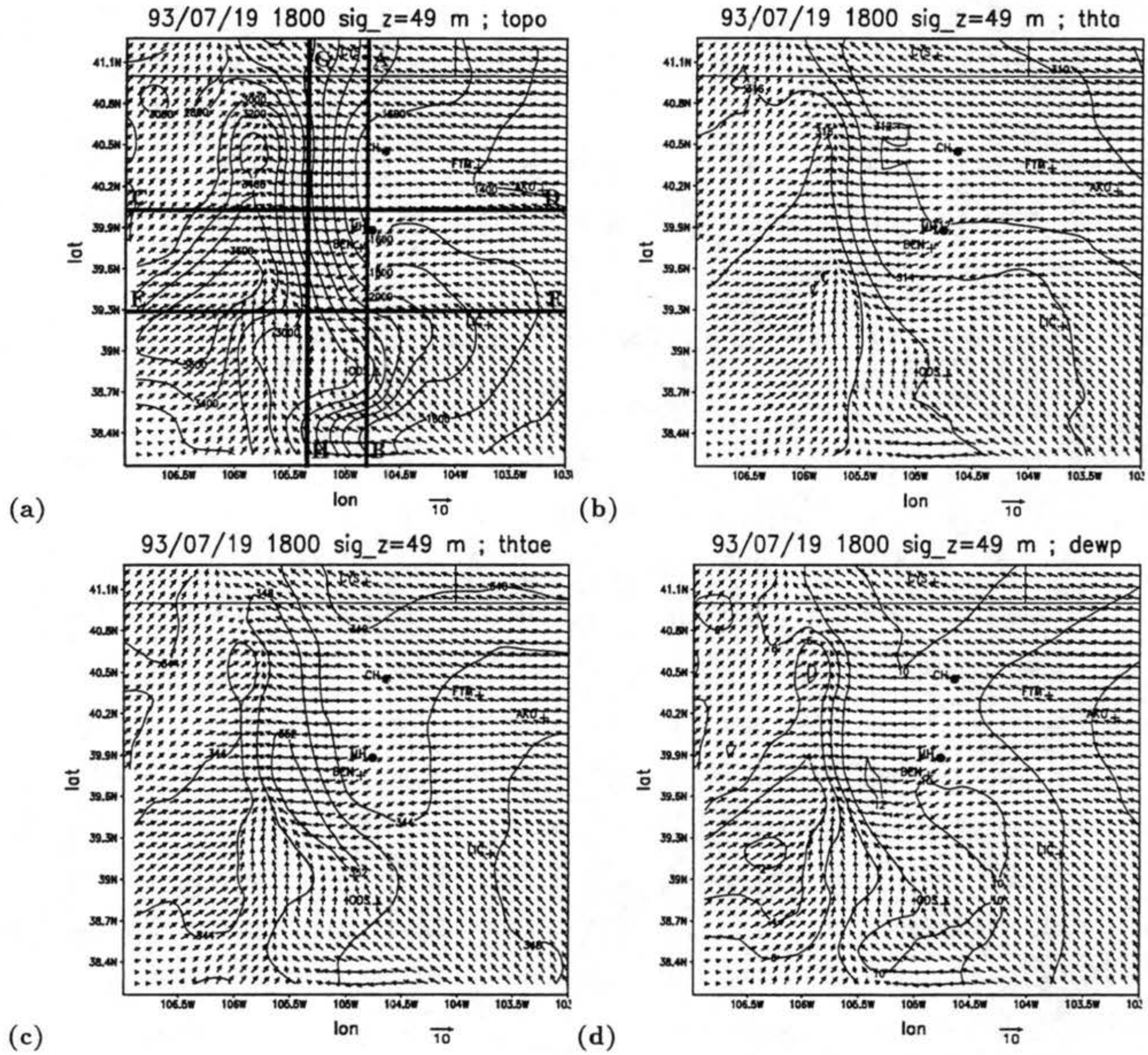

Figure 7.3: Model output on grid #3 at the lowest model σ level at 1800. Topography contoured at 200 m intervals is shown in (a); potential temperature is contoured at 2 K intervals in (b); equivalent potential temperature is contoured at 4 K intervals in (c); and dewpoint temperature is contoured at 2°C intervals in (d). Wind vectors are plotted and are scaled at the lower right of each panel. Heavy lines in (a) depict the positions of cross sections in Figs. 7.4–7.7.

cooler air on the northern side of the divide, while southeasterlies, which again were almost parallel to the potential temperature gradient, accomplished little advection. The shallow frontal structure was apparent in the meridional cross sections of potential temperature (Figs. 7.7a, 7.6a) as a region of cool air north of the divide not much more than a kilometer deep. Wilczak and Christian (1990) noted a similar vertical structure to the potential temperature field in their analysis of the Denver cyclone, although there was no preexisting frontal zone in their case.

These simulated features generally compared well with the mesonet observations discussed in Chapter 5. The Platte Valley divergence and Palmer Divide convergence during the late morning was observed (Fig. 5.2). However the model winds were generally smoother than the observations, and the weak Denver cyclone was not simulated. Instead, the model produced a more general region of cyclonic vorticity and convergence on the northern slope of the Palmer Divide. The observed cyclone on this day was quite weak, and the coarse model topography may not have been enough to resolve its formation. In the simulated moisture field, a tongue of slightly higher dewpoints (Fig. 7.3d) was feeding into the Platte Valley on the easterly flow. Although this feature was observed (Figs. 5.2 and 5.3), model dewpoints along the northern Front Range were $2 - 5°C$ too low. There, the soil parameterization may have been underestimating the anthropogenic moisture fluxes from sources such as crop irrigation. Other than that, the general pattern on the plains was correct. In the mountains, an arcing band of high moisture and θ_e (Fig. 7.3c) extended along the highest terrain, just east of the strongest mass convergence. This feature was not well observed due to the sparse station density on the southern and western edges of the mesonet. As discussed in Chapter 5, the dewpoints at all of the foothills mesonet stations steadily increased through the morning to values similar to those in the model. Thus the simulated moisture flux into the mountains appeared to be realistic.

7.2.3 Three–dimensional structure of the topographic solenoids

Zonal cross sections taken along the Platte Valley (Fig. 7.4) and the Palmer Divide (Fig. 7.5) reveal several important meridional variations in the structure of the topographic solenoids. The Platte Valley cross section closely resembled two–celled mountain–plains

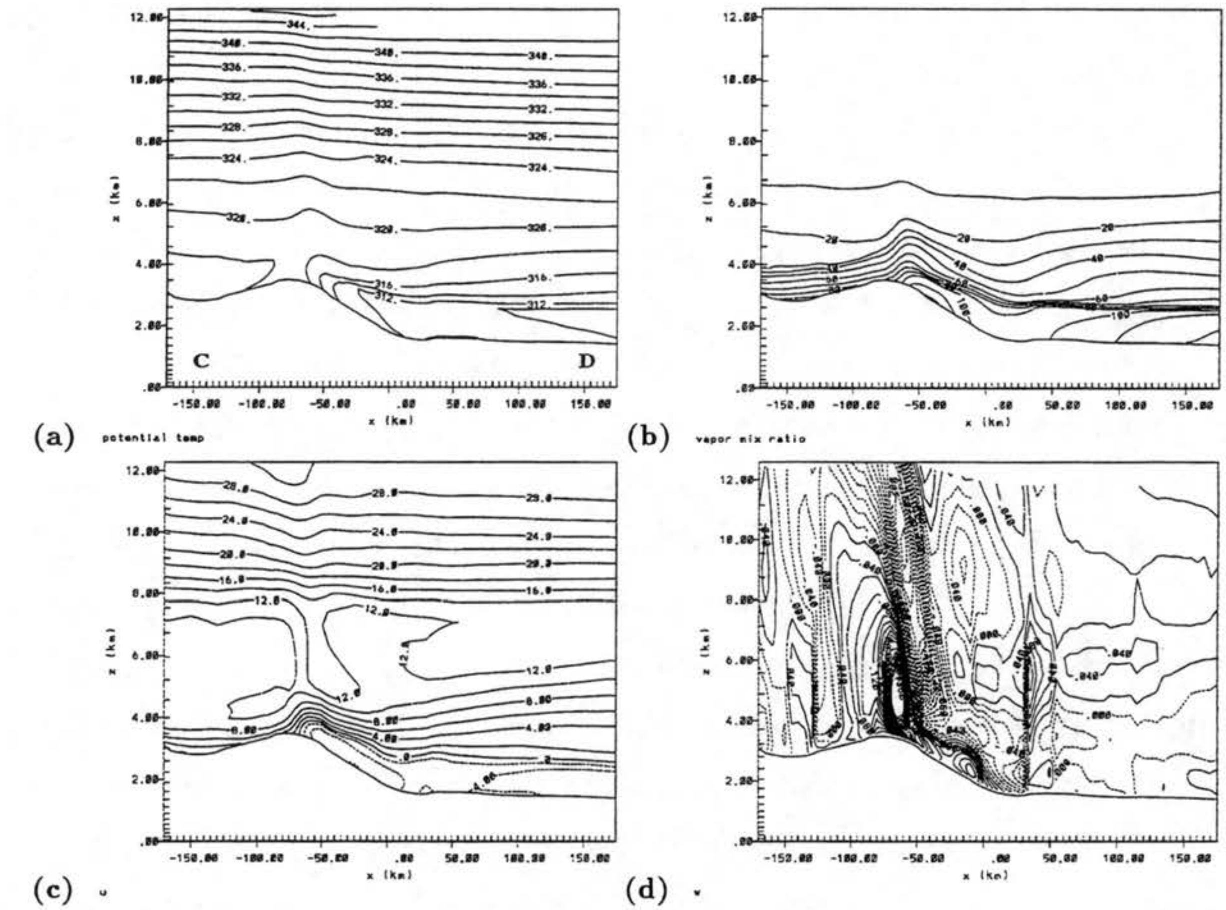

Figure 7.4: Vertical $x-z$ cross sections of model data at $y = 40°$ N. lat. at 1800 on grid #3, height on the z axis is in km MSL. The letters C and D at the bottom of (a) correspond to those in Fig. 7.3a. Potential temperature is contoured at 2 K intervals in (a); water vapor mixing ratio is contoured at 1 g kg^{-1} intervals in (b); the u wind component is contoured at 2 m s^{-1} intervals in (c); and the vertical velocity is contoured at 0.02 m s^{-1} intervals in (d). The abscissa is labeled in kilometers relative to $x = 105°$ W. lon.

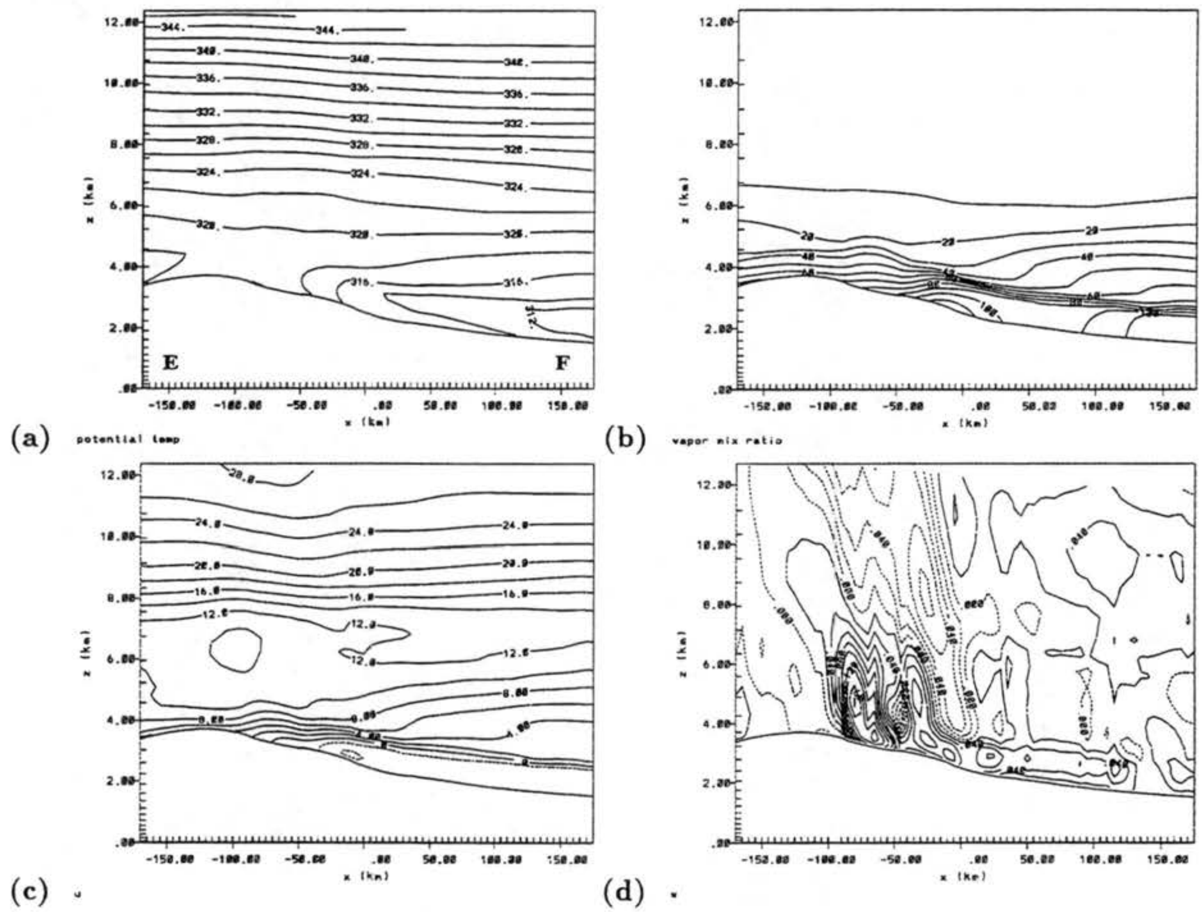

Figure 7.5: Same as Fig. 7.4 except $x - z$ cross sections at $y = 39.3°$ N lat. The letters E and F correspond to those in Fig. 7.3a

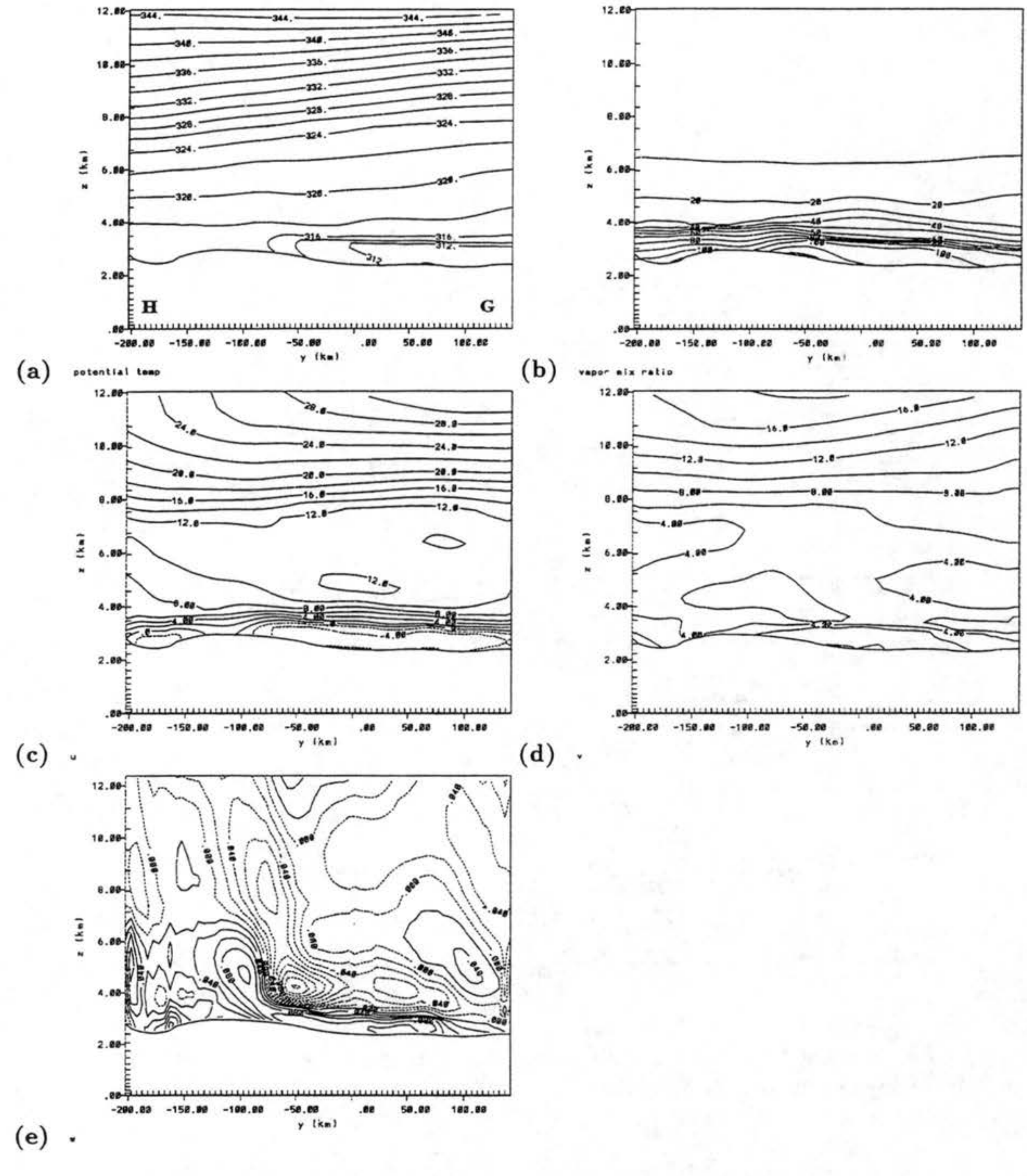

Figure 7.6: Vertical $y - z$ cross sections of model data at x = 104.8° W. lon. at 1800 on grid #3, height on the z axis is in km MSL. The letters G and H at the bottom of (a) correspond to those in Fig. 7.3a. Potential temperature is contoured at 2 K intervals in (a); water vapor mixing ratio is contoured at 1 g kg^{-1} intervals in (b); the u wind component is contoured at 2 m s^{-1} intervals in (c); the v wind component is contoured at 2 m s^{-1} intervals in (d); and the vertical velocity is contoured at 0.02 m s^{-1} intervals in (e). The abscissa is labeled in kilometers relative to x = 40° N. lat.

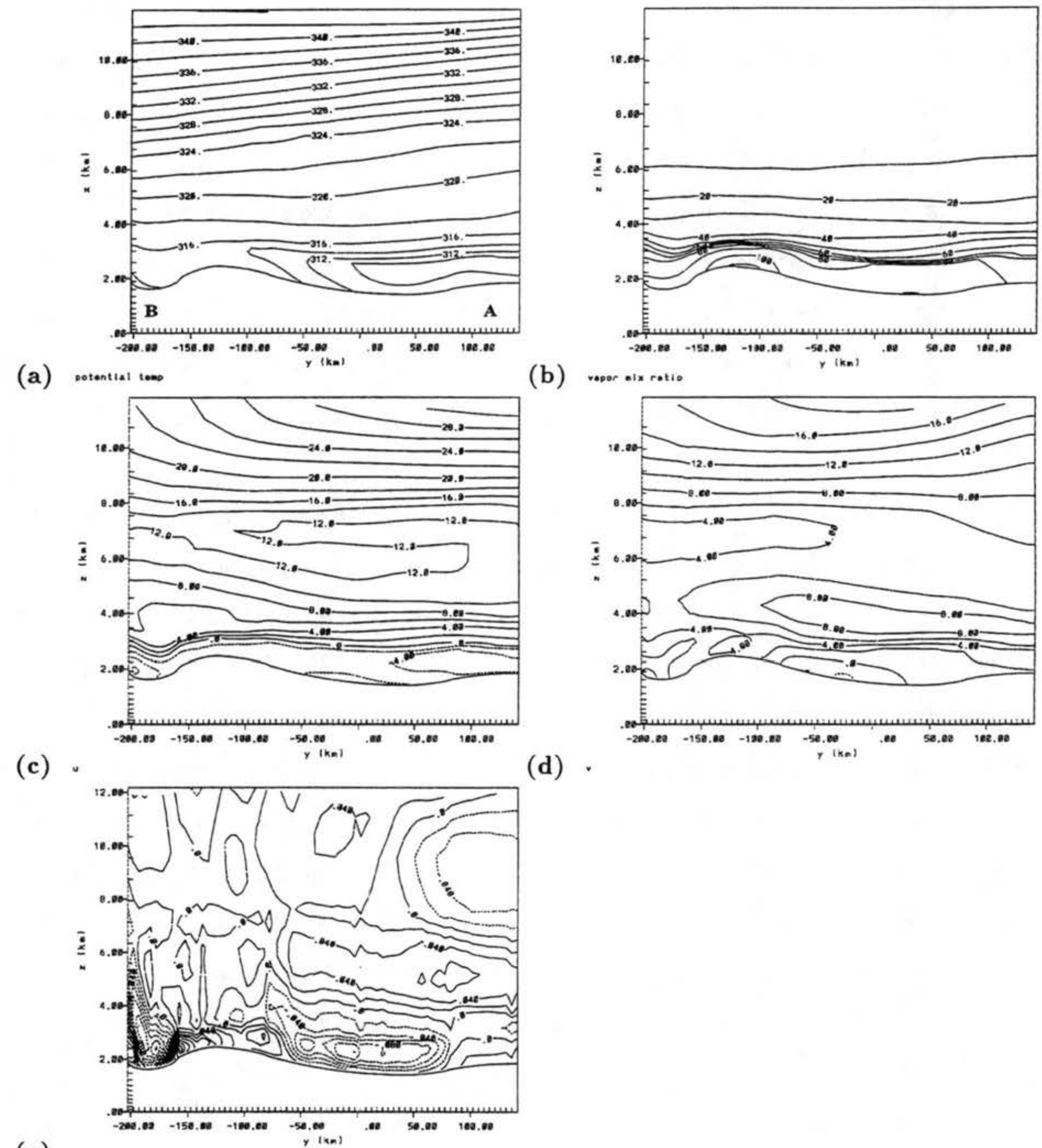

(a) potential temp (b) vapor mix ratio (c) u (d) v (e) w

Figure 7.7: Same as Fig. 7.6 except $y-z$ cross sections at $x = 105.4°$ W. lon. The letters A and B at the bottom of (a) correspond to those in Fig. 7.3a.

solenoid discussed by Dirks (1969) and Tripoli and Cotton (1989a). In the boundary layer, strong upslope advected cool and moist plains boundary layer well up into the foothills, almost to mountain top. Concentrated upward vertical motion occurred at the western edge of the upslope, creating the chimney effect discussed by Braham and Draginis (1960) (see Chapter 2). In turn, intense mid tropospheric subsidence developed on the lee (eastern) slope of the mountain. Some of this sinking was likely due to the return branch of the mountain–plains solenoid, especially below $z = 6$ km. However, the depth of the subsidence, along with the upper tropospheric deformation of the potential temperature and zonal velocity fields to the lee of the barrier indicates a mountain wave was also present. Over the western High Plains (near $x = 50$ km), the secondary region of weaker upward motion between the surface and about 8 km was the up–branch of the plains portion of the solenoid that was discussed above.

Cross sections along Palmer Divide (Fig. 7.5) show that the mountain–plains solenoid was considerably weaker there. Upward motion near mountain top was not as concentrated or as deep, with two broad maxima centered near $x = -75$ km and $x = -20$ km. The boundary layer along the entire eastern slope of the ridge was also dominated by upward motion due to the convergence along the Palmer Divide. The secondary up–branch of the plains solenoid was almost nonexistent, with only a very weak column of deepened upward motion near $x = 50$ km. Mid tropospheric subsidence was relatively weak as well, with maximum sinking only about 25 % of that further north. Although the upper tropospheric mountain wave structure was still apparent, it was not as sharp as it was to the north. All of this resulted in weaker upslope that in turn advected less cool, moist air westward.

Another view of the meridional variations along the Front Range is provided by vertical cross sections taken parallel to the Continental Divide. The westernmost section taken just downwind of the highest peaks (Fig. 7.6) shows that the quasi two–dimensional mountain–plains solenoid regime was present over most of the northern mountains, but was interrupted by the effects of the Palmer Divide (located near $y = -100$ km in Fig. 7.6). Strong lower tropospheric upslope and deep mid tropospheric sinking motion was uniformly distributed in the north, while the weaker circulation existed over the Palmer Divide. As mentioned above, the contrast between the cool, moist boundary layer air to the north and warmer air to the south was much like a frontal boundary. Although moisture content was slightly higher in the north (Fig. 7.6b), the equivalent potential temperatures were actually lower due to the lower temperatures (Fig. 7.3c).

East of the mountains, the meridional contrasts were dominated by the Palmer Divide–Platte Valley solenoid (Fig. 7.7). In the boundary layer, rising motion was occurring near ridge top, while sinking motion prevailed over the Platte Valley. The resulting meridional circulation was superimposed on the v wind (Fig. 7.7d) as weak northerly flow near the surface and enhanced southerly flow at $z = 4$ km. Above 4 km, upward motion over the Platte Valley was actually part of the secondary up–branch in the plains solenoid. Careful inspection of the vertical motions in Figure 7.4d shows that the majority of the plains up–branch is actually elevated, due to the superposition of the two perpendicular circulations.

The interactions between the preexisting front and the topographic solenoids strongly influenced the initiation and movement of the convective storms. Although the vertical motions in the high peaks along the northern Front Range were quite strong, developing convection was unable to persist as it moved off the mountains. The strong mountain–plains solenoid advected cool post–frontal air into the mountains, and while boundary layer moisture and θ_e increased, the strength of the cap increased as well. Thus, convective growth downwind of the mountain peaks was inhibited not only by the strong subsidence, but also by the strong cap. This explains why the observed and simulated storms along the northern Front Range completely dissipated after moving off the highest terrain. Had the post–frontal air not been there, convection probably would have redeveloped east of the lee side subsidence zone, as in Tripoli and Cotton (1989a, b), possibly resulting in a larger MCS.

Convection was thus highly favored along the Palmer Divide for several reasons. The mountain–plains solenoid was considerably weaker due to the more gentle slope (Tripoli, 1986), and although the upward branch was not as intense or consolidated, the downward branch was also not as strong. Meridional circulations generated by heating on the Palmer Divide itself created a second region of boundary layer upward motion along and just north of the ridge crest that extended eastward onto the plains. This circulation was not as deep as the mountain–plains solenoid, but the moisture convergence and destabilization provided a region where the cap could more easily be broken. The cap south of the divide was weaker to begin with in this case, due to the meridional contrasts along the frontal zone. Convergence near ridge top intensified the existing north–south thermal contrast creating an enhanced mesoscale front that extended eastward to about the position of LIC in Figure 7.3. In this way, the circulations along the Palmer Divide literally cut a very well defined channel through the mountain–plains subsidence zone through which convection was highly favored over the surrounding areas.

7.2.4 Convective development on the High Plains

Between 1900 and 2100, modeled and observed convection propagated along the Palmer Divide west of Denver mainly through new updraft development along the zonal convergence zone. Initial convection was cellular until about 2100, when sudden intensification began occurring just south of Mile High (Fig. 7.8). As discussed in Chapter 5, this is the climatological location of the DCVZ. The model results indicate that this was also where the secondary plains up–branch of the mountain–plains solenoid was superimposed upon the up–branch of the Palmer Divide–Platte Valley solenoid. Simulated vector velocities at 2100 (Fig. 7.8) show that near–surface convergence associated with the plains up–branch, which now extended southward from CHILL to the Palmer Divide, had increased considerably since 1800. The strongest convergence was located on the Palmer Divide, and was due to the combination of the approaching outflow boundary and the superposition of the topographic solenoids. Since the Denver cyclone was so weak in this case, convective intensification was likely dominated by these solenoidally driven effects.

Once convection intensified, a strong surface cold pool developed and the storm structure became more linear. With the dominance of the cold pool, system propagation became somewhat less dependent on the preexisting convergence zones, although the environment ahead of the growing line was quite inhomogeneous. The east–west convergence and baroclinic zone was still along the Palmer Divide, but its eastern portions were advecting northward in the prevailing southeasterly flow (Fig. 7.8b). Lower temperatures north of the Palmer Divide and lower dewpoints to the south resulted in a localized tongue of high equivalent potential temperatures that was feeding into the northern half of the storm (Fig.

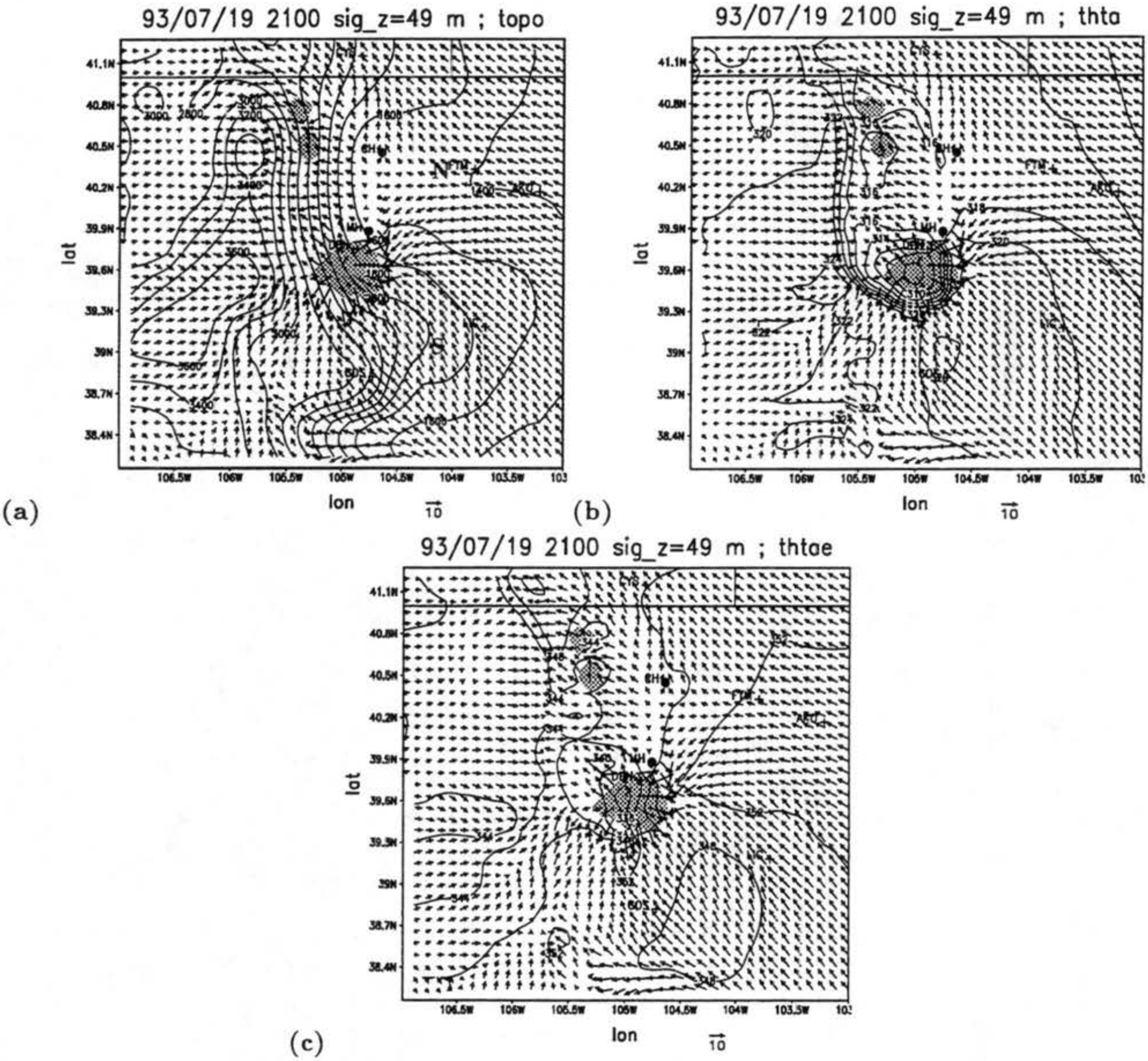

Figure 7.8: Model output on grid #3 at the lowest model σ level at 1800. The labels S and N in (a) correspond to the positions of soundings shown in Fig. 7.9a, b. Topography is contoured at 200 m intervals in (a); potential temperature is contoured at 2 K intervals in (b); and equivalent potential temperature is contoured at 4 K intervals in (c). Wind vector scaling is two thirds that in Fig. 7.3. Areas of total surface condensate (generally rain and hail) greater than 0.1 g kg^{-1} are shaded.

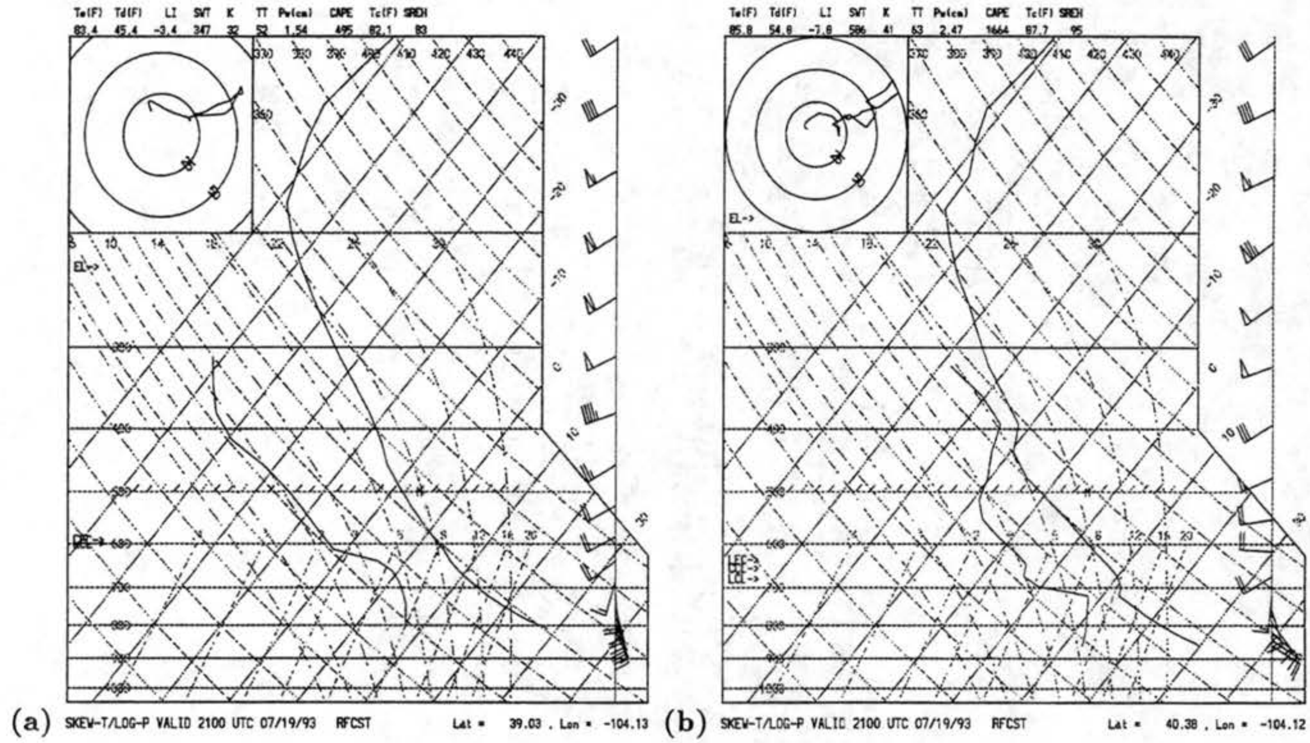

Figure 7.9: Skew-T log-P plots from grid #3 at 2100 at (a) position S in Fig. 7.8a and (b) position N in Fig. 7.8a. Temperature and dewpoint are depicted as dark solid lines. The moist parcel trajectory based on the temperature and dewpoint in the lowest 500 m is depicted by an M. Winds are shown as barbs on the right and a hodograph in the upper left inset. Full barbs are equivalent to 5 m s^{-1}, while flags represent 25 m s^{-1}.

7.8c). Soundings taken on grid #3 at 2100 show that the drying trend to the south was mainly the result of boundary layer mix-out. Near the center of the drying (Fig. 7.9a), the boundary layer had deepened to about 650 hPa, and the capping inversion was basically gone. However, convection was not breaking out in the model since the moisture depletion had reduced values of CAPE to a scant 495 J kg−1. The coarse resolution on grid #3 also prevented all but the most strongly forced convection from forming. No convection was observed in this area, although as discussed in Chapter 4, a small system did develop even further south along the Raton Mesa. North of the Palmer Divide (Fig. 7.9b), the cap remained in place resulting in a shallower boundary layer and more moisture. Temperatures near the level of the capping inversion were originally about the same in both regions, and the cap was mainly the result of cool, moist air advecting westward. Once the cap broke in the south, however, temperatures below about 600 hPa began increasing, resulting in a localized area of warming over the western plains south of the Palmer Divide. Later in the afternoon, this would come to play a significant role in the development of a very localized low level jet.

At 2200, two convergence zones were apparent ahead of the expanding cold pool (Fig. 7.10). The northernmost zone was the original area of convergence and baroclinicity that had formed north of the Palmer Divide. Over time this zone had continued to advect northward, and although it was within grid #4 no convective cells were simulated along it. The second convergence zone just northwest of LIC began forming around 2100 and had rapidly intensified with time. By 2200, towering cumulus were already occurring on grid #4, and as mentioned in Chapter 6, a thunderstorm soon formed. The rapid development of the second convergence zone suggests that it somehow may have been induced by the oncoming squall line. To investigate this, the simulation was rerun with grid #s 1–3 with all microphysical processes deactivated. Although the effects of water vapor were included, no clouds or precipitation processes were simulated. Both of the convergence zones along the Palmer Divide formed in a similar manner without the microphysics, thus any storm-generated effects likely played a minor role.

The extent to which these convergence zones were properly simulated is unknown due to the lack of surface observations. The subsequent convective development was simulated

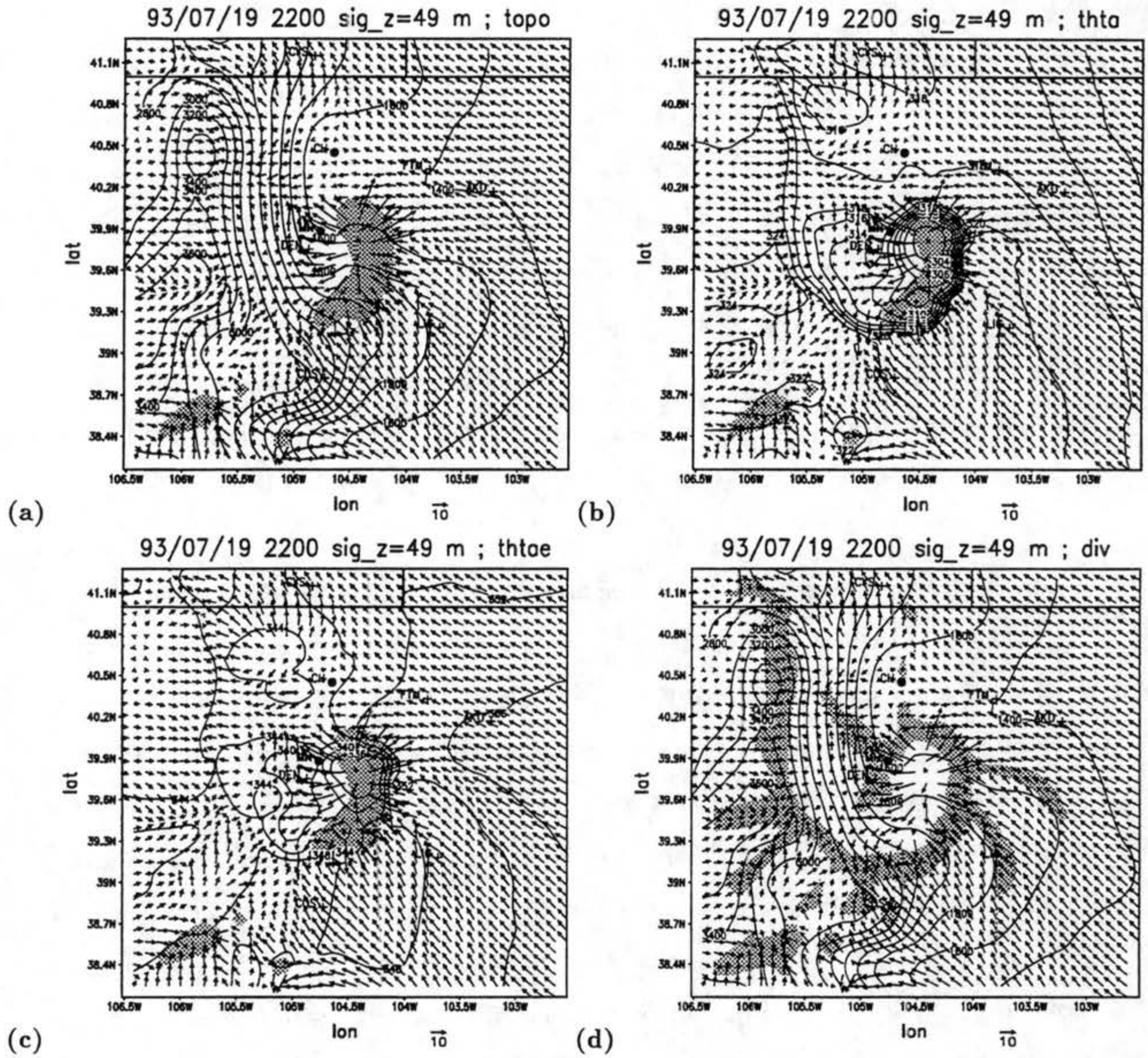

Figure 7.10: Panels (a–c) are as in Fig. 7.8 except at 2200. In (d) topography is contoured at 200 m intervals and areas of divergence less than -0.0002 s^{-1} are shaded.

incorrectly as the new convection actually became dominant. However, there are several indications that these convergence zones actually existed in some form. The scattered weak cells observed on radar ahead of the main line (Fig. 4.8e) were in the same general area where the model put the convergence zones. Furthermore, this weak convection was only observed in this one area, and did not occur at any other time or place while the system was on radar (2000–0145). Other evidence indicates that enhanced convergence is a recurrent feature in this region. López and Holle (1986) observed a maximum in average lightning frequency just northwest of LIC between 0000 and 0200 UTC during the summer of 1983. Grady and Verlinde (1997) also observed a squall line that went through a very similar cycle of intensification and collapse to that simulated here. That system became strong east of Denver and then almost completely collapsed, only to redevelop at about the same longitude as LIC. Washington County, located north and east of LIC is also well known to local weather forecasters for its unusually severe storms and large tornadoes. The existence of a statistically significant convergence zone in this area is thus an intriguing possibility that deserves further research. However, it presents a bit of a tangent to the topic of MCS genesis, so it is left for a future study.

7.2.5 Convective focusing by the low level jet

Although the low level jet is considered to be a nocturnal phenomenon, the southerly wind component over eastern Colorado began increasing after 2100. The strongest southerly flow was confined to the eastern plains of Colorado and was generally east of the developing MCS (Fig. 7.11a). Simulated winds steadily increased through the afternoon, to become an intense, concentrated jet by 0000 (Fig. 7.11b). The maximum flow was confined to a shallow layer near the top of the capping inversion, at about 1500 m AGL ($\sim$ 3000 m MSL), and was remarkably small in scale. The entire feature was only 200 km wide, while the strongest core winds were 50 km wide. Winds accelerated as they approached the convection, reaching speeds in excess of 20 m s^{-1} on grid #4. Convection grew explosively as the MCS intersected this strong flow at 2300, and the corresponding increase in the volumetric rain rate is clearly visible in Figure 6.7.

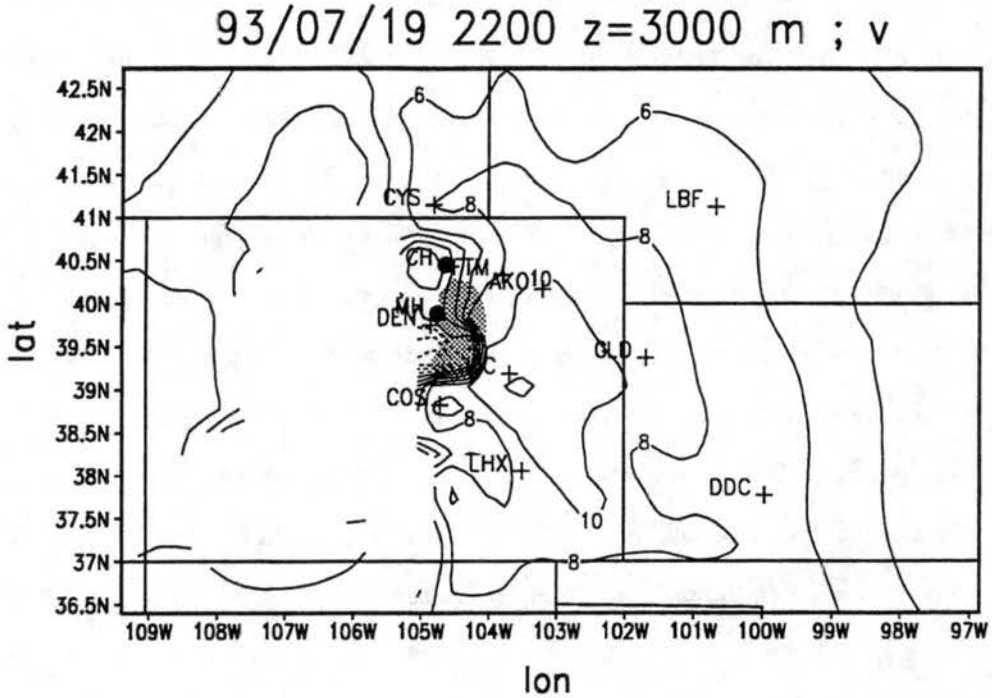

(a)

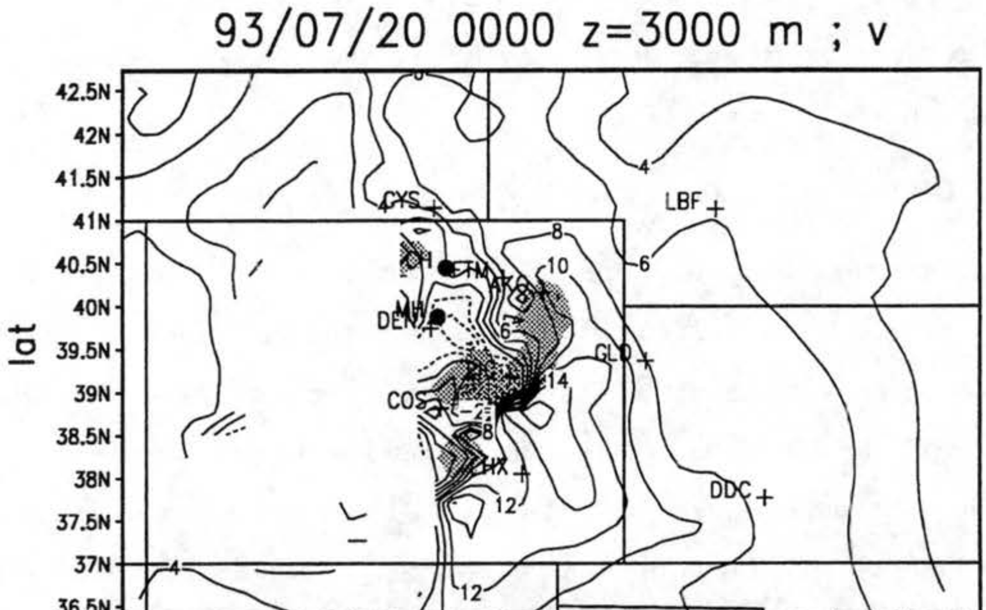

(b)

Figure 7.11: Constant height cross sections of the v wind component on grid #2 at z = 3000m for (a) 2200, (b) 0000, and (c) 0200. Contours are every 2 m s^{-1}. Areas of condensate greater than 0.1 g kg^{-1} are shaded. In (d), v component winds at 0200 from the no microphysics run are contoured as in (a–c).

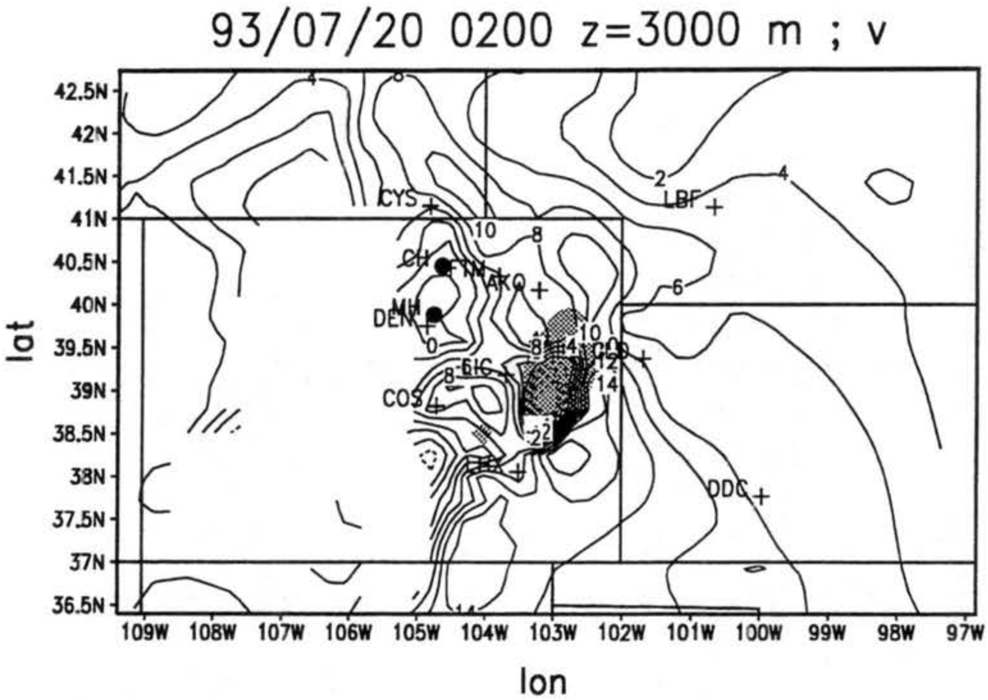

(c)

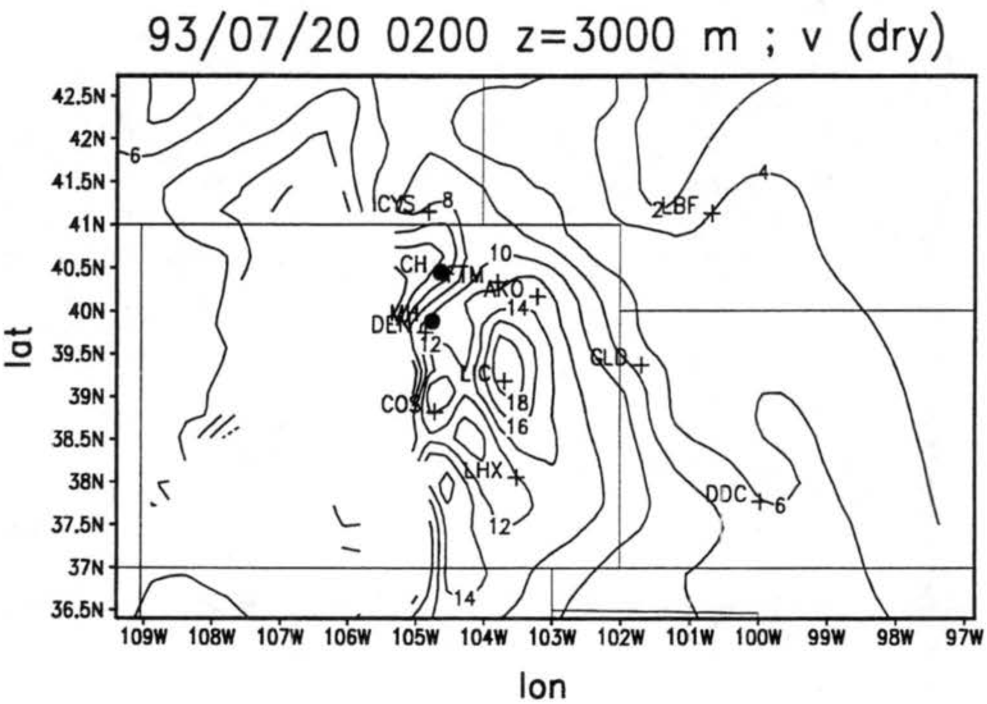

(d)

Figure 7.11: Continued

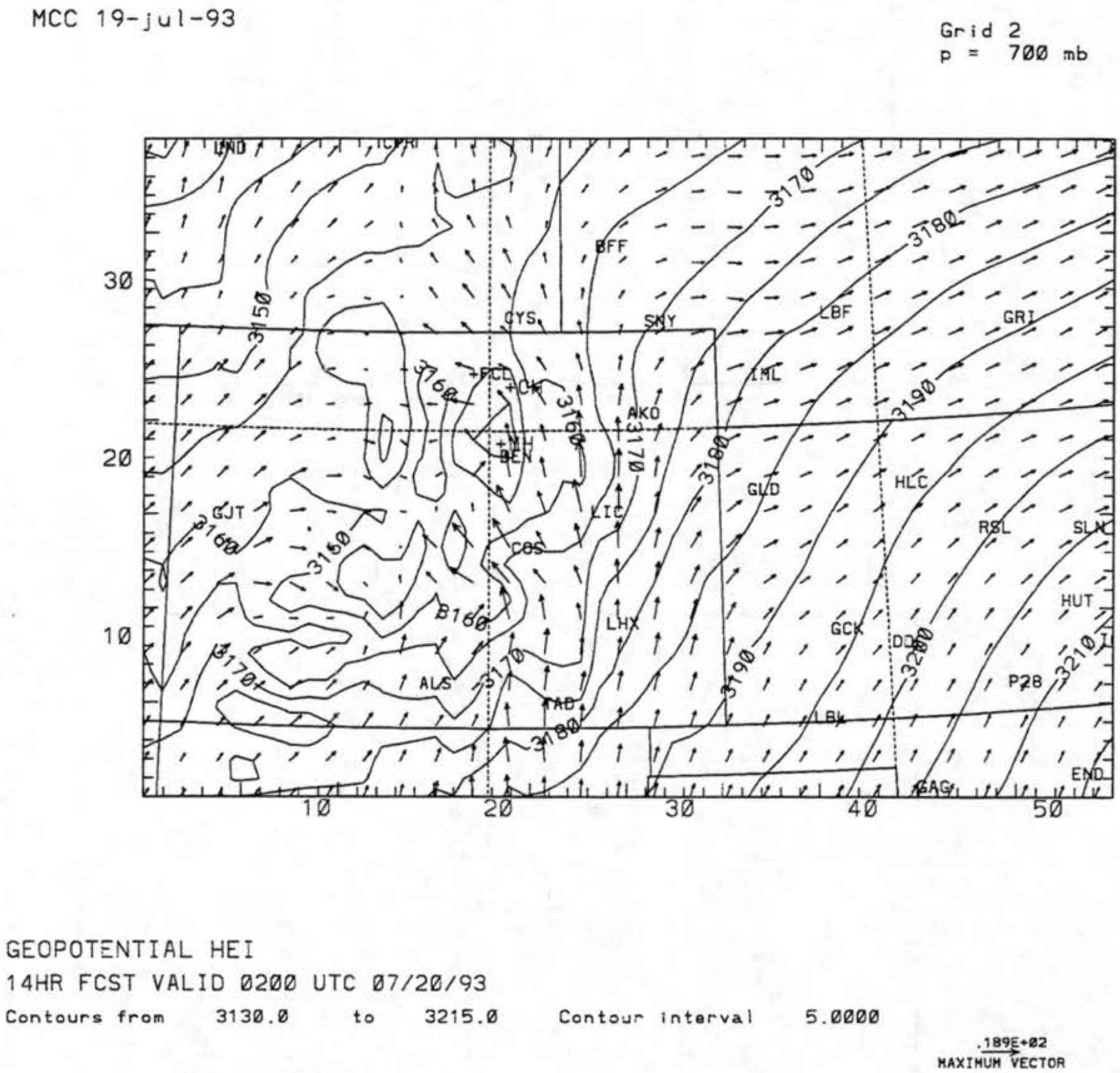

Figure 7.12: Constant pressure cross section at 700 hPa on grid #2 at 0200 from the no microphysics run. Heights are contoured at 5 m intervals and vector winds are scaled at the lower right.

This mesoscale jet remained nearly stationary as the MCS crossed and partially eclipsed it from the north (Fig. 7.11c). Convective storms along the leading line were initially enhanced by the strong convergence, then as the line moved east new simulated cells continually developed on the southern portion of the line, in effect elongating it. By 0300 the strongest convective cells were located in the southwestern corner of the MCS (Fig. 6.6f). Given the stationary nature of the jet, it is not surprising that it also developed in the run with the microphysics turned off. The winds were weaker and slower to develop than the run with convection, however by 0200 (Fig. 7.11d) a strong, narrow jet had developed with maximum winds of 20 m s^{-1} over LIC.

The small size of this jet makes its existence difficult to verify in the observations. However, the radar evolution does show some interesting parallels with the model. Radar-derived MCS–total rain rates nearly tripled between 2330 and 0000 (Fig. 5.28) as the observed system moved east of LIC, which is about where the model put the jet. At 0055 several weak cells extended from west to east across the Palmer Divide (Fig. 4.8f), however very strong cells started back–building from the main line just east of x = 120 km in Fig. 4.8f, or about the longitude of LIC. Over the next hour convection repeatedly developed in about the same spot as the original line moved east, resulting in the elongation of the convective line by about 50 km. However, during the same period, convection west of LIC remained weak. The same behavior was occurring in the model (Fig. 6.6e, f) as cells west of 103.4°w remained weak, while strong back–building repeatedly occurred near 103°w. These similarities suggest that at least the sharp western edge of the low level jet was well simulated. Although the exact width of the observed jet could not be determined, weak southerly flow below 700 hPa at DDC and LBF at 0000 (Fig. 4.6) indicates that the jet had not yet become pronounced there.

Although this jet was very small and intense, the processes behind its formation are quite physically plausible, and resemble the results derived by McNider and Pielke (1981). Geopotential heights at 700 hPa at 0200 from the no microphysics run (Fig. 7.12) show a tightened height gradient over southeastern Colorado south of LIC[2]. Recall from above

[2]Heights at several different levels were checked to account for possible contamination due to extrapolation below ground in the mountains. All but the highest simulated topography was below 680 mb (~ 3500

that diurnal heating was deep and strong west of there as the boundary layer mixed out south of the Palmer Divide. East of LIC, however, the cap remained unbroken due to the reduced heating brought on by the extremely wet soil over western Kansas. The result was an extension of the low height anomalies from the mountains out over the High Plains of southeastern Colorado. The geostrophic wind in the high gradient region was about 20 m s^{-1} or about double that further east. Significant cross-gradient flow streaming toward lower heights indicates ageostrophic flow was important as well, and boundary layer friction was likely playing an active role (Holton, 1967; McNider and Pielke, 1981).

If such small scale jet maxima like this do exist, they could explain the propensity for repeated convective development in very focused areas (Bluestein and Jain, 1985). They could also explain why many MCSs are very difficult to simulate using grid spacings on the order of 20 km or greater. *An attempt to simulate this case using convective parameterization would have likely failed since the attendant coarse grid spacing would not have properly resolved the jet.* One has to be careful even in the explicit simulation, because although this jet was easily resolved on the 5 km grid, any extension across the lateral boundaries onto the 20 km grid would not be resolved well. More studies need to be conducted with fine grids covering larger areas to determine the sensitivity of this feature to the grid structure. Unfortunately, these small scale phenomena are very difficult to verify with the current observational network. Profiler data, had it been available, would have been useful, but the two stations over the entire state of Colorado would not have adequately resolved the jet. True verification may have to wait for a future field project where airplane measurements are taken in the environment well removed from an MCS.

7.2.6 Summary of convective focusing mechanisms

The isolated convective focusing in this case indicates that the entire mountain–plains solenoid did not propagate eastward with convection as in Tripoli and Cotton (1989a, b). Rather, a number of different orographically induced processes in combination with a pre-existing synoptic front colluded to put convection in a very specific place. In this case, and

---

m MSL), and the lowered heights in southeastern Colorado were prominent at all pressure levels below 650 mb.

apparently in many others (Wetzel, 1973; Klitch et al. 1985; López and Holle, 1986), the Palmer Divide acted as an efficient channel by which convection escaped the detrimental effects of the suppression zone immediately to the lee of the mountains. The less steep, more uniform slope reduced the intensity of the upper subsidence, while boundary layer upward motion from the shallower Palmer Divide–Platte Valley solenoid provided a very favorable zone for convection to form. By the same token, subsidence in the mountain–plains and Palmer Divide–Platte Valley solenoids inhibited convection on either side of the divide. The convergent flow along the Palmer Divide also acted to locally increase the baroclinicity west of Limon. The resulting break in the mountain–plains solenoid explains why neither the simulated (Fig. 6.7) nor the observed (Fig. 5.28) convection went through the dramatic break–down phase discussed by Tripoli and Cotton (1989a).

Although the preexisting cooler air in the northern half of Colorado was difficult to detect in the surface potential temperatures, it too played several crucial roles. The westward advection of cool, moist air across the High Plains and into the mountains was enough to strengthen the cap north of the Palmer Divide, preventing any early convective development. To the south of the divide where the air was warmer, the cap broke, the boundary layer mixed out and deep heating and drying occurred. This inhibited convection to the south and lowered the pressures in the area between the Palmer Divide and the Colorado/New Mexico border. During the mid afternoon, convection propagated along the Palmer Divide between the dry area to the south and the capped area to the north, feeding on moisture advected in from the east.

By late afternoon, an intense, concentrated low level jet developed over southeastern Colorado along the eastern edge of the mesoscale low pressure. The cap had remained strong through most of the plains east of Limon, but convergence at the northern edge of the low level jet combined with lifting from the lower tropospheric cold pool was enough to break through the cap and maintain convection. The convective system rapidly intensified as it encountered the strong jet, and both the satellite and simulated anvils rapidly blossomed into the characteristic oval shape. Elsewhere, the strong cap acted to suppress most of the convection that tried to develop to the south and east of the main system.

These results indicate that this mesoscale convective system was intimately connected with its surrounding environment, and was much more than convection developing above an expanding surface outflow boundary. The localized nature of the positive forcing within the otherwise hostile environment resulted in intense convection over a very small area. With such strong focusing by the environment, it is not surprising that a long–lived system formed. It is also not surprising that the model predicted the convective evolution so well. As mentioned in Chapter 5, strong convective cells in close proximity will affect the environment in a unique way allowing for very strong upper level blocking and mid level inflow. The fine–scale three–dimensional details of the interaction between the convection and the surrounding environment are investigated in the second half of this chapter, starting with the next section.

7.3 Simulated MCS kinematic structure and evolution

The simulated MCS structure and evolution shared many characteristics with the observed case, and considerable agreement existed down to the scale of the individual Doppler scans. This is not a trivial accomplishment, for one convective cell in the wrong place can cause the solution to deviate significantly. In this case, the strong environmental forcing supplied a good framework for the model to build convection in the correct place. Such a high degree of accuracy provides confidence that many of the interactions between convection and its mesoscale surroundings were correctly simulated.

7.3.1 Analysis method

To facilitate comparisons with the observations, system–relative and environment–relative (or perturbation) wind fields for the simulated MCS were derived to be consistent with the methods discussed in Chapters 3 and 5. Simulated system motion was calculated for three separate intervals, $1930 - 2130, 2200 - 0000$, and $0030 - 0300$, because Doppler–estimated storm motions were only available for comparison from $2200 - 0000$ UTC. Also significant variations in system motion through the simulation necessitated several averaging intervals. System motion was defined by the average velocities of all discernable precipitation maxima at the lowest model level. Based on these calculations, the average motion was

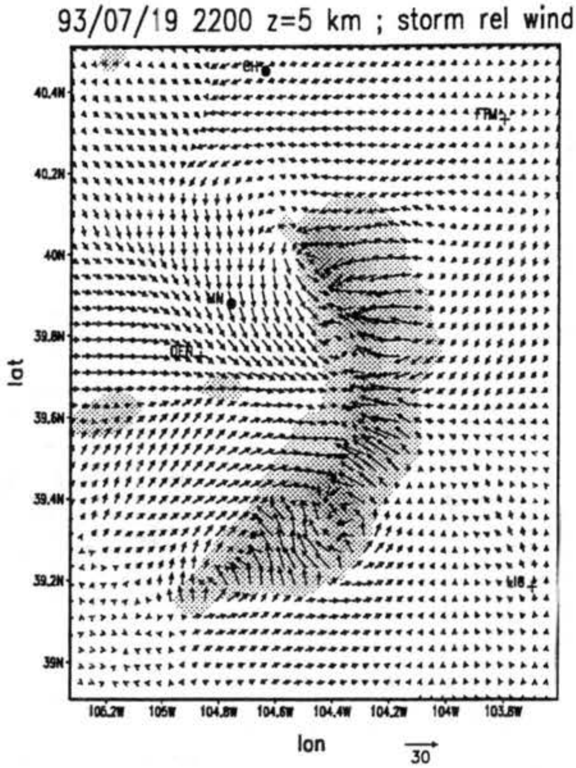

Figure 7.13: MCS–relative wind vectors and total model condensate on grid #4 at 2200 at a constant height of $z = 5$ km MSL. Total condensate is shaded at 0.5 g kg^{-1} increments at and above 0.5 g kg^{-1}, the 0.1 g kg^{-1} level is also shaded. The vector winds are scaled at the bottom of the figure. The locations of meteorological reporting stations are denoted by plus signs and the three–letter ID. The locations of the CHILL (CH) and Mile High (MH) are denoted by dots

$(u, v) = (7.8, -2.4), (10.1, 2.2)$, and $(5.6, -4.6)$ m s^{-1} for each respective time interval. For times between two intervals, the system motion was defined by the time–weighted linear average. Simulated storm motion for the 2200 – 0000 period agreed well with observed values of $(u, v) = (10.8, 4.8)$ m s^{-1}. The environmental mean winds were defined by averaging all values on grid #2 into a single vertical profile for each model output time. Mean simulated $\overline{u}$ and $\overline{v}$ components were often within 2 m s^{-1} of the observed 0000 UTC profile, indicating that the general flow pattern was not evolving significantly.

7.3.2 Simulated early MCS structure and comparison with Doppler data

"Early" is defined here as the interval from 2130 to 2300 when the system first moved onto the plains and assumed its linear shape. As mentioned in Chapter 6, the best agreement between the simulated and observed systems occurred before and during this period, with

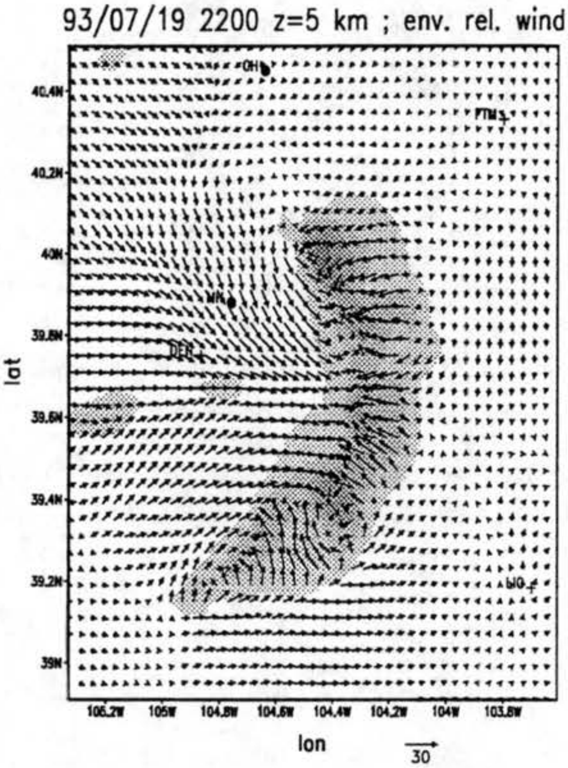

Figure 7.14: Same as in Fig. 7.13 except vectors are relative to the environmental average winds at this height

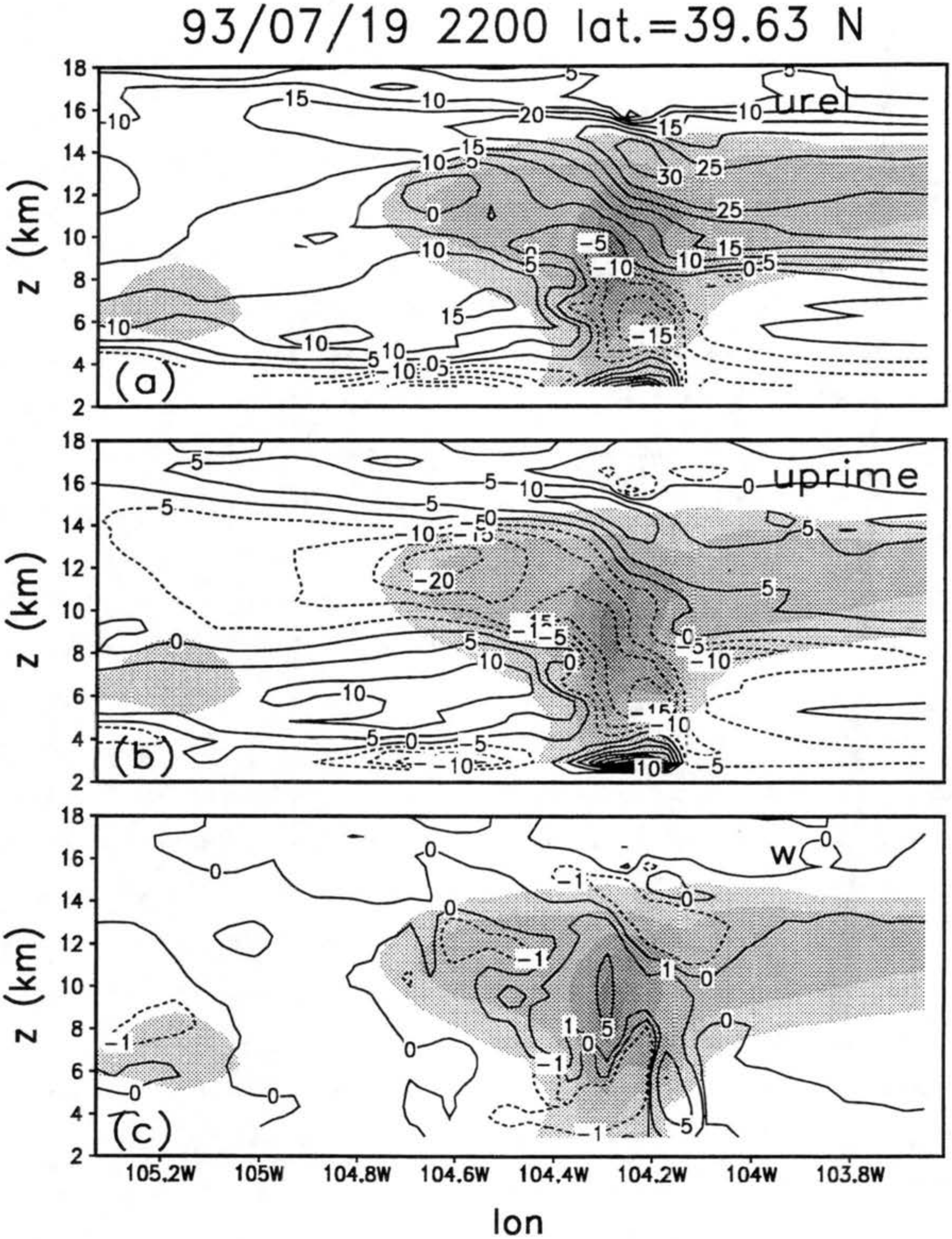

Figure 7.15: Vertical $x-z$ cross sections on grid #4 at 2200 at $y = 39.63°$ lat. In (a), storm relative winds are contoured at 5 m s^{-1} increments. In (b), winds relative to the environmental average are contoured at 5 m s^{-1} intervals, and in (c) vertical motion is contoured at the $0, \pm1, \pm5, \pm10$, and ±15 levels. Total condensate is shaded in each panel at 0.5 g kg^{-1} increments at and above 0.5 g kg^{-1}, the 0.1 g kg^{-1} level is also shaded.

particularly good agreement as convection developed in the DCVZ. Since the model was slightly fast in bringing the convection onto the plains, the simulated solution at 2200 is compared to the Doppler fields at 2233.

The resemblance at 5 km MSL between the model simulation (Figs. 7.13, and 7.14) and the radar observations (Fig. 5.17) was quite good. The general bowed appearance of the convective line was well simulated, as was the location of the strongest cells on the northern and southern line ends. The simulated system produced a forward anvil that was less extensive than observed at this level. However, the ($\sim$ 10 dBZ) reflectivities in the leading anvil corresponded to snow aggregate mass densities of only 0.02 g m^{-3} (Douglass, 1964; Battan, 1973), and similar ice contents were simulated in the leading anvil at 6 km. Neither the simulated nor the observed systems displayed significant trailing stratiform precipitation.

Like the observations, simulated storm relative mid level inflow accelerated towards the line from the east, while rear inflow approached from the west. The most conspicuous simulated features were the dual "bookend" vorticity maxima trailing the northern and southern ends of the line. Although these were not immediately apparent in the Doppler observations, cyclonic curvature in the rear inflow near $y = -46$ km in Figure 5.17, straight westerly rear inflow south of that, and weak southwesterly rear inflow near $y = -106$ km show evidence of their existence. This MCS–scale vorticity developed in–situ in both the simulation and the observations as westerlies accelerated towards the entire line from the rear. Recall in Chapter 5 that a much smaller vorticity couplet was also observed behind a cell within the convective line at 2209 near $x = 33, y = -91$ km in Figure 5.10. It is interesting to note that both scales of vorticity coexisted for a brief period prior to the dissipation of the storm–scale couplet. Weisman (1993) noted that this convective–scale vorticity was often transient. A similar scale coexistence was simulated at 2130 (not shown) when two strong storms within the developing line had supercell–like rotating updrafts.

Although most of the simulated anvil advected forward, cross sections (Fig. 7.15) reveal slightly more upshear anvil debris than was observed at 2233. In this respect, the simulated condensate field resembled the observed structure at 2209 (Fig. 5.14), and this was likely due to differences in timing of the convective updraft strength. Despite the differences

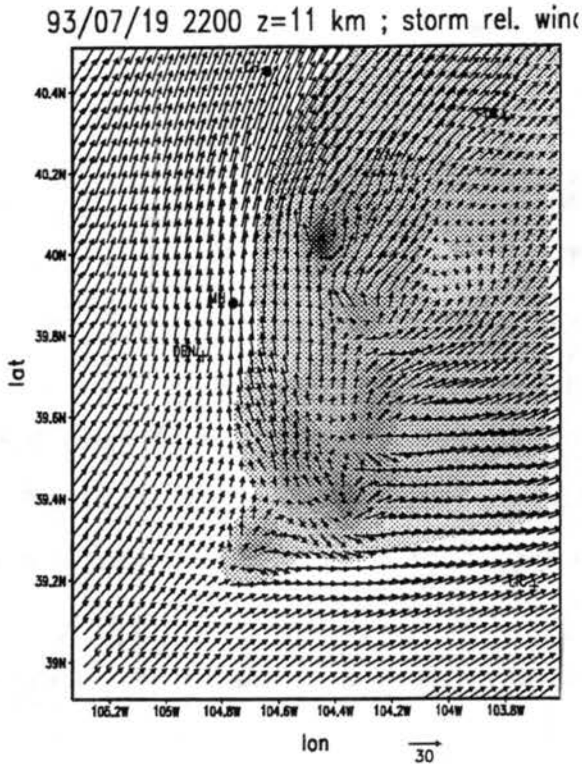

Figure 7.16: Same as in Fig. 7.13 except at z = 11 km MSL.

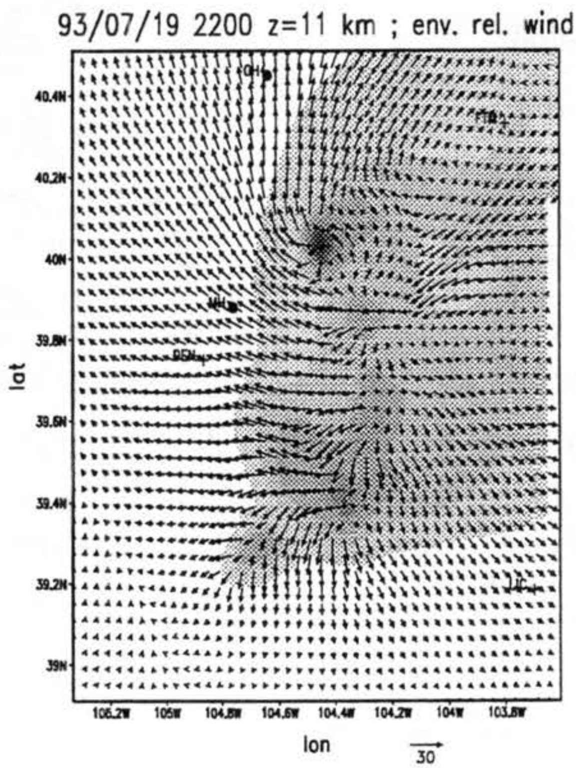

Figure 7.17: Same as in Fig. 7.14 except at z = 11 km MSL.

the vertical flow structure was similar in both cases. In the storm–relative sense, strong front–to–rear flow accelerated into relatively erect updrafts and for the most part turned eastward as it reached the upper troposphere. As in the observations, the environment–relative winds showed the opposite trend with the strongest perturbations on the western side of the system. Wind speeds were similar to those observed, especially at 2209 (Fig. 5.15). Rear inflow extended well beyond the convective line in both the environment–relative (Figs. 7.14, and 7.15b) and the storm–relative (Fig. 7.13) sense, despite lack of deep trailing stratiform precipitation (Fig. 7.16). A similar trend was noted in the Doppler observations, especially in the perturbation wind field (Figs. 5.15, 5.17, 5.18, and 5.19). Simulated perturbation upper tropospheric front–to–rear flow also extended well beyond the upper tropospheric anvil (Figs. 7.15b, 7.16, and 7.17). Not surprisingly, the rearward extent of the anvil condensate was close to the zero line in the storm–relative front–to–rear flow. The perturbation pattern compares well with the results obtained by Schmidt and Cotton (1990) and Pandya and Durran (1996), indicating that it was produced by upstream internal gravity wave propagation. Additional evidence of gravity wave forcing will be presented later in this chapter.

7.3.3 Simulated MCS weakening

As mentioned in Chapter 6, the simulated MCS temporarily lost some of its structure between 2300 and 0030 as a convective storm spuriously intensified along the presquall Palmer Divide convergence zone (Fig. 6.6c, d). Although this represents an error with respect to the observations, it provides a unique opportunity to study the effects of such an event on MCS mesoscale organization. Initially, all aspects of the new convection were independent of the original convective line, and the mesoscale circulations existed as a separate entities. As the line and the cell merged and intensified in the low level jet, their mesoscale circulations merged and the system became unified again. Structural comparisons between the unorganized phase at 0000 and the mature, merged phase at 0200 (next section) reveal a lot about how mesoscale circulations merge and grow upscale.

At 0000 the newly developed cell (labeled "A" in Figs. 7.18, and 7.20) was located near 39.1° lat., -103.2° lon. The original convective line, which had just caught up with

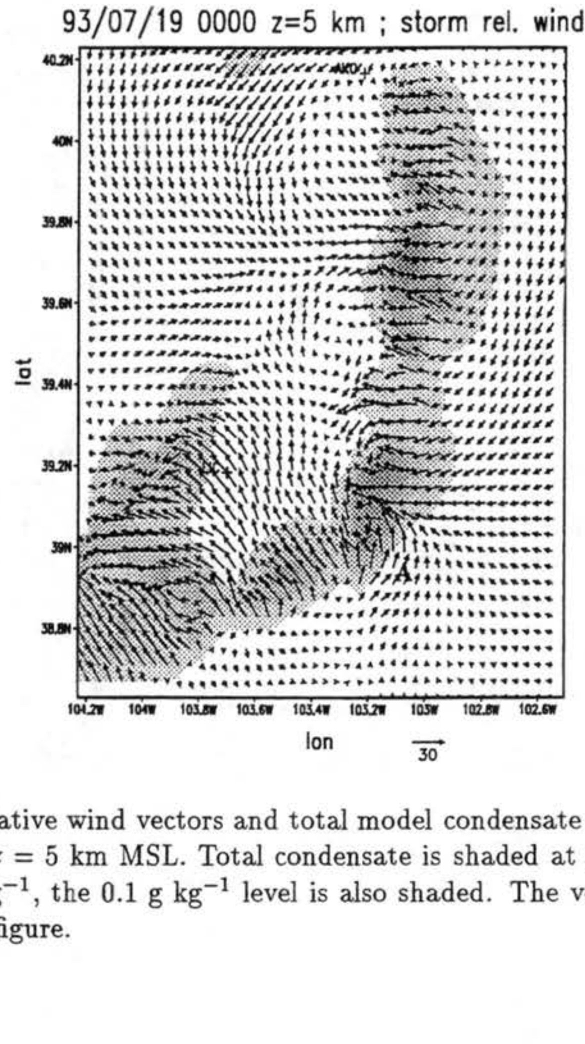

Figure 7.18: MCS–relative wind vectors and total model condensate on grid #4 at 0000 at a constant height of z = 5 km MSL. Total condensate is shaded at 0.5 g kg^{-1} increments at and above 0.5 g kg^{-1}, the 0.1 g kg^{-1} level is also shaded. The vector winds are scaled at the bottom of the figure.

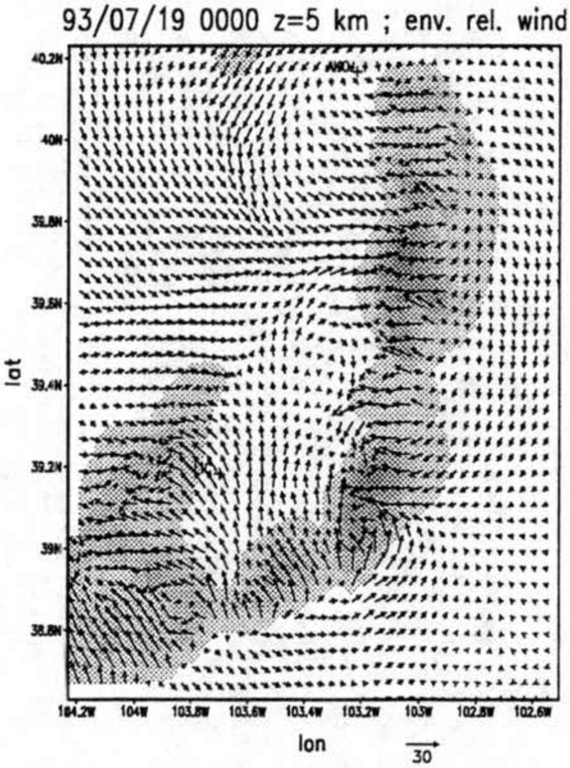

Figure 7.19: Same as Fig. 7.18 except vectors are relative to the environmental average winds at this height.

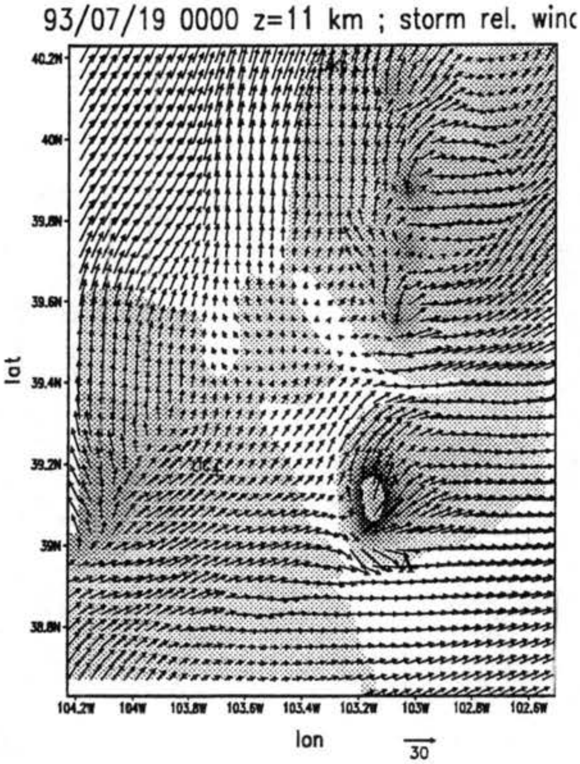

Figure 7.20: Same as Fig. 7.18 except at z = 11 km MSL.

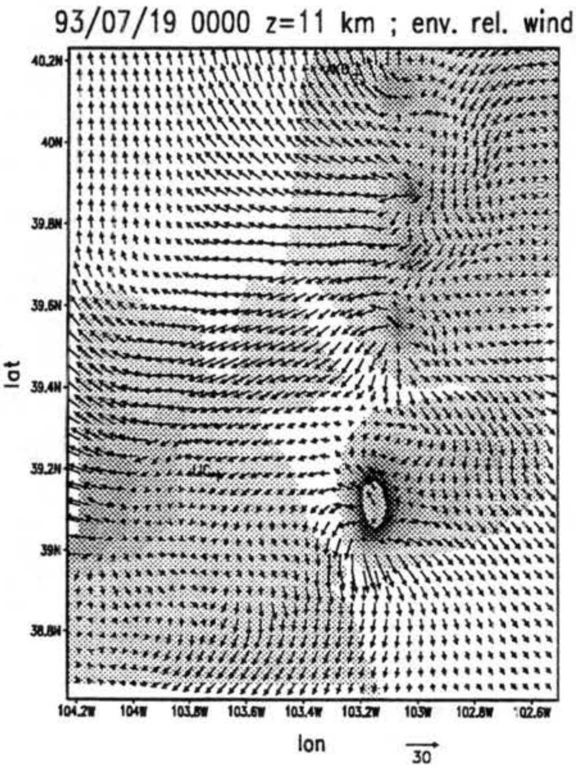

Figure 7.21: Same as Fig. 7.19 except at z = 11 km MSL.

cell A, extended northward almost to the boundary of grid #4. Additional storms to the southwest of the two main entities were associated with convergence along the trailing outflow boundary. As was mentioned previously, these storms were weak due to the relatively dry boundary layer air feeding into them. Convective updrafts within cell A were rapidly intensifying as it was starting to tap the strengthening low level jet. Core vertical velocities at 8 km MSL were already up to 21 m s^{-1}, and the updraft was displaying some cyclonic rotation. Further north the remaining portion of the original convective line had maintained its intensity from 2200, with core vertical velocities of 18 m s^{-1} at 8 km MSL.

Although the condensate along the length of the line had merged at 5 km, the mesoscale flow fields (Figs. 7.18, and 7.19) did not show the same degree of merger, and were less organized than at 2200. Rear inflow was still present to the west of the original convective line, but it was less extensive. No significant storm–relative or environment–relative rear inflow was present at any level west of cell A. Westerly wind speeds within the existing rear inflow were about the same as those at 2200, but the "bookend" vorticity couplet was not as prevalent. The southern anticyclonic branch had almost completely dissipated, with only a small remnant left near 39.5° lat., -103.3° lon. East of the convective line, the strongest inflow was streaming towards the intensifying cell A.

The separate nature of the convective storms in the leading line was most apparent in the upper troposphere (Figs. 7.20, and 7.21). The original line, cell A, and the weak southwestern convection were all generating three distinct anvils. Much of the storm–relative flow diverting around cell A was channeling through the gap between it and the northern line (Fig. 7.20). In contrast, the cells within the northern line acted collectively as a mesoscale entity in blocking the upstream flow. Some air was also diverting around the convection in the southwestern portion of the grid. In the environment–relative sense, the northern line was still perturbing the flow in a large, coherent region upwind of the anvil condensate, but cell A was producing only isolated perturbations.

7.3.4 Simulated MCS reconsolidation

By 0200, the MCS had regained its consolidated structure, especially in the upper troposphere (Figs. 7.22, and 7.23). At 11 km storm–relative flow behind the line had reversed

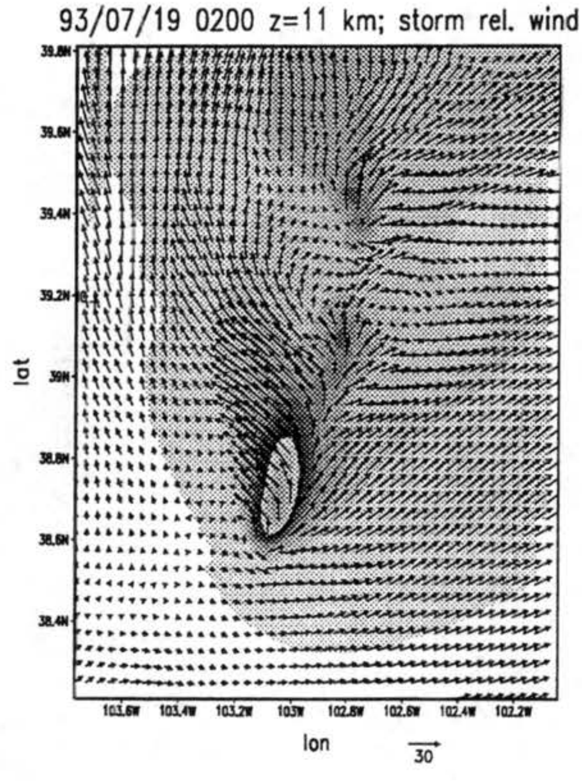

Figure 7.22: MCS–relative wind vectors and total model condensate on grid #4 at 0200 at a constant height of $z = 11$ km MSL. Total condensate is shaded at 0.5 g kg^{-1} increments at and above 0.5 g kg^{-1}, the 0.1 g kg^{-1} level is also shaded. The vector winds are scaled at the bottom of the figure.

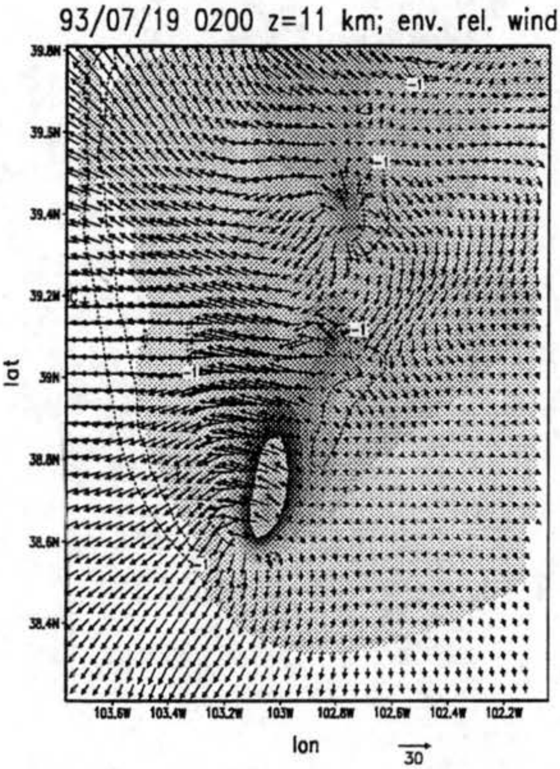

Figure 7.23: Same as Fig. 7.22 except vectors are relative to the environmental average winds at this height, and vertical motions of -1 m s^{-1} are contoured.

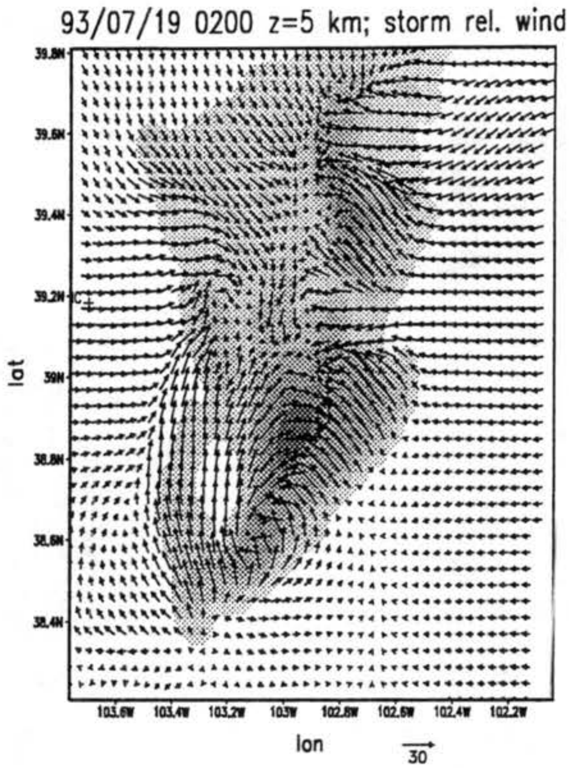

Figure 7.24: Same as in Fig. 7.22 except at $z = 5$ km MSL.

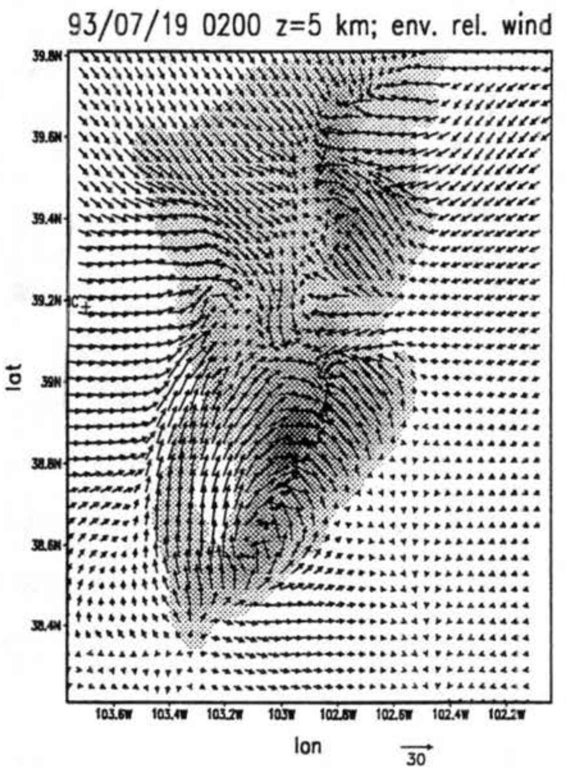

Figure 7.25: Same as in Fig. 7.23 except at $z = 11$ km MSL and no vertical motions are contoured.

direction, and was now associated with the development of a significant trailing anvil. In contrast to the structure at 0000, blocking and perturbation easterly flow had unified and propagated well west of the anvil condensate (Fig. 7.23). Although the separation between the northern and southern convective components was similar to that at 0000 (Fig. 7.24), the ambient upper tropospheric storm–relative flow was no longer channeling between them (Fig. 7.22).

At 5 km MSL (Figs. 7.24, and 7.25), the rear inflow jet was also stronger and more consolidated than it was at 0000. Rear inflow now approached the entire MCS from the west and northwest, splitting into two branches as it neared the convection. The northern branch headed directly for the back edge of the convective line, while the southern branch descended beneath a region of strong southerly flow and eventually met the convection at 3.5 km MSL. Stratiform precipitation trailed behind the convective line at this level especially in the north. This region of condensate was the combination of precipitation falling from the expanding upper anvil and remnant cloud material advecting in from the now dissipated trailing southwestern convection.

The development of these MCS–scale structures was rooted to the rearward propagation of convectively generated disturbances. As the MCS came under the influence of the low level jet between 0000 and 0200, the southern storm (cell A) grew explosively, elongating into an intense, nearly continuous line. Meanwhile, the northern convective component (the original northern line) retained its intensity. During this time, upper tropospheric storm–relative easterly flow expanded westward from the convection into the environment, leaving consolidated mesoscale flow in its wake (Fig. 7.23). Anvil condensate began advecting rearward as the storm–relative front–to–rear flow became negative. Schmidt and Cotton (1990) and Pandya and Durran (1996) have demonstrated in two dimensions that this process can result from the upstream propagation of internal gravity wave energy. It can also result from the direct advection of momentum and condensate within the expanding anvil outflow. The distinction between the two can sometimes be quite subtle. In this three–dimensional case, the leading edge of one particularly strong disturbance can be seen in the 0200 UTC vertical motion field at 11 km (Fig. 7.23) as an arcing front of downward motion at the western edge of the anvil. The downward motion marked the western boundary of intense rearward–punching storm–relative u–winds at 13 km (Figs. 7.26a, and 7.27a). This particular disturbance originated from the rapidly intensifying southern convective line shortly before 0100 UTC and expanded northwestward (this evolution will be discussed in detail in the next section). It remained discernable through the rest of the simulation, even as it propagated onto grid #3.

Vertical cross sections (Figs. 7.26, and 7.27) depict several interesting aspects of this perturbation. In the south, the leading edge of the disturbance (near 103.4° W in Fig. 7.26) was marked by weak upward motion below 8 km, capped by somewhat stronger downward motion between 8 and 13 km, with a return to upward motion between 13 and 15 km. Potential temperature cross sections averaged along the line (discussed in the next section, see Fig. 7.45) showed a sharp region of lower stratospheric cooling and upper tropospheric heating which coincided with this front. In the horizontal, upper tropospheric front–to–rear and mid tropospheric rear–to–front accelerations trailed the vertical motion disturbance. This vertical kinematic and thermodynamic structure is similar to the $n2$ buoyancy bores referred to by Mapes (1993), suggesting that the disturbance was a linear internal gravity wave. As mentioned in Chapter 2, Nicholls et al. (1991), Mapes (1993), and McAnelly et al. (1997) found that the $n2$ mode was initiated by a bimodal distribution of heating in the upper troposphere and cooling in the lower troposphere. Vertical divergence and perturbation potential temperature profiles discussed later in this chapter show that this structure was present within the convection.

In the northern cross section, the vertical motion along the wave front, located at 103.6° W. in Fig. 7.27c, displayed the same $n2$-like structure as it did further south: downward motion in the upper troposphere sandwiched between upward motion in the lower troposphere and lower stratosphere. However, the trailing upper tropospheric front–to–rear and mid tropospheric rear–to–front flow existed as maxima detached from the convective towers, unlike the section further south. This is because the perturbations appear to have *advected* into the plane of the cross section from the south. Although the northern convective line remained strong between 0000 and 0200, it did not emit an intense pulse like the southern convection did. The tendency for the leading edge of the wave to propagate by advective processes, along with several other attributes discussed in the next section, suggest that

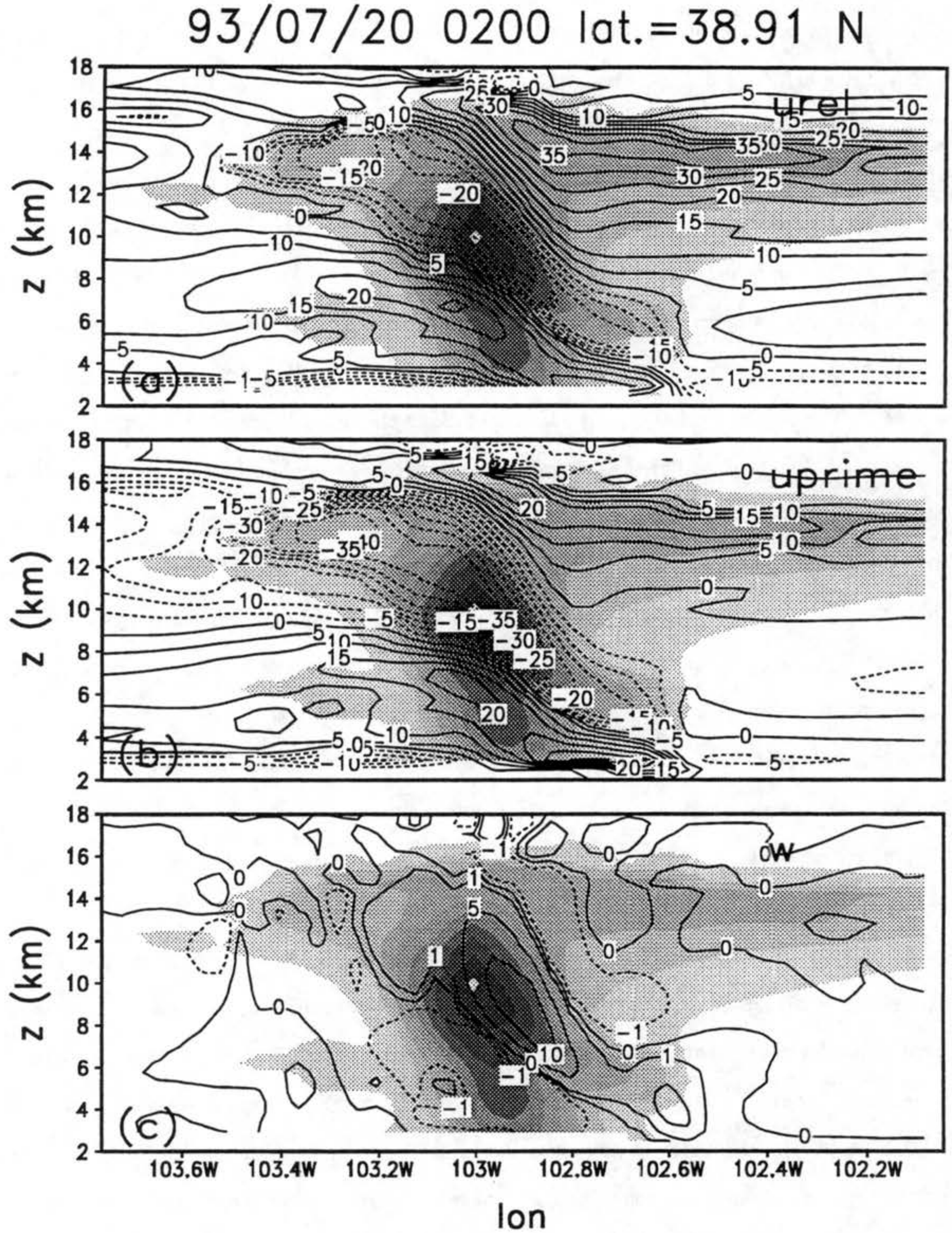

Figure 7.26: Vertical $x - z$ cross sections on grid #4 at 0200 at y = 38.91° lat. In (a), storm relative winds are contoured at 5 m s^{-1} increments. In (b), winds relative to the environmental average are contoured at 5 m s^{-1} intervals, and in (c) vertical motion is contoured at the $0, \pm1, \pm5, \pm10$, and ±15 levels. Total condensate is shaded in each panel at 0.5 g kg^{-1} increments at and above 0.5 g kg^{-1}, the 0.1 g kg^{-1} level is also shaded.

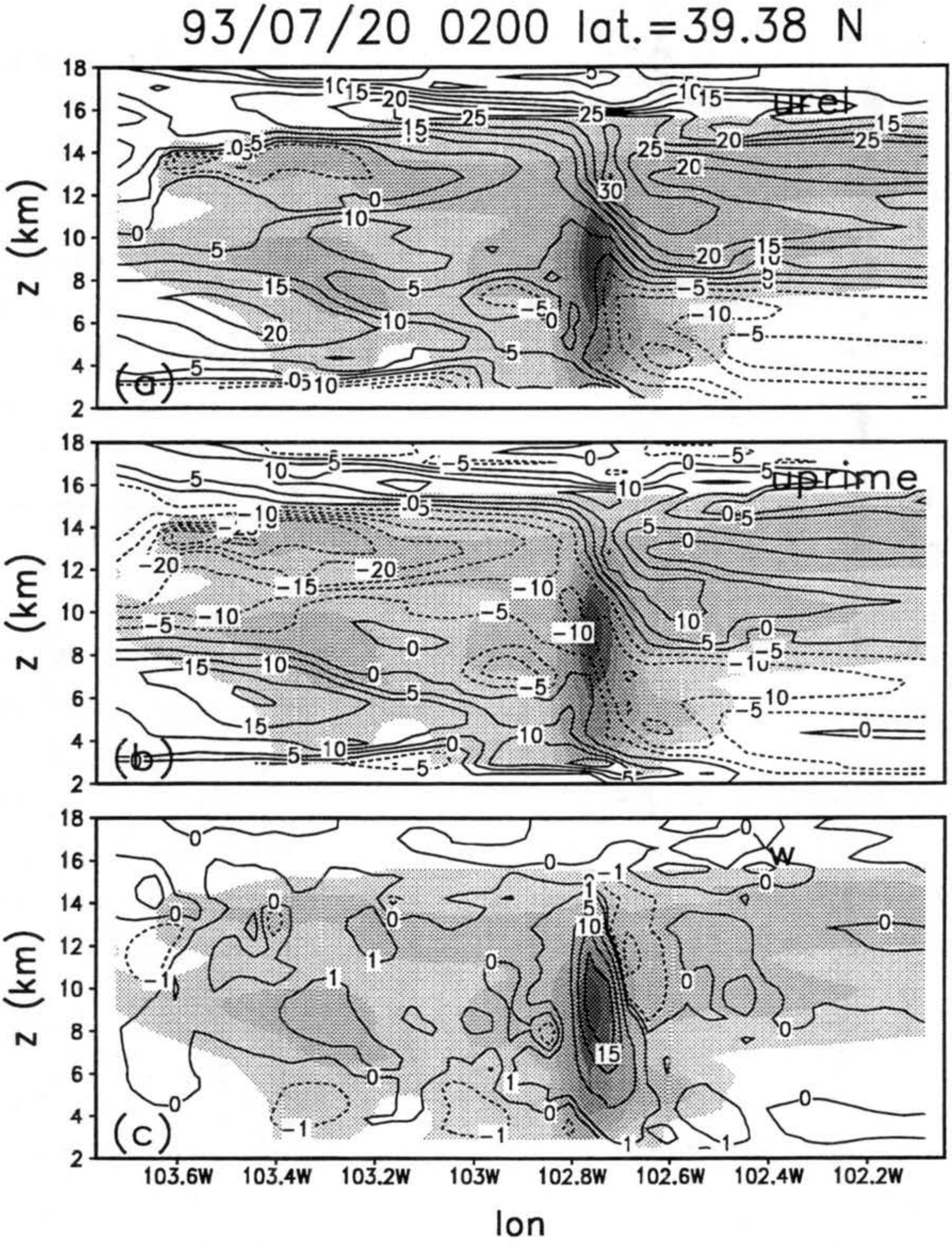

Figure 7.27: Same as Fig. 7.26 except vertical $x-z$ cross sections at $y = 39.38°$ lat.

this disturbance deviated from linear theory and was thus different from those of Nicholls et al. (1991), Mapes (1993) and McAnelly et al. (1997).

Regardless of the wave types, this case represents an example of merger between two meso–β–scale convective clusters that were pulsing out of phase. Although the dynamics are obviously quite different, the evolution is somewhat analogous to disturbances created by dropping pebbles into a pond (Houze, 1997). When a single handful of pebbles is dropped in together, the perturbations created by each pebble contribute to a larger disturbance that propagates into the far field. Disturbances generated by a closely–spaced group of individual convective cells can, in a similar way, generate a meso–β–scale environmental disturbance. Such was the case early in the MCS lifetime when it consisted of a single line of convective cells growing together along an expanding outflow boundary. Each cell contributed more or less equally to a greater, unified whole. This structure was especially apparent in the upper troposphere at 0000 (Figs. 7.20, and 7.21), when all of the small cells in the northern convective line induced a consolidated environmental perturbation, while cell A was growing as a separate entity. As cell A grew and elongated into a line over the next two hours, the individual cells within the line produced another, separate, stronger mesoscale circulation that rapidly enveloped the MCS. This is analogous to dropping a second handful of larger pebbles into the pond.

Once a large region of upper tropospheric blocking was established, other better known methods of MCS upscale growth began occurring. As stratiform precipitation became more prevalent, there was much more descent in the rear inflow (Figs. 7.26, and 7.27) compared to the elevated structure at 2200 (Fig. 7.15). Smull and Houze (1987) found that upper tropospheric heating and mid tropospheric cooling within the trailing stratiform region can cause strengthening and descent in the rear inflow jet. The transition to descending rear inflow in the southern convective line was also correlated with the development of a significant rearward tilt in the updraft. LeMone (1983) found this to be an important factor in the development of mid tropospheric low pressure and rear inflow behind the convective line. Despite the strong upper tropospheric blocking, the updrafts in the northern convective line did not lean rearward. Storm–relative velocities show that low level convective outflow was shallower and weaker to the north. Rotunno et al. (1988) point out that weaker cold pools generally lead to more erect updrafts.

This MCS was different than many others in the literature in that the strong upper tropospheric flow efficiently separated the diabatic anvil effects from the upstream adiabatic gravity wave effects. Before 0200, most of the convective condensate advected downstream, such that the rear–to–front or front–to–rear environmental perturbations behind the line were largely induced by the passage of low frequency gravity waves. Had a trailing anvil rapidly developed, the gravity wave effects would have been more difficult to isolate. In that case, the rearward propagation of front–to–rear and rear–to–front flow would have simultaneously occurred with the rearward propagation of anvil condensate. A pattern much like that was observed by Klimowski (1994).

It turns out that several wave propagation and mesoscale flow expansion events episodically occurred through the lifetime of this system. Since the simulation was three–dimensional, most of the wave fronts themselves were subtle and difficult to detect, even on the cloud resolving grid #4. As the waves expanded outward, the vertical motions at their leading edge rapidly became small compared to other atmospheric disturbances. However, as noted in Chapter 2, Bretherton and Smolarkiewicz (1989) showed that the horizontal wave numbers of these internal modes are quite small ($m >> k$ in equations 2.1 – 2.3), thus the disturbances were large in comparison to most of the convectively induced motions. This point in itself is important because the entire goal of this work is to examine how small–scale storms create a large–scale atmospheric disturbance, and the nature of these internal waves lends itself to such a process. In the next section several of these gravity wave events will be revealed by eliminating many of the small–scale perturbations through the use of horizontal and the vertical averaging.

7.4 Structure and propagation of convective internal gravity waves

7.4.1 Divergence, vertical mass flux and their relation to wave production

Throughout the simulation, convection produced waves at many different scales that propagated into the environment in all directions. However, as has already been discussed, the mesoscale environmental circulations propagated outward on a special set of wave modes

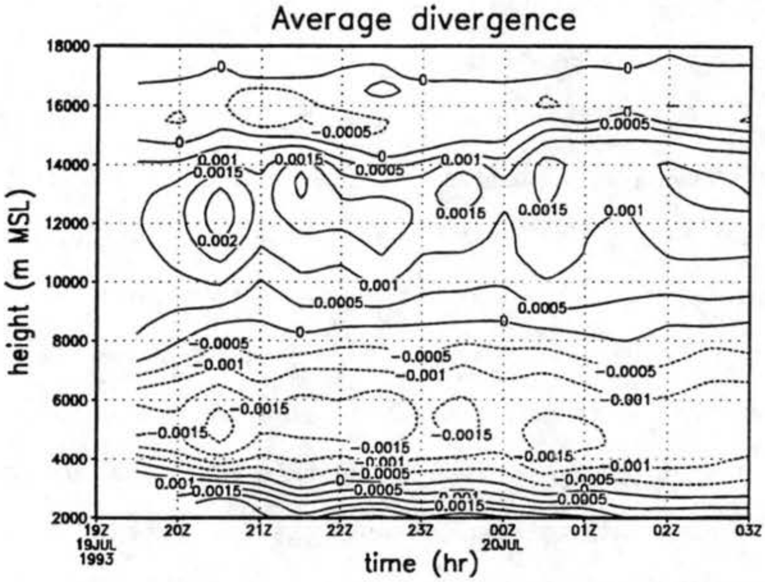

Figure 7.28: Time series of average divergence profiles for all columns with surface precipitation rates of 12.5 mm hr^{-1} or greater. Contours are every 0.0005 s^{-1}.

with very low horizontal frequencies. To review, the vertical structure of these waves is dictated by the vertical structure of the MCS latent heating, and Mapes (1993) found that the majority of the heating can be characterized by the superposition of the $n1$ and $n2$ modes (Fig. 2.1). The $n1$ mode is generally convective in nature, and is forced by deep heating through the depth of the troposphere. The divergence profile associated with this heating consists of deep lower tropospheric convergence and upper tropospheric divergence (profile d2 in Fig. 2.1). The $n2$ mode is characterized by lower tropospheric cooling and upper tropospheric heating, and is generally associated with the development of widespread precipitation. Mapes (1993) contended that the development of an elevated maximum in MCS–average divergence, like the profile d1 in Fig. 2.1, was characteristic of the superposition of the $n1$ and $n2$ modes.

It is important to realize that even at low frequencies, atmospheric convection produces a continuous spectrum of wave energy. Nicholls et al. (1991) and Mapes (1993) and investigated wave production from idealized analytic heating functions in a resting atmosphere of constant stability, and none of those constraints was placed on this simulation. Although certain modes will be dominant, variations in the convective forcing and the atmospheric stability and shear can cause considerable distortion of the wave fronts. To determine the

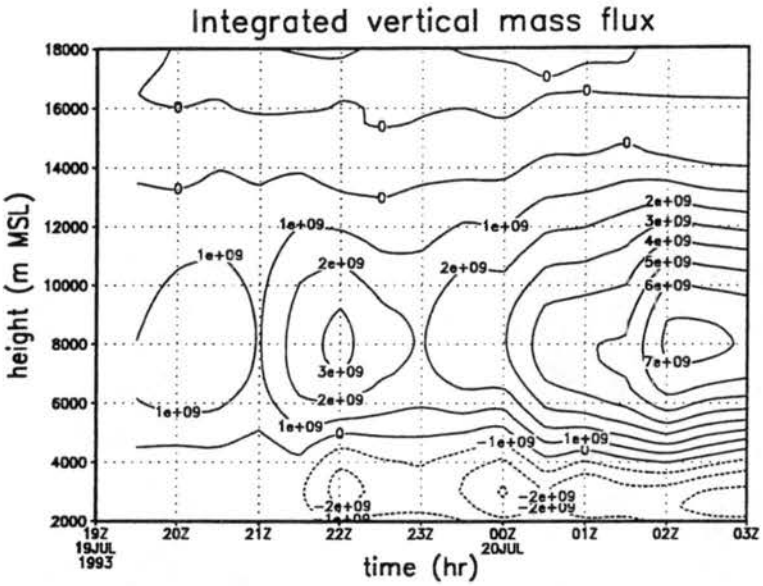

Figure 7.29: Time series of areally integrated vertical mass flux profiles for all columns with surface precipitation rates of 12.5 mm hr^{-1} or greater. Contours are every 1e+9 kg s^{-1}.

dominant modes in this system, time series of average divergence (Fig. 7.28) and areally integrated vertical mass flux at each level (Fig. 7.29) were derived from the model results. To isolate the most active portions of the MCS, the profiles were calculated for all columns experiencing surface precipitation greater than 12.5 mm hr^{-1}. The results show a divergence profile that remained quite consistent through the entire simulation. Little change in intensity or structure occurred, even through the convective reorganization between 0000 and 0200. As soon as the first significant precipitation occurred at 1930 an elevated convergence maximum developed at 5 km, indicative of the strong presence of both the $n1$ and $n2$ modes. This is somewhat surprising since this profile is often found in mature MCC–size systems with extensive stratiform precipitation (e.g. Rutledge et al. 1988; Alexander, 1995). However, the pattern does compare well with the Doppler observed values (Fig. 5.29). The magnitude of the lower tropospheric convergence in the clear air beneath the updrafts was underestimated in both the radar and model–derived statistics due to the bias toward precipitating areas. For additional insight, average divergence profiles were taken over all of grid #4. These did contain convergence through the entire troposphere below 8 km, but the maximum values were still located near 6 km, again indicating forcing from both the $n1$ and $n2$ modes.

The temporal consistency of the divergence field means that the MCS–average updraft (and downdraft) intensities did not change much either[3]. System intensity was instead modulated by the areal coverage of intense convective cells as indicated by the vertical mass flux (Fig. 7.29). The temporal evolution of the mass flux field between 2200 and 0000 is very consistent with the Doppler observations (Fig. 5.30), despite the shortcomings in the simulation of cell A. Both the modeled and the observed systems displayed a mass flux minimum near 2300 UTC between 6 and 9 km MSL. Even the numerical values were similar, although the modeled system reintensification occurred about an hour later than the observed system. Simulated mass flux and volumetric rain rates (Fig. 6.7) also correlate well, with large rain–rate increases from 2100 to 2200 and 0000 to 0200 corresponding to increased mass flux at those times.

Nicholls et al. (1991) and Pandya and Durran (1996) found that the strength of the leading edge vertical motion fields in the internal gravity waves was proportional to the time derivative of the convective heating. Similarly, the most significant wave events in this simulation were found shortly after large changes in convective vertical mass flux. Although convection was constantly pulsating, large coherent wave fronts were produced during the intervals when a large percentage of the convective cells intensified together. Three major wave events stood out during the simulated system lifetime, with the waves from each successive event getting stronger as the MCS areal coverage increased. The first event occurred shortly after 1900 as convection first developed in the relatively quiescent atmosphere. Although the convective mass flux and thus the compensating motions were rather weak, the lack of preexisting "noise" made this an ideal time to observe the initial expansion of the convectively induced perturbation flow. The second event occurred between 2100 and 2200 when the north–south convective line rapidly developed in the DCVZ. The sudden appearance of several strong convective cells resulted in rapid heating and mass flux increases that triggered several detectable waves. The third event, which was discussed in

[3] Maximum storm updrafts of about 40 m s^{-1} occurred before 2130 when convection was inflow–dominated in the lower troposphere. Once convection became outflow–dominated (after 2130), maximum updrafts decreased and leveled off to about 25 m s^{-1}.

the previous section, initiated shortly after 0100 as the southern convection intensified in the low level jet. This disturbance was unique in that it was strong enough to reverse the upper tropospheric storm relative flow, defining a large, oval cold cloud shield as it did so. All three of these events and their effects on the environment are discussed in detail below.

7.4.2 The first event: Convective initiation

The first deep low frequency waves appeared shortly after the convective storms developed in the mountains. Vertical motions averaged between 5 and 10 km MSL (Fig. 7.30) depict the initial disturbance as it broke away from the line of growing cells. In cross sections averaged along the line (Fig. 7.32), the leading edge of the wave was heralded by deep downward motion which propagated in both the upstream (west) and downstream (east) directions. This structure is very similar to the $n1$ modes discussed by Nicholls et al. (1991) and Pandya et al. (1992). Phase speeds were also typical of the $n1$ internal mode, with 11 m s^{-1} and 48 m s^{-1} in the upstream and downstream directions respectively, for a resultant average non–Doppler shifted velocity of 29.5 m s^{-1}.

Although the wave fronts on both sides of the line originated from the same cluster of storms, the time evolution of their vertical structures was considerably different. In the upstream direction, the wave remained a single coherent pulse of downward motion (Fig. 7.33). By 1942 (Fig. 7.34), a train of deep pulses followed the initial wave out the back of the line. As the wave fronts passed, they induced a westward–directed upper tropospheric, and eastward–directed lower tropospheric horizontal perturbation flow in their wake (Figs. 7.31, 7.32, 7.33, and 7.34). By 1942, these perturbations had extended well west of the erect convective towers. As these waves propagated rearward, the environment also warmed over a deep layer behind the storm. These responses were very similar to those simulated by Schmidt and Cotton (1990) in two dimensions.

In the downstream direction, the initial wave became elongated in the horizontal and weakened as it propagated eastward. At 1924, the initial downward pulse was followed by a nearly equal branch of upward motion, which propagated outward at roughly the same speed. The resultant perturbations on the horizontal flow resembled the roll–like circulations obtained by Nicholls et al. (1991) with a temporally finite heat source. The upper

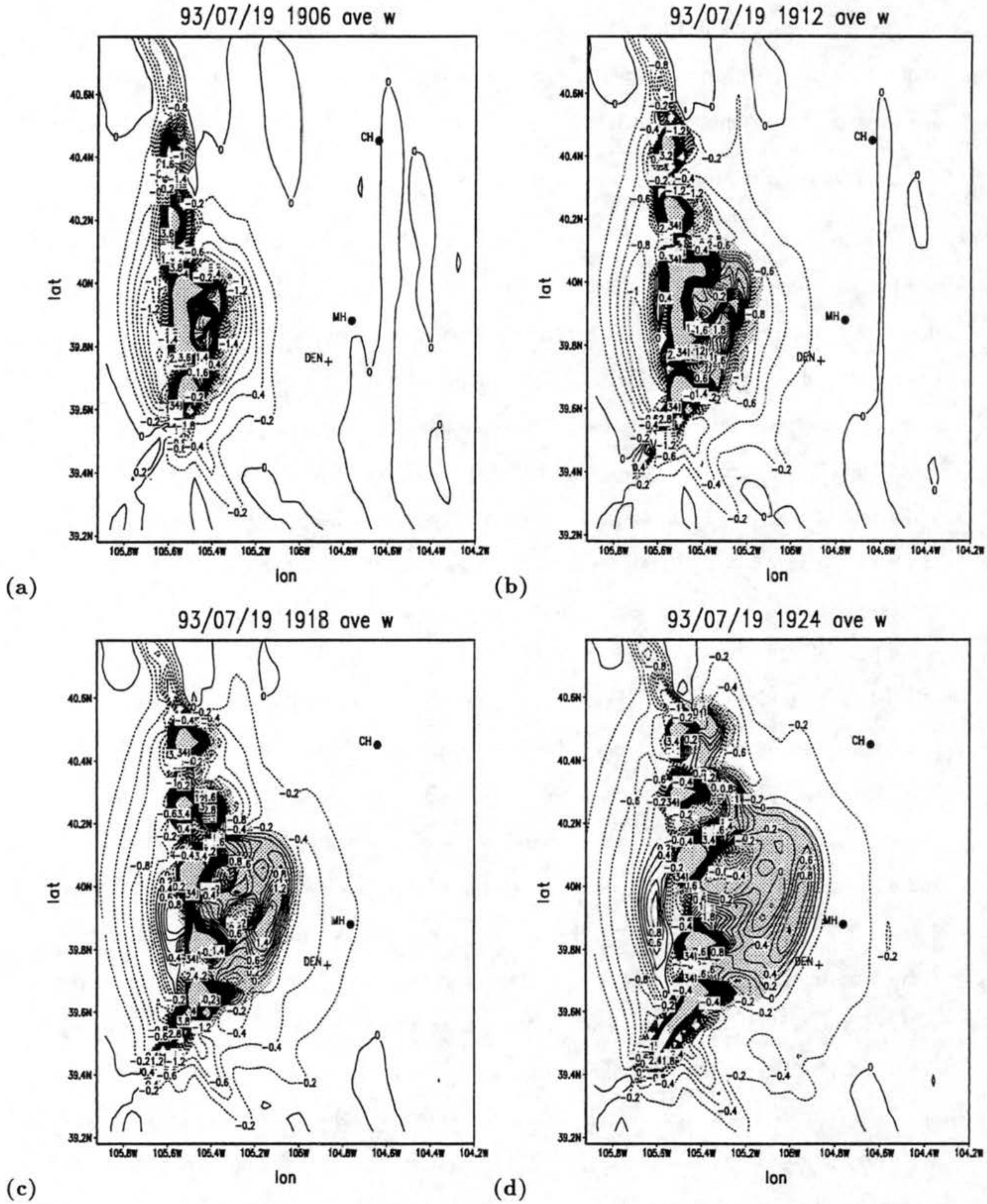

Figure 7.30: Vertically–averaged vertical motion between z=5 and z=10 km MSL on grid #4 at (a) 1906, (b) 1912, (c) 1918, and (d) 1924 UTC. The contour interval is 0.2 m s^{-1} between ± 4 m s^{-1}, and condensate greater than 0.1 g kg^{-1} at 10 km is shaded.

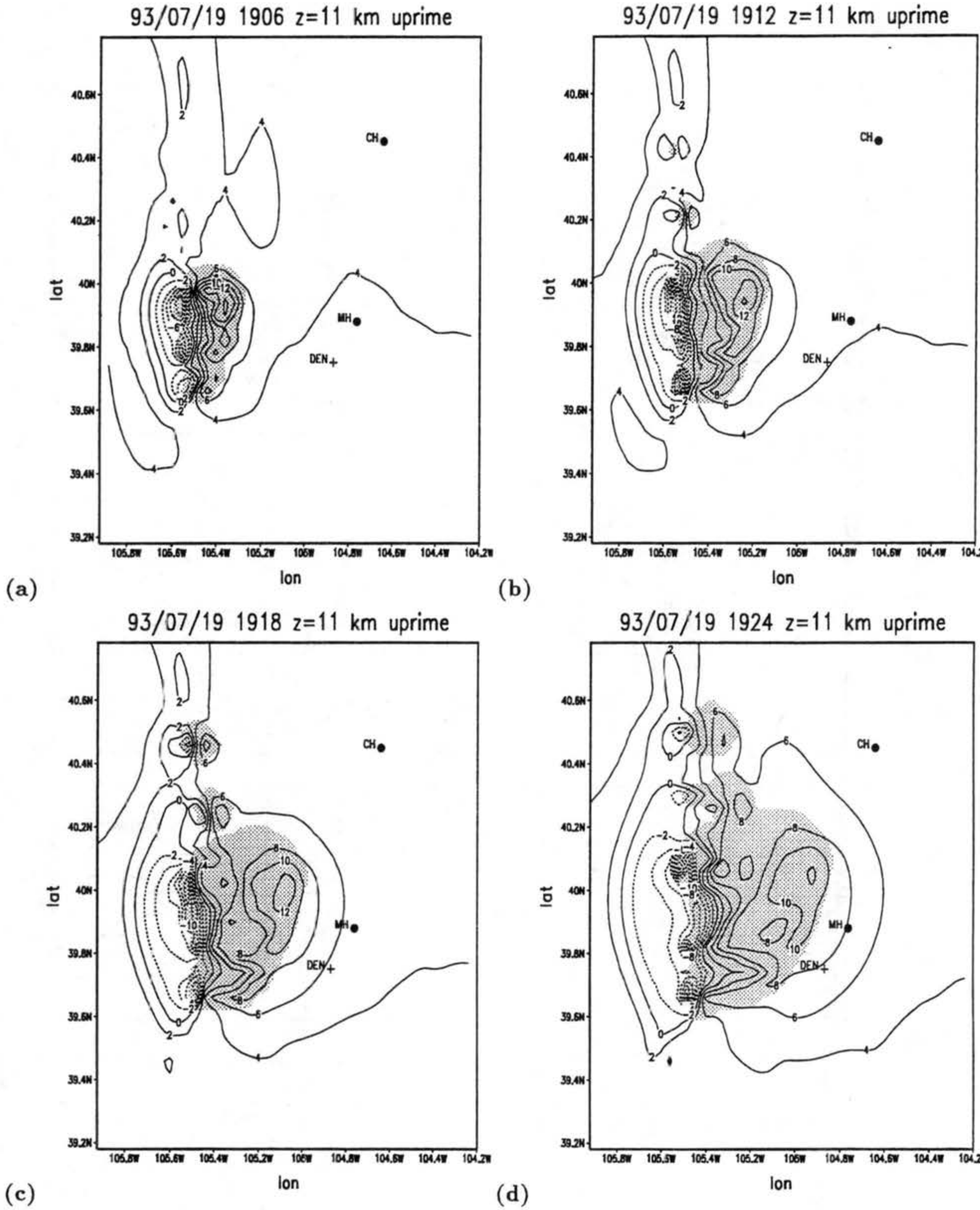

Figure 7.31: Environment–relative u winds at z=11 km MSL on grid #4 at (a) 1906, (b) 1912, (c) 1918, and (d) 1924 UTC. The contour interval is 2 m s^{-1}, and condensate greater than 0.1 g kg^{-1} at 11 km is shaded.

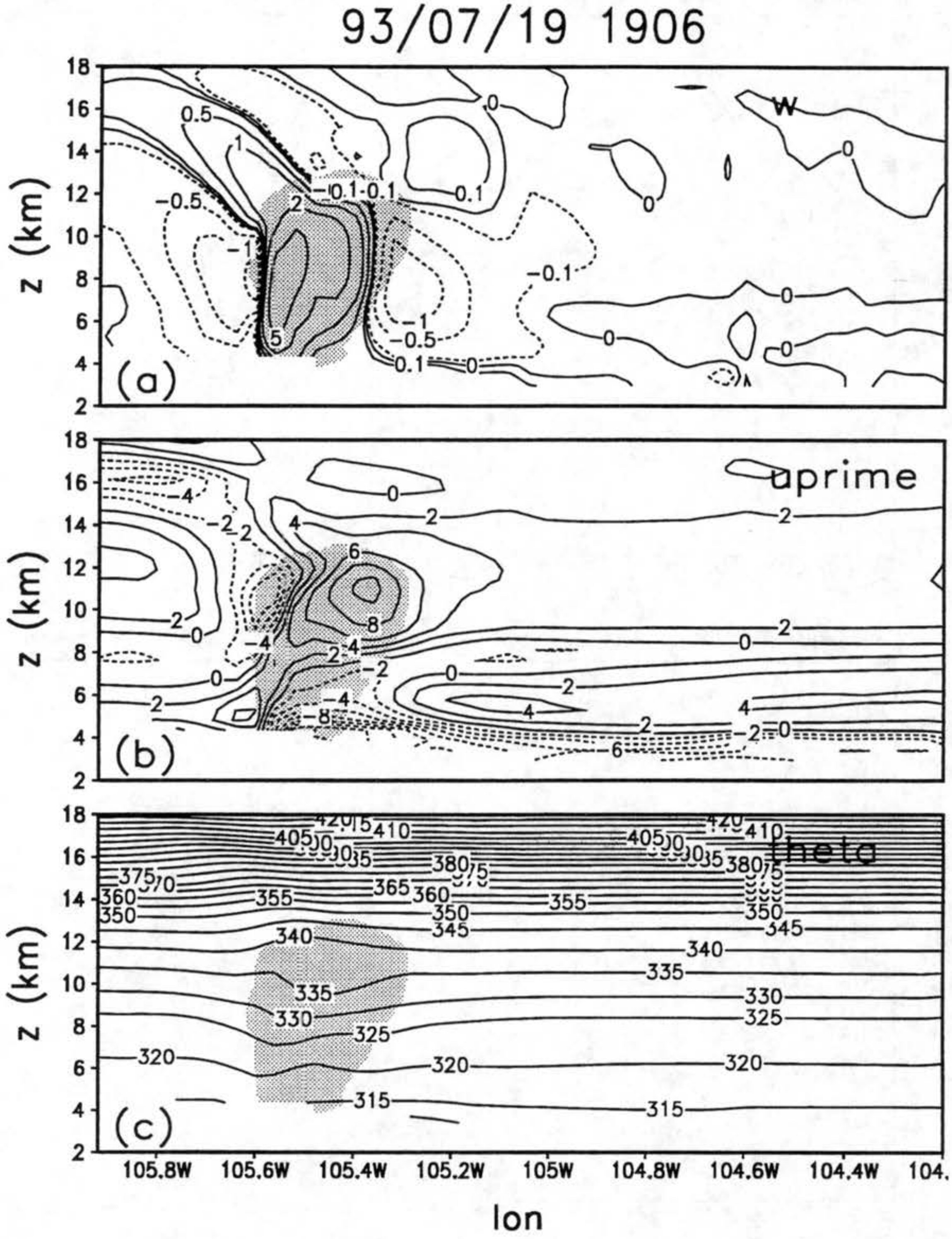

Figure 7.32: Vertical $x - z$ cross sections on grid #4 at 1906 derived by meridionally averaging (a) vertical motion, (b) perturbation flow (relative to the grid #2 environmental mean sounding), and (c) potential temperature. The averaging interval was from 39.7 to 40.0° lat. Averaged condensate greater than 0.1 g kg^{-1} is shaded.

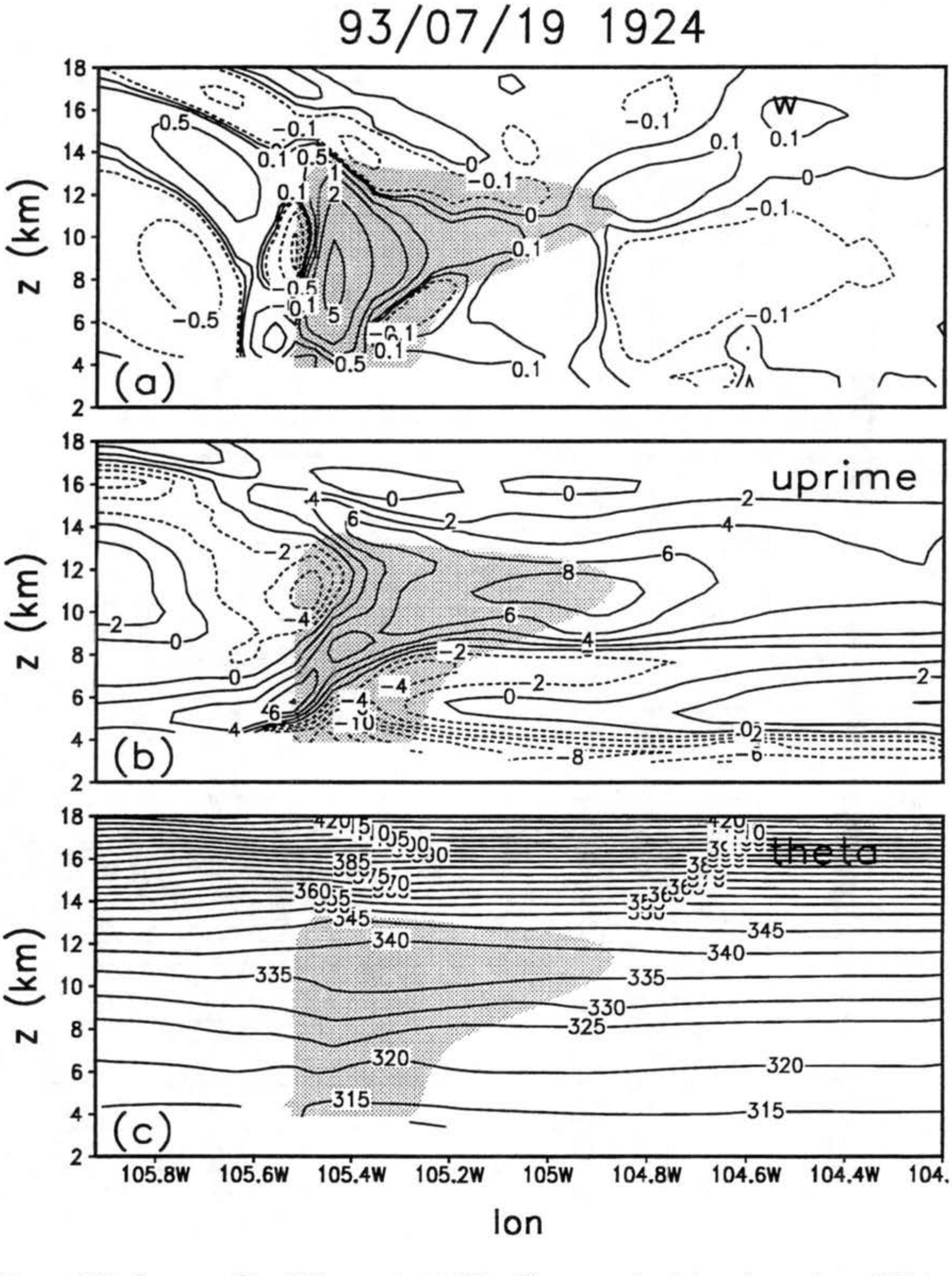

Figure 7.33: Same as Fig. 7.32 except at 1924. The averaging interval was from 39.6 to 40.2° lat.

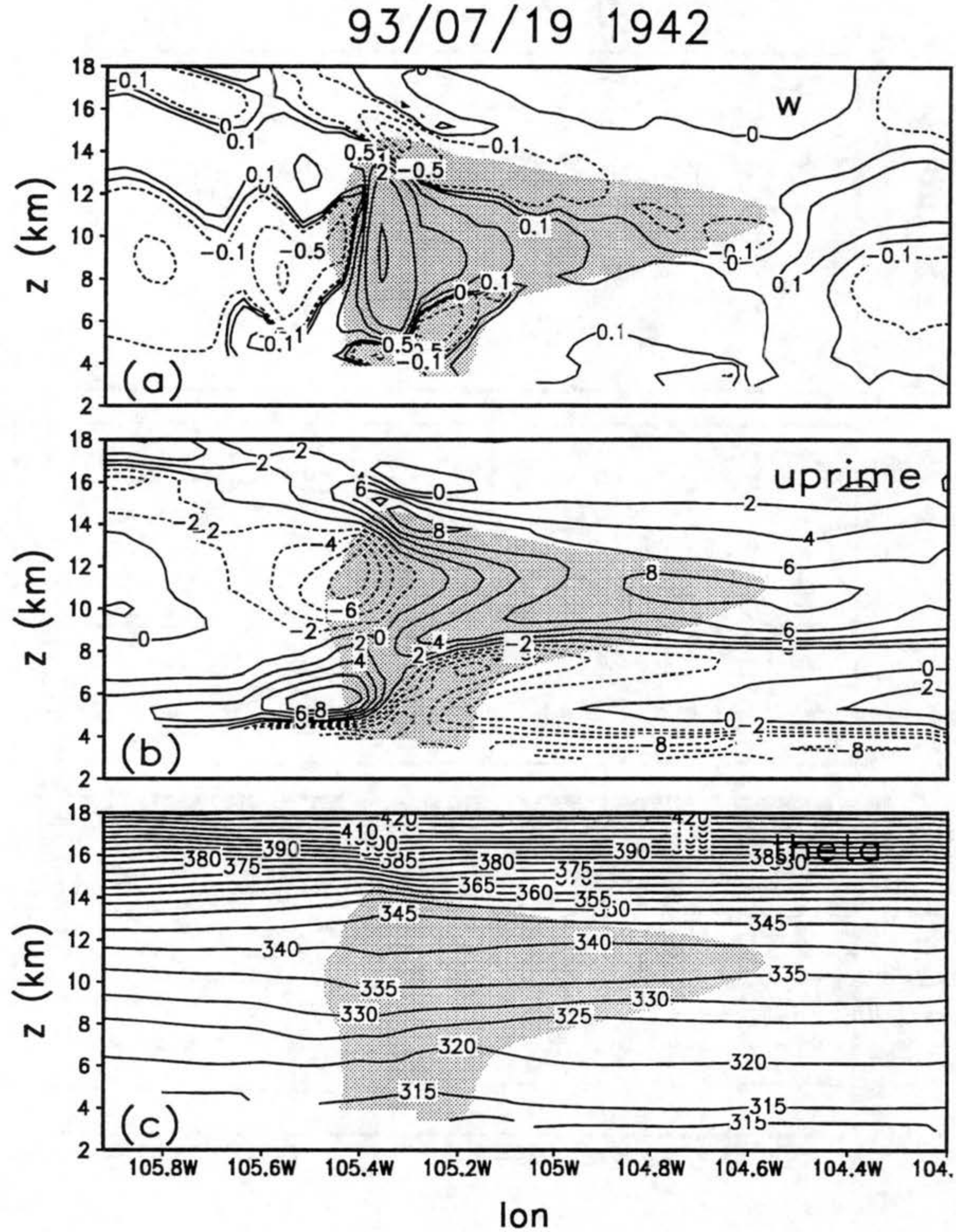

Figure 7.34: Same as Fig. 7.32 except at 1942. The averaging interval was from 39.6 to 40.2° lat.

tropospheric maximum perturbation flow rapidly outran the leading anvil and propagated eastward as a wave–induced surge of westerly momentum (Fig. 7.31). A mid tropospheric region of negative perturbation flow directed towards the storm also developed, but it remained weak and did not propagate far before dissipating. The strength of this flow may have been underestimated due to contamination from the shallow mountain–plains solenoid. The solenoid was not storm–induced, but it was still localized enough to appear as a perturbation with respect to the averaged winds on grid #2. Between 1906 and 1942, the solenoid was generally east of 102.5° W., and consisted of upslope easterlies below 5 km and downslope westerlies between 5 and 7.5 km.

The most important difference between the upstream and downstream responses was the distinct lack of eastward propagating gravity wave energy after the initial pulse. Although several different superimposed modes were apparent in the vertical motions to the west of the convection by 1942 (Fig. 7.34), eastern side vertical motions were quite smooth, and mostly the result of local diabatic forcing. For example, the downward motion near 6 km just east of the main updraft was associated with strong cooling within the precipitation and at the lower edge of the anvil. Perturbation horizontal velocities were responding to this by converging toward the cooling from the east, in a way not dissimilar to the rear inflow described by Smull and Houze (1987).

The wave propagation asymmetry continued through the rest of the simulation and was responsible for the almost exclusive development of perturbation flow on the western side of the system. Schmidt and Cotton (1990) noted a similar feature, in that the strongest gravity waves in their system occurred on the trailing[4] side of the convective line. Idealized experiments indicate that these asymmetries are produced when a wave emitter, such as a convective cloud, is oriented at an angle with respect to the vertical. Pandya and Durran (1996) found that idealized convective heat sources that leaned with height produced the strongest low frequency gravity waves in the direction of tilt. Thus, if the heat source leaned toward the west, the strongest gravity waves were found to the west of the heat source. Some

---

[4]with respect to the motion of the line

eastward propagating energy still existed, but it was much weaker. In a similar numerical experiment Fovell et al. (1992) found that waves generated by an oscillating cylindrical source experienced the same effect when the oscillator was tilted out of the vertical. The fact that this effect occurs for such different emitters suggests that leaning convection will generate more gravity wave energy overall in the direction of tilt. The orientation of the convective heating in the case studied herein was difficult to diagnose since the updrafts were almost erect, and most of the anvil condensate advected eastward in the strong upper tropospheric shear. However, new updrafts frequently built on the eastern side of existing convection (Fig. 7.15c), and this may have created an equivalent tilt to the heat source not visible in any one shapshot.

One could also argue that ambient vertical shear was distorting the downstream propagating waves and hiding their effects. However this is not likely since one downstream gravity wave pulse was simulated. Its roll–like nature indicates that the first convective cells generated symmetric disturbances, but that all subsequent convection developed in such a way that downstream gravity waves were no longer excited. To test this, a simple experiment, similar to those of Pandya and Durran (1996), was conducted with an erect heat source in two dimensions. The basic formulation for the heat source was similar to Nicholls et al. (1991) in that both the $n1$ and $n2$ modes were included. Quantitatively, the heat source was defined as:

$$Q_z = Q_0[sin(\frac{\pi z}{H}) - sin(\frac{2\pi z}{H})], \tag{7.1}$$

where Q_0 and H were set to 100 K hr^{-1} and 10 km respectively to simulate an intense convective cell. The horizontally homogeneous environment was defined by a sounding taken from the three–dimensional simulation about 100 km ahead of the developing MCS. The homogeneous simulation was run for two hours, with the heating slowly increasing to its maximum values over the first half hour. Although the wave fronts were considerably distorted by the shear, the perturbation u–velocity field after two hours (Fig. 7.35) clearly reflected strong gravity wave propagation in both directions. Although it was a simple test, it indicates that at least in two dimensions, upper tropospheric shear in and of itself does not prohibit the downshear gravity wave propagation.

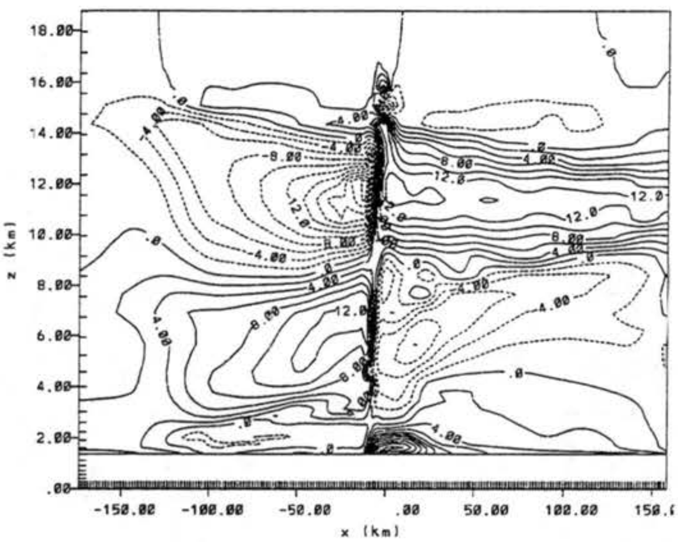

Figure 7.35: Horizontal velocity perturbations from the initial state at two hours in the idealized two–dimensional simulation. The stationary heat source was centered at $x = -8$ km. With respect to the initialized sounding winds, west is considered to be at the left side of the domain. The contour interval is 2 m s^{-1}.

7.4.3 The second event: Intensification in the DCVZ

Convection continued to produce gravity wave perturbations as it moved eastward out of the mountains as a cluster of storms (Fig. 6.6). However, the leading edge pulses were weak until the line rapidly grew northward along the DCVZ. After 2100, several rearward–propagating deep tropospheric waves were excited, consisting of both upward and downward motions (Figs. 7.36, 7.37, 7.38, 7.39, and 7.40). At least three coherent pulses can be identified in the vertical motion fields averaged between 5–10 km (Fig. 7.36). These wave fronts were oriented approximately north–south and at 2200 were located from west–to–east at 105.3, 105, and 104.7 west longitude. With an average upwind phase speed of 17 m s^{-1}, their westward propagation was faster than the waves emitted by the initial convection. However, since no downstream modes existed, average velocities without the Doppler shift could not be estimated. The line averaged vertical cross sections (Figs. 7.38, 7.39, and 7.40) indicate that this convection was about 2 km deeper than the initial mountain–generated storms, which would support a faster absolute wave propagation speed. Both the vertical and horizontal perturbation velocities were also considerably stronger after 2100 than they were at 1942, which indicates that the increased mass flux was resulting in stronger gravity wave responses.

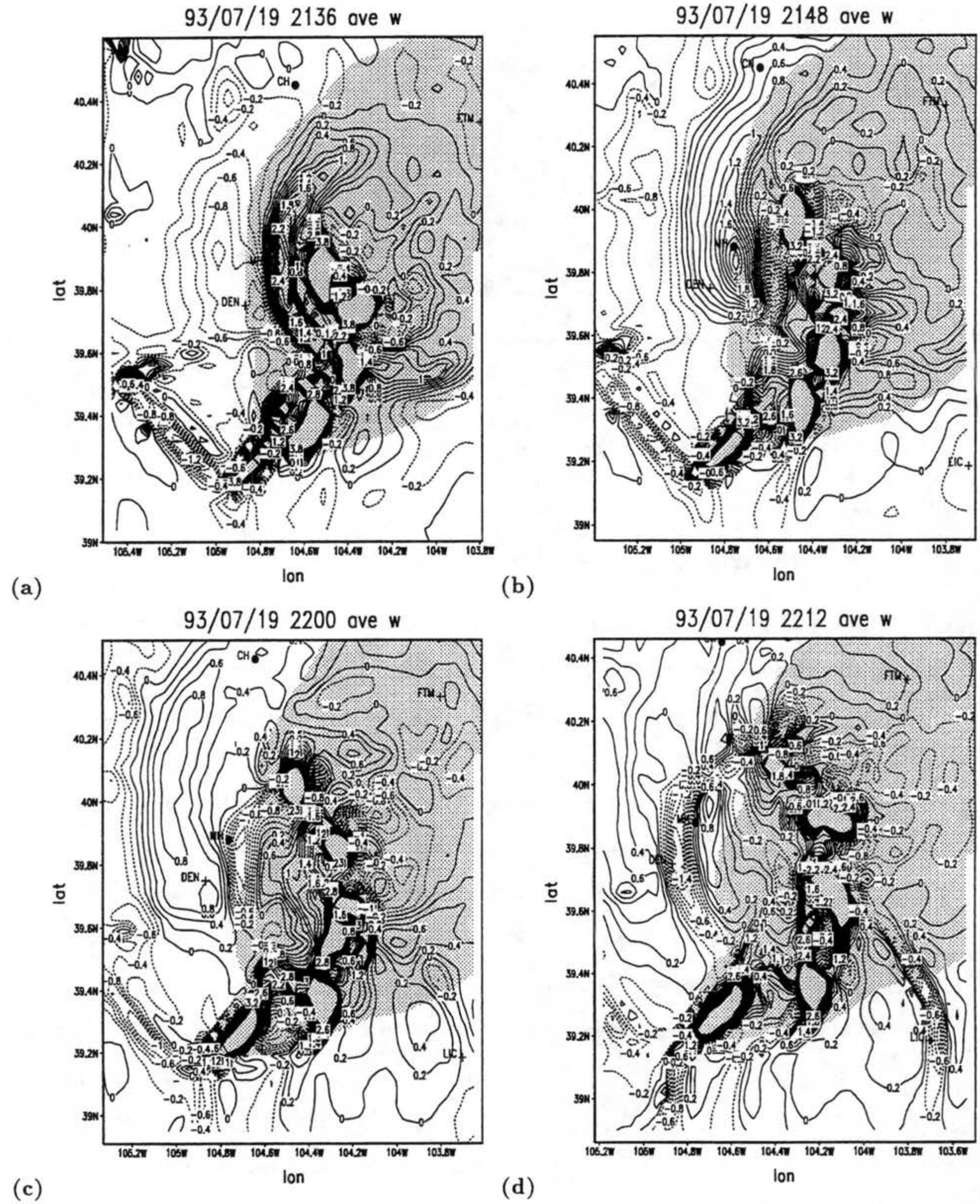

Figure 7.36: Vertically–averaged vertical motion between z=5 and z=10 km MSL on grid #4 at (a) 2136, (b) 2148, (c) 2200, and (d) 2212 UTC. The contour interval is 0.2 m s^{-1} between $\pm$4 m s^{-1}, and condensate greater than 0.1 g kg^{-1} at 10 km is shaded.

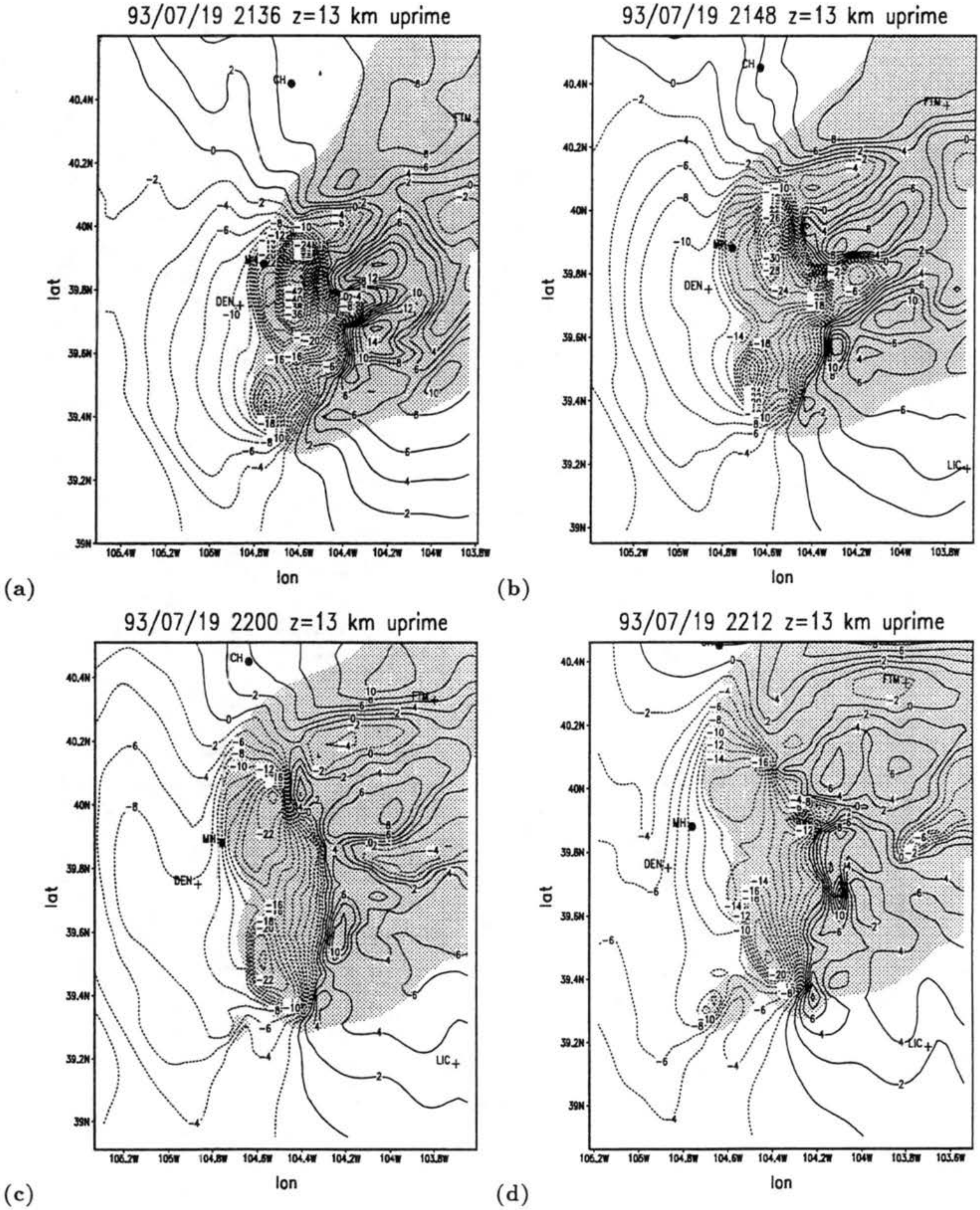

Figure 7.37: Environment–relative u winds at z=13 km MSL on grid #4 at (a) 2136, (b) 2148, (c) 2200, and (d) 2212 UTC. The contour interval is 2 m s^{-1}, and condensate greater than 0.1 g kg^{-1} is shaded.

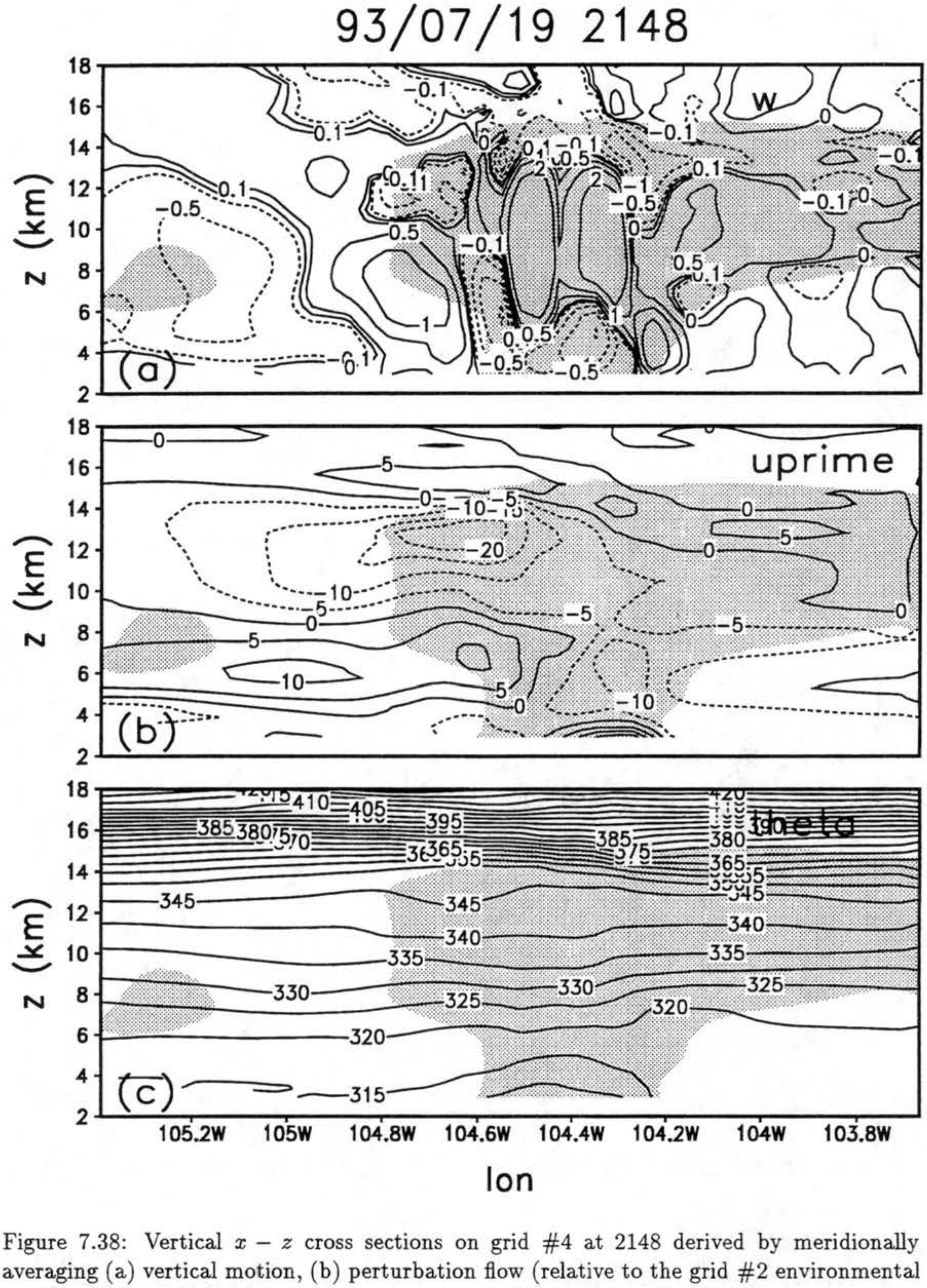

Figure 7.38: Vertical $x - z$ cross sections on grid #4 at 2148 derived by meridionally averaging (a) vertical motion, (b) perturbation flow (relative to the grid #2 environmental mean sounding), and (c) potential temperature. The averaging interval was from 39.5 to 40.1° lat. The averaged condensate greater than 0.1 g kg^{-1} is shaded.

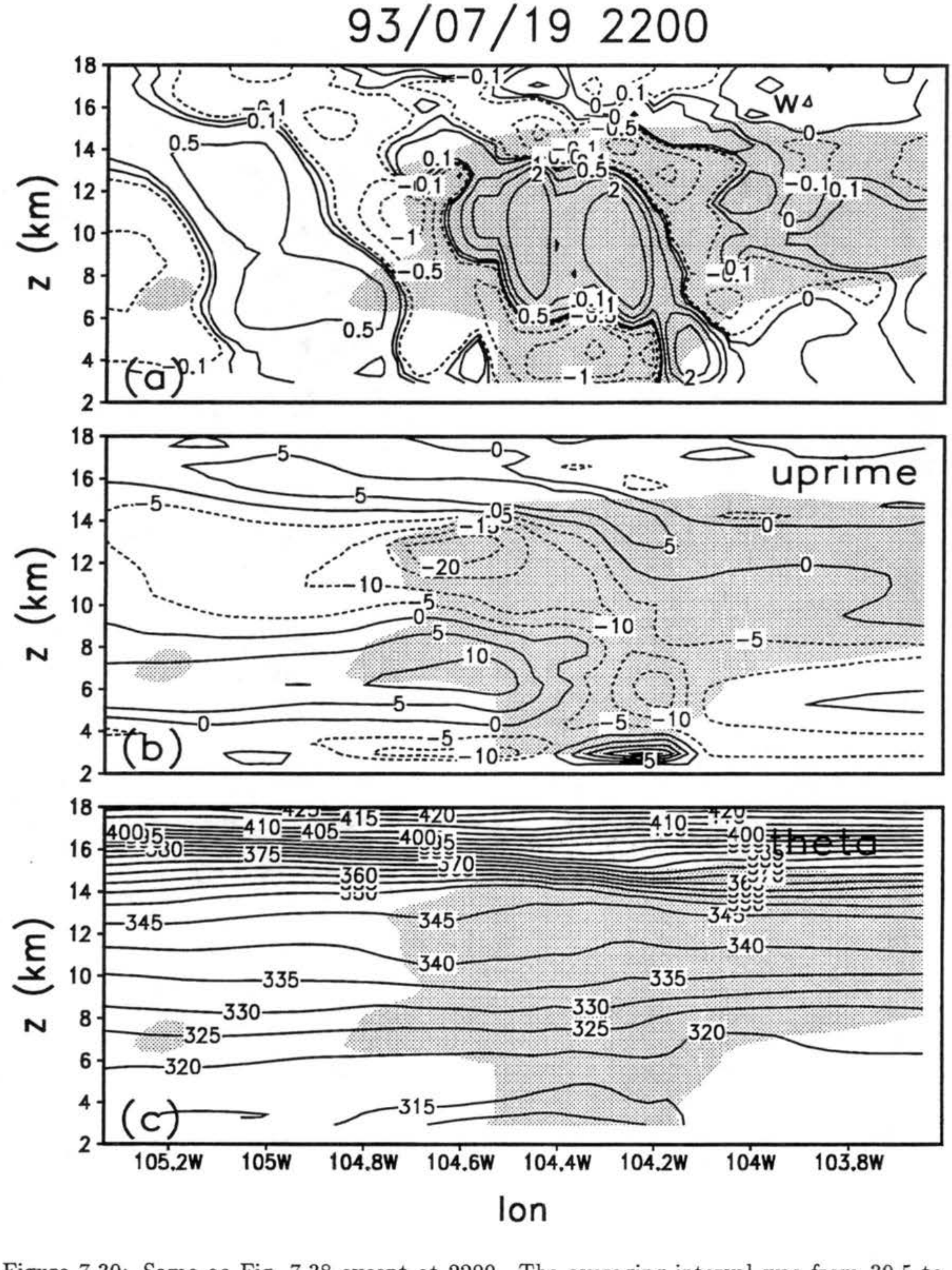

Figure 7.39: Same as Fig. 7.38 except at 2200. The averaging interval was from 39.5 to 40.1° lat.

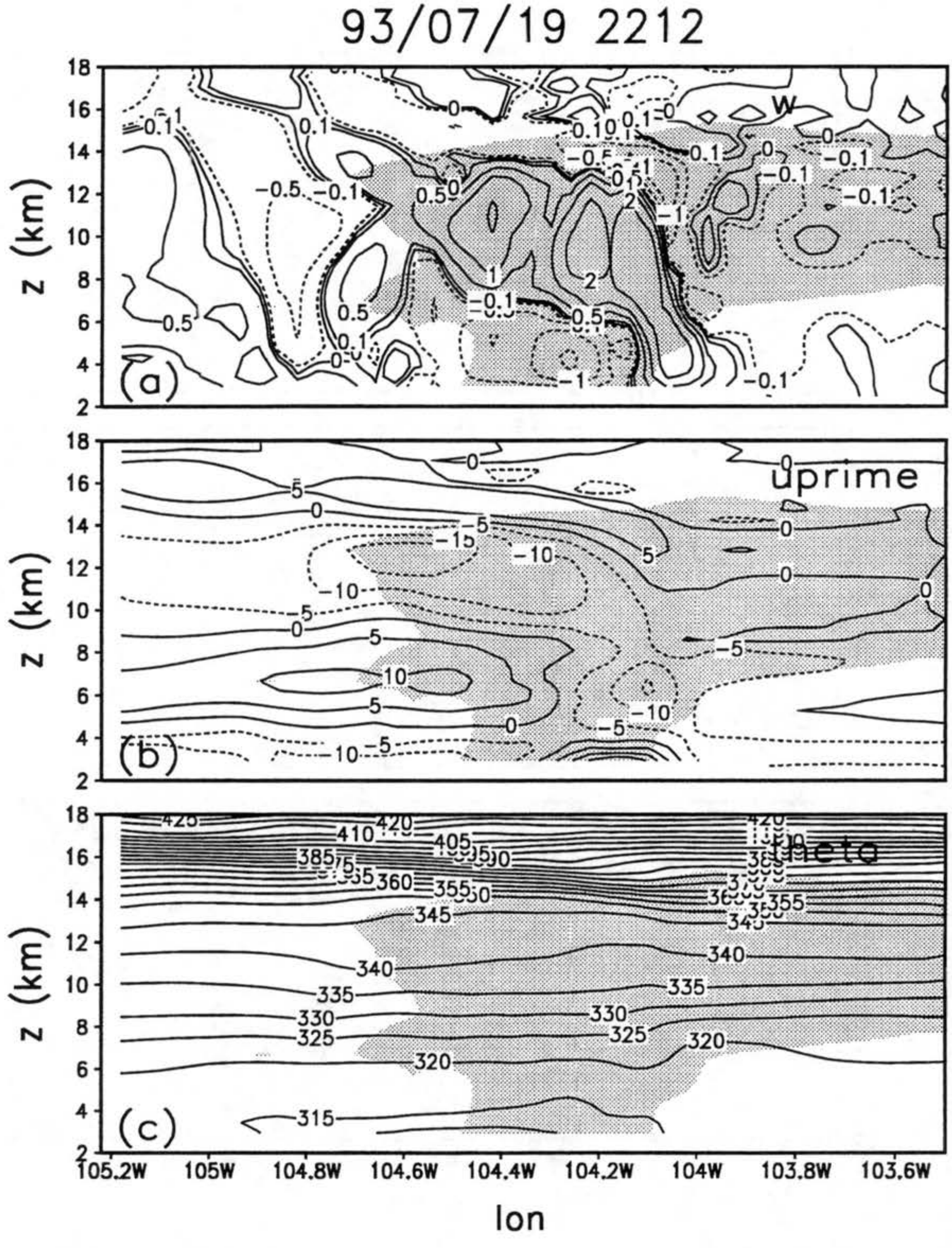

Figure 7.40: Same as Fig. 7.38 except at 2212. The averaging interval was from 39.5 to 40.2° lat.

The asymmetries in wave action on either side of the line continued as downstream vertical motions were not nearly as wave–like on the large scale, although numerous small–scale ripples existed[5]. Motions east of the convective line continued to be dominated by the microphysics in the anvil, with downward motion and elevated inflow in a region of cooling along the lower edge of the condensate. Note the upward bulging potential temperatures near 6 km in the cross sections.

All three of the deep tropospheric wave fronts observed between 2136 and 2212 were emitted from cells within the newly formed portion of the convective line north of 39.5 lat. Each individual pulse appeared during times of intense cell growth or decay, with downward and upward branches emanating from strengthening and weakening storms respectively. The strong upward branch which appeared shortly before 2136 (Fig. 7.36a), for example, was initiated by a decaying cell at the northern end of the line. As this and the other waves expanded westward, vertical motions along their leading edges rapidly broadened and weakened.

Perturbation horizontal flow at all levels behind the line (Figs. 7.37–7.40) was affected by the passage of each wave front. Downward branches increased the upper tropospheric front–to–rear and mid tropospheric rear–to–front perturbations, while the upward branch decreased these tendencies. This resulted in rearward propagating pulses in the front–to–rear and rear–to–front flows, not unlike that observed by Klimowski (1994). Although the vertical motion fields appeared to be dominated by the $n1$ mode, the time varying heights of the maxima and minima within each pulse indicates that several modes of different speeds were superimposed upon one another. Horizontal winds, which respond to the integrated net wave forcing, also indicated the presence of higher order ($\geq n2$) energy. The elevated rear inflow jet, for example, is intrinsically $n2$ in structure. Over time, the superposition of all of these waves emanating from storms along the line resulted in the strongest net concentration of wave activity immediately upstream of the line center. It will be shown later that this

---

[5]The arcing region of downward motion just southeast of the line at 2212 (Fig. 7.36d) was associated with the developing boundary layer convergence zone, and was not a convectively–induced gravity wave.

simple geometry concentrated the resultant thermal and momentum perturbations over a very specific area.

7.4.4 The third event: Intensification in the low level jet

As the southern storms in the leading convective line intensified, a particularly intense disturbance expanded outward from the convection, rapidly engulfing the entire system in a sharply defined oval cold cloud shield (Figs. 7.41–7.45). This process was independent of the eastward advecting remnants of the trailing southwestern convection (Figs. 7.41a, b, and 7.42a, b), which by 0200 had either merged with the MCS or advected eastward (Figs. 6.6e, f, 7.41c, d, and 7.42c, d). The simulated rapid growth was similar to the blossoming of the cold cloud tops observed on satellite shortly before 0100 (Fig. 4.7). Since these well defined cloud shields often distinguish MCCs from weaker convective clusters (Maddox, 1983; Velasco and Fritsch, 1987), understanding their expansion into the environment is quite important. This particular disturbance was unique in comparison to all of the low frequency gravity waves because, as suggested in the last section, its intensity, structure and propagation characteristics indicate that it may have been nonlinear.

The distinction between linear and nonlinear disturbances is subtle, but important. Gravity waves are generally linear in that they do not directly advect heat and momentum into the surrounding environment. Instead, the heat and momentum perturbations are *induced* in the environment away from the convective cells by the passage of the wave fronts. Consequently, convectively generated energy rapidly escapes into the surroundings at gravity wave speeds. Quantitatively, the anelastic equations (neglecting rotational and turbulent effects) linearized about a base–state of constant zonal flow are:

Equations of motion:

$$(\frac{\partial}{\partial t} + \overline{\mathbf{V}}_H \cdot \nabla_H)(u' + v') + \frac{1}{\rho_0}\nabla_H p' = 0 \tag{7.2}$$

$$(\frac{\partial}{\partial t} + \overline{\mathbf{V}}_{\mathbf{H}} \cdot \nabla_H)w' + \frac{1}{\rho_0}\frac{\partial p'}{\partial z} - \frac{\theta'}{\overline{\theta}}g = 0 \tag{7.3}$$

Mass continuity equation:

$$\overline{\mathbf{V}} \cdot \nabla\rho' + \rho_0 \nabla \cdot \mathbf{V}' = 0 \tag{7.4}$$

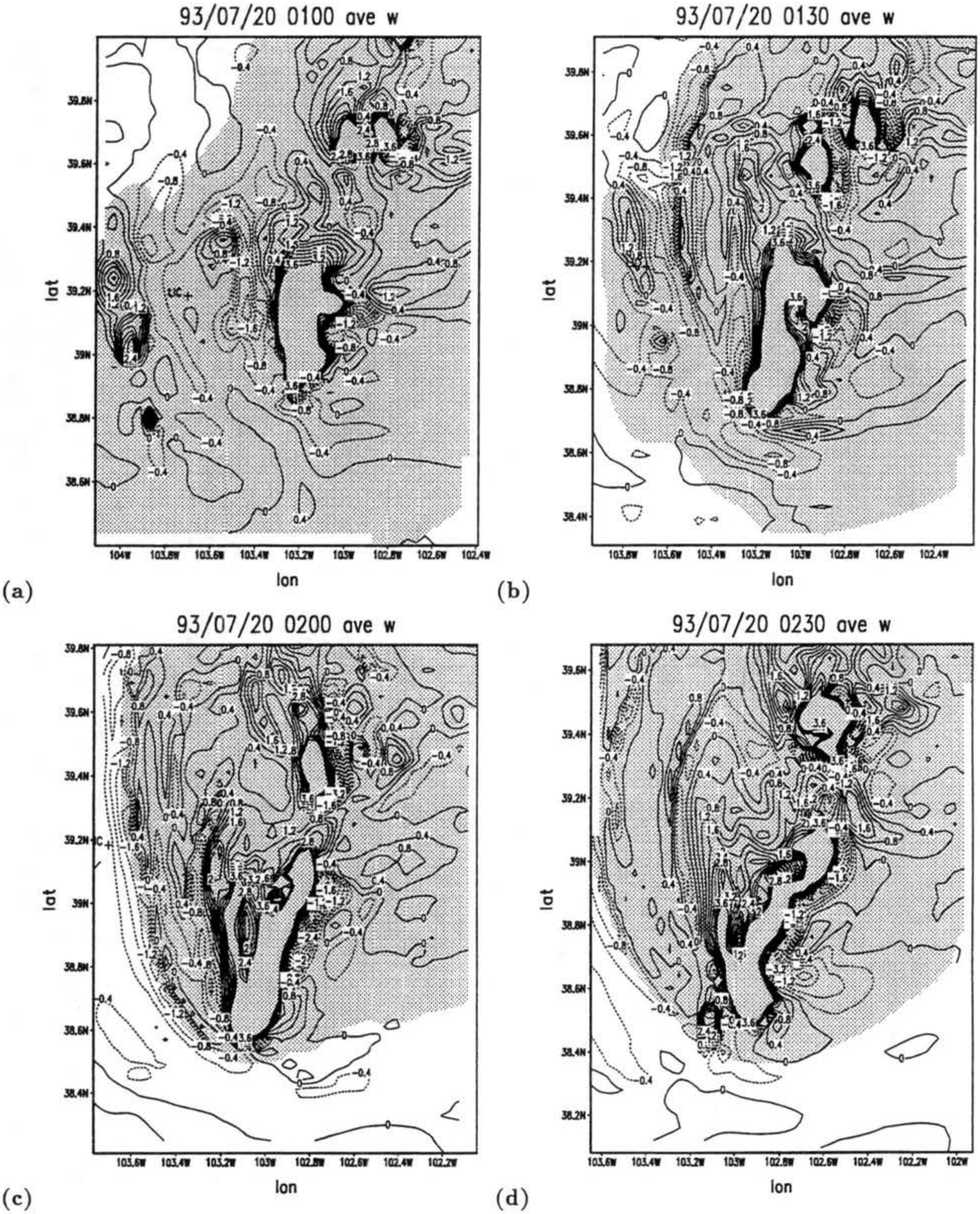

Figure 7.41: Vertically–averaged vertical motion between z=10 and z=13 km MSL on grid #4 at (a) 0100, (b) 0130, (c) 0200, and (d) 0230 UTC. The contour interval is 0.4 m s^{-1} between ± 4 m s^{-1}, and condensate greater than 0.1 g kg^{-1} at 13 km is shaded.

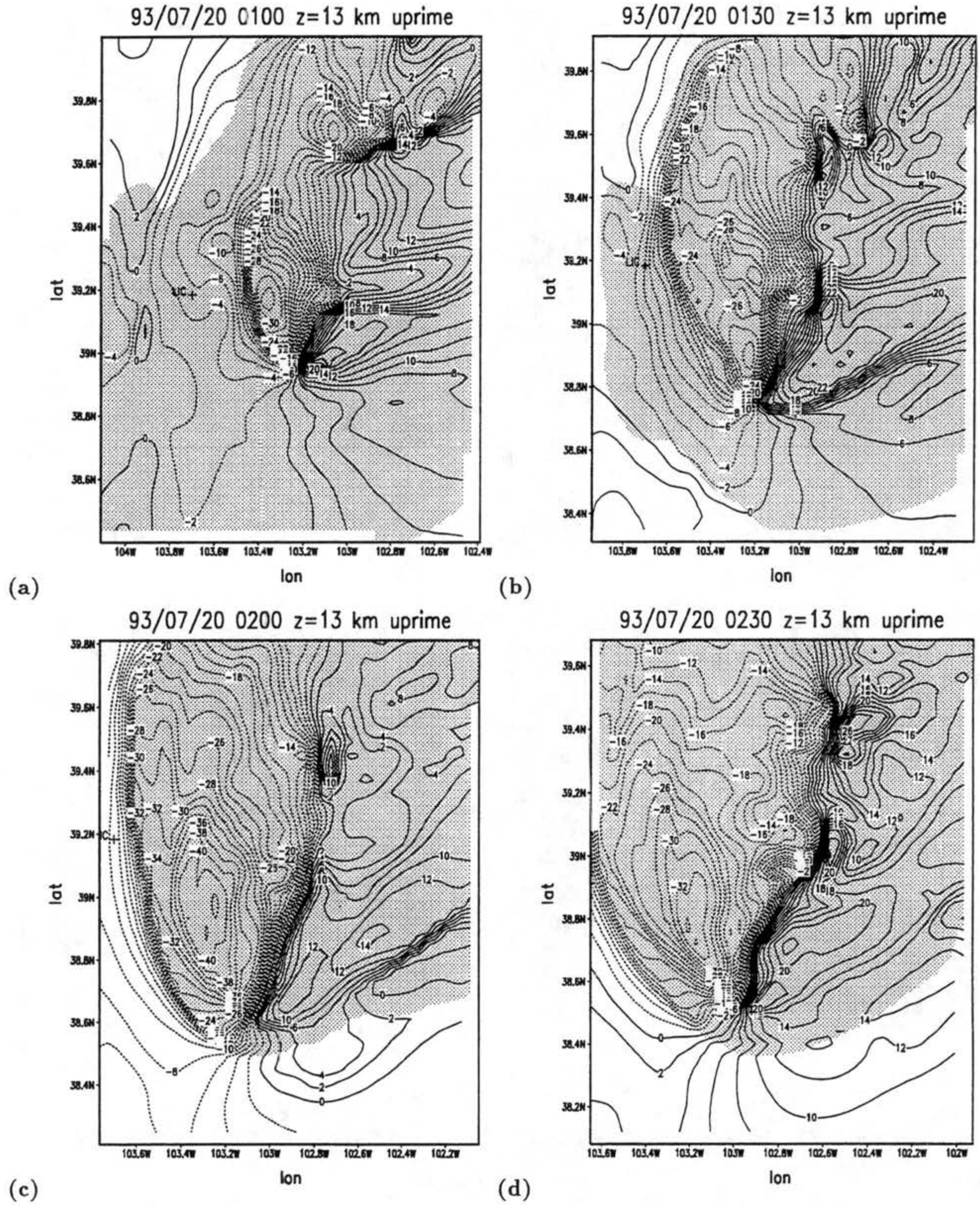

Figure 7.42: Environment–relative u winds at z=13 km MSL on grid #4 at (a) 0100, (b) 0130, (c) 0200, and (d) 0230 UTC. The contour interval is 2 m s^{-1}, and condensate greater than 0.1 g kg^{-1} is shaded.

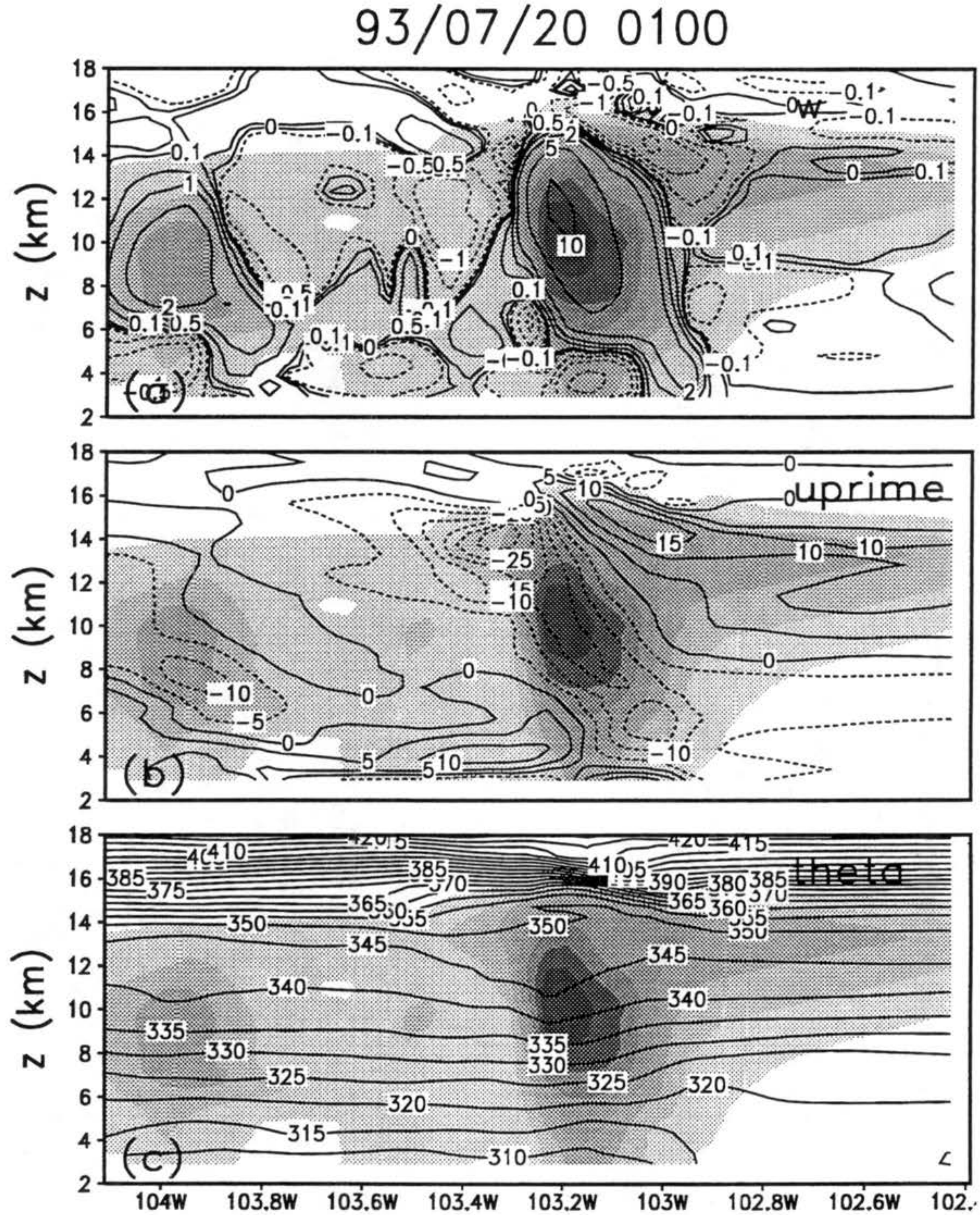

Figure 7.43: Vertical $x - z$ cross sections on grid #4 at 0100 derived by meridionally averaging (a) vertical motion, (b) perturbation flow (relative to the grid #2 environmental mean sounding), and (c) potential temperature across the southern convective line. The averaging interval was from 39.0 to 39.3° lat. The averaged condensate is shaded at 0.5 g kg^{-1} increments at and above 0.5 g kg^{-1}, the 0.1 g kg^{-1} level is also shaded.

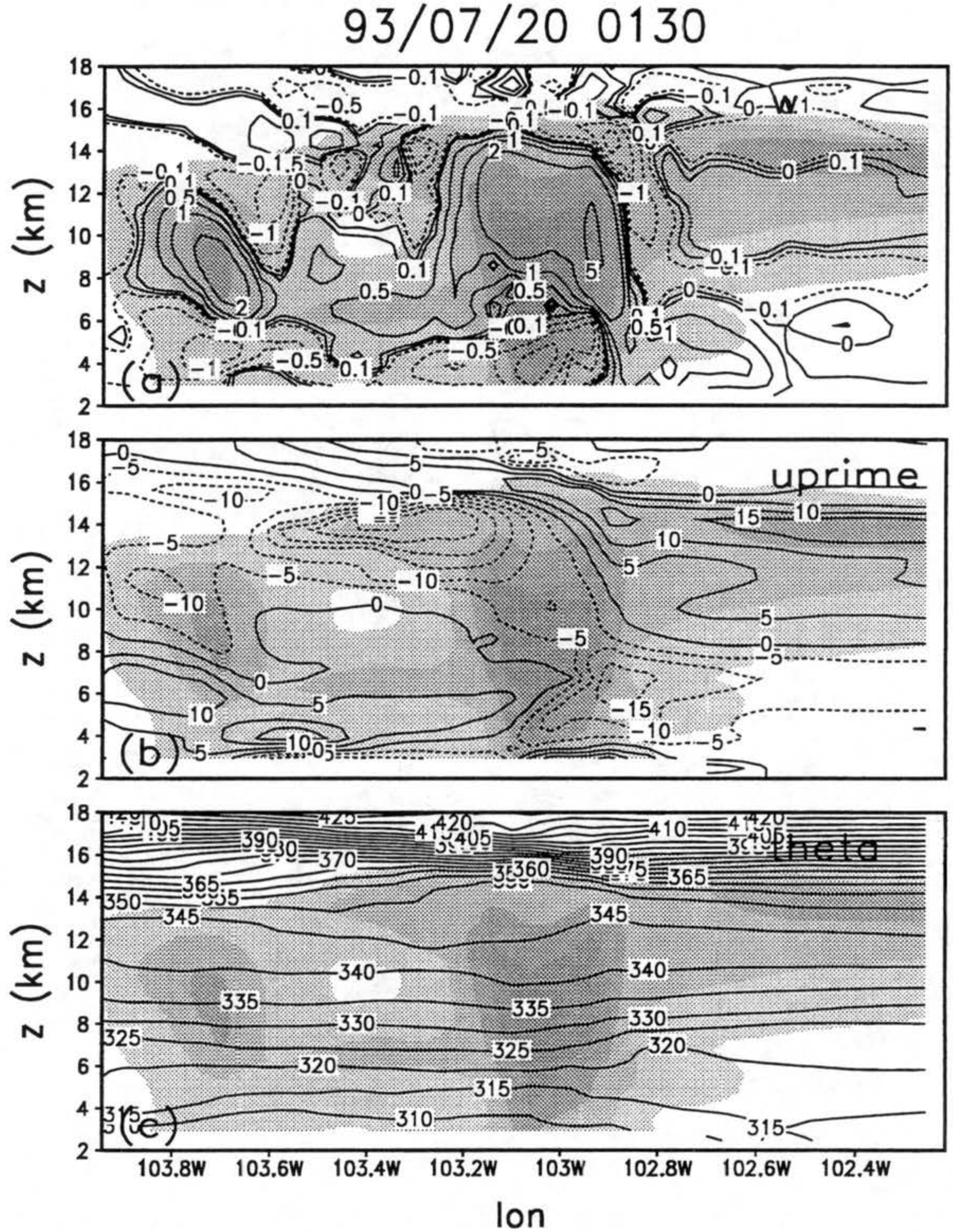

Figure 7.44: Same as Fig. 7.43 except at 0130. The averaging interval was from 39.0 to 39.4° lat.

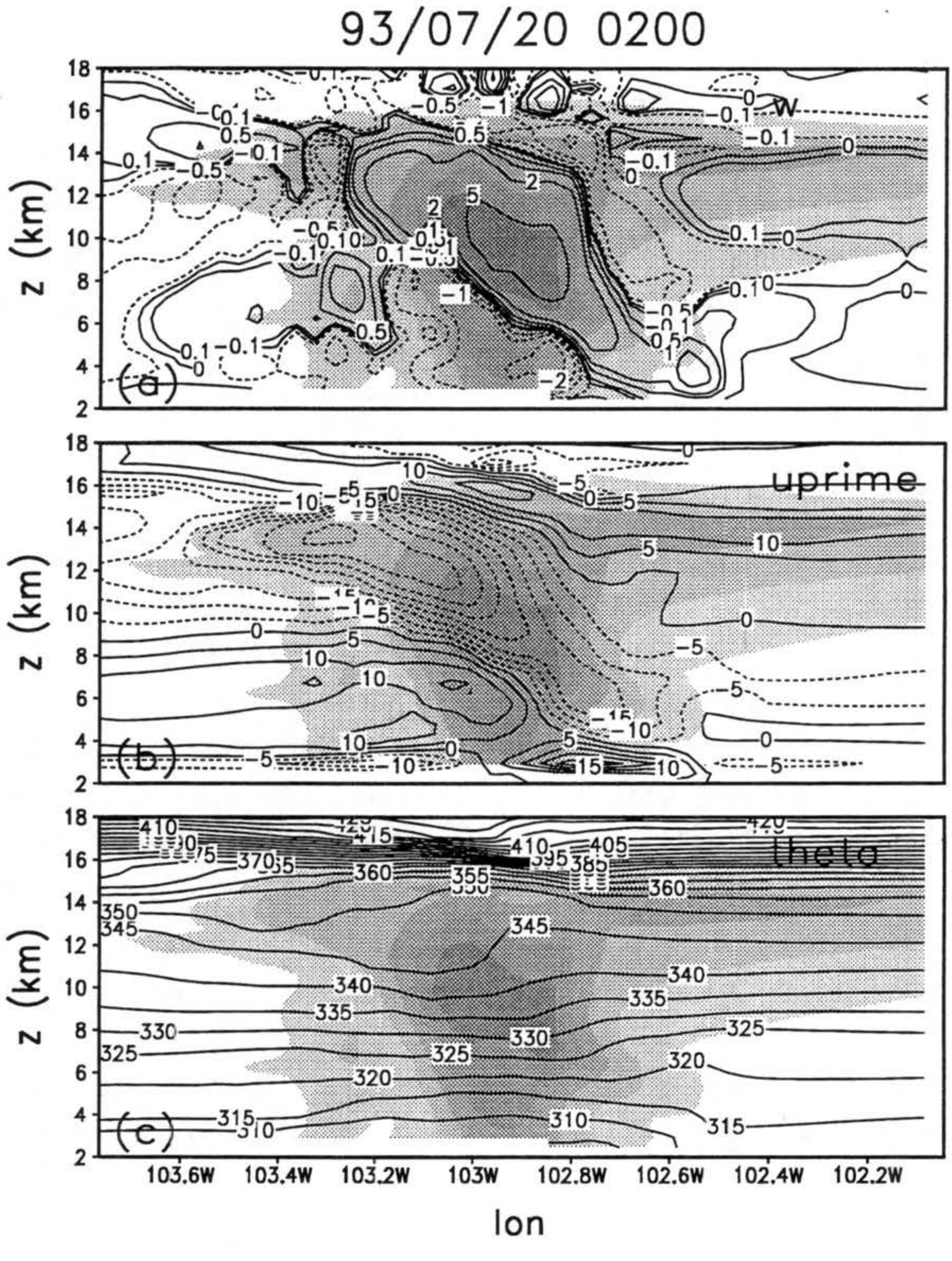

Figure 7.45: Same as Fig. 7.43 except at 0200. The averaging interval was from 38.8 to 39.2° lat.

Thermodynamic equation:

$$(\frac{\partial}{\partial t} + \overline{\mathbf{V}}_{\mathbf{H}} \cdot \nabla_H)\theta' + w'\frac{d\overline{\theta}}{dz} = 0 \tag{7.5}$$

where the subscript $_H$ indicates quantities on a constant z surface, the base–state vertical motion $\overline{w}$ is assumed to be zero, and the base–state pressure and potential temperature are assumed to vary only with height (Holton, 1992). Much of the gravity wave momentum perturbations are generated through divergent motions, wherein deep subsidence in the $n1$ mode, for example, induces upper (lower) tropospheric flow away from (towards) convection by continuity(Mapes, 1993). By the same token, the sinking motion creates positive thermal perturbations through adiabatic warming through the base–state θ gradient (eqn. 7.5).

Notably absent from equations 7.3–7.5 are nonlinear advective terms like $\mathbf{V}' \cdot \nabla \mathbf{V}'$ and $\mathbf{V}' \cdot \nabla \theta'$. Physically speaking, the nonlinear terms are associated with lower tropospheric density currents or intense divergent anvil outflow in convective storms. In contrast to gravity waves, heating and momentum perturbations in these disturbances are directly injected into the surrounding environment. Advective modes do not propagate or disperse like waves, and therefore energy is not necessarily diffused to the far field. If the environmental winds over a large area are weak, or are somehow blocked by the advective disturbance itself, then a considerable amount of energy may stay close to the convective cells that generated it. Herein lies an important difference between linear and nonlinear disturbances. If the atmospheric response to convection is dominated by the linear gravity waves, as it was in the early stages of this MCS, then most of the energy is dispersed to the surrounding environment. This energy is eventually trapped at the Rossby radius by rotational effects, but as Olsson and Cotton (1997) point out, the Rossby radii for a gravity waves can be quite large due to the rapid propagation speeds. At such large ranges, convectively generated energy is quite diffuse, and the intensity of the disturbance can only build slowly. Conversely, if a large portion of the energy is partitioned into an advective mode, the MCS energy density (as defined by the thermal and momentum perturbations) may be proportionately increased. Like the gravity waves, energy in the advective modes is also eventually trapped by rotational effects, however the Rossby radius would be expressed in terms of the advective velocity as opposed to the gravity wave phase speed. In this case, the advective velocity was considerably slower than the gravity wave phase speed, thus the disturbance remained more concentrated. When inertial effects eventually take over, the balanced portion of the disturbance is smaller but stronger.

A full examination of the thermal and momentum budget in this MCS is left for a future study. However, a few simple "back of the envelope" calculations demonstrate that the intense cold cloud shield was expanding outward in a nonlinear way. The terms in zonal component of the momentum equation were calculated at 0200 at the leading edge of the wave near LIC. At this time, the western edge of the velocity gradient was nearly stationary with respect to the ground, thus $\frac{\partial u}{\partial t} \sim 0$. The other terms were obtained with the model data, using the averaged data on grid # 2 as the mean state. These resulted in the following values: $\overline{u}\frac{\partial u'}{\partial x} \sim -0.07\text{m s}^{-2}$, and $\frac{1}{\rho_0}\frac{\partial p'}{\partial x} \sim 0.02\text{m s}^{-2}$. Additionally, the nonlinear momentum advection was calculated, obtaining: $u'\frac{\partial u'}{\partial x} \sim 0.07\text{m s}^{-2}$. Clearly, the nonlinear advection was of the same order of magnitude as the linear terms, and thus it could not be neglected. Calculations with the thermodynamic equation (eq. 7.5) yielded: $\frac{\partial \theta}{\partial t} \sim 0.001$ K s^{-1}, $\overline{u}\frac{\partial \theta'}{\partial x} \sim$ 0.046 K s^{-1}, and $w'\frac{d\overline{\theta}}{dz} \sim -0.014$ K s^{-1}, while nonlinear advection of potential temperature by the zonal outflow was $u'\frac{\partial \theta'}{\partial x} \sim -0.037$ K s^{-1}. Again the nonlinear advection was about the same order of magnitude as the linear terms, showing that it also could not be neglected. These simple calculations indicate that heat and momentum were directly injected into the atmosphere for considerable distances away from the convection. In contrast, most of the perturbation flow behind the line at 2200 was induced in the wake of the propagating gravity waves. Similar calculations indicated that the nonlinear advective terms were an order of magnitude smaller than the linear terms, thus the atmospheric response was largely linear.

Several qualitative aspects of the nonlinear anvil expansion also suggest that convectively generated perturbations did not rapidly diffuse to the far field. When the anvil mushroomed outward from the southern storm, upper tropospheric perturbation horizontal flow (Fig. 7.42) expanded westward like an advective outflow, with the western edge remaining sharply defined for 1.5 hours. Gravity wave disturbances at previous times did not retain this continuity (Figs. 7.31, and 7.37), and instead rapidly broadened and dispersed.

Vertical motions averaged from $z = 10 - 13$ km[6] were also nearly constant along the leading edge, and in some regions actually increased with time (Fig. 7.41). This consistent strength is not predicted by linear theory since even in the higher order modes, amplitude loss inevitably occurs as the wave front expands away from the source.

The outward anvil propagation was also different from previous events in that strong, organized upper tropospheric perturbation flow was present both upstream and downstream from the main convection. A similar situation occurred when storms first developed in the mountains (Figs. 7.30, and 7.31), but that was associated with the downstream propagation of the roll–like perturbation. Downstream vertical motions between 0100 and 0230 were not consistent with such a disturbance, and in general were poorly correlated with the upper tropospheric horizontal wind gradient. This was particularly apparent at 0130 and 0200 (Figs. 7.41b, c, and 7.42b, c) along the southern edge of the MCS. The western half of the outflow was bounded by an arcing region of downward motion while the eastern half was associated with weak, ill–defined upward motion. Similar results were obtained for several different averaging depths as well as on individual levels. As mentioned above, linear gravity waves propagate by means of divergent motion, characterized by a correlation between the horizontal and vertical perturbation winds. The weak correlations here strongly suggest the presence of nonlinear effects.

Although the nonlinear disturbance exhibited some $n2$ characteristics in the vertical, the structure was difficult to classify before 0200 due to interfering motions from the decaying southwestern convection (Figs. 7.43–7.45). The leading edge of the disturbance was located near 103.5 W at 0100 and 103.6 W at 0130 and 0200 in Figs. 7.43, 7.44, and 7.45, and the strongest perturbations in both the thermal and momentum fields were near the tropopause. Although somewhat smoothed by the along–line averaging, potential temperatures warmed 5 K in the upper troposphere and cooled by 5–10 K in the lower stratosphere as the disturbance passed. Brunt-Väisällä frequencies in many of the individual $x - z$ cross

---

[6]The $n2$–like structure necessitated a shallower averaging depth to properly track it.

sections dropped close to zero in the wake of the disturbance. None of the rearward propagating gravity waves to this point generated such a focused response so far outside the convection.

Prior to 0200, perturbation rear inflow existed below 6 km, but its structural evolution was not well correlated with the outward propagation of the front–to–rear flow. Although an isolated maximum at $z = 4$ km appeared to be propagating outward directly beneath the leading edge, rear inflow stayed constant or even decreased slightly between 0100 and 0130. Decaying convection to the west was generating a secondary region of descending rear inflow, located west of 103.7 W at 0130 (Fig. 7.44), which by 0200 had merged with the main storm. Other effects, such as the development of a westward leaning updraft in the leading line, conspired to make rear inflow evolution quite complicated. Any gravity wave induced perturbations were difficult to sift out, and the upper tropospheric advective disturbance was one of the few features that remained consistent through this evolution.

The development of the nonlinear mode in this case is likely related to the strength of the MCS–integrated vertical mass flux. Increases in the vertical mass flux preceded all three wave events, while the MCS–average divergence profile remained almost constant (Figs. 7.28, and 7.29). The linear response would be to simply partition more energy into the existing gravity wave modes. Comparisons between the first and second wave events show this to be the case for the most part. Wave–induced responses during the second event were stronger but the structure of the environmental perturbations away from the convection were quite similar in both cases. Vertical mass flux increases during the third event, however, were large in comparison to the first two. Between 0000 and 0200 vertical mass flux (Fig. 7.29) nearly tripled at many levels, while the height of the 1×10^9 kg s^{-1} contour increased from 12 to 13.5 km. Although, the strength and shape of the average divergence profile (Fig. 7.28) remained steady through this period, the resulting response was obviously quite different.

The dynamics of the nonlinear mode are likely quite complicated, and appear to be dependent upon the impulsive, Lagrangian nature of convection. Fritsch and Brown (1982) suggested that cooling associated with the direct injection of turbulent air into the lower stratosphere enhanced the strength of the upper tropospheric mesohigh above an MCC.

However, they also found that the mesohigh was qualitatively very similar, even without the parameterized lower stratospheric cooling. In fact, their results suggest that this cooling should not be parameterized by simply specifying a tendency at the top of a convective plume. The problem relates to how the cooling occurs. Since it is a turbulent process, the dynamics are likely dominated by the nonlinear terms, yet prescribing an Eulerian heat source (or sink) generates mainly linear disturbances. To demonstrate this, an attempt was made to reproduce an upper tropospheric advective mode with a prescribed heat source in the two dimensional nonhydrostatic, nonlinear model described in section 7.4.2. Several shear and heating profiles were tried, including actual soundings taken from the three–dimensional MCS simulation. The majority of the response in all of the experiments was projected onto the linear modes. In some cases, profiles with maximum heating as high as 400 K hr^{-1} were impulsively initiated, and while these produced many small–scale gravity waves, the low frequency response was still dominated by the linear waves. Pandya and Durran (1996) suggested that the linear solution dominates for prescribed heating experiments, and it apparently holds even when the heating rates are very high. This could be a serious problem if one is trying to simulate a nonlinear process.

Many more cases need to be studied to determine the extent to which these nonlinear disturbances exist. The results here are quite interesting because they suggest that the manner in which the anvil spreads is important. When the convective vertical mass flux is weak, the majority of MCS–induced atmospheric response can be described by linear dynamics. In cases of weak upper tropospheric shear, such as in the tropics, momentum and heat perturbations may simply spread away in the wake of the linear gravity wave modes as suggested by Pandya and Durran (1996). However, when the vertical mass flux becomes strong, such as when CAPE is high or many storms are closely concentrated, the upper tropospheric perturbations spread primarily by advection. The flux of heat and momentum away from convection is dependent on the efficiency and speed of the carrier modes. The long–lasting continuity of the nonlinear disturbance in the system studied here indicates that more energy was retained close to the convection. If this is the case, then as mentioned above, MCSs exhibiting strong advective modes may produce a significantly stronger and more concentrated balanced circulation than their weaker counterparts whose energy rapidly propagates as linear gravity waves due, to the reduced Rossby radius of the advective mode. In the next section, the nature of the linear energy propagation into the far field from this particular system is examined.

7.5 MCS interactions with the meso–α–scale environment

We now take a step back onto grid #2 to investigate the cumulative effects that several hours of convection had on the environment. In this analysis, the large–scale environmental gradients were removed by subtracting out the results of the no microphysics simulation. This was done because significant horizontal gradients still existed when the mean fields were subtracted out. It is important to realize that the environmental flow may have evolved somewhat differently in the absence of convection, especially close to the surface. Tripoli and Cotton (1989a) found that the mountain–plains solenoid was not as deep without moist convection, and experiments with this case indicated a similar situation. Also, the Palmer Divide–Platte Valley solenoid was shifted 20–50 km north after 0000 UTC in the dry simulation due to the lack of convective outflow. These differences were most pronounced at levels below 5 km MSL, thus the bulk of the analysis was conducted in the mid and upper troposphere. It is also important to note that the speed and strength of convectively generated disturbances will change as they propagate onto the coarser grids. Therefore, the emphasis is on the qualitative structure of the heat and momentum generation. Comparisons with the observed soundings, discussed below, show that the model was correctly reproducing the general pattern.

7.5.1 Upper tropospheric interactions

At 11 km MSL, most of the environment within and immediately surrounding the contiguous anvil had warmed to some degree by 0200 UTC (Fig. 7.46). Away from the convection, potential temperature perturbations were generally less than 2 K, with a maximum of 5.5 K centered near the strongest convection. West of the MCS, the wave–induced nature of the compensating motions, is revealed by the arc shaped oscillations in the potential temperature field. Coherent disturbances were apparent as far west as 108° lon., indicating considerable westward energy propagation. To the east, the warming was more uniform

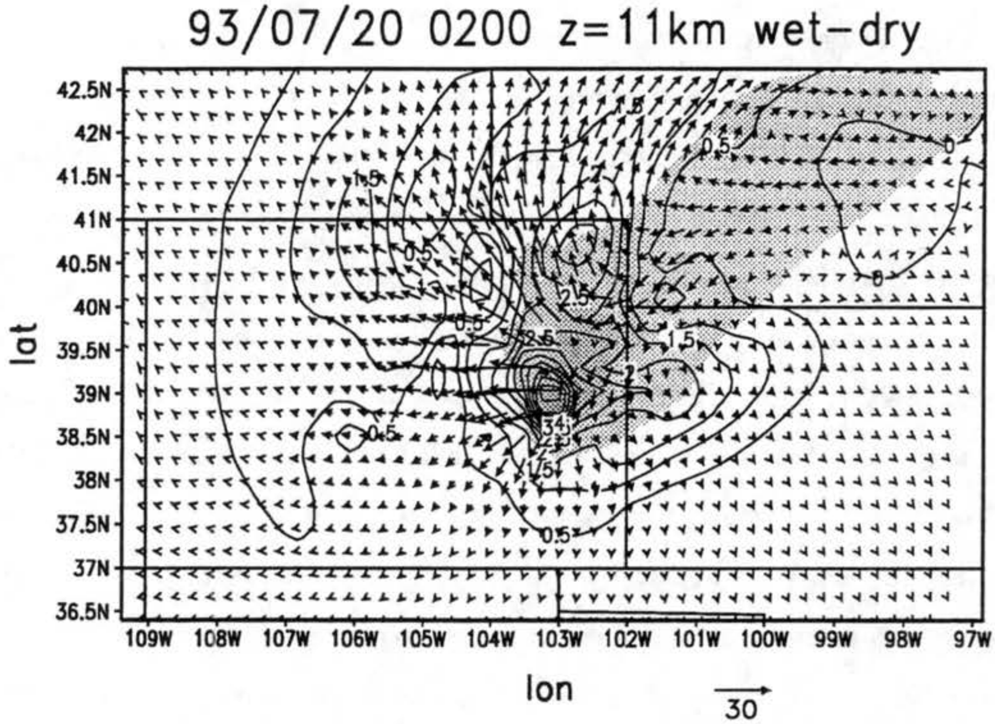

Figure 7.46: Potential temperature differences between the moist and no microphysics runs ($wet - dry$) on grid #2 at 0200 at a constant height of z = 11 km MSL are contoured at 0.5 K intervals. Total condensate greater than 0.1 g kg^{-1} is shaded. Wind differences between the moist and no microphysics runs ($wet - dry$) are represented as vectors that are scaled at the lower right.

and did not extend as far from the system. This pattern is consistent with the asymmetric westward propagation of the gravity wave responses. Deep vertical motions at the leading edge of each wave induced regions of environmental warming and cooling many kilometers from the initial source. In the net, subsidence, and therefore warming, dominated over any cooling forced by ascending wave fronts.

The highest potential temperatures on the eastern side of the main convection were flared outward along the edges of the downstream anvil. Weak downward motion existed around and just outside the southern edge of the anvil, indicating that subsidence was responsible for most of the warming. On the northern anvil edge (near the Colorado–Nebraska border and east), however, vertical motions were weak or even slightly positive. In this region, strong ground–relative winds were advecting in heat anomalies that had originated outside the anvil on the western side of the storm (Fig. 7.47a). This pattern is somewhat consistent with the composite conceptual model put forward by Fritsch (1975), in that most of the upper tropospheric subsidence occurred on the back (western) side of the convective towers. In the cross–wind direction, however, the Fritsch model depicted symmetric subsidence to the north and south of the cloud boundary, while in this case the subsidence was mainly to the south. This north–south asymmetry better matched the conceptual model of Blanchard et al. (1997), who suggested that northward accelerations in the upper tropospheric horizontal winds tended to reduce the subsidence north of the anvil.

Upstream of the MCS, ground–relative southwesterlies slowed down and turned northward as they approached the edge of the anvil, resulting in easterly to southeasterly perturbation flow (Fig. 7.47). Although the greatest deviations were closest to the back edge of the system, perturbed flow fanned out several hundred kilometers to the north and west, closely following the path of the greatest wave activity in the θ field (Fig. 7.46). Fritsch and Maddox (1980a, b), Maddox et al. (1981), and Blanchard et al. (1997) among others have noted the tendency for upper tropospheric jet streaks to form on the northern and eastern sides of an MCC. As discussed in Chapter 5, the accelerations in this case occurred as the ambient flow adjusted to the MCS–induced pressure perturbations aloft. To the west of the system, mesoscale high pressure developed through the cumulative effects of

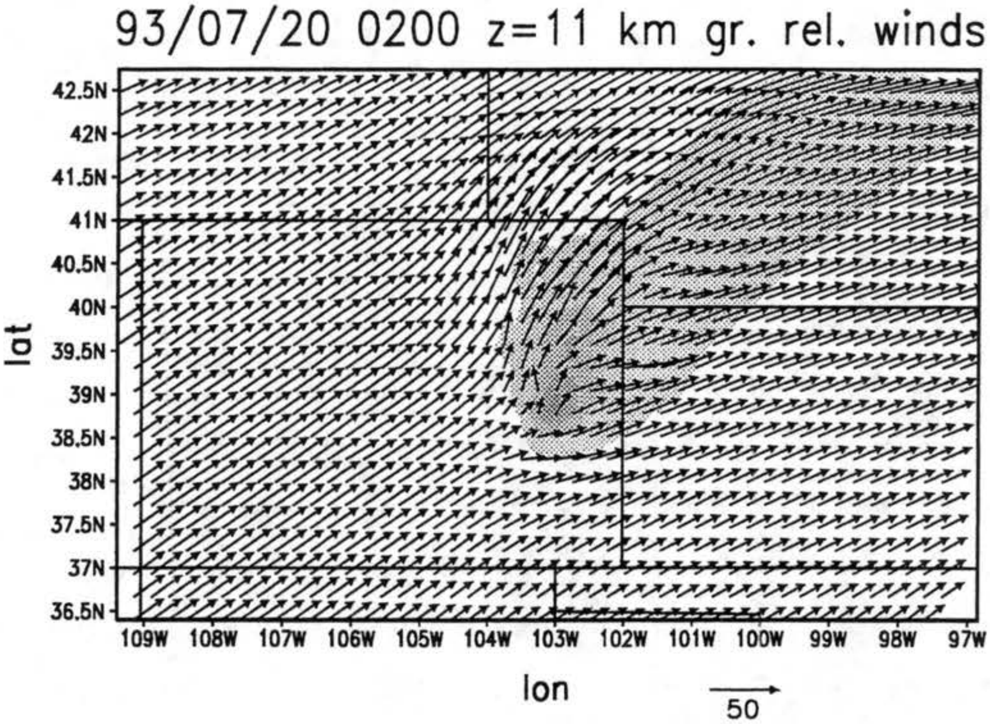

(a)

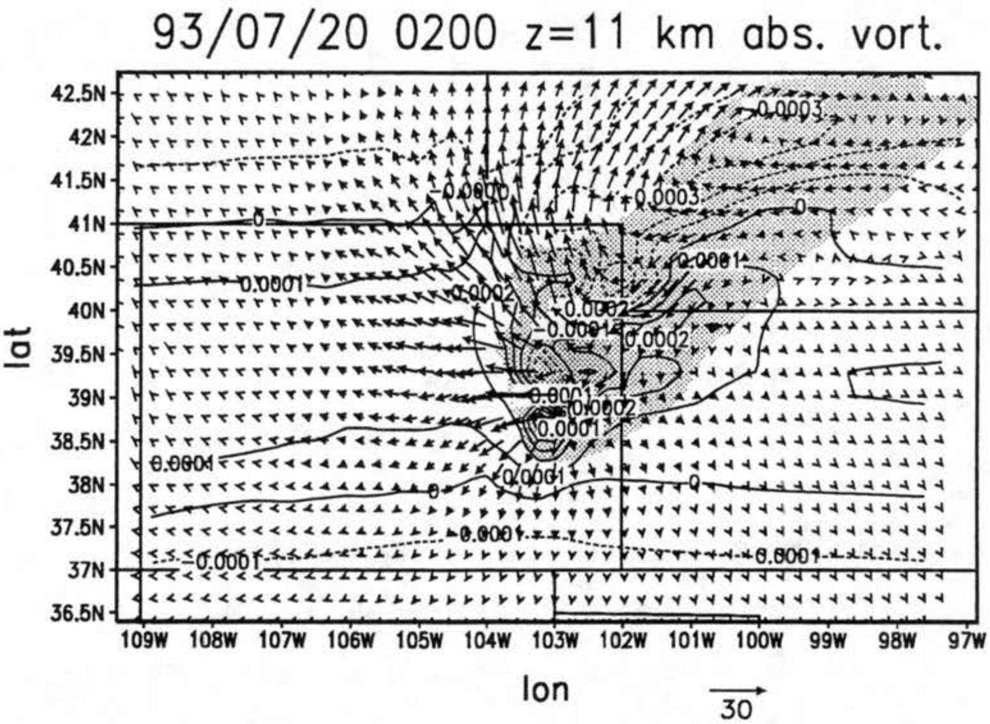

(b)

Figure 7.47: Same as Fig. 7.46 except in (a) ground relative vector winds from the moist run are plotted, while in (b), the absolute vorticity from the moist run is contoured at 0.0001 s^{-1} intervals, along with the perturbation vectors.

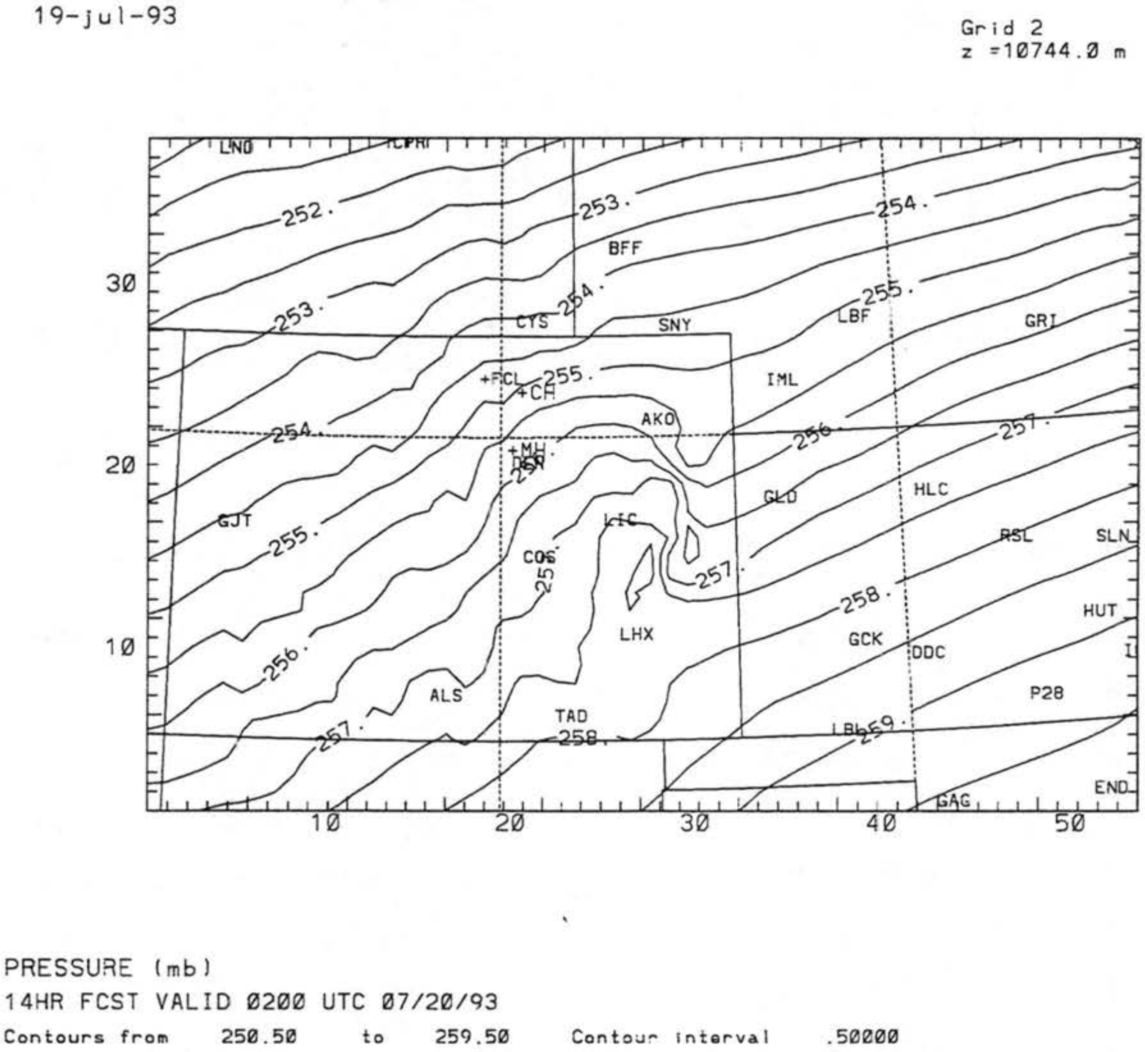

Figure 7.48: Total pressure in hPa at a constant height of z = 10.7 km MSL at 0200 20 July on grid # 2. The contour interval is 0.5 hPa.

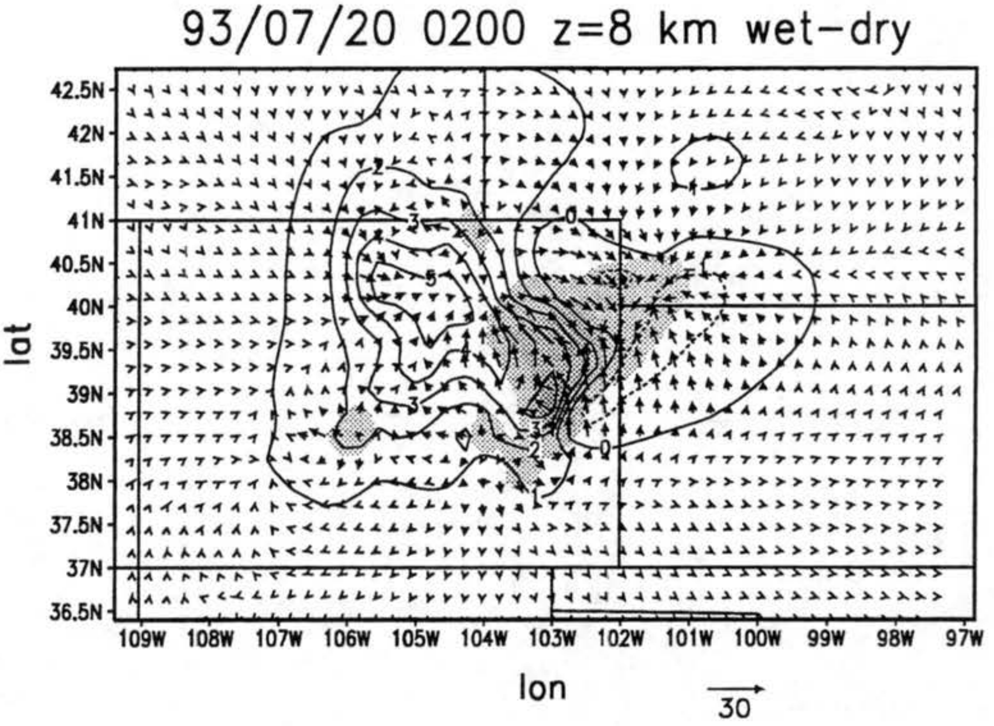

Figure 7.49: Same as Fig. 7.46 except at z = 8 km MSL. The contour interval is 1.0 K

the low frequency gravity waves (Fig. 7.48). The reduction in the upstream flow disrupted geostrophic balance and resulted in northerly accelerations towards lower pressure. By simple Bernoulli considerations, the northward shift of mass contributed to easterly accelerations to the northeast of the anvil. Blanchard et al. (1997) showed that the meridional extent of the upper tropospheric divergence signature is increased in environments of low inertial stability due to northward accelerations in the strong anticyclonic flow. Negative absolute vorticities (Fig. 7.47b) were prevalent over a large area directly north of the anvil cloud at 11 km, indicating this process was taking place.

7.5.2 Mid and lower tropospheric interactions

The upper tropospheric perturbations discussed above were representative of the layer between 10–12 km MSL. In the mid troposphere, perturbations in the 6.5 to 10 km layer were dominated by a pattern similar to that at 8 km (Fig. 7.49). At this level, the gravity wave–induced asymmetries were quite pronounced, with almost all of the heating restricted to a very focused area behind the convective line. Warming trailed well west of the system, with maximum potential temperature perturbations up to 5 K. No significant warming was occurring to the east, north, or south of the MCS. Such concentrated warming graphically illustrates that the deep sinking motions did not radiate out symmetrically, and were instead guided by gravity waves in a manner that was dependent upon the orientation and tilt of the convection. It also means that MCSs do not necessarily suppress convection from all competing systems, a point made quite evident by the development of a second MCS just north of this system (Fig. 4.7). In this particular case, the bulk of the subsidence warming occurred over regions where the boundary layer had already been cooled by convective outflow. This minimized the total area stabilized by the combination of lower tropospheric cooling and upper tropospheric warming.

Like the extreme low level jet, the localized region of subsidence warming is difficult to detect in the standard observations. However, as luck would have it the 0000 UTC, 20 July Denver sounding (Fig. 7.50a) was located in an ideal position to sample the temperature anomalies. Although the simulated Denver sounding was taken at 0200 (Fig. 7.50b), there was considerable agreement with the observations. Both soundings contained a warmed layer above about 450 hPa, with a sharp inversion at the base of observed warming (near 440 hPa in Fig. 7.50a). The lower boundary of the simulated warm layer was not as sharp, as the coarse vertical grid spacing likely resulted in some smoothing. Observed temperatures in the warmed layer were $3-5°$C higher than their morning values, which is consistent with the simulated warming. Moreover, this warm layer was completely absent from the North Platte (LBF) sounding (Fig. 4.6b), and only weakly apparent at Dodge City (DDC). Several small convective cells south of DDC at 0000 were likely affecting the local environment, and may have been responsible for the weak warming there. On a related note, MCSs have sometimes been observed to leave very distinct dry wakes for hundreds of kilometers in the satellite-observed upper tropospheric water vapor (Ray McAnelly, personal communication). The drying associated with the focused subsidence warming in the 0000 DEN sounding may be indicative of the formation of such a wake.

Horizontal perturbation flow was relatively weak at 8 km (Fig. 7.49) since this level was close to the inflection between front-to-rear flow above and rear-to-front flow below. Lateral inflow of about 10 m s^{-1} was streaming into the leading anvil on its northern and

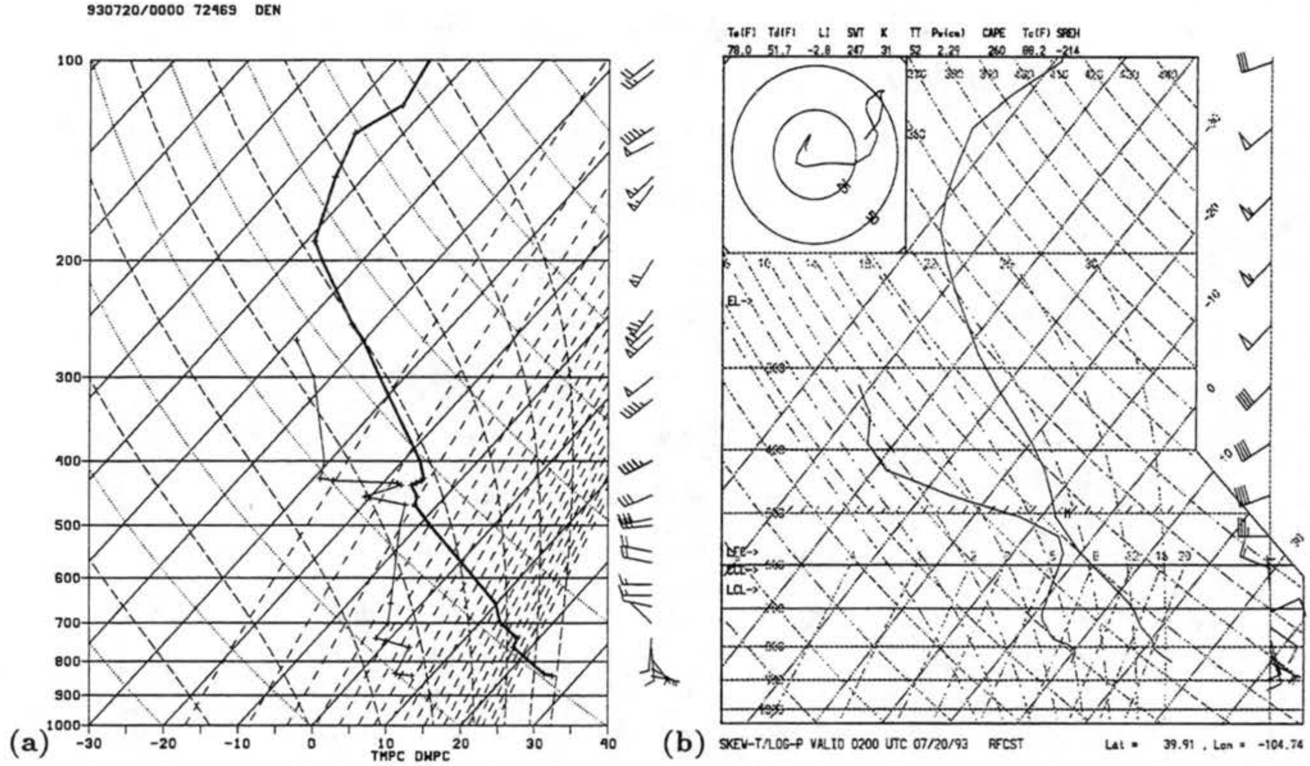

Figure 7.50: Thermodynamic soundings from (a) the Denver 0000 20 July observation, and (b) the closest grid point to Denver on grid #2 at 0200.

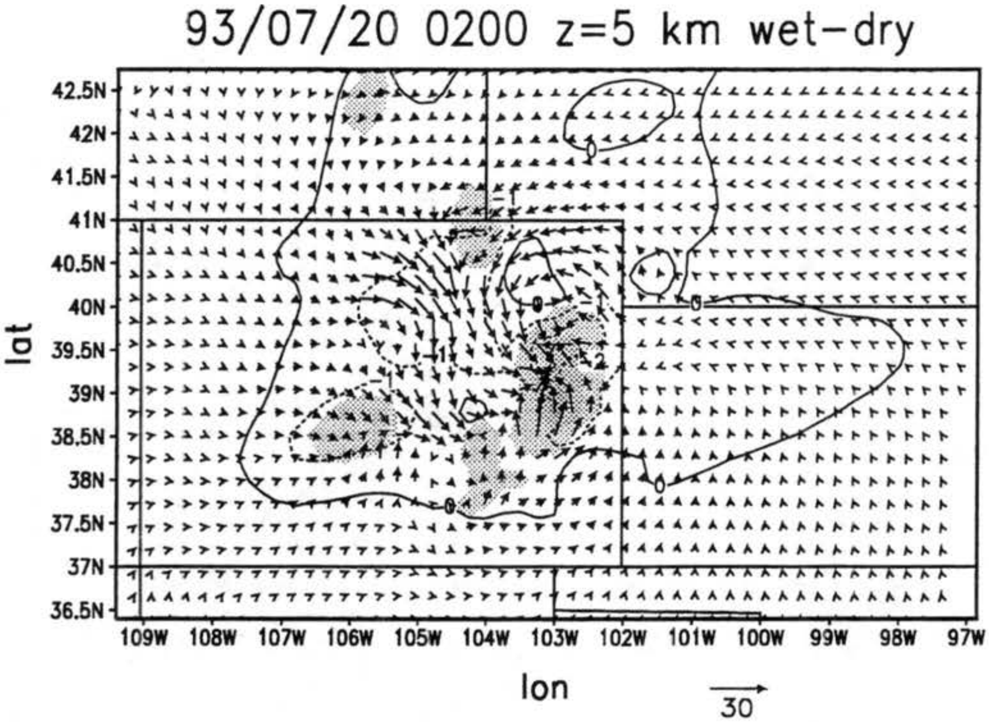

Figure 7.51: Same as in Fig. 7.49 except at z = 5 km MSL.

southern flanks. This region was dominated by weak cooling and downward motion, which was likely due to sublimation in the leading anvil. As discussed previously, this separation of the stratiform precipitation effects from the gravity wave effects is one of the many aspects that made this system a good case for study.

At 5 km, rear inflow, which extended several hundred kilometers to the northwest of the system (Fig. 7.51), was strongly correlated with the region of warming at 8 km. This is not surprising since both features were induced by the passage of the low frequency gravity waves. Thermal perturbations at 5 km actually showed some weak cooling which also extended northwestward within the rear inflow. Since this was well above any boundary layer density current, the cooling was likely induced by weak upward motion in rearward propagating $n2$ modes. This is consistent with the $n2$–like structure in the elevated rear inflow discussed in the last section.

Although the results at 3 km (Fig. 7.52) were somewhat contaminated by differences in the boundary layer north of the outflow boundary, the lack of southerly inflow perturbations in the low level jet south of the system is worthy of mention. Low level jet wind velocities in

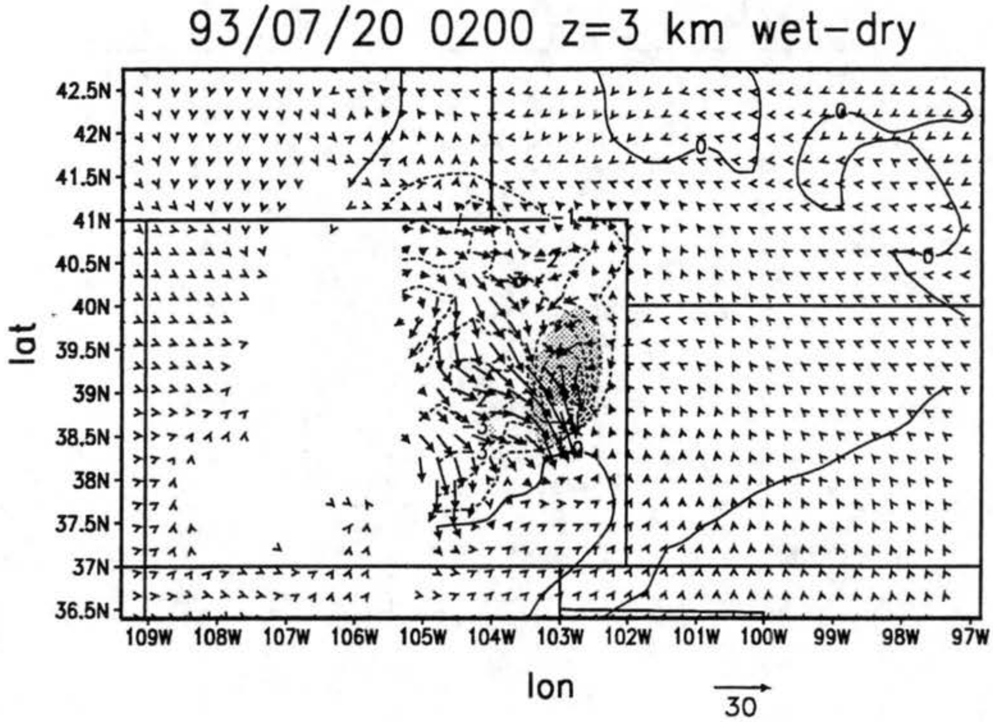

Figure 7.52: Same as in Fig. 7.49 except at z = 3 km MSL.

both the moist and dry runs were virtually identical, with most differences away from the convection of only about 1 m s^{-1}. This indicates that the lower tropospheric updrafts were driven by the expansion of the density current, and not by the acceleration of boundary layer air into lowered pressure at the base of a convective updraft. As convection intensified, the changes in heating intensity mainly resulted in the production of a stronger density current due to the increased precipitation. Boundary layer air was not being drawn in any faster than the environment could already provide it. Since most of the high CAPE air feeding this system came from low levels, increases in the total updraft mass flux were driven primarily by increases in the available energy supplied by the environment. This is an important result for it shows that heating–driven feedbacks were not increasing the strength of the updrafts as CISK theory (Ooyama, 1964) would suggest.

7.5.3 Vertical cross sections

The MCS–induced perturbations through the troposphere are summarized in the vertical cross sections averaged along the zonal (Fig. 7.53) and meridional (Fig. 7.54) extent of

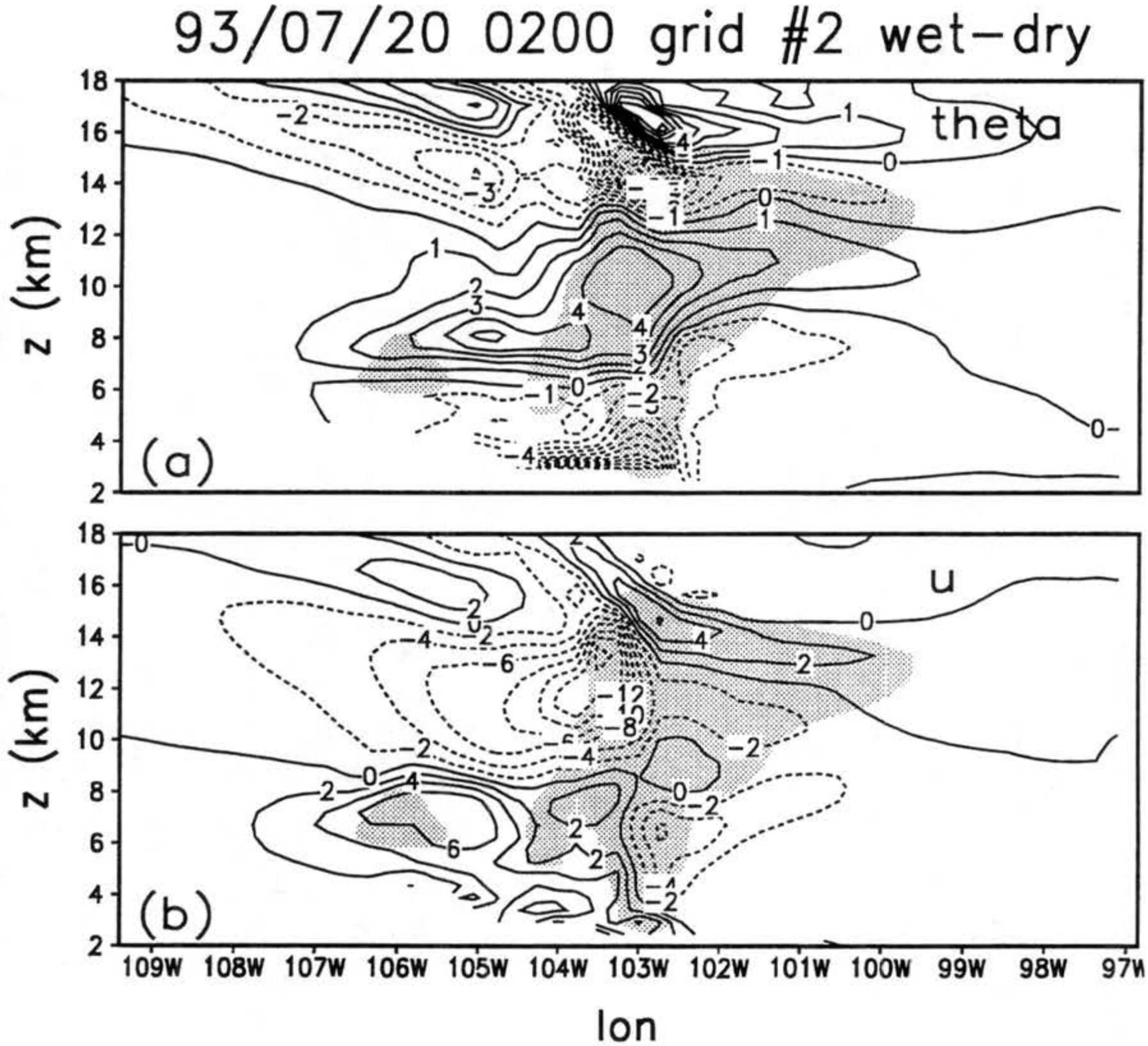

Figure 7.53: Vertical $x - z$ cross sections on grid #2 at 0200 of meridionally averaged (between 38 and 41° lat.) differences in (a) potential temperature and (b) u wind components between the moist and the no microphysics (*wet* − *dry*) runs. Average condensate greater than 0.1 g kg^{-1} is shaded.

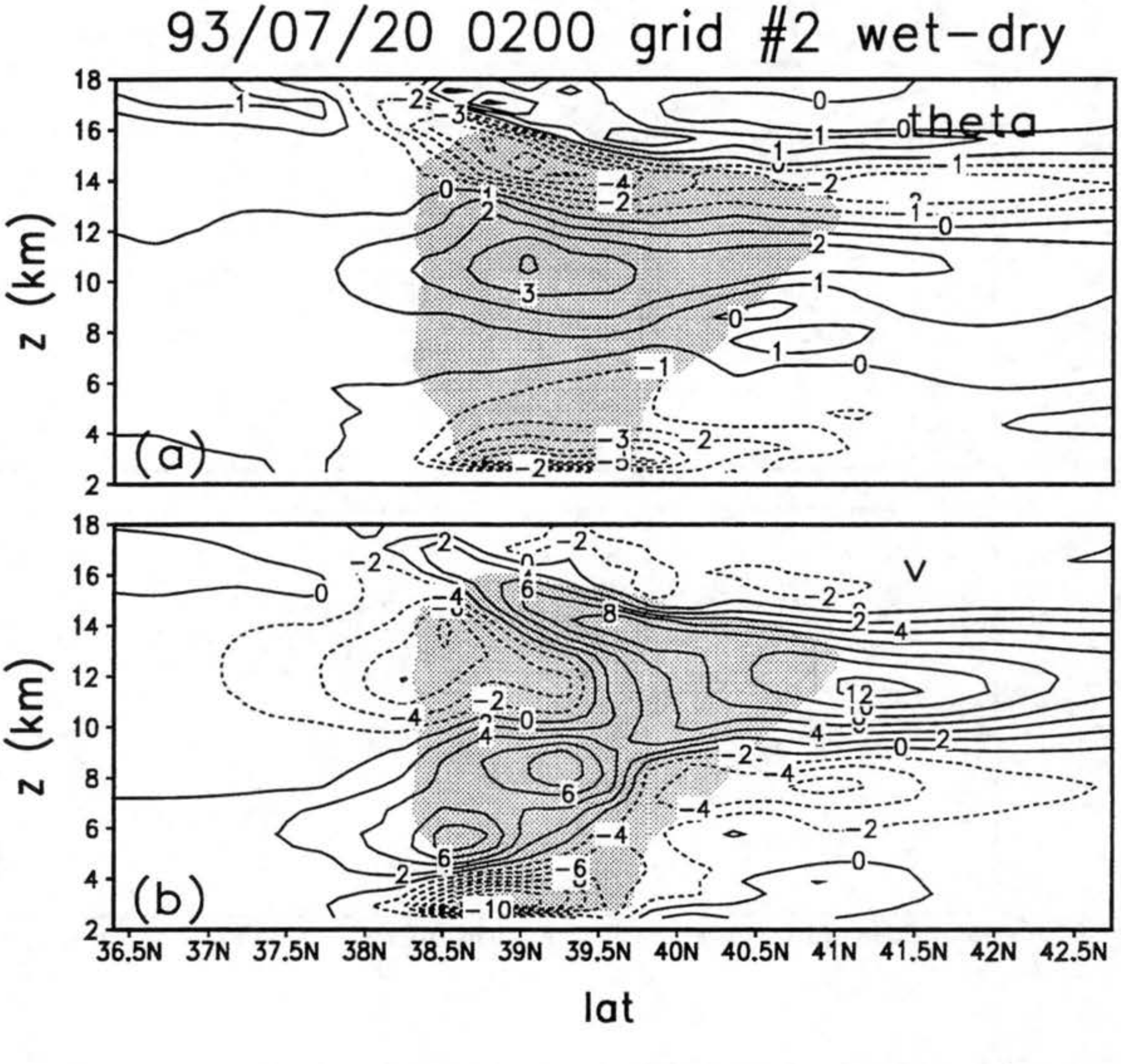

Figure 7.54: Vertical $y - z$ cross sections on grid #2 at 0200 of zonally averaged (between 101.5 and 104° W lon.) differences in (a) potential temperature and (b) v wind components between the moist and the no microphysics (*wet* − *dry*) runs. Average condensate greater than 0.1 g kg^{-1} is shaded.

the system on grid #2. In deriving the east–west cross sections, averages were taken from 38 to 41° lat., while averages for the north–south cross sections were taken from 104.0 to 101.5° lon.

In the zonal direction (Fig. 7.53), deep mid tropospheric heating extended for several hundred kilometers west of the condensate. Maximum potential temperature perturbations were at 8.0 km MSL, just below the front–to–rear and rear–to–front flow interface (Fig. 7.53b). Weak cooling between 3.8 and 5.8 km, as well as the elevated rear inflow perturbations reflect the presense of higher order $n2$ gravity waves. Johnson et al. (1995) noted similar evidence of $n2$ mode propagation in the clear air between two adjacent midlatitude MCSs. Additional, more intense cooling associated with the density current dominated the thermal perturbations below 3.8 km. In the upper troposphere, front–to–rear flow perturbations above 8 km extended out to the western edge of the grid. The gentle upward slope of this flow with distance from the MCS is indicative of vertical wave phase propagation. Stratospheric thermal and momentum perturbations fanning off the western edge of the overshooting convection at increasing angles with height is similar to the vertical propagation effects simulated by Fovell et al. (1992).

The strong east–west asymmetry dominated all levels, with only weak perturbations east of the convective line. Virtually none of these downstream effects extended beyond the anvil. At upper levels, the westerly flow perturbations extended through a very shallow layer near the tropopause, with maximum velocities of only 6 m s^{-1}. As observed in Chapter 5, the anvil condensate was for the most part passively advecting downstream in the mean environmental flow, while almost all of the compensating effects were propagating westward with the gravity waves. This pattern underscores the counter–intuitive nature of the environmental response to deep convective forcing, and reveals the perils of looking from *only* the storm–relative perspective.

Meridional asymmetries in the thermal field (Fig. 7.54) were not as strong as the zonal asymmetries. In and near the MCS, cooling dominated the lower troposphere and lower stratosphere with upper tropospheric heating sandwiched between. Outside the MCS, perturbations below 8 km were generally weak with no values exceeding 1 K above the density current. Between 8 and 12 km, weak warming extended northward from the condensate, while a layer of cooling extended northward between 12 and 14 km. Meridional winds, however, (Fig. 7.54) were quite asymmetric, especially at upper levels. Strong southerly perturbations extended along the northern anvil top between 9 and 14 km, reaching maximum speeds of 12 m s^{-1} just outside the condensate. To the south, northerly perturbations of 4–8 m s^{-1} were confined close to the condensate boundary. These asymmetries resemble the findings of Blanchard et al. (1997) who suggested that weak inertial stability aloft results in upper tropospheric accelerations on the northern side of an MCS. Negative absolute vorticities discussed above bolster this argument. The northward–directed synoptic pressure gradient also contributed to the asymmetries by retarding southerly flow and accelerating northerly flow around either side of the system.

Perturbation winds below 8 km resembled those in the zonal cross sections with northerly flow descending below the upper tropospheric southerly ascending flow. However, the meridional wind and thermal fields were not as directly correlated to one another as the zonal fields. As just discussed, the meridional velocity perturbations were more directly related to pressure gradient and inertial effects than gravity wave forcing. The lack of any vertical tilt or isolated maxima in the upper tropospheric/lower stratospheric heating/cooling north of the anvil suggests that it got there by advection rather than wave propagation.

7.6 Summary of convective effects

This MCS interacted with the surrounding atmosphere in a very systematic and focused way. As soon as convective storms developed over the mountains, deep tropospheric low frequency gravity waves propagated away, spreading heat and momentum adjustments in their wake. While waves from the first convective cells spread quasi–symmetrically in the zonal direction, all other waves, regardless of the mode, spread westward out the back side of the convective line. The resulting perturbations on the mean environmental flow resembled that of a leading–line/trailing–stratiform case. The condensate field did not reflect this, however since the ambient shear was so strong. Instead, almost all of the upper tropospheric cloud material passively advected eastward in the mean environmental flow. This separation of the gravity waves from the microphysical forcing made this case unique through most of the literature. Schmidt and Cotton (1990) were one of the few who have tried similar high–shear experiments, and the findings here are very similar to their two–dimensional results.

The exclusive westward gravity wave propagation is likely related to the upshear (westward) tilting of the equivalent heat source. In a series of idealized experiments, Fovell et al. (1992) and Pandya and Durran (1996) found that in a variety of shear and thermodynamic situations, gravity wave responses were focused in the direction of the heat source tilt. The results here concur with that theory, however it should be noted that none of those idealized experiments were conducted with strong upper tropospheric shear. More work needs to be done to compare the relative roles of strong shear aloft versus storm tilt.

The effects of the linear gravity waves upon the mid tropospheric upstream environment are summarized by the schematic in Figure 7.55. Pulsating convective cells are represented by the shaded disks, while the thin circles correspond to the wave fronts. In this idealized example, each wave front has the same intensity, and thus induces identical accelerations in the momentum field. As the waves propagate into the environment, the superposition of the component accelerations results in the strongest westerlies near the line center with strong northerly and southerly winds at either end of the line. This idealized pattern is very similar to the mid tropospheric environment–relative winds in both the Doppler (Fig. 5.11) and simulation (Fig. 7.14) data. In this way, convective cells are similar to sources in a phased array in that the superposition of the wave fronts dictates the shape of the response. However, since the effects are cumulative, the wave fronts do not have to be in phase to produce a coherent effect. Instead, the net accumulation of thermal and momentum perturbations from each cell determines the shape of the response. In this way, a line of convective cells that is pulsating completely at random will create a coherent, large scale environmental disturbance whose shape is dependent upon the orientation and tilt of the convection. This suggests that MCSs with linearly organized convection will affect the environment differently than those with more random convection. Clearly, more cases need to be studied to investigate the ramifications of this.

In addition to the linear waves, a nonlinear advective disturbance was produced when the vertical mass fluxes became very intense. Although the exact dynamics of this distur-

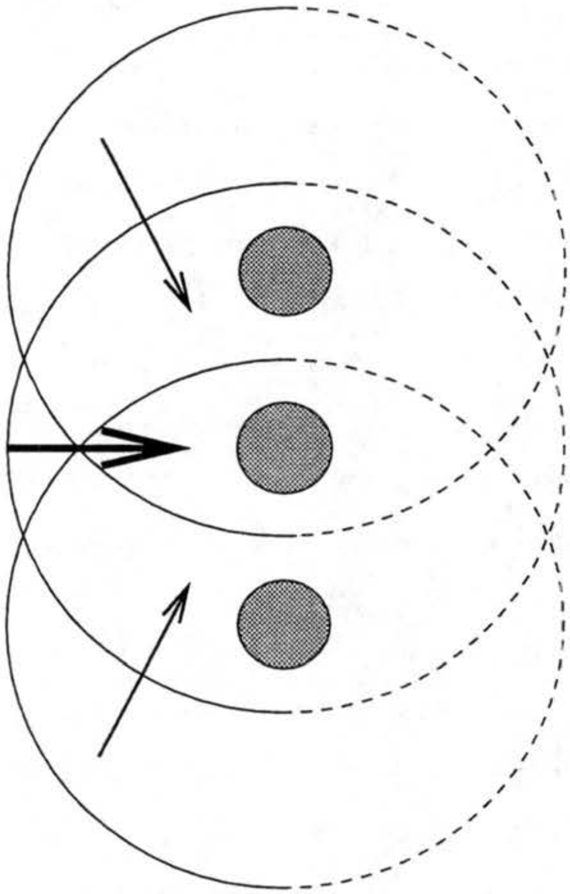

Figure 7.55: Conceptual model depicting the interaction between convectively generated gravity waves and the surrounding mid tropospheric environment. Each shaded disk represents a convective cell, while the open circles represent the leading edge of the gravity waves. In this case, all three convective cells intensified in unison, producing outwardly propagating $n2$ modes, which in turn induce net flow towards the line as depicted by the vectors. The superposition of the gravity wave effects is such that the strongest rear inflow occurs behind the central portion of the line. Although the wave fronts are drawn symmetrically for ease of display, most of the energy in the MCS studied here was focused towards the trailing side of the line. Also, since the horizontal wave numbers are so small, the same net horizontal flow pattern develops even when convection is pulsing out of phase.

bance remain unknown, it was likely associated with the direct injection of mass, heat and energy into the upper troposphere and lower stratosphere. The nonlinear mode was the only disturbance strong enough to punch upstream against the strong upper tropospheric flow, advecting condensate a significant distance upstream of the line. As viewed from above, the process looked very similar to the characteristic blossoming of the round, well defined anvil often observed in mid latitude MCCs. This process is not observed as often in weaker tropical oceanic convective clusters (Velasco and Fritsch, 1987). Herein lies a potentially critical difference between weak and strong convection. As weak convective cells perturb the atmosphere, the bulk of the energy propagates away as linear gravity waves. Heat and momentum are dispersed very efficiently as perturbations are induced in the far field by the passage of the wave fronts. Such was the case in the system studied herein before its interaction with the low level jet. The Rossby radius of deformation for these rapidly moving waves is quite large, thus convective heating is dispersed over a large area by the time inertial effects become important. However, when nonlinear advective disturbances become strong, heat and energy may not disperse as rapidly, especially in cases of weak to moderate shear. In the case studied herein, the nonlinear mode remained strong and coherent for hours, and its propagation speed was considerably slower than the gravity waves. Such a disturbance would have a smaller Rossby radius of deformation due to its slow movement. Thus, the energy density at the Rossby radius would be quite large, resulting in a greater projection onto the balanced scale.

At this point, many questions about this process remain unanswered. Again, more MCSs need to be studied to determine if nonlinear advective modes are important in the bulk of systems exhibiting sharply defined cold cloud tops. The quantitative aspects of the energy partitioning between the linear and the nonlinear modes needs to be investigated. Mapes (1993) suggests that although convection itself may possess significant nonlinearities the linear modes dominate at far distances. However, it is possible that proportionally less energy escapes into the far environment when convection, and thus the nonlinear response, is very strong.

Whether by linear or nonlinear processes, the rapid outward expansion of the convectively induced perturbations may be responsible the sudden transitions in MCS structure observed by Nachamkin et al. (1994). In that case, a pulsation in the upper tropospheric anvil was accompanied by a shift from ascent to descent in the rear inflow along with strengthening of the surface mesohigh and wake low. A strong $n2$ mode could easily produce these effects.

Chapter 8

DISCUSSION AND CONCEPTUAL MODELS

8.1 Convective focusing mechanisms over eastern Colorado

The consolidated structure of the MCS studied here was determined in a large part by its surrounding environment. On the synoptic scale, lifting associated with the anomalously strong upper tropospheric jet, combined with copious boundary layer moisture, provided considerable CAPE to the base–state atmosphere. In the absence of other forcing, wide-spread chaotic convection would likely have broken out over the entire area. In this case, however, topographically forced diurnal solenoids and a preexisting surface front focused convection in one intense, consolidated system.

The three–dimensional structure of the atmospheric forcing is summarized by the conceptual model in Fig. 8.1. Just after local noon, the first convection developed near mountain top along the up–branch of the mountain–plains solenoid (a and b in Fig. 8.1). With time, however, only those storms along the Palmer Divide survived the traverse onto the High Plains east of Denver. A three–dimensional flow structure similar to the horizontally homogeneous simulations of Tripoli (1986) was observed, in that the mountain–plains solenoid over the Palmer Divide (b in Fig. 8.1) was weaker due to the more uniform grade between the plains and the Continental Divide. Further north, the mountain–plains solenoid resembled that of Dirks (1969) and Tripoli and Cotton (1989a), with strong ascent near mountain top and subsidence over the lee side slopes (a in Fig. 8.1). A weaker secondary up–branch was also present just east of the mountain–plains slope interface. Superimposed upon these circulations was a shallower, meridional solenoid between the Palmer Divide and the Platte Valley (c in Fig. 8.1). This circulation provided boundary layer convergence and lifting along the divide and sinking over the valley.

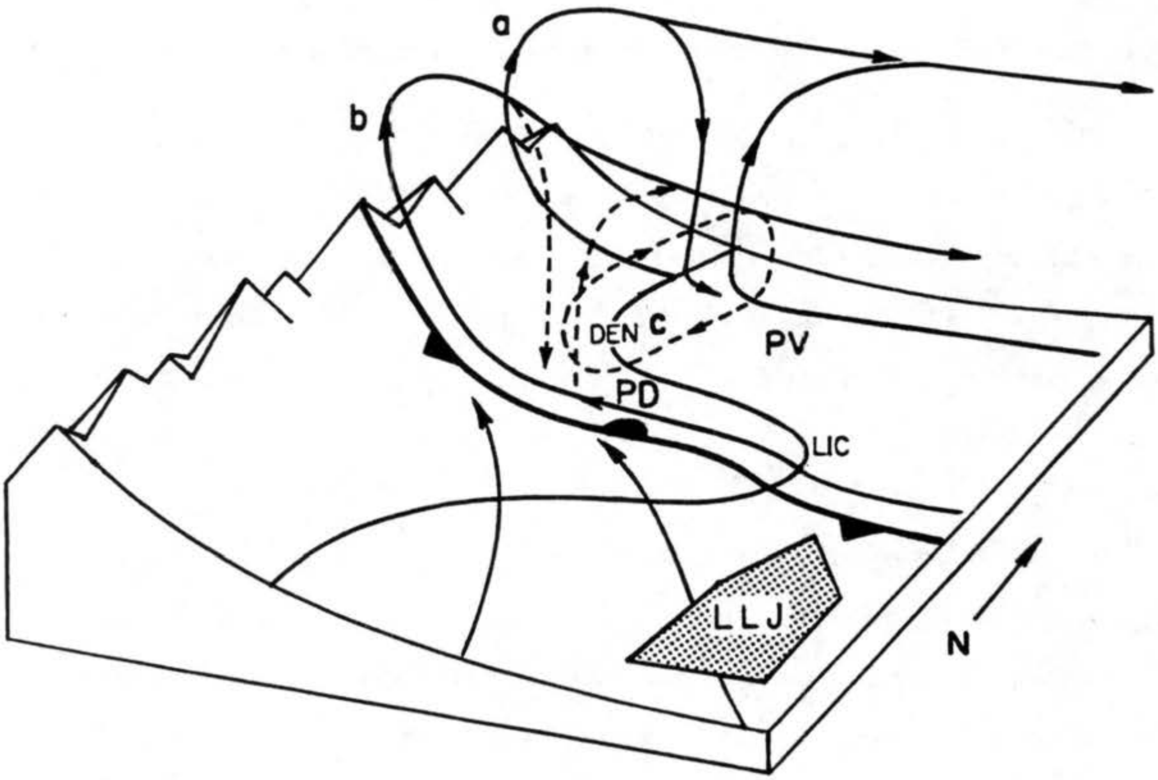

Figure 8.1: Conceptual model of the convective forcing elements over east central Colorado during the afternoon and evening of 19 July, 1993. The mountain–plains geography is depicted, along with the locations of the Palmer Divide (PD), Platte Valley (PV), and the cities of Denver (DEN) and Limon (LIC). The mountain–plains solenoids along the Platte Valley and Palmer Divide are shown respectively in circulations a and b, while the Palmer Divide–Platte Valley solenoid is depicted in circulation c. Solid streamlines indicate the strongest solenoidal flow. The surface frontal position is marked, and the low level jet is represented by the dark, wide arrow at the lower right.

In the absence of any other forcing, the weaker sinking motion aloft, combined with the boundary layer convergence along the length of the Palmer Divide, favored convection there. By the same token, convection in surrounding areas was inhibited by subsidence in the compensating branches of the solenoids. One particularly favored area was just east of DEN, where the up–branch of the Palmer Divide–Platte Valley solenoid overlapped the secondary up–branch of the mountain–plains solenoid. This region, which is often referred to as the Denver convergence and vorticity zone (DCVZ), is a statistical maximum for convective activity. Although the DCVZ is frequently associated with the Denver cyclone (Szoke et al. 1984), the cyclone was only weakly present in this case, suggesting that the solenoidal circulations were playing the dominant role.

In this case, a frontal zone was stalled along the Palmer Divide, where convergent flow had strengthened the baroclinicity and prevented the front from surging southward. Although the front was weak, in fact hardly discernable in the potential temperature field, differences in the cap strength across the front were important to the convective organization. Air south of the front was only weakly capped, and the boundary layer over most of southeastern Colorado mixed out, resulting in a deep, surface–based layer of warmer and drier air. North of the front, convection moved off the mountains, dissipated in the downstream subsidence zone, but failed to redevelop on the plains due to the strong capping inversion. Were this a horizontally homogeneous case, this convection would have likely redeveloped east of the mountain–plains subsidence zone as in Tripoli and Cotton (1989a). With the presence of the front, however, the only surviving convection propagated out along the Palmer Divide between the cool, capped air to the north and the warm, dry air to the south, feeding on both air masses.

The variations in the boundary layer depth influenced the structure of the low level jet. The deep warm layer over southeastern Colorado strongly contrasted with the shallower, cooler air near the Kansas border. Surface temperatures over Kansas remained cool due to wet soil from previous heavy rains, thus the cap never mixed out. The contrast resulted a strong, very localized zonal pressure gradient across southeastern Colorado. This in turn supported a small but intense jet which fed directly into the developing convection as it moved east of Limon (LIC in Fig. 8.1). Convection rapidly intensified after 2330 as it encountered the jet, producing the characteristic round, cold anvil as it did so.

The strong environmental forcing is reflected in the high accuracy of the model solution in comparison to the observations. The track, intensity, and for the most part even the convective structure were all well simulated. Not only were areas along the Palmer Divide favorable for convective development, but most other areas were unfavorable due to subsidence and/or variations in the strength of the capping inversion. This focusing role of the surrounding environment is often overlooked, especially in numerical studies of convection with horizontally homogeneous initial conditions. Although large convective systems can form in these situations, the boundary layer convergence for the updrafts is exclusively provided by the expansion of the lower tropospheric cold pool. Storm structure may be significantly altered when strong mesoscale convergence predates the development of a cold pool.

8.2 Interactions between convection and the environment

With such strong focusing, convection was able to develop into an intense, long–lived system. The corresponding effects on the environment were dependent upon the intensity and orientation of the convective heating over the area covered by the MCS. During the early stages of the MCS (before 2330 UTC), the integrated convective mass flux was of moderate strength and the environmental response was dominated by the rearward propagation of the linear gravity waves (Fig. 8.2a). As each mode passed, it left behind its own corresponding heat and momentum perturbations. Each individual pulse likely consisted of several superimposed modes. However, the MCS–average divergence profile as well as the resultant thermal and momentum perturbations indicate, as Mapes (1993) suggested, that the $n1$ and $n2$ modes dominated. In this case, the gravity wave energy propagated almost exclusively westward, depositing almost all of the perturbations to the rear (west) of the convective line. Fovell et al. (1992) and Pandya and Durran (1996) have shown that the gravity wave energy can be focused by the orientation of the heat source with respect to the vertical. In this case, since the net convective heat source leaned westward with height, most of the energy traveled westward as well. At the same time, the upper tropospheric shear

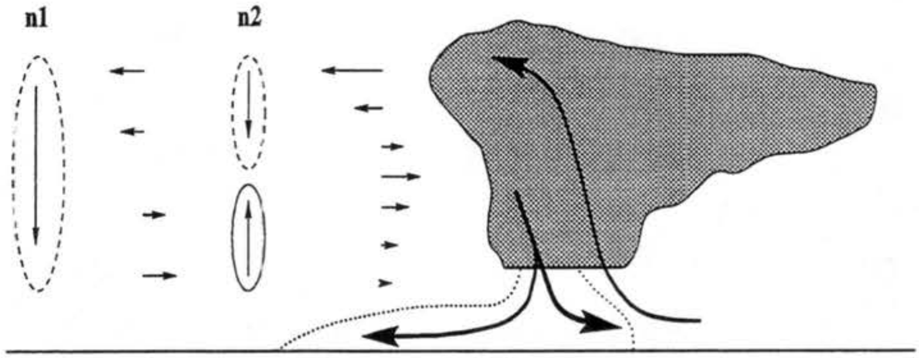

(a)

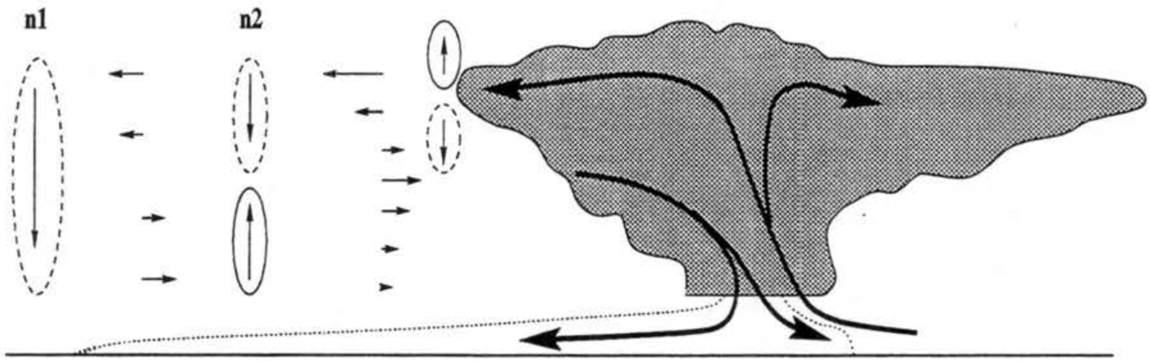

(b)

Figure 8.2: Conceptual model of the convectively induced environmental response in (a) the early MCS phase characterized by convection with moderate vertical mass flux, and (b) the late phase characterized by convection with strong vertical mass flux. The vertical motions associated with the linear gravity waves are are labeled with the appropriate mode. In (b), the vertical motions associated with the rearward expanding upper tropospheric nonlinear mode are unlabeled. The thick streamlines depict perturbation flow with respect to the ambient environment that was not induced by the gravity waves, while thin arrows depict the horizontal perturbation flow that was induced by the linear gravity waves. The gust front is represented by the dotted line, while the contiguous cloud shield is shaded.

advected most of the anvil condensate downstream. Thus, much of the heating to the rear of the line was primarily generated by convectively forced compensating motions. If these results are true for other systems exhibiting trailing stratiform anvils, then condensation heating within the stratiform region is likely playing only a secondary role in generating a large warm anomaly compared to the gravity wave forcing. This should not be surprising since by most estimates, 75 percent of the condensational heating in an MCS occurs within the convection (Gallus and Johnson, 1991).

It is important to understand that the divergence aloft during this early stage was primarily realized by the rearward propagation of the linear gravity waves. In essence, convection was perturbing the atmosphere, and the atmosphere was responding by producing the linear gravity waves that propagated away, *inducing* divergent flow in their wake. Since the perturbations left behind by these waves were not strong enough to reverse the upper tropospheric storm–relative flow, most of the upper tropospheric condensate ended up downstream. In this situation, individual parcels are not necessarily carried in the direction of energy propagation. Winds in the downstream anvil were basically not much different than those of the ambient environment, indicating that most of the condensate was *passively* advected along by the mean flow. In this configuration, most of the heat and energy quickly propagated away from the MCS in the gravity waves, leaving relatively little to be concentrated close to the initial convective disturbance.

However, once convection intercepted the low level jet and the vertical mass flux became large, a significant amount of heat, momentum and condensate began directly advecting away from the convective cores (Fig. 8.2b). This was manifested in a nonlinear disturbance near the tropopause that punched upwind, rapidly reversing the upper tropospheric storm–relative flow. Unlike the gravity waves, the nonlinear mode stayed coherent and relatively close to the convection for hours. Thus, the heat and momentum perturbations did not dissipate into the far field as quickly. The upper tropospheric condensate rapidly conformed to the shape of the disturbance, which led to the characteristically well defined, oval MCS anvil. A sustained maximum in mid tropospheric rear inflow did not propagate westward with the nonlinear disturbance, and instead rear inflow developed in–situ in the stratiform region and behind the leaning convective line. This suggests that something fundamentally different happened to the atmospheric response once convection became strong. A significant amount of the energy may have been directly advected into the environment in a nonlinear way as opposed to dispersing in the linear gravity wave modes. If this was the case, then these types of systems have an advantage over their weaker counterparts in that more energy stays concentrated near the system core. When this happens, the Rossby radius of deformation is smaller and the balanced component of the disturbance is stronger. Thus, any perturbation left behind after convection dissipates lasts longer and is more robust.

Chapter 9

SUMMARY

The fine–scale details of the interactions between an MCS and its surrounding environment were investigated using detailed observations and RAMS, a sophisticated numerical model. For this study, RAMS was run with four nested grids, the finest of which resolved the cloud–scale motions over the MCS as it moved across eastern Colorado. No convective parameterization of any kind was used. Instead, storms were allowed to develop from hot spots and convergence zones that evolved from the variably initialized topographical, soil and atmospheric fields. The results displayed considerable agreement with the observations, right down to the scale of the mesonet and dual Doppler derived winds. Such high accuracy was due to strong environmental forcing which consisted of the interaction between the topographic solenoids and a preexisting surface front. The strong agreement provided confidence that the model results in the unobserved, echo–free air were of high quality. Below is a summary of the significant findings that resulted from this work.

- Circulations along the Palmer Divide cut a well defined channel through the mountain–plains subsidence zone through which convection was highly favored. The mountain–plains solenoid was found to be much weaker over the Palmer Divide due to more uniform slope between the mountains and the plains. The lack of compensating subsidence prevented convection from collapsing over the Palmer Divide as it did further north.

- Strong convergence east of Denver resulted from the superposition of the up–branches of the mountain–plains and Palmer Divide–Platte Valley solenoids. The Denver cyclone was quite weak in this case.

- Convergence along the Palmer Divide strengthed a preexisting east–west frontal zone there. North of the front, advection of cool, moist air from the east strengthened the capping inversion and prevented convection from redeveloping east of the mountains. South of the front, the boundary layer mixed out, resulting in a deep layer of warmer, drier air over much of southern Colorado.

- Variations in the boundary layer depth between southeastern Colorado and southwestern Kansas resulted in the development of a small but intense low level jet. The jet was less than 200 km across, but velocities were 15 m s^{-1} greater than surrounding areas.

- The processes listed above deterministically confined convection to a very localized region, resulting in a consolidated system which in turn influenced the environment through very focused compensating motions. Low frequency linear gravity waves like those of Nicholls et al. (1991) and Pandya and Durran (1996) propagated well outside the contiguous anvil, leaving coherent heat and momentum disturbances in their wake. The responses were dominated by the $n1$ and $n2$ modes.

- The strong upper tropospheric shear advected most of the anvil condensate ahead of the convective line, in a way similar to that observed by (Grady and Verlinde, 1997). The separation of the diabatic and gravity wave induced responses provided a unique opportunity to study the relative strength of both processes.

- *Compensating motions were found to be highly asymmetric with respect to the convective line.* Although strong upper tropospheric shear advected most of the anvil debris eastward ahead of the line, gravity wave energy propagated almost exclusively westward out the back. When viewed with respect to the ambient environmental flow, gravity wave induced upper tropospheric front–to–rear and mid tropospheric rear–to–front perturbations trailed the line. However, only weak perturbations developed ahead of the line. Almost all of the environmental heating also traveled rearward with the gravity waves, leaving a long, concentrated zone of perturbation potential temperatures up to 5 K higher than surrounding areas. The results suggest that convective cells act like a phased array, focusing gravity wave energy in very specific directions.

- *The structure of the circular cold cloud top suggests a fundamental difference exists between moderate and strong convective clusters.* Before intercepting the low level jet, the integrated convective mass flux was of moderate strength, and the environmental response was dominated by the linear gravity waves. When the MCS intercepted the low level jet, however, the vertical mass flux more than tripled and an intense nonlinear disturbance centered near the tropopause punched outward from the convection. The cold cloud tops blossomed into the characteristic oval shape in the wake of the disturbance. Storm–relative winds reversed direction behind the line, carrying heat, momentum and condensate into the trailing environment. The leading edge did not propagate at a consistent speed, nor did it disperse with time like a gravity wave. Instead it stayed coherent for hours, eventually becoming stationary with respect to the ground. These properties indicate that a direct nonlinear upper tropospheric mass injection was traveling a significant distance away from the convection. Although the linear gravity waves were still present, considerable energy was also going into the advective mode. This suggests that intense MCSs and MCCs with well defined anvils have a significant advantage over their weaker counterparts in that proportionately less energy is lost to gravity waves.

9.1 Future research

This work poses many new questions about MCS convection and its interactions with the surrounding environment. A few suggestions for further research are listed below.

- The dynamics of the nonlinear upper tropospheric disturbance need to be more quantitatively studied. Heat and momentum fluxes emanating from several weak and strong convective complexes should be calculated to see how much energy actually escapes from each type. If the hypotheses in this work are true, then proportionately less energy will exist in the far field when convection gets strong. Ideally, the equations could be Reynolds averaged into the mean environmental and storm–induced components to calculate the fluxes from both the linear and nonlinear terms.

- The gravity wave subsidence pattern is sensitive to the orientation of the convective cells with respect to their vertical slope and with one another, and MCSs with varying convective organization may produce different environmental responses. Simple three–dimensional experiments could be conducted using groups of analytically specified heat sources with structures similar to Pandya and Durran (1996). By arranging the "cells" in varying patterns with respect to one another, the structure of the linear responses could be gauged.

- With respect to the convective environment in eastern Colorado, modeling and mesonet studies could be conducted in and near the Limon area to look for a climatological convergence zone similar to the DCVZ. Recall that in this study, and in Grady and Verlinde, (1997), new convective cells developed along a convergence zone ahead of the leading line near Limon. Tests with varying flow fields and different mesoscale environments would determine the existence and structure of a Washington County convergence zone (WCCZ).

- Experiments could be conducted to determine the strength of the environmental convective forcing in this case. Warm bubbles could be generated to produce convection in places other than where it originally developed. It would be interesting to see if an MCS inevitably develops in the same place, or if one convective cell in the "wrong" place could cause a different system to become dominant elsewhere. These tests could also determine the extent of the detrimental effects of subsidence on adjacent convective clusters. In that light, when the computer power becomes available, running the simulation with a cloud resolving grid large enough to contain both the Wyoming and Colorado MCSs would be quite interesting.

- Most importantly, focused observational studies need to be conducted well outside the contiguous MCS anvil to obtain reliable measurements of the phenomena discussed herein. Many of these observations could be conducted at relatively little expense by a well instrumented airplane flying along the southern and western periphery of a growing MCS. The ELDORA would be ideal for sensing any nonlinear modes in the upper tropospheric anvil. The sensitive radar is one of the only instruments available that could detect motions within the very low power returns of a newly formed anvil cloud. Sensitive pressure and vertical motion detectors could also be used to measure the linear gravity waves in the clear air. Other measurements could be taken from a mobile network of pressure sensors mounted on vehicles. In fact, a small version of such an experiment has already been successfully conducted (Mel Nicholls, personal communication). From a global modeling standpoint, these experiments would be useful in the development of large–scale convective parameterization schemes. To properly parameterize convection on that scale, the compensating environmental effects must be accounted for.

Chapter 10

REFERENCES

Alexander, D.G. 1995: The use of simulations of mesoscale convective systems to build a convective parameterization scheme. Ph.D. Thesis, Colorado State University, Dept. of Atmospheric Science, Fort Collins, CO 80523, 232 pp. (Atmospheric Science Paper No. 592).

Augustine J.A., and K.W. Howard, 1991: Mesoscale convective complexes over the United States during 1986 and 1987. *Mon. Wea. Rev.*, **119**, 911–919.

Avissar, R. and Y. Mahrer, 1988: Mapping frost-sensitive areas with a three-dimensional local-scale numerical model. Part I: Physical and numerical aspects. *J. Appl. Meteor.,* **27,** 400-413.

Bartels, D.L., and R.A. Maddox, 1991: Midlevel cyclonic vortices generated by mesoscale convective systems. *Mon. Wea. Rev.*, **119**, 104–118.

Bosart, L.F., and F. Sanders, 1981: The Johnstown Flood of July 1977: A long-lived convective system. *J. Atmos. Sci.,* **38,** 1616-1642

Battan, L.J., 1973: *Radar Observation of the Atmosphere.* The University of Chicago Press, 324 pp.

Bell, G.D., and J.E. Janowiak, 1995: Atmospheric circulation associated with the midwest floods of 1993. *Bull. Amer. Meteor. Soc.*, **76**, 681-695.

Bell, G.D., and L.F. Bosart, 1988: Appalachian cold–air damming. *Mon. Wea. Rev.*, **116**, 137–161.

Benjamin, S.G., K.A. Brewster, R. Brümmer, B.F. Jewett, T.W. Schlatter, T.L. Smith, and P.A. Stamus. An isentropic three–hourly data assimilation system system using ACARS aircraft observations. *Mon. Wea. Rev.*, **119**, 888–906.

Barnes, 1964: A technique for maximizing details in numerical weather map analysis. *J. Appl Meteor.*, **3**, 396-409

Blanchard, D.O., W.R. Cotton, and J.M. Brown, 1997: Mesoscale circulation growth under conditions of weak inertial stability. *Mon. Wea. Rev.*, **126**, 118-140.

Bluestein, H.B. and M.H. Jain, 1985: Formation of mesoscale lines of precipitation: severe squall lines in Oklahoma during the spring. *J. Atmos. Sci.,* **42,** 1711-1732.

Braham, R.R. and M. Draginis, 1960: Roots of orographic cumuli. *J. Appl. Meteor.,* **17,** 214-226.

Brandes, E.A., 1990: Evolution and structure of the 6-7 May 1985 mesoscale convective system and associated vortex. *Mon. Wea. Rev.*, **118**, 109-127.

Bretherton, C.S. and P.K. Smolarkiewicz, 1989: Gravity waves, compensating subsidence, and detrainment around cumulus clouds. *J. Atmos. Sci.* **46**, 740–759.

Brown, J.M., 1979: Mesoscale unsaturated downdrafts driven by rainfall evaporation: A numerical study. *J. Atmos. Sci.,* **36,** 313-338.

Buettner, K.J.K., and N. Thyer, 1965: Valley winds in the Mount Rainier area. *Archiv für Meteorologie, Geophysic und Bioklimatologie*, **B14**, 125–147.

Clark, T.L., and R.D. Farley, 1984: Severe downslope windstorm calculations in two and three spatial dimensions using anelastic interactive grid nesting: A possible mechanism for gustiness. *J. Atmos. Sci.,* **41,** 329-350.

Clark, T.L., and W.D. Hall, 1991: Multi–domain simulations of the time dependent Navier–Stokes equations: Benchmark error analysis of some nesting procedures. *J. Comput. Phys.* **92**, 456–481.

Cotton, W.R., M.S. Lin, R.L. McAnelly, and C.J. Tremback, 1989: A composite model of mesoscale convective complexes. *Mon. Wea. Rev.,* **117,** 765-783.

Cotton, W.R., G.D. Alexander, R. Hertenstein, R.L. Walko, R.L. McAnelly and M. Nicholls, 1995: Cloud venting - A review and some new global annual estimates. *Earth–Science Reviews*, **39**, 169–206.

Davies, H.C., 1983: Limitations of some common lateral boundary schemes used in regional NWP models. *Mon. Wea. Rev.*, **111**, 1002–1012.

Dempsey, D.P., and R. Rotunno, 1988: Topographic generation of mesoscale vortices in mixed-layer models. *J. Atmos. Sci.*, **45**, 2961–2978.

Douglas, R.H., 1964: Hail size distribution. *Proc. Eleventh Radar Wea. Conf.*, Boston, Amer. Meteor. Soc., 146–149.

Dirks, R., 1969: A theoretical investigation of convective patterns in the lee of the Colorado Rockies. Atmospheric Science Paper No. 145, Department of Atmospheric Science, Colorado State University, Fort Collins, Colorado, 80523, 122 pp.

Fosberg, M.A., 1967: Numerical analysis of convective motions over a mountain ridge. *J. Appl. Met.*, **6**, 889–904.

Fortune, M.A., W.R. Cotton and R.L. McAnelly, 1992: Frontal wave-like evolution in some mesoscale convective complexes. *Mon. Wea. Rev.*, **120**, 1279–1300.

Fovell, R., D.R. Durran, and J.R. Holton, 1992: Numerical simulations of of convectively generated stratospheric gravity waves. *J. Atmos. Sci.* **49**, 1427–1442.

Fritsch, J.M., 1975: Cumulus dynamics: Local compensating subsidence and its implications for cumulus parameterization. *Pure Appl. Geophys.,* **113,** 851-867.

Fritsch, J.M. and J.M. Brown, 1982: On the generation of convectively driven mesohighs aloft. *Mon. Wea. Rev.,* **110,** 1554-1563.

Fritsch, J.M., and R.A. Maddox, 1981a: Convectively driven mesoscale weather systems aloft. Part I: Observations. *J. Appl. Meteor.*, **20**, 9–19.

Fritsch, J.M., and R.A. Maddox, 1981b: Convectively driven mesoscale weather systems aloft. Part II: Numerical simulations. *J. Appl. Meteor.*, **20**, 20–26.

Fritsch, J.M., J.D. Murphy, and J.S. Kain, 1994: Warm core vortex amplification over land. *J. Atmos. Sci.*, **51**, 1780–1807.

Frank, W.M., 1983: The cumulus parameterization problem. *Mon. Wea. Rev.,* **111,** 1859-1871.

Fujita, T.T., 1963: Analytical Mesometeorology: A review. *Meteor. Monogr.*, **5**, 77-125.

Fujita, T.T., 1982: Principle of stereoscopic height computations and their applications to stratospheric cirrus over severe storms. *J. Meteor. Soc. of Japan*, **60**, 355-368.

Gal-Chen, T., 1978: A method for the initialization of the anelastic equations: Implications for matching models with observations. *Mon. Wea. Rev.*, **106**, 587–606.

Gallus, W.A., and R.H. Johnson, 1991: Heat and moisture budgets of an intense midlatitude squall line. *J. Atmos. Sci.*, **48**, 122-146.

Grady, R.L., and J. Verlinde, 1997: Triple Doppler analysis of a discretely propagating long–lived High–Plains squall line. *J. Atmos. Sci.* (in press)

Holton, J.R., 1967: The diurnal boundary layer wind oscillation above sloping terrain *Tellus*, **19**, 199–205.

Holton, J.R., 1992. *An introduction to dynamic meteorology.* Academic Press, 3rd edition, 511 pp.

Houze, R.A., Jr., S.A. Rutledge, M.I. Biggerstaff and B.F. Smull, 1989: Interpretation of Doppler weather radar displays of midlatitude mesoscale convective systems. *Bull. Amer. Meteor. Soc.*, **70**, 608–619.

Houze, R.A., Jr., B.F. Smull, and P. Dodge, 1990: Mesoscale organization of springtime rainstorms in Oklahoma. /it Mon. Wea. Rev., /bf 118, 613-654.

Houze, R.A., Jr., 1997: Stratiform precipitation in regions of convection: A meteorological paradox? *Bull. Amer. Meteor. Soc.*, **78**, 2179–2196.

Johnson, R.H., B.D. Miner, and P.E. Ciesielski 1995: Circulations between mesoscale convective systems along a cold front. *Mon. Wea. Rev.*, **123**, 585–599.

Johnson, R.H., and D.L. Bartels, 1992: Circulations associated with a mature–to–decaying midlatitude mesoscale convective system: Part II Upper level features. *Mon. Wea. Rev.*, **120**, 1301–1320.

Johnson R.H., and P.J. Hamilton, 1988: The relationship of surface pressure features to the precipitation and air flow structure of an intense midlatitude squall line. *Mon. Wea. Rev.*, **116**, 1444–1472.

Klemp, J.B. and R.B. Wilhelmson, 1978a: The simulation of three-dimensional convective storm dynamics. *J. Atmos. Sci.,* **35,** 1070-1096.

Klemp, J.B. and R.B. Wilhelmson, 1978b: Simulations of right- and left-moving storms produced through storm splitting. *J. Atmos. Sci.,* **35,** 1097-1110.

Klitch, M.A., J.F. Weaver, F.P. Kelly, and T.H. VonderHaar, 1985: Convective cloud climatologies constructed from satellite imagery. *Mon. Wea. Rev.* **113**, 326–337.

Klimowski, B. A., 1994: Initiation and Development of rear inflow within the 28–29 June 1989 North Dakota mesoconvective system. *Mon. Wea. Rev.*, **122**, 765–779.

Klitch, M.A., J.F. Weaver, F.P. Kelly, and T.H. VonderHaar, 1985: Convective cloud climatologies constructed from satellite imagery. *Mon. Wea. Rev.*, **113**, 326–337.

Lafore, J., and M.W. Moncrieff, 1989: A numerical investigation of the organization and interaction of the convective and stratiform regions of tropical squall lines. *J. Atmos. Sci.*, **46**, 521-544.

Laing, A.G., 1997: The large scale environment of mesoscale convective complexes: Comparisons with other deep convective weather systems. *Preprints, 22nd Conf. on Hurricanes*, Fort Collins, CO. Amer. Meteor. Soc., 415–416.

Laing, A.G., and J.M. Fritsch, 1993a: Mesoscale convective complexes over the Indian monsoon region. *J. Clim.*, **6**, 911–919.

Laing, A.G., and J.M. Fritsch, 1993b: Mesoscale convective complexes in Africa. *Mon. Wea. Rev.*, **121**, 2254–2263.

Laing, A.G., and J.M. Fritsch, 1997: The global population of mesoscale convective complexes. *Quart. J. Royal Met. Soc.*, **123**, 389–405.

Lanicci, J.M., and T.T. Warner, 1991a: A synoptic climatology of the elevated mixed–layer inversion over the southern Great Plains in spring. Part I: Structure, dynamics, and seasonal evolution. *Wea. and Forecasting*, **6**, 181–197.

Lanicci, J.M., and T.T. Warner, 1991b: A synoptic climatology of the elevated mixed–layer inversion over the southern Great Plains in spring. Part II: The life cycle of the lid *Wea. and Forecasting*, **6**, 198–213.

Lanicci, J.M., and T.T. Warner, 1991c: A synoptic climatology of the elevated mixed–layer inversion over the southern Great Plains in spring. Part III: Relationship to severe–storms climatology *Wea. and Forecasting*, **6**, 214–226.

Leary, C.A., and R.A. Houze, Jr., 1979: Melting and evaporation of hydrometeors in precipitation from the anvil clouds of deep tropical convection. *J. Atmos. Sci.*, **36**, 669–679.

Leise, J.A., 1981: A multidimensional scale-telescoped filter and data extension package. NOAA Tech. Memo. ERL WPL-82, Wave Propagation Lab., Boulder CO, 20 pp. [NTIS N82-31994]

LeMone, M.A., 1983: Momentum transport by a line of cumulonimbus. *J. Atmos. Sci.,* **40,** 1815-1834.

López, R.E., and R.L., Holle, 1986: Diurnal and spatial variability of lightning activity in northeastern Colorado and central Florida during the summer, *Mon. Wea. Rev.*, **114**, 1288–1312.

Louis, J.F., M. Tiedke and J.F. Geleyn 1981: A short history of the PBL parameterization at the ECMWF. Workshop on Planetary Boundary Layer Parameterization, Shinfield Park, Reading, United Kingdom, ECMWF, 59–80.

Loveland, T.R., J.W. Merchant, D.O. Ohlen, and J.F. Brown, 1991: Development of a land-cover characteristics database for the conterminous U.S. *Photo. Eng. Rem. Sens.*, **57**, 1453–1463.

Maddox, R.A, 1980: Mesoscale convective complexes. *Bull. Amer. Meteor. Soc.*, **61**, 1374–1387.

Maddox, R.A., 1983: Large-scale meteorological conditions associated with midlatitude, mesoscale convective complexes. *Mon. Wea. Rev.*, **111**, 1475–1493.

Maddox, R.A., D.J. Perkey and J.M. Fritsch, 1981: Evolution of upper tropospheric features during the development of a mesoscale convective complex. *J. Atmos. Sci.*, **38**, 1664–1674.

Mapes, Brian E., 1993: Gregarious Tropical Convection. *J. Atmos. Sci.,* **50,** 2026-2037.

Mahrer, Y. and R.A. Pielke, 1977: A numerical study of the airflow over irregular terrain. *Beitrage zur Physik der Atmosphere,* **50,** 98-113.

McAnelly, R.L., and W.R. Cotton, 1986: Meso-β-scale characteristics of an episode of meso-α-scale convective complexes. *Mon. Wea. Rev.,* **114,** 1740-1770.

McAnelly, R.L., and W.R. Cotton, 1989: The precipitation lifecycle of mesoscale convective complexes over the central United States. *Mon. Wea. Rev.*, **117**, 784–808.

McAnelly, R.L., and W.R. Cotton, 1992: Early growth of mesoscale convective complexes: A meso-β-scale cycle of convective precipitation?. *Mon. Wea. Rev.*, **120**, 1851–1877.

McAnelly, R.L., J.E. Nachamkin, W.R. Cotton, and M.E. Nicholls, 1997: Upscale evolution of MCSs: Doppler radar analysis and analytical investigation. *Mon. Wea. Rev.* **125**, 1083–1110.

McNider, R.T., and R.A. Pielke, 1981: Diurnal boundary–layer development over sloping terrain. *J. Atmos. Sci.*, **38**, 2198–2212.

Messinger, F. and A. Arakawa, 1976. Numerical methods in atmospheric models. GARP Publication Series No. 17. World Met. Org.

Miller, L.J., C.G. Mohr, and A.J. Weinheimer, 1986: The simple rectification to Cartesian space of folded radical velocities from Doppler radar sampling. *J. Atmos. Ocean. Tech.*, **3**, 162-174.

Miller, R., and J. McGinley, 1978: Using satellite imagery to detect and track comma clouds and the application of the zone technique in forecasting severe storms. General Electric MATSCO, Beltsville, MD.

Mohr, C.G., L.J. Miller, R.L. Vaughn, and H.W. Frank, 1986: The merger of mesoscale datasets into a common Cartesian format for efficient and systematic analyses. *J. Atmos. Oceanic Tech.*, **3**, 143-161.

Nachamkin, J.E., R.L. McAnelly, and W.R. Cotton 1994: An observational analysis of a developing mesoscale convective complex. *Mon. Wea. Rev.* , **122**, 1168–1188.

Nicholls, M.E., R.A. Pielke, and W.R. Cotton 1991: Thermally forced gravity waves in an atmosphere at rest. *J. Atmos. Sci.* **48**, 1869–1884.

Olsson and Cotton, 1997: Balanced and unbalanced circulations in a primitive equation simulation of a midlatitude MCC. Part II: Analysis of balance. *J. Atmos. Sci.*, **54**, 479–497.

Ooyama, K., 1964: A dynamical model for the study of tropical cyclone development. *Geofis. Intern.*, **4**, 187-198.

Orlanski, I., 1975: A rational subdivision of scales for atmospheric processes. *Bull. Amer. Meteor. Soc.*, **56**, 527-530.

Oye and Carbone, 1981: Interactive Doppler editing software. *Preprints, 20th Conf. on Radar Meteorology*, Boston, Amer. Meteor. Soc., 683-689.

Pandya, R.D. D. Durran, and C. Bretherton, 1993: Comments on "Thermally forced gravity waves in an atmosphere at rest." *J. Atmos. Sci.* **50**, 4097–4101.

Pandya, R.D. D. Durran, 1996: The influence of convectively generated thermal forcing on the mesoscale circulation around squall lines. *J. Atmos. Sci.* **53**, 2925–2951.

Parsons, D.B., C.G. Mohr, and T. Gal-Chen, 1987: A severe frontal rainband. Part III: Derived thermodynamic structure. *J. Atmos. Sci.*, **44**, 1615–1631.

Pratte, J.F., J.H. Van Andel, D.G. Ferraro, R.W. Gagnon, S.M. Maher, and G.L. Blair, 1991: NCAR's mile high meteorological radar. Preprints, *25th Conf. on Radar Meteorology*, Paris, France, Amer. Meteor. Soc., 863–866.

Raymond, D.J., and H. Jaing, 1990: A theory for long–lived mesoscale convective systems. *J. Atmos. Sci.*, **47**, 3067–3077.

Rotunno, R., J.B. Klemp, and M.L. Weisman, 1988: A theory for strong, long-lived squall lines. *J. Atmos. Sci.,* **45**, 463-485.

Rutledge, S.A., R.A. Houze, Jr., M.I. Biggerstaff and T. Matejka, 1988: The Oklahoma–Kansas Mesoscale Convective System of 10–11 June 1985: Precipitation structure and single-Doppler radar analysis. *Mon. Wea. Rev.*, **116**, 1409-1430.

Rutledge, S.A., P.C. Kennedy, and D.A. Brunkow, 1993: Use of the CSU–CHILL radar in radar meteorology education at Colorado State University. *Bull. Amer. Meteor. Soc.*, **74**, 25–31.

Silverman, B.A., 1960: The effect of a mountain on convection. *Cumulus Dynamics*, C.E. Anderson, ed., Pergamon Press, New York, 4–27.

Shapiro, M.A., and P.J. Kennedy, 1981: Research aircraft measurements of jet stream geostrophic and ageostrophic winds. *J. Atmos Sci.*, **38**, 2642-2652.

Schmidt, J.M., and W.R. Cotton, 1990: Interactions between upper and lower tropospheric gravity waves on squall line structure and maintenance. *J. Atmos. Sci.*, **47**, 1205–1222.

Schubert, W.H., and J.J. Hack, 1982: Inertial stability and tropical cyclone development. *J. Atmos. Sci.*, **39**, 1687–1697.

Skamarock, W.C., M.L. Wesman, and J.B. Klemp, 1994: Three–dimensional evolution of simulated long–lived squall lines. *J. Atmos. Sci.*, **51**, 2563–3584.

Smagorinsky, J., 1963: General circulation experiments with the primitive equations. Part I, The basic experiment. *Mon. Wea. Rev.,* **91**, 99-164.

Smith, R.B., 1989: Comment on "Low Froude number flow past three dimensional obstacles, Part I: Baroclinically generated lee vortices". *J. Atmos. Sci.*, **46**, 3611–3613.

Smolarkiewicz, P.K., and R. Rotunno, 1989: Low Froude number flow past three dimensional obstacles, Part I: Baroclinically generated lee vortices. *J. Atmos. Sci.*, **46**, 1154–1164.

Smull, B.F., and R.A. Houze, 1985: A midlatitude squall line with a trailing region of stratiform rain: Radar and satellite observations. *Mon. Wea. Rev.*, **113**, 117–133.

Smull, B.F., and R.A. Houze, Jr., 1987: Rear inflow in squall lines with trailing stratiform precipitation. *Mon. Wea. Rev.*, **115**, 2869–2889.

Storm Data, July, 1993. National Oceanic and Atmospheric Administration Environmental Data Series, **35** Ashville, NC.

Stumpf, G.J., 1988: Surface pressure features associated with a midlatitude mesoscale convective system in OK PRE-STORM. Atmos. Science Paper No. 435, Dept. of Atmos. Sci., Colorado State University, Ft. Collins, CO 80523, 148 pp.

Stumpf, G.J., R.H. Johnson, and B.F. Smull, 1991: The wake low in a midlatitude mesoscale convective system having complex convective organization. *Mon. Wea. Rev.*, **119**, 134–158.

Szoke, E.J., and R.H. Brady, 1989: Forecasting implications of the 26 July 1985 northeastern Colorado tornadic thunderstorm case. *Mon. Wea. Rev.*, **117**, 1834–1860.

Szoke, E.J., M.L. Weisman, J.M. Brown, F. Caracena and T.W. Schlatter, 1984: A subsynoptic analysis of the Denver tornado of 3 June 1981. *Mon. Wea. Rev.*, **112**, 790–808.

Toth, J.J., and R.H. Johnson, 1985: Summer surface flow characteristics over northeastern Colorado. *Mon. Wea. Rev.*, **113**, 1458–1469.

Tremback, C.J. and R. Kessler, 1985: A surface temperature and moisture parameterization for use in mesoscale numerical models. Preprints, 7th Conference on Numerical Weather Prediction, 17-20 June 1985, Montreal, Canada, AMS.

Tremback, C. J., 1990: Numerical simulation of a mesoscale convective complex: model development and numerical results. Ph.D. dissertation, Atmos. Sci. Paper No. 465, 247pp. [Available from the Dept. of Atmospheric Science, Colorado State University, Fort Collins, CO 80523.

Trier, S.B., and D.B. Parsons, 1993: Evolution of environmental conditions preceding the development of a nocturnal mesoscale convective complex. *Mon. Wea. Rev.*, **121**, 1078–1098.

Tripoli, G., and W.R. Cotton, 1989a: A numerical study of an observed orogenic mesoscale convective system. Part 1. Simulated genesis and comparison with observations. *Mon. Wea. Rev.*, **117**, 273–304.

Tripoli, G., and W.R. Cotton, 1989b: A numerical study of an observed orogenic mesoscale convective system. Part 2. Analysis of governing dynamics. *Mon. Wea. Rev.*, **117**, 305–328.

Velasco, I., and J.M. Fritsch, 1987: Mesoscale convective complexes in the Americas. *J. Geophys. Res.*, **92**, 9591–9613.

Walko, R., W.R. Cotton, M.P. Meyers, and J.Y. Harrington, 1995: New RAMS cloud microphysics parameterization. Part I: The single–moment scheme. *Atmos. Res.*, **38**, 29–62.

Weisman, M.L., 1992: The role of convectively generated rear-inflow jets in the evolution of long-lived mesoconvective systems. *J. Atmos. Sci.*, **49**, 1826–1847.

Weisman, M.L., 1993: The genesis of severe, long–lived bow echos. *J. Atmos. Sci.*, **50**, 645–670.

Weisman, M.L., and J.B. Klemp, 1984: The structure and classification of numerically simulated convective storms in directionally varying wind shears. *Mon. Wea. Rev.*, **112,** 2479-2498.

Weisman, M.L., W.C. Skamarock, and J.B. Klemp, 1997: The resolution dependence of explicitly modeled convective systems. *Mon. Wea. Rev.*, **125**, 527–548.

Wetzel, P.J, 1973: Moisture sources and flow patterns during the Northeast Colorado hail season. M.S. Thesis, Dept. of Atmospheric Science, Colorado State University, Fort Collins, CO.

Wetzel, P.J., W.R. Cotton and R.L. McAnelly, 1983: A long-lived mesoscale convective complex. Part II: Evolution and structure of the mature complex. *Mon. Wea. Rev.*, **111**, 1919–1937.

Wetzel, P.J., and J.T. Chang, 1988: Evapotranspiration from nonuniform surfaces: A first approach for short-term numerical weather prediction.*Mon. Wea. Rev.*,**116**, 600–621.

Wilczak, J.M., and T.W. Christian, 1990: Case study of an orographically induced, mesoscale vortex (Denver Cyclone). *Mon. Wea. Rev.* **118**, 1082–1102.